Studies on Bi_2O_3-ZnO-Nb_2O_5 based pyrochlore ceramics and thin films for microwave electronic applications

A thesis submitted for the degree of

DOCTOR OF PHILOSOPHY

By

Sudheendran K

School of Physics
University of Hyderabad
Hyderabad 500 046
India

August 2009

DEDICATED TO MY FAMILY

DECLARATION

I here by declare that the matter embodied in this thesis entitled "**Studies on Bi_2O_3-ZnO-Nb_2O_5 based pyrochlore ceramics and thin films for microwave electronic applications"** is carried out by me, under the supervision of **Dr. K. C. James Raju**, School of Physics, University of Hyderabad, Hyderabad, India.

K. Sudheendran

Place:
Date:

CERTIFICATE

This is to certify that the thesis entitled "**Studies on Bi_2O_3-ZnO-Nb_2O_5 based pyrochlore ceramics and thin films for microwave electronic applications**" submitted by **K. Sudheendran** to the University of Hyderabad is a bonafide work carried out by him under my supervision. The matter embodied in this thesis has not been submitted to any other institute or university for the award of any degree or diploma.

Place: Hyderabad

Date:

(Dr. K. C. James Raju)

Thesis Supervisor

Dean

Acknowledgements

I have great pleasure in expressing my gratitude to all those who have helped me. Many people have directly or indirectly contributed to the successful completion of this thesis.

I am deeply indebted to **Dr. K. C. James Raju**, for his guidance and support during the entire span of my doctoral research. Besides introducing me to the field of microwave materials and characterization techniques, the facilities and collaborations he established over the years have helped me enormously. He gave me unlimited freedom and I think that I have utilized it constructively.

I would like to extend my sincere appreciation to **Dr. M. Ghanashyam Krishna** for his constructive suggestions and continuous discussions throughout my research. His constant encouragement and experimental support have been crucial as far as my doctoral research is concerned. I sincerely thank my doctoral committee member **Prof. G. Rajaram** for his constant support and for introducing me to the world of micro fabrication techniques.

I take this opportunity to thank **Prof. Ram S. Katiyar** and **Dr. Manoj K. Singh**, University of Puerto Rico for helping me to do Raman measurements in my samples. I would also like to thank **Dr. Mohan V. Jacob** of James Cook University, Australia for carrying out cryogenic microwave measurements on some of my bulk ceramic samples. I also thank **Prof. Guru Subrahmanyam** of University of Dayton, USA for his constant interaction through emails for clearing my doubts regarding the broadband microwave characterizations techniques for thin films. His visit to our lab and interactions with him during various conferences helped us a lot in the establishment of the microwave characterization techniques for thin films. I would also like to express my sincere thanks to **Dr. S. R. Brahman** of CSR Indore for doing XPS measurements on my samples.

It is my pleasure to acknowledge, **Dr. Baruva** and **Dr. Bhatnikar**, **Mrs. Arunakumari** and **Mrs Vasundhara** of DLRL Hyderabad for extending their facilities and helping me to make photo masks for my test structures. I would also like to express my sincere thanks to Mr. **Kapil K. Jain** and **Mr. Dhahulkhandi** of SSPL Delhi for helping me to fabricate contact masks for my experiments. I would also like to express my sincere thanks to **Mr. Santheep Chathurvedi** and **Dr. G Saisaravanan**, GAETEC for their support. My heartfelt thanks are also to **Dr. A. R. James** of DMRL Hyderabad

and **Dr. N. Synu** BEL banglore for their timely help. I would also like to express my sincere thanks to **Dr. Madhurima**, Missoram University.

I am also extremely thankful to our dean **prof. C .Bansal** and former Deans **Prof. V S S Sastry& Prof. Vipin Srivastava,** for their support and providing the necessary facilities. I am also thankful to **Prof. R. Singh** for extending me the RF sputtering facilities. I would also like to thank other faculty members of school of physics. I would like to extend my sincere thanks to T. S. **Abilash**, school of physics for helping me to learn photolithography. I thank **Mr. Abraham** and other office staff of the school for their timely help on every occasion. I am thankful to all the staff members of the central instrumentation laboratory. I should express my sincere thanks to CMSD, University of hyderbad for providing necessary computational facilities. I should also express my sincere thanks to my Msc and Mphil supervisor **Prof.T.K Nambi Narayanan** of Pondicherry University who brought me to the field of dielectrics.

It is with enormous pleasure that I acknowledge the support and encouragements that I received from my colleagues and lab mates. **Mr. Venkatasaravanan** and **Mr. G. Lakhminarayana Rao** have especially helped me in my experiments. I also thank **Dr. Pamu**, **Dr. Kiran**, **Dr. Prasanth**, **Mr. Rajeeb Brahma**, **Mr. Vasu** , **Mr. Ram Babu, Mr Anil** and **Mr Bashaya** for their support.

I would not have reached here without the love, help, encouragement and support of friends from my school and college days. Some of them are Suresh, Toni, Jil, Biju, Ajith, Jeevan, Manoj, Seema, Sheri, Deepthi, Mumtaz, Rubeena, Sreekala, Sreerekha, Ramesh, Sasi, Rajeev, Hari, Ram Narayan, Krishankumar, Sunil, Lekha, Prajith, Mahesh, Rajan OA,OK, and Santhosh.

I would like to remember Vinu, Krishna prasad (ammavan), Wilson, Hema, Bharathi, Muruganadham, Damu, Kumar, Rugmini, Arout, Prathibha, Sajina, Fabiyola,Ramesh, chitra, sreelalitha, santhi and lisy who were my Msc classmates. I am also thankful to all my M. Phil class mates, especially to Girija, Geetha, Subhashree and Chithra. I am also greatful to Shibu, Rajesh, Harshan, Manu, Tinu, rexzy, sumesh and Raji, some of my friends from Pondicherry University.

Let me also thank my fellow researchers and friends from the School of Physics. Sanjeev, Basheed, Ashuthosh, Shinto, Yugendar, Lishma, Ravi, Deva, Sathish, Ramu, Swaroop, Riswan, Joji, Sultan, Gnanavel, Sandhya ,Sundhraya, Jayasree, Bari, Rajasree, Sudha, Juby, Sai preethi , Chaithaniya, Saipriya, Venkaya, Vijayan have always been exciting and encouraging. I consider myself fortunate in being able to continue my

association with some of my friends from Pondicherry University Santhesh, Dr, Dhamodharan, Dr. Bharathi mohan and Dr. Manimaran, Rajeev, Saravanan, Gnanavel, Harshan in the School of Physics.

There are many friends and comrades who made my stay in the University of Hyderabad during the last five years quite enjoyable and meaningful. I would like to express my sincere thanks to all my comrades of the University for their support. I would specially like to mention Rohith, Dr. Ajith, Dr. Sambit and Dr. Pradeep who have been of great help for me. I am thankful to Rajesh, mash, Anver, Azhar, Dinesh, Muneer, Stuvert, Reni, Siraj, Ali, Ashique, Ashly, Santhosh, Yasar and Viju who made my stay in the NRS a pleasant experience. I would also like to mention Masoom, Bheem, Bharath, Bhoopathi, Naresh, Paramesh, Jack, Vikram, Abishek, Teja, Shafeq, Soumesh, Shyju, Sharath, Guptha, Nelson, Deepanjan and Jayaram for their various helps and supports.

I acknowledge DLRL Hyderabad and University of Hyderabad for providing financial support through project associate ship and through revised fellowship scheme. I also thank CSIR, New Delhi for the award of Senior Research Fellowship. Facilities provided by NPSM, DLRL, ISRO, UGC DST and UPE are gratefully acknowledged. The financial assistance from UPE, DST, CSIR, and University of Hyderabad enabled me to attend the international conferences at Thailand, Japan and China. I would like to express my gratitude's to all the teachers who have been instrumental in molding me. Mrs. and Mr. **Prof. C. S. Bhat** were extremely supportive of us during the last couple of years during our stay at Doyance.

Above all, it is the constant sacrifice and ceaseless encouragements of **my parents** that made it possible for me to realize my goals and dreams. I also thank Suja and my in-laws and all my relatives for their moral support. And finally, this work would not have materialized without the inexhaustible support and complete understanding of my wife **Uma.**

CONTENTS

Preface

The pyrochlore in the Bi_2O_3-ZnO-Nb_2O_5 systems offers two related composition those are important for microwave applications. The compositions $Bi_{1.5}Zn_{1.0}Nb_{1.5}O_7$ (c-BZN) is suitable for tunable microwave devices and $Bi_2Zn_{2/3}Nb_{4/3}O_7$ (m-BZN) is suitable for LTCC and DR applications. c-BZN in thin film form is one of the few compositions known to exhibit voltage tunable dielectric properties out side the family of ferroelectrics. Being a non-ferroelectric, it is inherently capable of giving lower dielectric losses. More over the films of these materials are reported to have low crystallization temperature along with very low leakage characteristics which make them suitable as a high K dielectric layer in polymer electronics. Hence the c-BZN and m-BZN compositions in the Bi_2O_3-ZnO-Nb_2O_5 systems are chosen for a systematic study in this work. Understanding the behaviour of these dielectric materials with respect to variations in electric field field, temperature and frequency are of particular importance for the present day electronics. Most of the previous works are on the growth of poly crystalline BZN films on single crystal substrates such as sapphire and lanthanum aluminate. The growth of these films on a low cost, low loss and low dielectric permittivity substrate such as fused silica is important for the microwave application of these thin films. Its low dielectric constant permits the design of transmission lines of a wide range of impedances. Moreover, its low losses make it possible to obtain overall low losses for the device at a given impedance. However, growing crystalline thin films on amorphous substrates is challenging and requires serious process optimization which is an important objective in this study.

This thesis consists of seven chapters and a brief overview of each chapter of the thesis is as follows.

Chapter I

The first chapter gives a brief introduction to the development of the physics of dielectrics as an important area in solid state physics and material science. It discusses various theories about dielectric materials and classification of dielectric materials. This chapter also presents the details about the application of dielectric materials to microwave electronics and a brief review of tunable dielectrics and tunable microwave devices. It also discusses the importance of the development of non ferroelectric tunable dielectric materials. The importance of the Bi_2O_3-ZnO-Nb_2O_5 based pyrochlore ceramics is described. A detailed review of the work being carried out on these material systems is

discussed. Based on these understanding, the major objectives of the present study is identified and presented.

Chapter II

The second chapter describes the preparation and characterization techniques used for the BZN pyrochlore ceramics and thin films. The parallel capacitance (C) and the dissipation factor D for all the bulk samples were measured using an Agilent 4294A impedance analyzer in the frequency range of 100Hz-1MHz in a temperature range of 300 to 600K with a Lab –Equip temperature control unit. Dielectric Post (DP) resonator techniques have been employed for the microwave characterisation of the ceramic samples. An introduction to the pulsed laser deposition technique employed for the preparation of BZN thin films is also presented in this chapter. Characterization techniques such as EDAX, XPS and XRD used for the structure and composition analysis, AFM for microstructural analysis, envelope technique for optical properties and Raman studies for local structural analysis are discussed in detail. The details about the photolithography and lift off techniques developed for the fabrication of test devices and structures are given in this chapter. This chapter also contains the details of the parallel plate capacitor technique, Inter Digitated Capacitor (IDC) technique and MOS capacitor techniques used for the electrical and low frequency dielectric characterization of the BZN thin films grown on various substrates.

Chapter III.

The third chapter deals with the details about the microwave characterization techniques that are used for thin films. It gives a detailed description of the resonance, transmission and reflection techniques. The dielectric properties and loss tangent of the thin films grown on low dielectric constant substrates such as fused silica were characterized using the modified cavity perturbation technique and split post dielectric resonator (SPDR) technique. This chapter gives the details about the microwave netwok analysis, on-wafer measurements and calibration procedure. Details about the calibration comparison technique which makes use of two identical coplanar wave guide transmission lines patterned on the film and bare substrates for the broad band measurement of dielectric properties of thin films grown on various substrates are provided. The chapter also discusse about the circular patch capacitor technique used for the microwave characterization of permittivity, loss tangent and tunability of thin films grown on a conducting substrates. All the above mentioned techniques have been set-up and implemented as part of the current thesis.

Chapter IV

The fourth chapter gives the results of the structural, microstructural, dielectric and Raman analysis of the BZN ceramics prepared. c-BZN, m-BZN and titanium doped m-BZN ceramic systems were prepared using the solid state reaction method. All the reflections in the X-ray diffractogram show the formation of the cubic pyrochlore structure with all the major peaks corresponding to the Fd3m space group for c-BZN ceramics. For m-BZN ceramics with the monoclinic zirconolite like structure, all the major peaks could be indexed to the C2/c space group. As the Ti content increases the crystallite size start decreasing. As the Ti doping increases the grain morphology changes. The samples with higher percentage of Ti doping have shown needle type grain morphology. The measured dielectric constant and loss tangent for the c-BZN ceramics at 1MHz is found to be 134 and 1.2 $x10^{-3}$, respectively whereas the m-BZN ceramics is having a dielectric constant and loss tangent of 75 and $0.4x10^{-3}$ respectively. The dielectric constant is found to be increasing from 75 to 120 while the dielectric loss tangent is increased from 0.0002 to 0.061 with an increase in x value from 0 to 0.4. The Ti substituted ceramics shows dispersion in dielectric constant and corresponding increase in dielectric loss tangent, which shows a peak at about 200K when measured at a frequency of 3GHz. The peak in the dielectric loss tangent becomes more prominent with increase of Ti content. The temperature where the dielectric loss tangent peak appears is found to be decreasing slightly with the increase of titanium doping. The observed dielectric characteristics of the titanium doped m- BZN ceramics are attributed to the presence of a relaxation in these materials originating from the disorder caused by the Ti^{4+} substitution.

Chapter V

The fifth chapter deals with the results of the compositional, structural, microstrutural, optical and Raman analysis of the thin films of the bismuth zinc niobate systems deposited on various substrates. The composition and chemical state near the film surface were obtained by X-ray photo electron spectroscopy (XPS). It has seen that Bi, Zn, Nb, and O exist near the surface. No other impurity elements are detected in the spectrum up to 1200eV except carbon probably due to contamination. The XPS spectra of Bi 4f, Zn 2p and Nb 3d of the BZN thin films show that Bi, Zn and Nb ions are in the chemical state of 3^+, 2^+ and 5^+ states respectively This indicates that only one chemical state exists in the film for each Bi, Nb and Zn. From the XRD analysis it has seen that the as deposited

films were amorphous in all cases. After annealing above at 500°C or above, peaks of the cubic and monoclinic BZN could be detected in the respective cases. The crystallite size analysis reveals that there was a decrease in crystallite size with the increase in oxygen pressure during deposition. The investigation of the influence of oxygen pressure on the microstructure in the PLD grown BZN thin films revealed that the oxygen pressure can significantly alter the surface morphology of the as grown BZN thin films. The surface roughness of the BZN thin films increased with increase in annealing temperature.

Raman modes were observed at 139, 195, 251, 271, 337, 369, 537, 624, and 764 cm^{-1} in c-BZN thin films, which are comparable to the values in literature. The Raman modes in thin film are relatively more intense and additional Raman modes appear in thin films in the low frequency range. These results suggested that the local symmetry in thin films is different from that of the bulk due to strain in thin films. Raman modes are observed at 778, 849, 1053 cm^{-1} in m-BZN thin films, which are comparable to the earlier reported Raman spectra of m-BZN bulk materials with the same monoclinic symmetry. The Raman modes are broad due to the disorder of Zn^{2+} and Nb^{5+} on the B site of the pyrochlore structure.

The c-BZN film with a thickness of 420 nm deposited at 10 mTorr oxygen pressure shows a transmittance T of 90% at a wavelength of 546nm. The refractive index decreases with the increase in oxygen pressure. The as deposited films show a decrease in refractive index with increase in oxygen pressure from 2.52 to 2.36. Post deposition annealing, however, results in a relatively pressure independent refractive index of 2.55±0.2. All the films show optical band gap values of the orders of 3.30 to 3.60eV. The un annealed m- BZN films deposited at different oxygen pressures shows a transmittance T of 70-80% in the visible region. All the films show optical band gap values of the range of 3.50 to 3.60eV.

Chapter VI

The sixth chapter describes the electrical and microwave dielectric properties of BZN thin films grown on different substrates. The leakage characteristics of these materials in thin film form is also reported in this chapter. The leakage current density of these thin films is found to be in the range of 2-3 $\mu A/cm^2$ at 50KV/cm. From the analysis of the leakage current characteristics it has concluded that the conduction process in these thin films is predominantly electronic in nature. The leakage current in BZN thin films increased with the increase in annealing temperature and is attributed to the presence of

free electrons in these films produced by the formation of oxygen vacancies due to high temperature annealing. The leakage current is found to be higher for the films deposited at lower oxygen pressure which is attributed to the presence of large number of oxygen vacancies which will produce free conduction electrons in the films. The low frequency dielectric properties of these films grown on substrates such as MgO, fused silica, $LaAlO_3$ and sapphire (Al_2O_3) are measured using interdigitated capacitor geometry. The BZN thin films exhibit different dielectric behaviour when grown on different substrates. The films deposited on sapphire substrate exhibited larger dielectric constant as compared to films deposited on fused silica substrate. The microstructural analysis of these films revealed that films grown on fused silica substrates are having smaller grain size compared to that of the films grown on single crystal substrates. From the Raman analysis it was evident that the films grown on these substrates are under different stress state. There is a reduction of dielectric constant of BZN thin films grown on MgO and fused silica substrates which is attributed to the compressive stress in these films. The dielectric properties of c-BZN and m-BZN thin films deposited on p-type silicon substrates were studied using the MOS capacitor structures as a function of annealing temperatures. These studies found to be directly relevant to determine suitability of c-BZN and m-BZN thin films as gate dielectric in microelectronic devices and CMOS technology. The high frequency C-V behavior of these films shows the typical n-type MOS responce showing accumulation, depletion and inversion behaviours at the BZN- silicon interfaces. The microwave dielectric constant and loss tangent of the as deposited and annealed c-BZN thin films were measured at a spot frequency of 12.15GHz. It is observed that the as deposited amorphous films show low values of dielectric permittivity and loss tangent when compared to that of the annealed crystalline films. The low value of the dielectric constant of amorphous films implies that the formation of the electrical polarization is largely suppressed in the amorphous films. After annealing at 600°C these films exhibit high dielectric constant. It is observed that there is a strong dependence of the microwave dielectric constant and loss tangent (tanδ) on the oxygen pressure during deposition. The dielectric constant of c-BZN films varied from 95-126 where as the dielectric loss tangent varied from 0.005 to 0.0075 with a variation of deposition pressure from 1-10 mTorr. The microwave dielectric constant and loss tangent of the annealed m-BZN thin films measured at a spot frequency of 10GHz using the SPDR techniques. It is observed that there is a strong dependence of the microwave dielectric constant and loss tangent (tanδ)

on the deposition pressure. The dielectric constant varied from 56-71 where as the dielectric loss tangent is varied from 1.4 $x10^{-3}$ to 2.5 x 10^{-3} as the pressure varied from 2 to 10 m Torr. Broadband microwave dielectric properties of c-BZN and m-BZN thin films deposited on various substrates were determined using the calibration comparison technique.

The tunability studies on c-BZN thin films revealed that the films grown at 10 m Torr of oxygen pressure is having relatively high tunability with higher quality factor a combination suitable for tunable microwave devices. The quality factors for the thin films deposited above 10 m Torr of oxygen pressure decreases and this may be due to the leakage conduction produced due to the interstitial oxygen atoms. The tunability of c-BZN thin films on sapphire substrates was approximately around 4.8% at 10KV/cm. The loss tangent of this film on sapphire substrates at 10GHz was estimated to be approximately 0.0049 at 100V. Similarly the calculated dielectric permittivity for the c-BZN thin films grown on fused silica is 125.73 (at zero bias) and 122.07 (at 10KV/cm). The estimated tunability for c-BZN films on fused silica substrate was 2.91% at the measurement frequency of 10 GHz. Interdigitated and parallel plate varactors were fabricated and characterized on fused silica substrates and platinised silicon substrates respectively. The IDC varactors realized on fused silica substrates showed a tunability of 9% with a Q factor of 38. The observed Q factor on fused silica substrates is found to be comparable to the reported Q factor of BST thin films based varactors on single crystal substrates. The c-BZN thin films on fused silica substrates seem to be a very promising technology for the realization of low cost tunable varactors.

Chapter VIII

The seventh chapter will present the major conclusions drawn from the present study and it also gives some scope for future works on these systems.

Chapter 1

INTRODUCTION

1.1 *D*ielectric materials and their technological importance *in* modern industry

Electrical insulator materials which will prevent the flow of current in an electrical circuit are being used since from the beginning of the science and technology of electrical phenomena. Dielectrics are insulating materials that exhibit the property of electrical polarization, thereby they modify the dielectric function of the vacuum.

The first capacitor was constructed by Cunaeus and Mussachenbroek in 1745 which was known as Leyden jar [1]. But there were no studies about the properties of insulating materials until 1837. Faraday published the first numerical measurements on these materials, which he called dielectrics [2]. *He* has found that the capacity of a condenser was dependent on the nature of the material separating the conducting surface. This discovery encouraged further empirical studies of insulating materials aiming at maximizing the amount of charge that can be stored by a capacitor. Throughout most of the 19^{th} century, scientists searching for insulating materials for specific applications have become increasingly concerned with the detailed physical mechanism governing the behavior of these materials. In contrast *to* the insulation aspect, the dielectric phenomena have become more general and fundamental, as it has the origin with the dielectric polarization.

Mossotti [3, 4] and Clausius [5] have done a systematic investigation about the dielectric properties of materials. They attempted to correlate the specific inductive capacity, a macroscopic characteristic of the insulator introduced by Faraday [2] which is now popularly termed as dielectric constant with the microscopic structure of the material. Following Faraday in considering the dielectrics to be composed of conducting spheres in a non-conducting medium, Clausius and Mossotti succeeded in deriving a relation between the real part of the dielectric constant ε_r and the volume fraction occupied by the conducting particles in the dielectric.

In the begning of 20^{th} century, Debye [6] realized that some molecules had permanent electric dipole moments associated with them, and this molecular dipole moment is responsible for the macroscopic dielectric properties of such materials. Debye succeeded in extending the Clausius -Mossotti theory to take into account the permanent

moments of the molecules, which allowed him and others to calculate the molecular dipole moment from the measurement of dielectric constant. His theory was later extended by Onsager [7] and Kirkwood [8, 9] and is in excellent agreement with experimental results for most of the polar liquids. Debye's other major contribution to the theory of dielectrics is his application of the concept of molecular permanent dipole moment to explain the anomalous dispersion of the dielectric constant observed by Drude [10]. For an alternating field, Debye deduced that the time lag between the average orientation of moments and the field becomes noticeable when the frequency of the field is within the same order of magnitude as the reciprocal relaxation time. This way the molecular relaxation process leads to the macroscopic phenomena of dielectric relaxation, i.e., the anomalous dispersion of the dielectric constant and the accompanying absorption of electromagnetic energy over certain range of frequencies.

Debye's theory shows excellent agreement with the experiments for the polar liquids while the dielectric behaviour for solids was found to be deviating considerably. Several modifications and extensions of Debye's theory have been proposed to correct this. There are two major approaches in the extension of Debye's theory. The first approach, pioneered by Cole [11], Davidson [12] and William [13], interprets the non –Debye relaxation behavior of the material in terms of the superposition of an exponentially relaxing process, which then leads to a distribution of relaxation times. The second approach by Joncher [14] proposes that the relaxation behaviour at the molecular level is intrinsically non-Debye-like due to the cooperative molecular motions.

After more than eighty years of development, the theory of dielectrics is still a active area for research. Understanding the behaviour of dielectric materials with the variations of field, temperature and frequency is of particular importance for present day electronics. Modern day electronics demand dielectric materials with narrowly defined properties tailored for particular applications. The scaling of metal-oxide-semiconductor (MOS) devices for ultra large-scale integration (ULSI) applications has been placing an ever-increasing burden upon the performance of gate dielectrics [15]. Durability has become an issue as the dielectric thickness is decreased leading to a search for dielectrics with better properties than the conventional SiO_2 dielectric. The gallium arsenaide (GaAs) based metal - insulator- semiconductor field effect transistor (MISFET) is still largely unavailable due to the lack of a suitable dielectric material for the insulation layer [16]. Recent advances in wireless communication technologies have elevated the interest in materials with the unusual combination of properties like high dielectric constant, low

dielectric loss and low values of temperature dependence of dielectric constant [17]. The constant need for miniaturization provides a continuing driving force for the discovery and the development of increasingly sophisticated materials to perform the same or improved function with decreased size and weight. The dielectric materials mentioned above are used as the basis for resonators and filterers for the microwaves carrying the desired information [18]. These materials are presently employed as bulk ceramics in microwave communication devices. They are not integrated into the microelectronics but are being used as discrete components. The need for better dielectrics with improved properties suitable for modern integrated manufacturing needs is the motivation behind the present study.

1.2 Theory of dielectrics

This section presents a brief description of the atomic interpretation of the dielectric and optical properties of insulator materials on the basis of classical theory. This section is essentially concerned with the static dielectric constant, the frequency dependence of dielectric constant and dielectric losses.

1.2.1 Electric susceptibility and permittivity

It was Michael Faraday who first noticed that when a capacitor of value C_0 under vacuum is filled with a dielectric material, its charge storage capacity (capacitance) increases to a value of C. The ratio χ' of the increase of capacitance $\Delta C = C - C_0$ to its initial capacitance- C_0,

$$\chi' = \frac{C - C_0}{C} = \frac{\Delta C}{C_0} \qquad (1.1)$$

χ' is called the electrical susceptibility of the dielectric. The most often used terminology is the dielectric permittivity or dielectric constant instead of susceptibility, which is defined as the ratio of the capacitance C of the capacitor filled with a dielectric to the value C_0 of the same capacitor under vaccum.

$$\varepsilon_r = \frac{C}{C_0} \qquad (1.2)$$

From the above equations the relationship between the electric susceptibility and the dielectric permittivity is given as:

$$\chi' = \varepsilon_r - 1 \qquad (1.3)$$

Thus, by definition, the electric susceptibility and permittivity are non-dimensional real quantities. The dielectric constant or permittivity of a material is a measure of the extent to which the electric charge distribution in the material can be distorted or polarized by the application of an electric field.

1.2.2 Mechanism of electric polarization

At the atomic level, all matter consists ultimately of positively and negatively charged particles whose charges balance each other macroscopically in the absence of an electric field giving rise to overall charge neutrality. Once the electric field is applied, the balances of charges are perturbed by the following four basic polarization mechanisms [19].

Electronic polarization: It occurs in neutral atoms when an electric field displaces the nucleus with respect to the negative charge. Thus electronic polarization is an induced polarization effect.

Atomic/ionic polarization: It is observed when different atoms that comprise a molecule share their electrons asymmetrically, and cause the electron cloud to be shifted towards the stronger binding atom, the atoms acquire charges of opposite polarity and an external field acting on these net charges will tend to change the equilibrium positions of the atoms themselves, leading to the atomic polarization.

Dipolar/orientational polarization: When an ionic bond is formed between two molecules by the transfer of some valence electrons, a permanent dipole moment will originate in them. This permanent dipole moment is equal to the product of the charges of the transferred valence electrons and the inter-atomic distance between them. In the presence of an electric field E, the molecules carrying a permanent dipole moment will orient to align along the direction of the electric field E. This process is called the dipolar or orientational polarization. This occurs only in dipolar materials possessing permanent dipole moments.

Space charge polarization: It is present in dielectric materials which contain charge carriers that can migrate for some distance through the bulk of the material (via diffusion, fast ionic conduction or hopping, etc.) thus creating a macroscopic field distortion. Such a distortion appears to an outside observer as an increase in the capacitance of the sample and may be indistinguishable from the real rise of the dielectric permittivity. Space charge polarization is the only type of electrical polarization that is accompanied by macroscopic charge transport (and in the case when the migrating charge carriers are ions a macroscopic mass transport as well). In general, the space charge polarization can be

grouped into hopping polarization and interfacial polarization. In dielectric materials, localized charges (ions and vacancies, or electrons and holes) can hop from one site to another site, which creates the hopping polarization. Similarly the separation of the mobile positive and negative charges under an electric field can produce an interfacial polarization.

1.2.3 Polarization and dielectric constant

The ability of a dielectric material to store electric energy under the influence of an electric field, results from the field-induced seperation and alignment of electric charges. Polarization occurs when the electric field causes a separation of the positive and negative charges in the material. The larger the dipole moment arms of this charge separation in the direction of a field and the larger the number of these dipoles, the higher the material's dielectric permittivity.

In the presence of electronic, ionic and dipolar polarization mechanisms, the average induced dipole moment per molecule P_{av} will be the sum of all the contributions in terms of the local field (effective field) acting on each individual molecule.

$$P_{av} = \alpha_e E_{loc} + \alpha_i E_{loc} + \alpha_d E_{loc} \tag{1.4}$$

Here, α_e, α_i, α_d are the electronic, ionic and dipolar polarizabilities. E_{loc} is the local field or the effective field at the site of an individual molecule that causes the individual polarization. Each effect adds linearly to the net dipole moment of the molecule. Interfacial polarization cannot be simply added to the total polarization as $\alpha_{ij}E_{loc}$ because it occurs at the interfaces and cannot be put into an average polarization per molecule in bulk. Moreover, the fields are not well defined at the interfaces.

For simple dielectrics (eg. gases) one can take the local field to be the same as the macroscopic field. This means that E_{loc}=E the applied field and therefore the polarization is,

$$P = \chi_e \varepsilon_e E = (\varepsilon_r - 1)\varepsilon_0 E \tag{1.5}$$

$P = N.P_{av}$ where N is the number of atoms or molecule per unit volume [20].

$$\varepsilon_r = 1 + N\alpha/\varepsilon_0 \tag{1.6}$$

α is the polarizability of the molecule.

1.2.4 Clausius and Mossotti relation for dielectric permittivity

Consider a molecule of a dielectric medium situated in a uniform electric field E. The total electric field acting on this molecule E_{loc} will have three main components- E_1, E_2, and E_3. Here E_1 is the applied electric field E, E_2 is the field from the free ends of the dipole chain and E_3 is the near field arising from the individual molecular interactions. In solids we have to consider the actual effective field acting on a molecule in order to estimate the dielectric permittivity. For electronic and ionic polarization, the local field for cubic crystals and isotropic liquids can be given by the Lorenz field, given by

$$E_{loc} = \frac{1}{3\varepsilon_0} P \tag{1.7}$$

By assuming the near field E_3 is zero, Clausius and Mossotti derived a relation for the dielectric constant of a material under electronic and ionic polarization [21].

$$\frac{\varepsilon_r - 1}{\varepsilon_r + 2} = \frac{1}{3\varepsilon_0}\left(N_i \alpha_i + N_e \alpha_e\right) \tag{1.8}$$

Here, ε_r is the relative permittivity at low frequencies, α_i is the effective ionic polarizability per ion pair, N_i is the number of ions pair per unit volume, α_e is the electronic polarizability and N_e is the number of ions (or atoms) per unit volume exhibiting electronic polarization. The atomic/ionic polarizability α_i and the electronic polarizability α_e cannot be separated at low frequencies and hence they are together represented as the induced polarizability α_{ind}

Hence equation 1.8 can be written as:

$$\frac{\varepsilon_r - 1}{\varepsilon_r + 2} = \frac{1}{3\varepsilon_0}\left(N_m \alpha_{ind}\right) \tag{1.9}$$

This is known as the clausius –Mossotti equation for non polar dielectrics.

Above the frequencies of ionic polarization relaxation, only electronic polarization will contribute to the relative permittivity, which will be lowered to $\varepsilon_{r\infty}$ (relative permittivity at optical frequencies).

$$\frac{\varepsilon_{r\infty} - 1}{\varepsilon_{r\infty} + 2} = \frac{N_e \alpha_e}{3\varepsilon_0} \tag{1.10}$$

By using the Maxwell relation for a lossless (non-absorbing), non magnetic medium,

$$n^2 = \varepsilon_{r\infty} \tag{1.11}$$

where n is the index of refraction of the material, equation (1.10) can be rewritten as:

$$\frac{n^2-1}{n^2+2} = \frac{N_e \alpha_e}{3\varepsilon_0} \tag{1.12}$$

In this form, it is known as Lorentz-Lorenz equation. It can be used to approximate the static dielectric constant ε_r of non polar and non magnetic materials from their optical properties. In the case of dipolar materials we cannot use the simple Lorentz field approximation and hence the Clausius–Mossotti equation cannot be used in the case of dipolar materials.

1.2.5 Debye theory for polar dielectrics

In addition to the induced polarization present in all dielectrics, the polar dielectrics possess an orientational polarization that exists even in the absence of an applied electric field. It should be noted that the polarizability α_o corresponding to the orientational polarization is related to the orientation of the molecules which are heavier than that of atoms or electrons that are involved in induced polarization. Hence the α_o contributes to the total molecular polarizabilty α at much lower frequencies than α_{ind} does. So the dielectric constant that remains after the relaxation of orientational polarization (the dielectric constant due to the induced polarization) can be designated separately and it is usually represented by ε_∞ in the case of dipolar dielectrics. So the equation (1.9) can be written as:

$$\frac{\varepsilon_\infty - 1}{\varepsilon_\infty + 2} = \frac{N_m}{3\varepsilon_0}\alpha_{ind} \tag{1.13}$$

To account for the orientational contribution to the dielectric constant, Debye [22] used classical Boltzman statistics and the Langevin function $L(y) = \coth y - \frac{1}{y}$ from the theory of paramagnetism, to estimate the temperature dependence of permanent dipole orientation. Assuming that these dipoles do not interact with each other, Debye derived the following equation for the orientational polarizability.

$$\alpha_o = \frac{\mu^2}{3KT} \tag{1.14}$$

Using Clausius-Mosotti's internal field argument discussed above, this additional polarization contributes to the static dielectric constant according to the following formulae:

$$\frac{\varepsilon^1 - 1}{\varepsilon^1 + 2} = \frac{N_m}{3\varepsilon_0}\alpha_{ind} + \frac{N_d}{3\varepsilon_0}\alpha_o \tag{1.15}$$

Here N_d is the number of dipolar molecules per unit volume which is same as N_m.
This equation can be rewritten in the following form using equation (1.13).

$$\frac{\varepsilon^1 - 1}{\varepsilon^1 + 2} - \frac{\varepsilon_\infty - 1}{\varepsilon_\infty + 2} = \frac{N_d \mu^2}{9\varepsilon_0 KT} \tag{1.16}$$

This result, from Debye [23], has been used successfully to predict the static dielectric constant of many polar gases and polar liquids. However, when applied to the condensed state of matter, Debye's theory breaks down while predicting the infinite dielectric susceptibility (Mosotti catastrophe). The reason for this breakdown lies in the assumption that is made in the expression for the Clausius-Mosotti local field. The near field in this case is assumed to be zero. In the condensed phase, permanent dipoles tend to loose their individual freedom of orientation through association and steric hindrance. Their interaction with their surroundings has to be taken into account and the near field cannot be neglected.

1.2.6 Onsager theory

To avoid the Mossotti catastrophe, Onsager modified the Debye theory by introducing a cavity. In his new approach to the problem, the electric field was represented by the sum of a 'cavity field' and a 'reaction field'. If the surroundings of each molecule are considered to be a homogeneous continuum having the macroscopic properties of the substance, then the 'cavity field' is the field inside a cavity of molecular dimensions due to a uniform external field. This cavity field is the field in the cavity resulting from the polarization induced in the surrounding medium by the molecule in the cavity. This part of the field exerts no torque on the molecule. Onsager's molecular model consisted of a sphere with a permanent dipole moment and an isotropic polarizability. Based on this model he arrives at the following expression, linking the molecular dipole moment with the static dielectric constant:

$$\frac{\varepsilon^1 - 1}{\varepsilon^1 + 2} - \frac{\varepsilon_\infty - 1}{\varepsilon_\infty + 2} = \frac{3\varepsilon^1(\varepsilon_\infty + 2)}{(2\varepsilon^1 + \varepsilon_\infty)(\varepsilon^1 + 2)} \frac{N_d \mu^2}{9\varepsilon_0 KT} \tag{1.17}$$

Onsager's relation is quite well satisfied for non associated polar liquids [24, 25] and can also be applied to weakly bound Van der Waals solids. In general, most of the solid dielectrics do not obey any of the local field expressions at sufficiently low frequencies due to the charge carriers present in these materials, mostly ions, but possibly also electrons. This renders any meaningful measurement of the low frequency dielectric permittivity very difficult, making the comparison with local field theory rather doubtful.

1.2.7 Dielectric loss

The permittivity of a dielectric material has both real and imaginary mathematical representations. The imaginary part of permittivity is represented in mathematical equations as ε^{II}. This imaginary part of permittivity describes the energy loss from an AC signal as it passes through the dielectric. The real part of permittivity, ε_r is also called the dielectric constant and relative permittivity. The permittivity of a material describes the relationship between an AC signal's transmission speed and the dielectric material's capacitance. When the word "relative" is used in front of permittivity, the implication is that the number is reported relative to the dielectric properties of a vacuum**.** The imaginary part of the dielectric permittivity which is a measure of how much field is lost as heat during the polarization of a material by an applied alternating electric field is also termed as dielectric loss. The characteristic orientation of the dipoles in an electric field results in a frequency variation of dielectric constant and loss over a broad band of frequencies. The typical behavior of real and imaginary part of the permittivity as a function of frequency is show in Figure 1.1 [26].

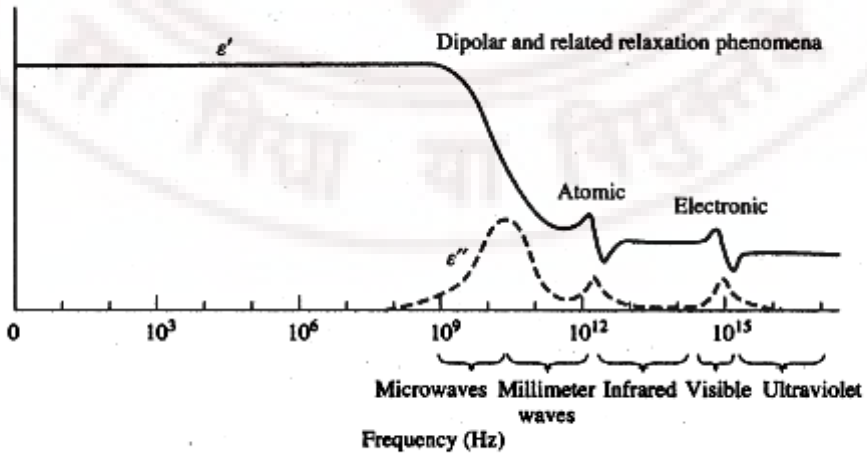

Figure1.1 Frequency dependence of dielectric permittivity for an ideal dielectric material.

The relative permittivity of material is related to a variety of physical phenomena that contribute to the polarization of the dielectric material. In the low frequency range the ε^{11} is dominated by the influence of ion conductivity. The variation of permittivity in the microwave range is mainly caused by dipolar relaxation, and the absorption peaks in the infrared region and above, are mainly due to atomic and electronic polarizations.

The dielectric properties of solid dielectrics at microwave and radio frequencies are highly influenced by the ionic positions and changes caused by the lattice vibrations. Two types of dielectric losses are identified in crystalline solids at high frequencies, namely intrinsic losses and extrinsic losses. The dielectric dispersion in solids depends on the factors such as ionic masses, electric charge/valence state of the ions, spring constant of the bond, lattice imperfections etc. The dielectric losses close to the lattice vibration frequencies are generally estimated in terms of the anharmonicity of lattice vibrations. The low frequency phonons are responsible for the intrinsic dielectric losses in solid dielectrics. The intrinsic loss mechanism occurs due to the interaction between the phonons and the microwave field or due to the relaxation of the phonon distribution function. The lattice phonon modes will determine intrinsic limits of the high frequency dielectric losses in crystalline solids. The extrinsic losses are occurred due to the interaction between the charged defects and the microwave fields.

1.2.8 Complex dielectric permittivity and Maxwell equations

In case of dielectric polarization, the polarization of the material is related to the electric field by:

$$P = \varepsilon_0 \chi_e E \tag{1.18}$$

This leads to:

$$D = \varepsilon_0 (1 + \chi_e) E = \varepsilon_o \varepsilon_r E \tag{1.19}$$

.

For real materials D can be described as[27]:

$$D = (\varepsilon - j\varepsilon_p) E \tag{1.20}$$

Here, $\varepsilon = \varepsilon_0 \varepsilon_r$, the real part of permittivity, and $\varepsilon_p = \varepsilon_o \varepsilon''$ is a factor describing the dielectric (polarization) losses.

For a region filled with homogeneous isotropic material, the first Maxwell equation can be written as:

$$\nabla \times H = \frac{\partial D}{\partial t} + \sigma E \tag{1. 21}$$

Here, σ is the conductivity of the material. Substituting for D from equation [1.20] the equation (1.21)becomes:

$$\nabla \times H \quad = i\omega(\varepsilon - i(\varepsilon_p + \sigma / \omega))E \tag{1.22}$$

The complex dielectric constant is defined as below:

$$\varepsilon^* = \varepsilon - i(\varepsilon_p + \sigma / \omega) \tag{1.23}$$

Here, ε is the real part of the permittivity and is defined as:

$$\varepsilon = \varepsilon_r \varepsilon_o \tag{1.24}$$

Here ε_r is known as the relative permittivity or dielectric constant and ε_0 is the permittivity of free space. Here the first and second term in the imaginary part of the complex permittivity represent the dielectric and ohmic losses respectively [28].

The loss tangent is given as:

$$\tan\delta = \frac{\varepsilon''}{\varepsilon'} \tag{1.25}$$

In this thesis ε_r is used throughout to represent relative permittivity of the materials and tanδ is used to represent a measure for the dielectric loss.

1.3 Classification of Dielectric materials

Dielectric materials can be classified into two major categories: Linear (normal dielectric) materials and non linear dielectric materials. The linear dielectric materials can be again subdivided into three classes based on the mechanism of electric polarization as non polar and dipolar materials.

1.3.1 Linear dielectric materials

The dielectric materials which are exhibiting a linear relationship between the polarization and applied electric field are known as linear dielectrics. This class of materials gets polarized with the application of the field and gets depolarized on the

removal of field. Based on the nature of the polarization mechanism, the linear dielectrics can be grouped as follows [29]:

Non polar materials: In materials of this class, an electric field can cause only elastic displacement of the electron cloud (mainly the valence electron cloud). So they have only electronic polarization. Such materials are generally referred to as elemental materials.

Polar materials: In materials of this class an electric field can cause only elastic displacement of electron clouds as well as elastic displacement of the relative positions of ions. These materials have both electronic and ionic polarization. The material may be composed of molecules and each of the molecules is made of more than one kind of atom without any permanent dipole moment. Examples of such materials are ionic crystals; in this case the total polarizability is the sum of the ionic and electronic polarizabilities.

$$\alpha = \alpha_e + \alpha_i \tag{1.26}$$

Dipolar materials: The materials of this class have all three fundamental polarizations: electronic, ionic and orientation. Thus the total polarizbility for them is

$$\alpha = \alpha_e + \alpha_i + \alpha_o \tag{1.27}$$

Materials, whose molecules posses a permanent dipole moment, belong to this class examples are water, methyl alcohol.

1.3.2 Non linear dielectric materials

The materials which have got a spontaneous polarization even in the absence of an external field are grouped into the class of non linear dielectrics. The spontaneous polarization appears in these class of materials due to its crystal structure. A necessary condition for a solid to fall in the class of non linear dielectrics is the absence of a center of symmetry. Amoung the 32 crystal classes, 11 of them have a center of symmetry and hence they won't exhibit spontaneous polarization. Out of the remaining 21 classes of crystals without a centre of symmetry, 20 of them are piezoelectric, ie these crystals can be polarized under the influence of an external stress. Ten out of the 20 pieozoelectric crystals exhibit the pyroelectric effect, ie the polarization of these classes of materials can be changed with the change of temperature. The ferroelectric materials discussed below are part of the spontaneously polarized pyroelectrics.

1.3.3 Ferroelectric Materials:

A ferroelectric material is a non-linear dielectric that exhibits a remanent polarization in the absence of an external electric field and its direction can be switched by an applied electric field [30]. The name ferroelectricity comes from the similarities between polarizations of ferroelectric materials with the magnetization of ferromagnetic materials. Ferroelectric materials display a hysteresis effect of polarization with an applied field. The hysteresis loop is caused by the existence of permanent electric dipoles in the material. When the external electric field is initially increased from zero value, the polarization increases as more of the dipoles are lined up along the direction of the field. When the field is strong enough, all dipoles are lined up with the field, so the material is in a saturation state. If the applied electric field decreases from the saturation point, the polarization also decreases. However, when the external electric field reaches zero, the polarization does not reach zero. The polarization at the zero fields is called the remanent polarization. When the direction of the electric field is reversed, the polarization decreases. When the reverse field reaches a certain value, called the coercive field, the polarization becomes zero. By further increasing the field in this reverse direction, the reverse saturation can be reached. When the field is decreased from this saturation point, the sequence just reverses itself.

In a ferroelectric material a transition occurs from a centro symmetric to a non-centro symmetric unit cell at the Curie point T_c. The shift in structural symmetry affects both the structural and physical properties of the crystal. Ferroelectricity can be maintained only below the Curie temperature. When the temperature is higher than T_c, a ferroelectric material is in its paraelectric state. Ferroelectric materials have great application potential in developing smart electromagnetic materials, structures, and devices, including miniature capacitors, electrically tunable capacitors, filters and phase shifters in recent years. Their application in the microwave frequencies are still under intensive investigations.

1.4 Tunable dielectrics

The dielectric materials, which have a voltage-dependent dielectric constant, are termed as tunable dielectric materials [31]**.** Generally this class of materials exhibits a large change in dielectric constant with an applied DC electric field. The major classes of materials being considered for tunable dielectric applications are ferroelectrics in their paraelectric state. The ferroelectric materials (FE) have been investigated in the microwave range since the 1950s. Only recently, monolithically compatible processing of

certain ferroelectric thin-film compounds become possible, and has generated great interest and promises for designing a new class of tunable microwave devices. For a microwave engineer the main attraction of a tunable material is the strong dependence of their dielectric permittivity ε on the applied bias electric field E_0. This characteristic is commonly described by a parameter named tunability n, defined as the ratio of the permittivity of the material at zero electric field ε(0) to its permittivity at some non-zero electric field ε(E) as given by equation (1.28). The relative tunability n_r is defined by equation (1.29) [31].

$$n = \frac{\varepsilon(0)}{\varepsilon(E)} \tag{1.28}$$

$$n_r = \frac{\varepsilon(0) - \varepsilon(E)}{\varepsilon(0)} \tag{1.29}$$

The dielectric loss of a tunable dielectric material is also dependent on the applied DC electric field. Experiments show that a ferroelectric material with higher loss tangent usually has larger tunability. Since the loss tangent of a material is an important factor affecting the performances of the electric circuit, in the development of electrically tunable ferroelectric microwave devices, a figure of merit K (*K*-factor), defined by K=Tunability/tanδ

$$K = \frac{\varepsilon(0) - \varepsilon(E)}{\varepsilon(0)} \times \frac{1}{\tan\delta} \tag{1.30}$$

is often used to indicate the quality of the tunable dielectric materials. Usually, in the calculation of *K*, the loss tangent at the maximum external DC electric field is used [32].

1.4.1 Tunable materials for microwave devices

Microwave materials have been widely used in a variety of applications ranging from communication devices to satellite services, and the study of their properties at microwave frequencies and the development of functional microwave materials have always been among the most active areas of solid-state physics, materials science, and electrical and electronic engineering. In recent years, the increasing requirements for the development of high speed and high frequency circuits and systems made a through understanding of the properties of materials at microwave frequencies a necessity [33].

The wireless systems operating in the microwave region is required to be lightweight, compact and of low cost, which could be addressed by miniaturization and integration. Meanwhile, the need of frequency agile applications demands the use of low loss, and highly tunable devices to allow multi-bandwidth operation with little impact on the component count. Microwave tunable passive devices mainly include filters, phase shifters, delay lines and matching circuits in connection with applications such as reconfigurable antennas, software defined radios, etc [34, 35]. Implementing several separate transceiver circuits in a single hardware device increases the component count and hence the overall cost. Therefore in terms of RF front end circuitry, significant cost saving can be achieved by using electronically tunable components. In this scenario a single tunable component is employed to replace several fixed components. For example, a band pass filter (BPF) with a tunable pass band could replace several fixed filters or a tunable delay line could replace a set of fixed delay lines in the beam-forming network of a phased array antenna [36].

Electronically tunable capacitors known as varactors can be used to fabricate reconfigurable components for RF and microwave applications [37]. The established technology for microwave varactors is based on semiconductors typically employing GaAs or silicon technology. The varactor diodes are now a proven technology for tunable microwave devices [38]. Another advantage of varactor diodes fabricated on silicon substrates is that they are easily incorporated in the standard complementary metal oxide semiconductor (CMOS) integrated circuit processes. However the semiconductor varactor diodes have smaller power handling capability and the silicon based varactors are more lossy above 10GHz frequency [39].

Micro electro mechanical system (MEMS) technology can also be used to fabricate varactors [40]. The advantage of MEMS varactors include high power handling and low inter modulation distortion. However MEMS devices require a careful packaging and reliability is an issue due to mechanical moving parts. Further, MEMS devices have a lower tuning speed than semiconductor varactors.

The ferroelectric material Barium strontium titanate (BST) is of particular interest for tunable microwave devices since it has a high dielectric constant that can be tuned by applying an electric field, and it exhibits relatively low losses at microwave frequencies [41]. The high dielectric constant is useful for minimizing the size of the component fabricated from BST, leading to higher integration. Another useful property of BST is that the microwave dielectric properties can be tailored for specific application by controlling

the ratios of barium and strontium according to the formula $Ba_xSr_{1-x}TiO_3$. BST is being explored as a tunable dielectric material for varactor fabrications. BST varactors have some important advantages over semiconductor varactors including higher power handling and lower cost. It has been shown that BST varactors have lower device losses than silicon based varactors at frequencies above 10GHz [42].

There are several ferroelectric materials that have been considered as possible candidates for tunable microwave devices. The most attention has been paid to $SrTiO_3$ and its solid solutions with $BaTiO_3$ and $PbTiO_3$ [43]. The bulk form of $SrTiO_3$ exhibits large tunabilities at cryogenic temperatures while at room temperature a large electric field is required for its tuning [44]. Voltage tunable $(Ba,Sr)TiO_3$ thin films and ceramics have been extensively investigated due to their high power handling capacity and large tunability over a wide frequency range. Thin films of BST type materials are desirable, because they can be easily integrated with standard IC processing procedures and can therefore be scaled for mass production [45]. In addition to barium strontium titanate (BST), lead strontium titanate (PST) has been proposed as a potential candidate material for high frequency tunable devices [46]. Ferroelectric sodium potassium niobium oxide $Na_xK_{(1-x)}NbO_3$ is another candidate material considered for the tunable applications[47]. It is a continuous solid solution of KNbO3 and $NaNbO_3$, having a pervoskite structure for $x<0.97$. The dielectric properties of these ceramics were well studied by many researchers. The NKN thin films deposited on various oxide substrates have shown high dielectric permittivity and voltage tunability. Because of their excellent crystallinity and electrical properties, NKN films were studied for memory and tunable microwave device applications.

1.4.2 Tunable devices based on BST

BST is essentially a solid solution of $BaTiO_3$ and $SrTiO_3$. $BaTiO_3$ is in the ferroelectric (polar) phase at room temperature, and has a ferroelectric to paraelectric transition temperature (Curie point) of 130± ℃, while $SrTiO_3$ is a paraelectric (non-polar) down to zero Kelvin [48]. For microwave applications, it is generally suggested that BST thin films should be in the paraelectric phase at room temperature. In the paraelectric phase, BST has simultaneously high tunability and relatively low dielectric loss at microwave frequencies [31]. At room temperature the paraelectric phase can be achieved by adjusting the chemical composition so that $x = 0.5$ in $Ba_xSr_{1-x}TiO_3$. In the ferroelectric polar phase, BST is also piezoelectric, and dielectric losses in this phase are

associated with mechanical damping caused by domain wall motion [48]. This results in high dielectric loss at microwave frequencies. Many research groups implemented tunable filters and phase shifters based on BST thin films over the past 10 years.

At NASA, Glenn centre, Subramanyam et al [49,50] have fabricated a YBCO/$SrTiO_3$ thin film based K-band tunable band pass filter on lanthanum aluminates substrate. The two-pole filter had a center frequency of 19 GHz and a bandwidth of 4%. Tunability was achieved through the nonlinear temperature dependence as well as the electric field dependence of dielectric constant of $SrTiO_3$ thin films. BST thin film based low pass and band pass filters were reported by Tombak et al[51]. These circuits have used lumped inductors and tunable BST capacitors. Jayesh Nath et al[52] reported a tunable third order combline band pass filter using BST varactors fabricated on sapphire substrates. The application of a 0-200V DC bias varied the center frequency of the filter from 2.44 to 2.88 GHz (16% tuning) with 1 dB bandwidth of 400 MHz. The insertion loss varied from 5.1 dB at zero bias to 3.3 dB at full bias. An electronically tunable impedance transformer and matching network were fabricated using BST capacitors on sapphire substrates by Chen et al [53]. The impedance transformer was able to vary electronically from a 4:1 to 2:1 transformation in a 50 ohm environment. BST based microwave filters have already been commercialized. Paratek Microwave Inc has commercialized two types of BST based band pass filters [54]. Filters based on hybrid microstripline configuration (f ~ 2GHz) and finline waveguide resonator configurations (f~22.5GHz) both employing BST thin films have been reported. The first device is a 4 pole microstrip combline band pass filter with tunable BST capacitors.

The first phase shifter using BST was reported by Flaviis in 1997[55]. Bulk BST with thickness of 0.1 to 0.15 mm was used in the microstripline circuits. In 1999 Van Keuls et al[56] reported a thirteen segment Ku band coupled microstrip phase shifters, in which BST based interdigitated capacitors were used as the series coupling components. S.Lee et al[57] demonstrated an X-band loaded transmission line type phase shifter by using BST thin films. The phase shifter consisted of coplanar waveguide (CPW) lines that are periodically loaded with voltage tunable BST varactors. The voltage tunable BST varactors showed a large dielectric tunability of 69% and a quality factor of 29.5 at a frequency of 10 GHz. The most comprehensive work on phase shifters based on ferroelectric thin films has been carried out by York et al [58, 59] at the University of California, Santa Barbara. They have reported several phase shifters using parallel plate and interdigital BST capacitors. Moon et al [60] fabricated a phased array antenna using

four element ferroelectric phase shifters with CPW transmission line structures based on BST thin films. This X-band phased array antenna system with the ferroelectric BST phase shifters was capable of having a beam steering of 15° in either direction.

1.4.3 Need for non ferroelectric tunable materials

Till date, almost exclusively, BST and $SrTiO_3$ have been investigated for tunable microwave application**.** Most of the literature on RF applications of tunable dielectrics has focused on the $Ba_xSr_{1-x}TiO_3$ (BST) thin films, and numerous devices and circuit demonstrations have been reported [61,62]. A promising RF performance has been achieved but in general, the RF losses of BST-based devices are high. All these tunable dielectric materials investigated till date fall under the group of ferroelectrics and they exhibit temperature dependent structure and dielectric properties. They also exhibit the phenomena of hysterisis in their ferroelectric state. The dielectric properties of ferroelectric thin films are found to be highly thickness dependent. All these things put together make such materials lossier at microwave frequencies. If one can employ a non ferroelectric material for tunable microwave application, one can avoid the loss originating from the coupling of the soft modes with electromagnetic fields which is a characteristic feature of all ferroelectrics. Also, ferroelectric thin films are vulnerable to the process related strain and impurities, which in effect would increase the dielectric losses in these thin films [31]. These limitations of the ferroelectric thin films enhance the search for non ferroelectric tunable materials having low loss at the microwave frequencies, even if the tunability is relatively lower since the low losses could lead to higher K factor.

1.4.4 Bismuth Zinc Niobate as a possible non ferroelectric tunable material

Bismuth based pyrochlore ceramics were discovered in the early 1970s and have attracted additional study during the last 10 years due to their possible applications in high frequency capacitors and microwave resonators [63]. Recently, researchers are showing much interest in the ternary oxides of the Bi_2O_3-ZnO-Nb_2O_5 (BZN) system which exhibit a high dielectric permittivity (ε_r), relatively low dielectric loss (tanδ), and a compositionally tunable temperature coefficient of capacitance (τ_c) [64]. These properties, combined with lower sintering temperatures (less than 950°C), make these materials attractive candidates for high frequency filter applications and in multilayered capacitors based on co-fired ceramic structures [65]. There are two main phases in the Bi_2O_3-ZnO-Nb_2O_5 system: $Bi_{1.5}Zn_{1.0}Nb_{1.5}O_7$ (c-BZN) with cubic pyrochlore structure, in

which at least some Zn atoms occupy A site positions with $\varepsilon_r \sim 160$ at room temperatures and $Bi_2Zn_{2/3}Nb_{4/3}O_7$ (m-BZN) which has $\varepsilon_r \sim 80$ with a monoclinic zirconolite like structure. Bi_2O_3- ZnO-Nb_2O_5 based pyrochlore ceramics are presently being considered as smart microwave material because of their unique dielectric properties in the microwave range. It is one of the few non ferroelectric material known today exhibiting voltage dependent dielectric permittivity. Because of being non ferroelectric, this material exhibits low loss and high figure of merit in the microwave frequency region.

1.4.5 Crystal chemistry of BZN

The bismuth zinc niobate has got the pyrochlore structure. The pyrochlore structure belongs to one of the oxygen octahedron based families. The general formulae for the oxide pyrochlores can be written as $A_2B_2O_7$. The A cations are eight coordinated and the B cations are six coordinated [67]. In spite of the immense flexibility of chemical composition in the pyrochlore system, a cubic structure with eight molecules per unit cell (Z=8) and space group Fd3m is the predominant phase.

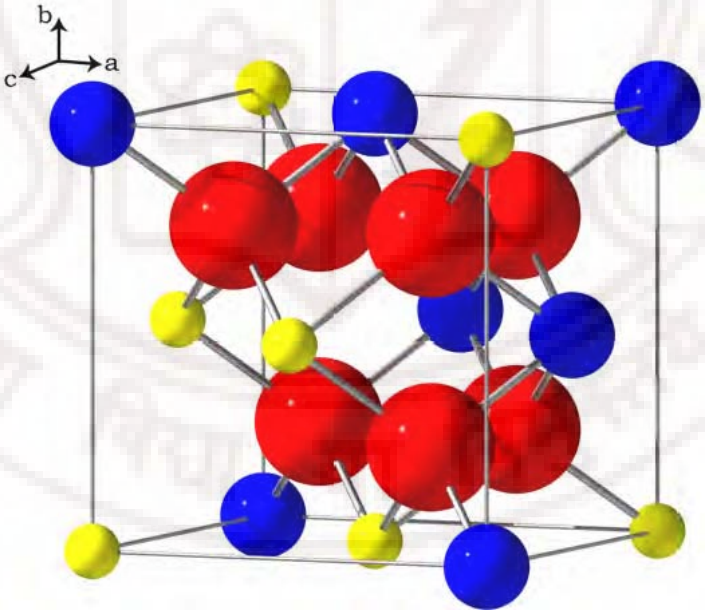

Figure 1.2 The Pyrochlore structure (1/8 unit cell). Large blue spheres are $'A^{3+}$ ions, small yellow spheres are B^{4+} ions, and large red spheres are O^{2-} ions.

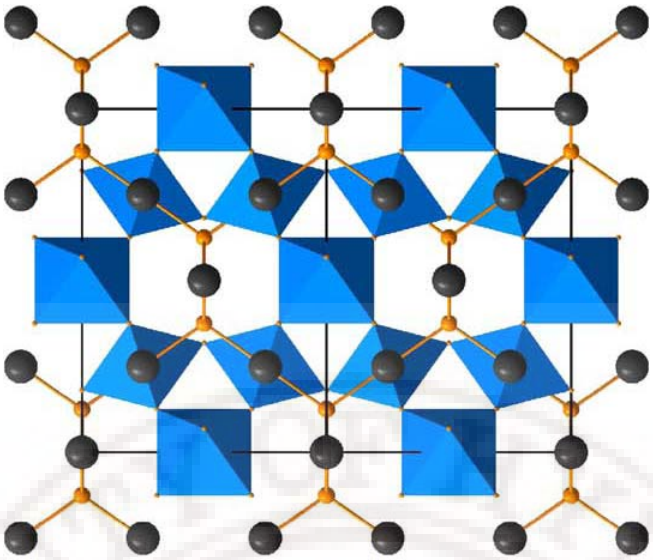

Figure 1.3 Ideal pyrochlore $A_2B_2O_6O'$ crystal structure in the Fd 3m space group[77] showing black A atoms, orange O′ and the network of corner-connected BO_6 octahedra (blue).

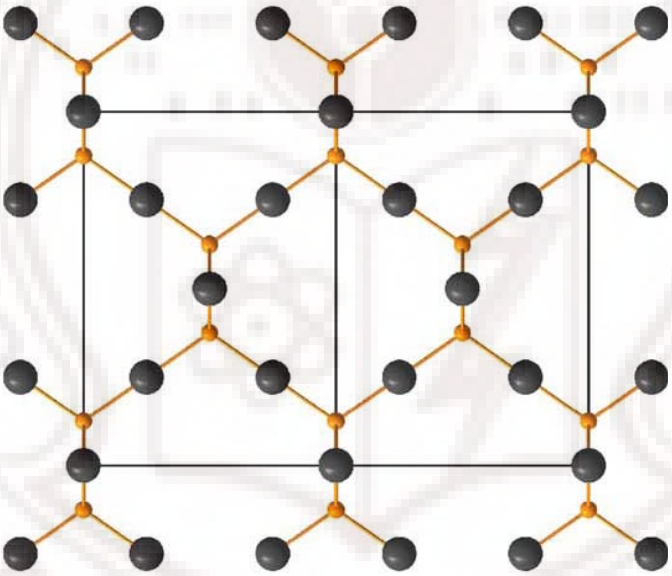

Figure1.4 A view of the tetrahedral A_2O' sub lattice [77]

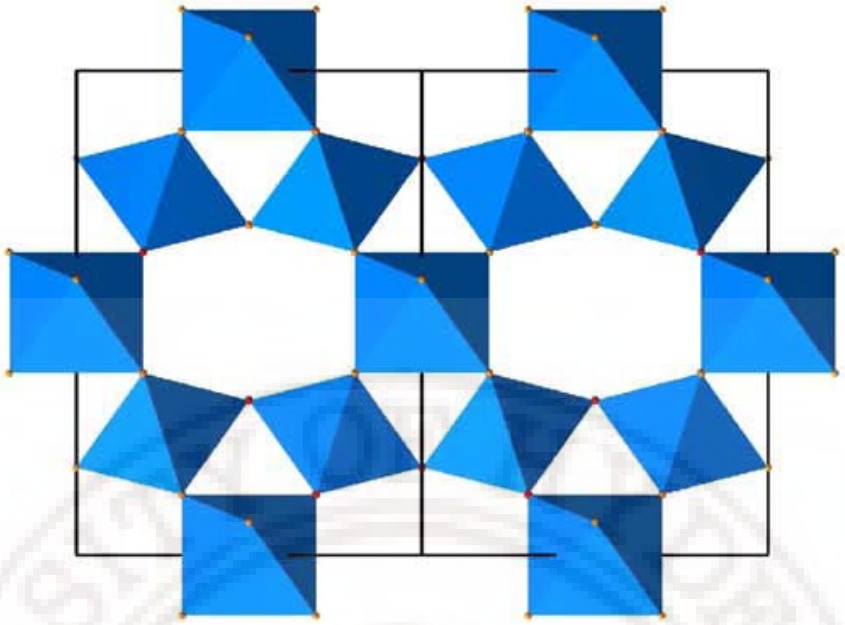

Figure 1.5. A view of the B_2O_6 sub lattice [77].

The $A_2B_2O_7$ pyrochlore structure is often described by the formula $B_2O_6.A_2O'$ (where O′ is the oxygen atom attached only to the A cations) which emphasises that the structure is built of two interpenetrating networks: BO_6 octahedra sharing the vertices from a three dimensional network resulting in large cavities which contain the O′ and A atoms in an A_2O' tetrahedral net, as shown in figures1.2-1.5. The A cations are randomly displaced by ~0.39Å from the ideal eightfold coordinated positions. The displacement occurs along the six <122> directions perpendicular to the O'-A-O' links. In addition, the O′ ions are randomly displaced by ~0.46Å along all twelve 110 directions. In the compound with the pyrochlore structure, noncubic symmetry occurs frequently in the case when A cations are with inert lone pairs of electron such as Bi^{3+}, Pb^{2+} and so on [66]. The BZN family is one of the large and rapidly growing group of inherently disorderd cubic $A_2B_2O_7$ cubic pyrochlore. Apart from the cubic structure, the BZN pyrochlore can also exit in a monoclinic zirconolite-like structure with four molecules per unit cell (z=4) with C2/c space group. The cubic pyrochlore phase that has the chemical composition $Bi_{1.5}ZnNb_{1.5}O_7$ is termed as c-BZN and a monoclinic zirconolite-like pyrochlore that has the chemical composition $Bi_2Zn_{2/3}Nb_{4/3}O_7$ is termed as m-BZN. Many research groups have actively studied the structure and dielectric properties of the BZN ceramics. A brief overview of some of the important studies on the BZN ceramics reported by various research groups is given below.

X.Wang et al [67] have investigated the structure, phase transformation and dielectric properties of Bi_2O_3-ZnO-Nb_2O_5 systems. They have identified two-distinct phases in this system having the composition $Bi_{1.5}Zn_{1.0}Nb_{1.5}O_7$ (c-BZN) and $Bi_2Zn_{2/3}Nb_{4/3}O_7$ (m-BZN) respectively. The c-BZN has got a cubic pyrochlore structure with a unit cell volume of 1117Å^3 and a theoretical density of 7.11g/cm^3. The m-BZN ceramic has got a monoclinic structure with a cell volume of 583 Å^3 and a theoretical density of 7.94g/cm^3. The c-BZN ceramics had a dielectric constant about 170, tanδ<0.0004 and a temperature coefficient of capacitance T_c –400ppm/°C. The m-BZN ceramics had a dielectric constant of 80, tanδ<0.0004 and a temperature coefficient of capacitance about +150ppm/°C. The local symmetry of the c-BZN ceramics as well as the Sn^{4+},Ti^{4+} substituted BZN ceramics was studied by Liue et al [68]. The structural properties of the B site substituted c-BZN ceramics are found to be remarkably similar to that of c-BZN ceramics it self. The underlying crystal chemistry of BZN and BZN related pyrochlore is shown to result from strong local Bi/Zn ordering rules and associated large amplitude structural relaxation. Frequency dispersion associated with the dielectric relaxation phenomena in polycrystalline c-BZN ceramics was analyzed by Nino et al [69]. Measurements at cryogenic temperatures and at high frequencies reveal a broad distribution of relaxation times in these ceramics. The dielectric loss data could be modeled using a function convoluting the Vogel-Fulcher law and Gaussian distribution.

The complex dielectric responses of the c-BZN [70] ceramics were investigated between 100Hz to 100 THz by Kamba et al. They have observed a dielectric relaxation over a wide frequency and temperature range. The dielectric permittivity and loss maxima shift to the higher temperature values as the frequency increases. The relaxation is assigned to the local hopping of atoms in the A and O^1 positions of the pyrochlore structure among the several potential minima. Temperature dependence of the reflectance of the cubic bismuth pyrochlores $Bi_{3/2}ZnTa_{3/2}O_7$, $Bi_{3/2}MgNb_{3/2}O_7$, and $Bi_{3/2}ZnNb_{3/2}O_7$ were investigated by Chen et al [71]. The spectra were collected from 30 to 3300cm^{-1} between 50 and 300K and the optical constants were estimated by Kramers-Kroning analysis and classical dispersion theory. In addition, BZN was studied from the tera hertz frequencies to lower frequencies. Infrared-active phonon modes have been assigned to specific bending and stretching vibrational modes. The splitting of the B-O stretching phonon modes and O-B-O bending modes are assigned to mixed cation occupancy.

c-BZN ceramics with 0-1.5 mole percentage titanium content in the B site were synthesized and investigated by Wang et al [72]between 100Hz to 100 THz by means of broadband dielectric spectroscopy, infrared reflectivity spectroscopy and Raman spectroscopy. c-BZN ceramics were found to be exhibiting a microwave relaxation which slows down and broadens remarkably on cooling. They also reported that the relaxation originates from the hopping of disordered Bi and a part of Zn atoms being in the A sites of the pyrochlore structure. Substitution of Ti atoms in the B site results in an increase of dielectric permittivity. Du et al [73] studied the relaxation behavior of c-BZN ceramics substituted with Ti at the B site. They have observed a relaxor type behavior at cryogenic temperatures in this system.

Hong Wang et al [74] studied the impact of ion substitution at the A site of the monoclinic bismuth zinc niobate (m-BZN) ceramics. They have shown that the structure and permittivity of the m-BZN ceramics with various ion substitutions in the A site is almost equal to that of pure m-BZN ceramics. The barium substituted compound was having higher dielectric permittivity due to a multiphase structure. The higher microwave quality factor with lower sintering temperature makes these materials suitable for LTCC application.

c-BZN –Ag composites were prepared by Sebastian et al using the conventional solid state reaction technique [75]. These composites were able to get sintered at a temperature of 850°C. The dielectric constant of these composites is found to be increased with the increase of silver content. They have reported a dielectric constant of 2350 for the composites with 0.14 volume fraction of silver and a large dielectric constant $\varepsilon_r \approx 10^5$ for the composites with 15 volume percentage of silver.

The displacive disorder in the bismuth oxide based pyrochlores was studied by Seshadri et al [76]. They have found that the A and O' sites splits due to the displacement from their ideal positions. Each O' site can be split in to the 12 different sites through the displacement from the ideal positions and each A site is split in to six different sites through displacements. The local displacements in the A and O' sites are responsible for the higher dielectric constant in these materials. They have also found that the static displacement in the pyrochlore structure is as large as 20% or more of the typical bond length. In general, for the crystals with such a large extent of disorder to be stable they should be in the proximity of a phase transition. But the BZN pyrochlores are found to remain in their cubic phase till the lowest temperatures. This behaviour is thought to be

due to the intrinsic difficulty of distorting the cubic ice like lattice of the pyrochlore in a coherent fashion [77].

1.4.6 Review of tunable dielectric properties of BZN thin films

This section provides a review of existing research into the BZN thin films for various microwave and electronics applications. It also presents the advantages of amorphous fused silica as a substrate material for BZN deposition. Most of the BZN thin films prepared as part of this thesis work were deposited on amorphous fused silica substrates. Finally, based on the existing work, opportunities for further investigations are identified.

c-BZN and m- BZN pyrochlore thin films were prepared on platinised Si substrates by the metal organic deposition technique by Ren et al [**78**]. They have studied the dielectric properties of these thin films in detail with respect to the processing conditions. The c- BZN thin films were having a dielectric constant of 150 and the m-BZN thin films were having a dielectric constant of 80. The dielectric loss tangents of both these films were less than that of 0.008. The c-BZN thin films were highly tunable with a tunability of 16% where as the m- BZN thin films were having a nearly field independent dielectric constant. Jiang et al [79] investigated the dielectric properties of pulsed laser deposited c-BZN thin films on $Pt/SiO_2/Si$ substrate. They have observed that the c-BZN thin films had pure cubic pyrochlore structure in the deposition temperature range of 500°C-650°C. The thin films were having a low loss tangent and a maximum voltage tunability of 6%.

A detailed investigation of composition, structure and crystallinity of c-BZN thin films deposited using RF magnetron sputtering was done by Lu et al [80]. They could obtain a crystalline phase for the films deposited at 400°C or above and the complete crystallinity was obtained for the films deposited at 750°C. The films were grown on platinised silicon substrate as well as on platinised sapphire substrates. The crystalline films deposited at 400°C were having a dielectric constant of 49 and the films deposited at 750°C were having a dielectric constant of 170. The increase in dielectric constant with temperature was attributed to the increase in crystallanity. The dielectric constant started degrading for higher annealing temperatures and it was attributed to the loss of volatile components. The films deposited on platinised silicon exhibited a tunability of 29.6% whereas the films deposited on platinised sapphire were having a dielectric tunability of 23%. The dielectric loss tangent of these films is about 0.002.

Yan et al [81] investigated the microwave dielectric properties of c-BZN-BST composite thin films deposited on $SrTiO_3$ and MgO substrates via pulsed laser deposition technique. The thin films on STO and MgO substrates showed a dielectric constant of 435 and 401, a dielectric loss tangent of 0.0043 and 0.0037 and dielectric tunability of 6% and 5.7% respectively. This study showed that the dielectric loss tangent of this composite thin film is considerably low compared to that of BST thin films. W.Fu et al [82] investigated the dielectric properties of BZN-Mn-doped $Ba_{0.5}Sr_{0.5}TiO_3$ hectero layered films grown by the pulsed laser deposition technique on Nb doped $SrTiO_3$ substrate. These hecterolayered films were found to possess a medium permittivity of around 200, low loss tangent of 0.0025 and a relatively high tunability up to 25%. They have proposed a maximum tunability of about 40% based on the layer structure model developed by them. H.Wang et al [83] investigated the dielectric and C-V chaecteristics of the BST-BZN composite thin films deposited on platinised silicon substrates by pulsed laser deposition. The dielectric constant and loss tangent for these thin films were found to be 200 and 0.001 respectively, at room temperature. The measured in plane tunability for these films were greater than 50-60%.

Cheng et al [84] investigated the effect of laser annealing on the crystallization temperature of the c-BZN thin films. The c-BZN thin films got crystallized at a substrate temperature of 400°C when they are initially annealed at a laser fluence of energy density 27mJ/cm^2. The films were having a dielectric permittivity of 156 and a tunability of 33%. The low crystallization temperature obtained for c-BZN thin films by this process makes them suitable to integrate with polymeric substrates.

Effects of substrate heating on the structure and dielectric properties of the c-BZN thin films were investigated by Ha et al [85]. The films were deposited on platinised silicon substrate by RF magnetron sputtering at various substrate temperatures. The films deposited at 550°C followed by a post deposition annealing of 800 °C show a tunability of 26.5% at 1 MHz. The dielectric constant of the films was about 160 and the loss tangent was about 0.002.

Y.P Hong et al [86] investigated the voltage tunable dielectric properties of c-BZN thin films deposited on platinised Si substrates by RF magnetron sputtering. The prepared dielectric thin films were found to exhibit a dielectric constant of 153, tanδ of 0.003 and a maximum tunability of 14% when measured at a frequency of 1 MHz**.** Cao et al [87] deposited c- BZN thin films with different thickness and preferred orientations on

Nb doped $SrTiO_3$ substrates by pulsed laser deposition. They found that the dielectric constant increases and the loss tangent decreases with the increase in thickness. Tunability was found to be independent of the film thickness. They also observed that the (111) oriented films exhibited higher dielectric loss compared to (100) oriented films. c-axis oriented c-BZN thin films were grown on Nb doped $SrTiO_3$ substrates by W.Y.Fu et al by pulsed laser deposition [88]. They obtained the dielectric permittivity of 187, loss tangent of 0.002 with a tunability of 6% for the c axis oriented films. The effect of thermal strain on the dielectric properties of c-BZN thin films was studied by Funakubo et al [89]. They have found that the c-BZN thin films have high stability of dielectric constant and tunability against thermal strain when compared to BST thin films. They have attributed this high dielectric stability against thermal strain to the smaller electrostictive coefficient of c-BZN thin films.

Recently Park et al [90] demonstrated the fabrication of metal insulator metal capacitors on a polymeric substrate using c-BZN thin films by pulsed laser deposition. The c-BZN thin films were deposited at ambient and annealed at 150°C. The films were having a dielectric constant of 70 even though it was in an amorphous state. This was one of the highest dielectric constant reported for thin films processed below 200°C. Choi et al [91] fabricated a low voltage organic thin film transistor (OTFT) using c-BZN thin film for gate dielectric. The c-BZN based OTFT was having an operating voltage less than 2V because of the high permitivity and the low leakage characteristics of c-BZN thin films processed at low temperatures.

A monolithic Ku-band phase shifter employing a voltage tunable c-BZN thin film parallel plate capacitor is reported by Jaehoon Park et al [92]. They have designed a nine section distributed coplanar waveguide loaded line phase shifter as shown figure 1.6.

Figure1.6 Photograph of the BZN phase shifter fabricated by Jaehoon Park et al

These phase shifters were reported to have a differential phase shift of 175° with a maximum insertion loss of 3.5 dB at 15 GHz. This reported insertion loss is significantly better than that of the BST 5 based phase shifters using a similar design.

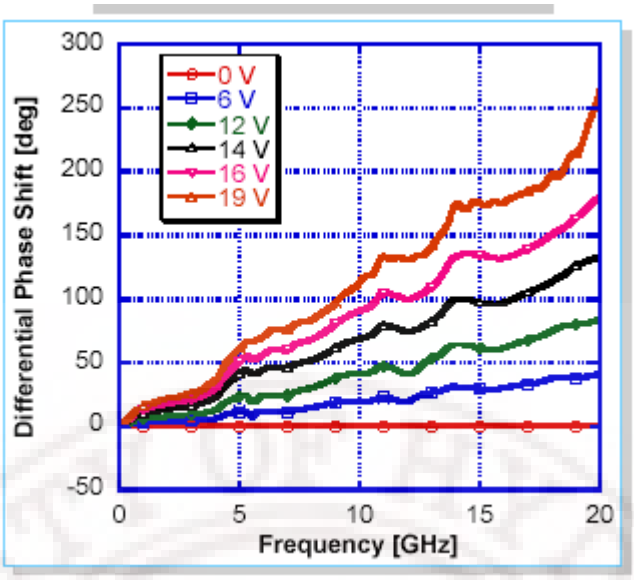

Figure 1.7 Differential phase shifts with applied DC bias of c-BZN based phase shifter fabricated by Jaehoon Park et al [92].

The BST phase shifter was having an insertion loss of 3dB at 10 GHz [93] whereas the BZN phase shifter was having an insertion loss of only 1.8dB at 10 GHz. This shows that the BZN thin film devices maintain relatively low losses well into the microwave frequency region.

1.4.7 Physics of tunability in c- BZN independent of ferroelectric origin.

Till date, large dielectric tunabilities have only been observed in ferroelectric materials. c-BZN is not a ferroelectric material. To have a better understanding about the nature of tunability in these materials certain models were reported. Dielectric tunability is believed to be related to the off-centering of ions in the cubic pyrochlore structure and the hopping of ions between the energetically equivalent positions. Under an applied field, off-centered ions can hop between energetically equivalent sites. A simple model based on the electric field E as a function of Temperature T which is needed to achieve a given tunability n can be expressed as [94]

$$E_n = \frac{kT}{p_0} \ln\left(\sqrt{n} + \sqrt{n-1}\right) \qquad (1.31)$$

Here, p_0 is the dipole moment.

This model could not explain the experimental data that have been obtained for c-BZN. A better model has been developed based on the idea of hopping dipoles under the influence of a random field in the structure which is given below.

$$E_n = \frac{kT}{p_0}\ln\left(\sqrt{1+(n-1)\cosh^2(p_0E_r/kT)} + \sqrt{(n-1)\cosh^2(p_0E_r/kT)}\right) \quad (1.32)$$

A cubic pyrochlore structure with random off-centering of ions hopping between the off-centered positions is the physical basis of the model used to describe the tunability n. The random fields in the crystal structure are thought to be originating from the random substitution of Zn on the Bi-sites. A schematic diagram of the cation hoping in c-BZN pyrochlores is shown in figure 1.8

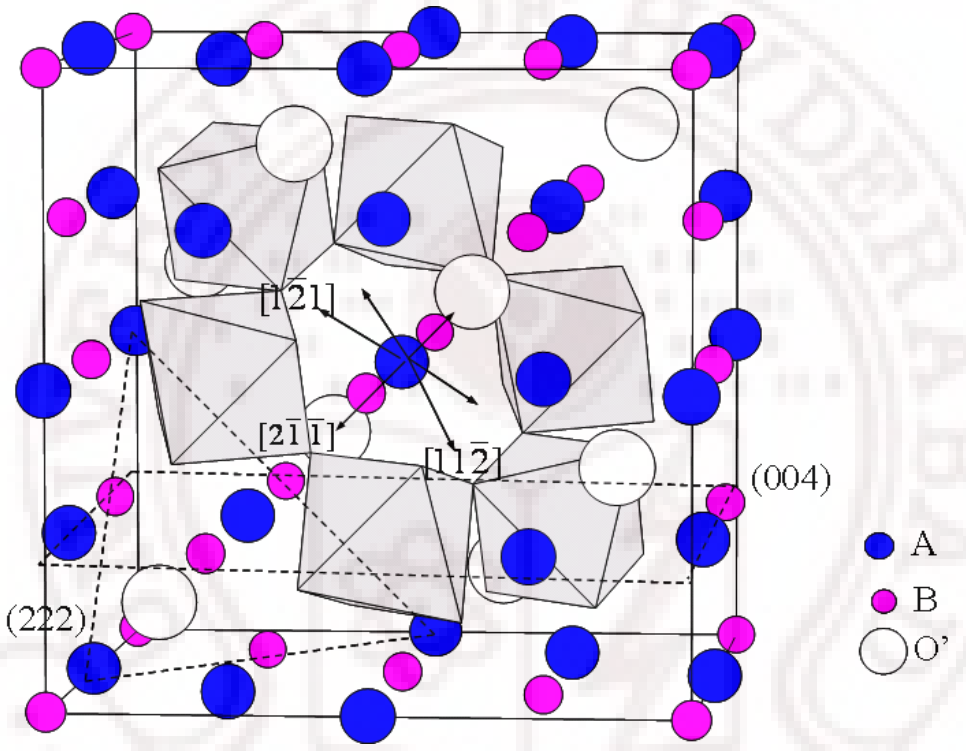

Figure 1.8 Schematic diagram of A site cation hoping in c-BZN pyrochlores

Recently Seshadri et al [77] found that the A and O' sites are split due to the displacement from their ideal positions. The O' sites can split in to the 12 different sites through the displacement from the ideal positions and each A site is split in to six different sites through displacement. Hopping of the A and O' ions in these equivalent states is considered to be responsible for the tunability in these materials.

1.5 Research objectives

In summary, the ternary oxides in the Bi_2O_3-ZnO-Nb_2O_5 (BZN) system exhibit high values of dielectric constants (ε_r), relatively low dielectric losses, and a compositionally tunable temperature coefficient of capacitance (τ_c). Such properties, combined with sintering temperatures of less than 950°C, render these materials as

attractive candidates for multilayer capacitors and low temperature co-fired ceramics (LTCC) for many technological applications [95]. The two members of this family that have received most of the attention $Bi_{1.5}ZnNb_{1.5}O_7$ (c-BZN) ($\varepsilon_r \approx 145, \tau_c \approx -400$ppm/°C) and $Bi_2Zn_{2/3}Nb_{4/3}O_7$ (m-BZN) ($\varepsilon_r \approx 80, \tau_c \approx +200$ppm/°C), were shown to adopt cubic and monoclinic zirconolite-like stoichiomectric pyrochlore structures. Thin films of these materials may have the advantage of lower crystallization temperatures and smaller device size than bulk ceramics and could get potentially integrated in to microelectronic devices .

The cubic pyrochlore $Bi_{1.5}ZnNb_{1.5}O_7$ (c- BZN) ceramics are presently being considered as a smart microwave material because of the unique dielectric properties in the microwave frequency range [89]. It is one of the few non-ferroelectric materials known today exhibiting a voltage dependent dielectric permittivity**.** Recently numerous investigations have focused on integration of c-BZN thin films for use in microwave devices for communication purposes, taking advantage of its voltage dependent dielectric constant. More over the c-BZN thin films based microwave devices are having low dielectric loss and high figure of merit than the ferroelectric based tunable devices. Although the bulk dielectric properties of the c- BZN and m-BZN are reasonably studied, thin films of these materials are not well understood in the microwave range.

For the effective microwave application of these thin films, the choice of the substrate is an important factor. Most of the previous works are on the growth of poly crystalline BZN films on single crystal substrates such as sapphire and lanthanum aluminate [78]. The growth of these films on a low cost, low loss and low dielectric permittivity substrate is important for the microwave application of these thin films. Fused silica is one of the ideal substrates for the growth of thin films meant for microwave applications, because it satisfies these requirements. Its dielectric characteristics permit the design of transmission lines of high impedance and matched impedance as per the requirements. Its low losses make it possible to obtain overall low losses for the device at a given impedance. The integration of these thin films appropriately to the existing silicon technology is a very attractive area of research. The tunable thin films have been earlier deposited directly on to silicon wafers for this purpose. However the low resistivity of the silicon limits the realization of low loss microwave transmission lines and other passive components on these thin films. The other possible alternative explored was high resistive silicon which also found to loose its

high resistivity due to the high temperature processing required for these thin films. An alternate technology coming up for integration of these thin films is silicon on sapphire (SoS) technology where thick layer of silicon will be deposited on sapphire substrates and appropriate active and passive circuits were incorporated in the same wafer. This technology could provide high isolation and higher operating speed but the high cost of the sapphire substrate has become a limiting factor for the wide spread use of this technology.

However if these films could grow on fused silica (amorphous SiO_2) substrates, it opens an easy and cost-effective way for the integration of these materials with the existing silicon technology. Already, industrially compatible fabrication processes are available for Si and SiO_2. The SiO_2 can be directly deposited on Si substrates or it can be produced by the surface oxidization of the Si substrates. The tunable dielectric films can be grown directly on the SiO_2 layer and the required passive circuits can be fabricated. The active circuits can also be incorporated in the same wafer by exposing Si substrates through the selective etching of the SiO_2 layer. Thus the tunable thin films on SiO_2/Si substrates will lead to a cost effective way of integration of microwave tunable circuits in to the existing silicon technology. Hence a study on the growth of BZN thin films on amorphous SiO_2 (fused silica) substrates and the impact of thermal treatments on them will be an important milestone to develop the process technologies for the BZN thin films compatible with Si technology. However, growing crystalline thin films of these materials on amorphous fused silica substrates is challenging and requires serious process optimization.

An important focus of this thesis is on understanding the relationship between the material and microwave properties of c-BZN and m-BZN thin films on amorphous fused silica substrate. The influences of the deposition condition on the structure, microstructure and microwave dielectric properties were also investigated. From these studies a set of deposition conditions which provide a high dielectric constant, low dielectric loss and high tunability (for c-BZN thin films) can be determined. Establishing these conditions is important since the relationship between the deposition conditions and microwave properties of BZN thin films grown directly on these substrates especially on amorphous fused silica has not been systematically studied. For achieving this major objective a series of intermediate objectives have to be set and achieved. The first

objective was the identification of a suitable deposition method for fabrication of thin films.

Out of many techniques available for the deposition of thin fims, the Pulsed Laser Deposition (PLD) technique has been selected to deposit c -BZN and m- BZN thin films in the current study. It provides excellent control of the stoichiomectric composition of oxide films with many components, which is especially necessary for BZN thin films due to the high volatility of Zn and Bi. As composition is the key factor that determines the crystal structure and dielectric properties of BZN thin films, PLD is expected to provide the attractive advantage of control to realize the cubic and monoclinic pyrochlore structure of the BZN thin films.

Preparation of the high-density ceramic targets of c-BZN and m-BZN for pulsed laser deposition has become an intermediate objective in this study. It is desirable to have a fair knowledge about the structural and electrical properties of these bulk ceramics before making them in the thin film form. So the preparation and characterization of the bulk m-BZN and c-BZN ceramics become an essential objective in the present work.

The second major objective of this study was the development of suitable techniques for the characterization of these thin films at the microwave frequency range. Currently most of these materials are characterized at much lower frequencies compared to the frequency of operation of the devices in which they are a part. Unambiguous measurement of dielectric constant and loss of dielectric thin films on insulating substrates in the microwave region has long been an important objective in micro/nano-electronics. The difficulty lies in the predominant response of the dielectric substrate submerging the response of the film or the requirement of a metallised circuit layer over the film thereby losing information about the as-deposited state of the film. So the development of various characterization techniques to measure the dielectric constant, loss tangent and tunability at microwave frequency regions becomes the most challenging objective of the present investigation.

For the microwave characterization of these thin films, various test structures have to be fabricated. Hence demonstrating a suitable micro fabrication process flow suitable for BZN thin films has become an important objective of this study. A lift of based photolithographic process, which allowed the fabrication of CPW lines circular patch capacitors and IDC structures, has to be established. Using this process flow one could be able to pattern small feature sizes in the order of 8-10 μm.

It is also interesting to know the low frequency dielectric properties and electrical properties of c-BZN and m-BZN thin films grown on different substrates. So the characterization of the leakage conduction mechanisms and dielectric properties at low frequencies are also an objective of the present study.

The present investigation also aims to understand the voltage dependent dielectric properties of c-BZN thin films deposited on platinised silicon substrates as well as amorphous fused silica substrates. The dielectric properties of both c-BZN and m-BZN thin films on fused silica substrates are studied in comparison to that of the films grown on single crystal substrates such as LAO, ALO and MgO.

As stated earlier, BZN films are mainly being considered for microwave dielectric applications. However, the optical properties of these thin films are also interesting for a number of reasons, including identifying the electronic component of polarisability and monitoring the film growth and degradation processes. Optical properties such as refractive index and band gap are good indicators of the growth patterns of the dielectric films and can be effectively used to monitor their growth.

A major issue in thin film dielectrics is the difference between the thin film properties and those of the corresponding bulk materials. Since the dielectric properties and lattice dynamics are closely related, Raman spectroscopy provides a potentially valuable technique for the study of dielectric materials. It is highly sensitive to local structure and local symmetry. Moreover, it is a nondestructive technique, which does not require any special treatment of samples. Owing to the technological importance of BZN thin films, we present the Raman spectral analysis of these films to have a better understanding of their dielectric behavior.

Lastly the basic element of a tunable device in the microwave frequencies is a varactor. Hence fabrication and testing of the planar and parallel plate varactors using BZN thin films becomes the final objective of this work.

Reference

1. P.Van Musschen Broek, Introduction Philosophion Naturalem, Luchtman,Leiden (1762)
2. M.Faraday, *Phil.Trans* 128:1 79 265 (1837)
3. O.F.Mossoti, *Bibl.univ.modena* 6, 193(1847)
4. O.F.Mossoti, *Mem. di Mathem e.di.fisica in modena,* 24(2) 49 (1850)
5. R.Clausius Volume 2 Vieweg. Braunschweigh (1879)
6. P.Debye, *Phys.Z*, 13,97(1912)
7. L.Onsager, *J.Amer.Chem.Soc*, 58,1486(1936)
8. J.G.Kirkwood J.Chem.Phys, 7, 911(1939)
9. J.G.Kirkwood and R.M.Fuoss, *J.Chem.Phys*, 9,329(1941)
10. P.Drude, Z.phys.Chem, 23,267 (1897)
11. K.S.Cole and R.H.Cole, *Journal of Chemical phys*, 9, 341 (1941)
12. D.W.Davidson and R.H.Cole. *J.Chem.Phys*, 19,1484(1951)
13. G.Williams and D.C.Watt Trans Faraday Soc, 66, 80 (1970)
14. A.K.Jonsher, Dielectric relaxation in solids, Chelsea dielectric press, London (1983)
15. R.Chau, J.Brask, S.Datta,G.Dewey,A.Majumdar *Microelectronic Engineering* 80, 1(2005)
16. P.P.Jenkins, A.N.Maclnnes, M.Tabib Azar and A.R.Barron, *Science* 263, 1751(1994)
17. R.J.Cava *J.Mater.Chem*, 11, 54 (2001)
18. S.J.Fiedziuzko,I.C.Hunter,T.Itoh,Y.Kobayashi,T.Nishikawa,S.N.Stitzer,K.Wakio, *IEEE Trans. Microwave Theory and Tech*, 50, 706 (2002)
19. C.P.Smyth, *Annual Review of Physical Chemistry* ,17, 433(1966)
20. W.H.Rodebugh and C.R.Eddy *J.Chem.Phys*, 8,424(1940)
21. S.O.Kasap in Principles of Electronic Materials and devices, Mcgraw –Hill(2006)
22. P.Debye. *Phys.Z*.13,97(1912)
23. P.Debye, Polar molecule, Dover ,Newyork (1929)
24. L.Onsager, *J.Amer.Chem.Soc*, 58,1486(1936)
25. A.R.VonHippel, Dielectric and waves John wiley &Sons,Newyork (1954)
26. Simon Ramo, John R.Whinnery, Theodore Van Duzer. *Field and Wave in Communication Electronics*. 3rd edition, John Wiley Sons, ISBN 0-471- 58551-3(1994)

27. J.C.Maxwel, A.Treatise on Electricity and magnetisem, Clarendon press, Oxford, (1892)
28. A.K.Jonscher *J.MaterScience*, 16, 2037(1981)
29. Frohlish.H. The theory of dielectrics,London, Oxford university press, Second edition
30. Valasek. *J.Phy.Rev*, 17,475(1921)
31. A.K.Taganstev, V.O.Sherman, K.F.Astafiev, J.Venkatesh, N.Setter, *Journal of electro ceramics*, 11, 5(2003)
32. J.Y.Kim and A.M.Grishin *Integrated ferroelectrics* ,66,291(2004)
33. J.Y.Kim and A.M.Grishin, *Appl.Phys.Lett*, 88 192905 (2006)
34. M.J.Lancaster,J Powell and A. Porch, *Super cond.Sci.Technol*, 11,1323 (1998)
35. Manas .K.Roy and Jerzy Richter, *proceedings of IEEE ISAF* (2006).
36. F.W. Van Keuls, R.R.Romanofsky, D.y.Bohmon, M.D.Winters, F.A.Miranda, C.H.Muller, R.E.Treece and D.Galt *Appl.Phys.Lett* 70,3075(1997)
37. Y.Zhu and L.C.Sengupta US patent No. US6,686,817B2(2004)
38. S.R.Chandler, I.C.Hunter and J.G.Gardiner, *IEEE Guided Wave Letters*, 3, 70 (1993)
39. S.P.Voinigescu, D.S.Mcpherson, F.Pera, S.Szilagyi, M.Tazlauana and H.Trani, *International Journal for high speed electronics and systems*,13, 27 (2003)
40. C.L.Goldsmith,A.Malczcwski,J.J.Yao.S.Chen,J.Ehmk and D.H.Hinzel, *Int.J.RF microwave CAE* 9,362(1999)
41. F.A.Miranda, G.Subramanyam, F.W.Vankeuls, R.R.Romanotsky, J.D.Warner and C.H.Muller *IEEE Trans. On Microwave Theory and technique*, 48 ,1181(2000)
42. S.Gevorgian, A.Vorobiev, D.Kuylenstierna, A Deleniv,S.Abadei,A.Erikson and P.Rundqvist, *Integrated Ferroelectrics*, 66, 125 (2004)
43. S.J.Lee, S.E Moon, M.H.Kwak, Y.T.Kim, H.C.Ryu, S.K.Han, *Appl Phys Lett*, 82, 2133(2003)
44. I.Wooldridge, C.W.Turner, P.A.Warburton, E.J.Romans, *IEEE.Trans.Appl. Supercond*, 9, 3220(1999)
45. G.H.Lin,R.Fu, S.He, J.Sun, X.Zhang, L.Sengupta, *Mat.Res.Soc.symp.proc* 720 (2002)
46. M.Jain, Yu.I.Yuzyuk, R.S.Katiyar, Y.Somiya, A.S.Bhalla, F.A.Miranda and F.W.Vankeuls, *Mat.Res.Soc.symp.proc* 811(2004)
47. C.R.Cho, A.M.Grishin *J.Appl.physics,* 87, 4439 (2000)

48. B.Jaffe, W.R.Cook and H.Jaffe, Piezoelectric Ceramics , accdemic press London,(1971)
49. G.Subramanyam, F.V.Keuls and F.A.Miranda, *IEEE MTT-S Int.Microwave. Symp.Dig*, 1011(1998)
50. G.Subramanyam, F.V.Keuls and F.A.Miranda, *IEEE Microwave guided wave letters,* 8, 78 (1998)
51. A.Tombak, J.P.Maria, F.T.Ayguavives, Z.Jin,G.T.Stauf, A.I.Kingon and A. Mortazawi, *IEEE.Trans.Microwave Theory and Tech*, 51, 462(2003)
52. Jayesh Nath, Dipankar Ghosh,Jon Paul Maria, Angus.I.Kingon,Wael Fathelbab,Paul D. Fran Zon Michael .B.Steer, *IEEE Trans.Microwave theory and technique*, 53, 2707(2005)
53. L.Y.Vicki Chen, Roger Forse, D.Chase,R.A.York IEEE MTT-S Digest 261(2004)
54. www.paratek.com
55. F.D.Flaviis, N.G.Alexopouls, O.M.Stafsudd, *IEEE.Trans.Microwave Theory and Tech*,45,963(1997)
56. F.W.Van Keuls, C.H.Muller, F.A.Miranda, and R.R.Romanofsky, IEEE MTT-S *Int.Microwave. Symp.Dig*, 2, 737(1999)
57. S.J.Lee, H.C.Ryu, S.E.Moon, M.H.Kwak, Y.T.Kim and K.Y.Kang, *Journal of the Korean physical society*, 48,1286 (2006)
58. L.Y.Vicki Chen,R.F.D Chase and R.A.York, *IEEE MTTS-digest* ,7803(2004)
59. B.Acikel, Y.Liu, A.S.Nagara, T.R.Taylor,P.Periyaswamy,J.Speck and R.A.York *IEEE MTT-S Int.Microwave. Symp.Dig* ,2, 737(2001)
60. S.E.Moon, H.C.Ryu, M.H.Kwak, Y.T.Kim, S.J.Lee and K.Y.Kang, *ETRI Journal* 27,677 (2005).
61. E.A. Fardin, A.S. Holland, and K. Ghorbani, *IEE Electronics Letters*, 42, 353, (2006).
62. E.G.Erker, A.S.Nagara, Y.Liu, P.Periyaswamy, T.R.Taylor, JSpeck and R.A.York *IEEE Microwave guided wave letters*, 10,10(2000)
63. Z.P. Wang et al., *Electronic Components Mater*, 1 **,**11 (1979),
64. H. Wang and X. Yao, *J. Mater. Res,* 16, 83 (2001).
65. H. Wang, X. Wang and X. Yao, *Ferroelectrics*, 195, 19 (1997),
66. H. Wang, R.Elsebrock, T.Schneller, R.Waser,and Xi Yao, *Solid state communications,* 132, 481 (2004)
67. X.Wang, H.Wang and X .Yao, *J.Am.Ceram Soc*, 80 2745(1997)

68. Y.Liu, R.L.Withers, T.R.Welberry, H.Wang, H.Du, *Journal of solid state chemistry,* 179, 2137(2006)
69. J.C.Nino, M.T.Lanagan and C.A.Randal, *Journal of applied physics,* 89, 4512(2001)
70. S.Kamba, V.porokhoskyy, A.Pashin,J.Petzelt, J.C.Nino, S.T.Mckinstry, M.T.lanagan, C.A.Randall, *Physical review B*, 66, 054106(2002)
71. M.Chen, D.B.Tanner, Juan C.Nino, *Physical review B*, 72, 054303(2005)
72. H.Wang, S.Kamba, H,Du, C.T.Chia,S.Veijko,S.Denisov,F.Kadlec,JPetzelt,Xi yao *Journl of applied physics*,100,014105(2006)
73. Du Huiling, Yao Xi , Physica B, 324, 121(2002)
74. Wang, S.Kamba, M.Zhang, Xi Yao, S.Denisov, F.Kadlec,JPetzelt, *Journal of applied physics*, 100,034109(2006)
75. S. George, J. James, M.T.Sebastain, *J.Am.Ceram.Soc*, 90,3522(2007)
76. B.Melot, E.Rodriquez, T.Proften, M.A.Hayward, R.Seshadri, *Material research bulletin*, 41, 961(2006).
77. R.Seshadri, *Solid state science*, 8, 259(2006)
78. W.Ren, S.T.Mckinstry,C.A.Randall and T.R.Shrout, *J.Appl phys,* 89, 767(2001)
79. S.W.Jiang, B.Jiang ,X.Z.Liu and Y.R.Li ,*J.Vac.Sci.Technol A*, 24,261, (2006)
80. J.Lu, Z.Chen, T.R.Taylor and S.Stemmer, *J.Vac.Sci.Technol A*, 21,1745(2003)
81. L.Yan, L.B.Kong,L.F.Chen,K.B.Chong,C.Y.Tan and C.K.Ong, *Applied physics letters*, 85 ,3522(2004)
82. W.Fu,L.Cao, S.Wang, Z.Sun,B.Cheng,Q.Wang,H.Wang, *Applied physics letters*, 89,132908(2006)
83. W.Fu,H.Wang,L.Cao,Y.Zhou, *Applied physics letters*, 92, 182910(2008).
84. J.G.Cheng, J.Wang,T.Dechakupt,S.T.Mckinstry, *applied physics letters,* 87, 232905 (2005)
85. Y.P.Hong, S.Ha, H.Y.Lee, Y.C.Lee, K.H.Ko, D.W.Kim, H.B.Hong, K.S.Hong, *Appl.phys.A*, 80, 585(2005)
86. Y.P.Hong, S.Ha, H.Y.Lee, Y.C.Lee, K.H.Ko, D.W.Kim, H.B.Hong, K.S.Hong, *Thin solid films*, 419**,**183(2002)
87. L.Z.Cao, W.Y.Fu, S.F wang, Q Wang, Z.H. Sun, H.Yong,B.L.Cheng, H.Wang and Y.L.Zhou, *J.PhysD. Appl. Physics*, 40 **,**2906(2007)
88. L.Z.Cao, W.Y.Fu, S.F wang, Q Wang, Z.H. Sun, H.Yong,B.L.Cheng, H.Wang and Y.L.Zhou, *J.PhysD. Appl. Physics*, 40 **,**1460(2007)

89. Hiroshi Funakubo, Shingo Okaura, Muneyasu Suzuki, Hiroshi Uchida, Seiichiro Koda, Rikyu lkariyama,Tomoaki Yamada, *Appl.phys.Lett*, 92, 182901(2008)
90. J.H.Park, W.S.Lee, N.J.Seong, S.G.Yoon, S.H.Son, H.M.Chung ,Y.S.Oh. App.phys.lett, 88, 192902(2006)
91. Y.W.Choi, D.Kim .H.L.Tuller and A.I.Akinwande, *IEEE Transactions on electronic devices*, 52, 2819(2005)
92. Jaehoon park, Jiwei W.Lu, Damien S.Boesch,Susanne Stemmer and Robert A.York, *IEEE Microwave and wireless components letters*, 16, 264(2006)
93. E.Erker, A.S.Nagara, Y.Liu, P.Periaswamy, T.R.Taylor, J.Speck, R.A.York, *IEEE microwave. Guidedwave Lett,* 10, 10(2000)
94. A.K.Tagantsev, J.W.Lu, S.Stemmer, *Applied physics letters*, 86,032901(2005).
95. G.Jean Pierre, P.Michel, D.Olivier, G.Claude, *Ceramic transactions*, 179,207(2006)

2.1 Preparation and characterization techniques for bulk Bi_2O_3-ZnO-Nb_2O_5 ceramics

Though one of the major objectives of the present work is the preparation and characterization of Bismuth Zinc Niobate thin films, it is desirable to have a fair knowledge about the structural and electrical properties of these materials in their bulk form before making them into thin films. This section deals with the preparation and characterization techniques used for bulk BZN composition. Since this material has to be characterized for its dielectric properties in the microwave range, it has to be prepared in a regular geometry with the highest possible densification. This being a ceramic oxide material, the available methods for its preparation are (a) Solid-state reaction method (or ceramic method) (b) Chemical methods and (c) Mechanical methods [1-3]. Of these, the method used for bulk BZN preparation in this study is the solid-state reaction method.

2.1.1 Solid-state reaction method

Ceramics are polycrystalline materials having fine crystalline grains and imperfections like grain boundaries, impurities segregated in the grains and grain boundaries, pores etc. Since they are, in general, brittle refractories, shaping them and densifying them without cracks and deformation is a challenge. The solid-state reaction method is used for forming c-BZN, m-BZN and Ti substituted m-BZN compositions from the reagents. The shaping and densification are separate processes, which are described in subsequent sections.

The conventional solid state reaction method involves the following steps: (a) Uniform mixing of the initial reagents (b) Phase formation of the required compound at a high temperature, which is called the calcination stage. The main disadvantages of this method are that it needs high processing temperatures in order to achieve the best properties and this process increases the particle size. But cost effectiveness and simplicity are the major advantages of this process.

2.1.2 Stoichiometric weighing of reagents

Raw materials Bi_2O_3, ZnO and TiO2 of purity >99.9% from Aldrich Chemicals and Nb_2O_5 of purity >99.9% from NFC, Hyderabad were weighed according to the respective compositions of $Bi_{1.5}Zn_{1.0}Nb_{1.5}O_7$, $Bi_2Zn_{2/3}Nb_{4/3}O_7$, and $Bi_2Zn_{2/3}Nb_{4/3-x}Ti_xO_7$. The purity of the initial reagents is important to achieve control over impurities in the product and to maintain reproducible microwave dielectric properties. An electronic balance (A&D technologies, Model GR-120) is used to weigh the reagents, which has an accuracy of up to 0.001mg.

2.1.3 Uniform mixing of reagents

The individual reagents are to be mixed uniformly in order to increase the points of contact between the reagents, which will act as product layer formation centers. Therefore, the initial stoichiometric reagents mixture must be mixed uniformly with a suitable mixing medium. The weighed batches were mixed in an agate mortar by hand grinding. Acetone was used as a mixing medium.

2.1.4 Calcination stage

The solid-state, diffusion controlled chemical reaction between the initial reactants resulting in the desired phase formation is called calcination. It is the intermediate heat treatment at lower temperatures prior to sintering. Calcination could involve chemical decomposition reactions in which solid reactants are heated to produce a new solid phase and remove the gases which are commonly associated with the initial metal oxide compounds such as carbonates, hydroxides, nitrides, sulphates, acetates and other metal salts. The parameters of the calcination stage such as temperature, duration of heating and atmosphere are important factors influencing shrinkage during sintering. In the present case, the reagents being oxides, they do not undergo any decomposition. All the reagents used in the present study were calcined at 800°C to form the required composition and the phase formation is confirmed by XRD.

2.1.5 Uniaxial pressing

After reducing the particle size of the calcined powder, the fine powder is compacted into cylindrical specimens (green pellets) by uniaxial pressing. The compaction of the powder should be done slowly to facilitate the escape of the entrapped air. To make the green pellets of the ceramic powder, a rigid die, which is rust free, is needed. To make the inner walls of the die smooth, stearic acid is used as an internal lubricant. The pressure gradient on the die as a function of the distance from the upper punch is given by the equation

$$P_x = P_a e^{-4\mu KL/D} \quad (2.1)$$

where, μ is the coefficient of friction, P_a is the applied pressure, L is the length and D is the diameter of the die and K is a constant [4].

2.1.6 Solid-state sintering

In ceramics, porosity is an important parameter which governs many of its properties. For maximizing properties such as the dielectric constant, quality factor, mechanical strength, translucency and thermal conductivity, it is desirable to eliminate as much of porosity as possible. The purpose of sintering is the reduction of porosity in the compact. The development of microstructure and densification during sintering is a direct consequence of mass transport through several possible paths and one of these paths is usually predominant at any given stage of sintering [5]. In the present study all the samples were sintered at a temperature range of 950°C-1100°C for 2 hrs.

2.2 Characterization techniques used for the bulk compositions

a. Powder X-Ray Diffraction
b. Scanning Electron Microscopy
c. Low frequency impedance and dielectric characterization
d. Microwave characterization

2.2.1 X-ray diffraction

Powder X-Ray Diffraction is a powerful non-destructive method for determining a range of physical and chemical characteristics of materials. The applications include the type and quantities of phases present in the sample (phase analysis), the crystallographic unit cell and crystal structure, crystallographic texture, crystallite size, macro-stress and micro-strain and also electron radial distribution functions [6].

In the present work, two types of X-ray diffractometeres were used to characterize the samples. One is with Co Kα (λ=1.7889Å) radiation in a wide angled powder X-ray diffractometer (INEL Model CPS120) equipped with a position sensitive detector and the other one is with Cu K_α (λ=1.54056 Å) radiation, using a Philips PW 1830 diffractometer. Calibration using a Si standard was done to account for the instrumental line broadening and the value was approximately 0.15^o.

2.2.2 Scanning Electron Microscopy

In a Scanning Electron Microscope (SEM), electrons are thermionically emitted from a tungsten cathode and are accelerated towards an anode. Alternatively, electrons can be emitted via field emission (FE). The electron beam, which typically has an energy ranging from a few hundred eV to 50 keV, is focused by one or two condenser lenses into a beam with a very fine focal spot size of 1 nm to 5 nm. The beam passes through pairs of scanning coils in the objective lens, which deflect the beam in a raster fashion over a rectangular area of the sample surface. Through these scattering events, the primary electron beam effectively spreads and fills a teardrop-shaped volume, known as the interaction volume, extending from less than 100 nm to around 5 μm into the surface. Interactions in this region lead to the subsequent emission of electrons, which are then detected to produce an image. X-rays, which are also produced by the interaction of electrons with the sample, may also be detected in an SEM equipped for energy-dispersive X-ray spectroscopy or wavelength dispersive X-ray spectroscopy. The most common imaging mode monitors low energy (<50 eV) secondary electrons. Due to their low energy, these electrons originate within a few nanometers from the surface. The electrons are detected by a scintillator-photomultiplier device and the resulting signal is rendered into a two-dimensional intensity distribution that can be viewed and saved as a digital image. This process relies on a raster-scanned primary beam.

The brightness of the signal depends on the number of secondary electrons reaching the detector. If the beam enters the sample perpendicular to the surface, then the activated region is uniform about the axis of the beam and a certain number of electrons "escape" from within the sample. As the angle of incidence increases, the "escape" distance of one side of the beam will decrease, and more secondary electrons will be emitted. Thus, steep surfaces and edges tend to be brighter than flat surfaces, which result in images with a well-defined, three-dimensional appearance. Using this technique,

resolutions less than 1 nm is possible [7].In addition to the secondary electrons, backscattered electrons can also be detected. Backscattered electrons may be used to detect contrast between areas with different chemical compositions.

2.2.3 Low frequency impedance and dielectric measurements

The low frequency dielectric spectroscopy is emerging as an important material characterization tool [8]. The low frequency dielectric measurements are unequaled in their ability to dynamically monitor the many chemical and physical processes important in the investigation of new materials such as polymerization, phase transition and diffusion. The conventional way for making the low frequency measurement (below<10MHz) of the dielectric properties of solids is to place a sample between closely spaced parallel conducting plates and monitor the AC equivalent capacitance $C_{(\omega)}$ and the dissipation factor (also known as the loss tangent) $D_{(\omega)}$ of the resulting capacitor [9]. Normally one has to design the plate spacing to be much less than the plate size as this serves to minimize the effect of the fringing field. The material under test in the parallel plate configuration can be modeled as a frequency dependent capacitance $C_{(\omega)}$ in parallel with a frequency independent resistor R_0. The DC resistance R_0 takes into account processes such as tunneling, thermally activated hopping and ionic conduction. The capacitance $C_{(\omega)}$ is proportional to the complex dielectric function of the material under test which can be represented as follows,

$$\varepsilon_{(\omega)} = \varepsilon_{r(\omega)} - j\varepsilon^{''}_{(\omega)} \tag{2.2}$$

The capacitance $C_{(\omega)}$ can be measured by a typical capacitance bridge which can be used to calculate the real part of the complex dielectric function $\varepsilon^{'}_{(\omega)}$.

$$C_{(\omega)} = \frac{\varepsilon_{r(\omega)}\varepsilon_0 A}{d} \tag{2.3}$$

Here, A is the cross section area of the capacitor, d is the separation between the plates and ε_0 =8.85 x10^{-12}F/m is the absolute permittivity of free space. The other measured quantity, the dissipation factor (the loss tangent) given by

$$D_{(\omega)} = \frac{\varepsilon^{''}_{(\omega)}}{\varepsilon_{r(\omega)}} + \frac{d}{\omega \cdot \varepsilon_0 \cdot \varepsilon^{'}_{(\omega)} \cdot A \cdot R_0} \tag{2.4}$$

and can be used to extract the imaginary part of the dielectric function $\varepsilon''_{(\omega)}$.

Figure 2.1 Photograph of the temperature dependent dielectric measurement set up.

For the dielectric measurement silver paint was applied on both sides of the pressed pellets and the samples were fixed in the spring loaded sample holder attached to a heating and cooling chamber. The parallel capacitance (C) and the dissipation factor (D) for all the samples were measured using an Agilent 4294A impedance analyzer in the frequency range of 100Hz-1MHz in a temperature range of 300 to 600K with a Lab – Equip temperature control unit. The temperature and measurement process were controlled electronically by a homemade programme using lab view software. The temperature was maintained with an accuracy of ±1K. A photograph of this measurement set up is given in figure2.1

2.2.4 Microwave measurements

Dielectric Post (DP) resonator techniques have been employed for the microwave characterisation of the ceramic samples. The sample under test is placed over a low loss support material and is enclosed in a cylindrical copper cavity, which acts as a resonating structure. The TE_{011} mode is identified for each resonator. The measurement system consisted of a Network Analyser (HP 8722C), closed cycle refrigerator (APD DE-204), temperature controller (LTC-10), Vacuum Dewar, a PC and the Hakki-Coleman dielectric resonator in the transmission mode. These measurements were carried out at the James Cook University, Australia. The real part ε_r of relative permittivity was computed from the measured resonance frequency of the resonator containing the sample under test. The

S_{21}, S_{11} and S_{22} parameters have been measured around the resonance and the loaded Q-factor (Q_L) and coupling coefficients k_1 and k_2 calculated accurately using the transmission mode Q factor (TMQF) method. A simplified TMQF [10] is used to remove effects of non-calibrated measurement cables, connectors, coupling structures, noise and cross talk between the coupling loops. Precise values of the loss tangent (tanδ) of the material under test was then calculated from the unloaded Q-factor (Q_0) computed using Eq.2.5 [11]

$$Q_0 = Q_L(1 + k_1 + k_2) \tag{2.5}$$

2.3 Processing of BZN thin films

Deposition techniques for thin films may be divided into physical vapor deposition (PVD), chemical vapor deposition (CVD) and chemical solution deposition. The PVD technique includes RF magnetron sputtering, pulsed laser deposition (PLD) and molecular beam epitaxy (MBE), which are generally used for the deposition of oxide thin films [12,13]. The CVD route that can be employed includes metal organic chemical vapor deposition (MOCVD) and low pressure CVD. The chemical solution techniques that can be used are mainly metal organic deposition (MOD) and solgel techniques. The main criteria for choosing a suitable deposition technique are (a) low temperature growth (b) large uniform area of deposition (c) high purity and density (d) controlled composition stoichiometries (e) high degree of structural perfection (f) good electrical properties (g) excellent adhesion and (h) high growth rate.

Each technique has its own merits and drawbacks. Chemical deposition routes such as CVD and MOCVD offer a large area of uniform deposition, but require a higher processing temperature. Magnetron sputtering has its drawback in having stringent conditions for maintaining the stoichiomectry in deposited films, although it offers a large area and commercial scale production. Pulsed laser deposition offers good quality stoichiomectric films at a lower processing temperature, but suffers from a drawback of small area deposition for non-rastering substrates. Among the various techniques available, the deposition methods such as rf sputtering, metal organic decomposition (MOD), metal organic chemical vapour deposition (MOCVD) and pulsed laser deposition (PLD) have been used to deposit BZN thin films by many research groups [14,15]. Compared with other deposition methods, PLD has the advantage of a high deposition rate and precision in stoichiometry control. It also gives the freedom of a vast range of

operating pressures. Large area uniform deposition is also possible by using movable target substrate geometry. There is no film damage due to the surface bombardment effect when compared to other PVD techniques. Therefore, PLD was used for the deposition of BZN thin films in this work. A complete study has been followed regarding the effect of process parameters on the film's crystalline and electrical properties.

2.3.1 Laser ablation setup

A KrF excimer laser (248nm wavelength, Model Compex pro201F of Lamdaphysik, Germany) was used for the deposition process. A schematic diagram of the laser ablation system is shown in figure 2.2 and the picture of the laser ablation system used for the deposition of BZN thin films in this study is shown in figure 2.3. The set up can be used either for single or multi-target ablation. The laser used was a 248nm UV with a maximum energy output of 600 mJ for a fresh fill of gases. The laser could be operated at frequencies in the range of 1-10 Hz. The beam density was calculated by dividing the beam energy by the beam area. The laser beam was collimated using a slit to use the uniform region and condensed using a quartz lens. The beam energy density at the target (fluence) was calculated using the following relation:

$$E_{target} = E_{input} \times m^2 \tag{2.6}$$

Here, m is the magnification of the lens and is given by

$$m = \frac{b - f}{f} \tag{2.7}$$

where, b is the lens to target distance and *f* is the focal length of the lens used. The laser was allowed inside the deposition chamber through the quartz vacuum port. The vacuum chamber was evacuated using a turbo molecular pump to a base pressure of 4 x10^{-6}Torr. Films were grown in a pure oxygen atmosphere at a pressure ranging from 1 to 25 m Torr.

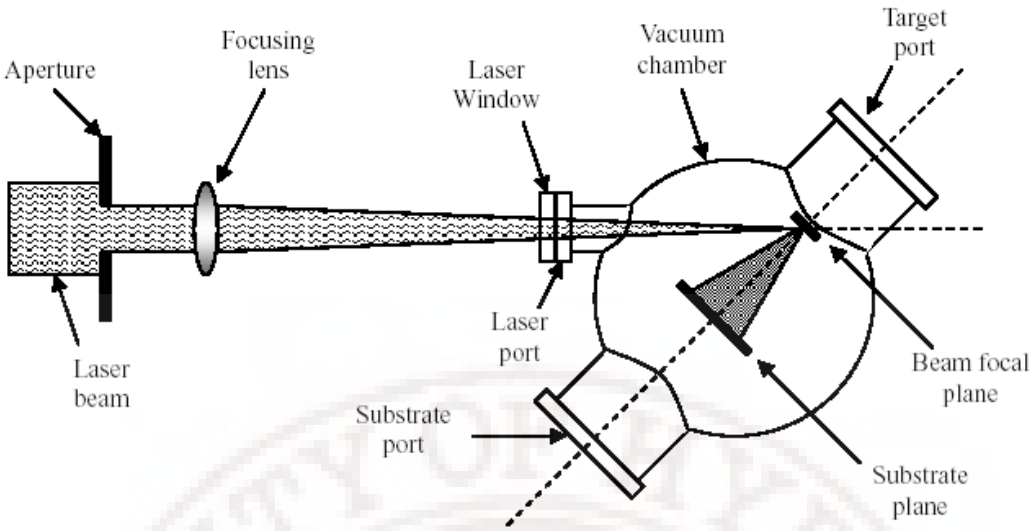

Figure 2.2 Schematic diagram of the laser ablation set up

Figure 2.3 Laser ablation set up employed for the thin film deposition and the plume generated when the laser strikes the target.

2.3.2 Target preparation

Highly dense pellets of c-BZN and m-BZN ceramics were prepared by the conventional solid state reactions. Starting powders of Bi_2O_3, Nb_2O_5 and ZnO (99.9% purity, Aldrich chemicals) were used for the solid state reactions. The details of the solid state reaction process are given in section 2.1.1. The calcined powders were then pressed into pellets in a hydraulic press using a 20mm die. The pressed pellets were placed on a

platinum foil in a furnace for the final sintering process. The targets were sintered at 1050°C for two hours. Finally both the surface of the pellets were ground, cleaned and polished to ensure a proper surface finish. Polishing the surface was necessary to improve the ablation properties. The crystallographic structure of the targets was determined from the X-ray diffraction (XRD) pattern. The XRD patterns of the c-BZN and m-BZN ceramic targets aregiven in figure 2.4.

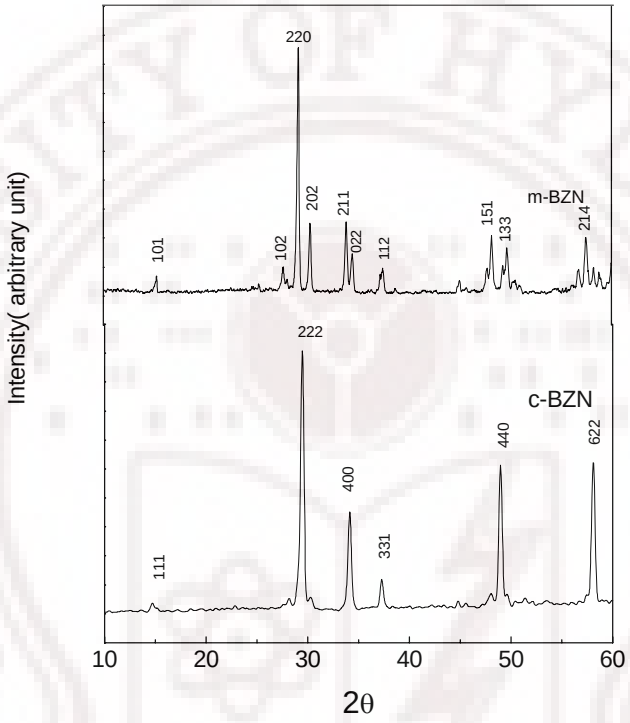

Figure 2.4 X-ray diffraction pattern for the sintered targets.

The prepared pellets show a cubic pyrochlore structure for c-BZN and a monoclinic Zirconolite structure for m-BZN with perfect phase formation. The composition of the targets was obtained by using the energy dispersive spectroscopy method in a scanning electron microscope and the stoichiomectry was confirmed.

2.3.3 Substrates

The substrates used in the present study are mainly amorphous fused silica. Apart from this, the films were also deposited in various single crystal substrates such as lanthanum aluminate, sapphire and MgO. P type silicon and pt coated silicon were also used as the substrates for specific studies. All the substrates used were properly cleaned ultrasonically using acetone, isopropanol and finally in de-ionized water in a laminar flow table. The substrates were finally dried under dried nitrogen gas blown through a nozzle.

2.3.4 Deposition conditions

The target was made to rotate using a stepper motor which was connected out side the deposition chamber. The substrates were loaded in a stainless steel substrate mount equipped with of a heater block. All the depositions were carried out at an ambient temperature followed by an exsitu annealing treatment at 550-600°C to obtain crystallization. The depositions were carried out in the presence of oxygen at various pressures. Pure oxygen (99.9%) was fed into the chamber using a mass flow controller. The deposition pressure was varied between 1 to 25 mTorr. All the films were deposited at ambient temperatures. The list of optimum deposition conditions is given in table 2.1.

Deposition condition	
Base Pressure	: 4.5 x10^{-6} Torr
Deposition Pressure	: 1-25mTorr
Fluence	: 2-4J/cm^2
Laser Reprate	: 1-5Hz
Target substrate distance	: 35mm
Deposition temperature	: Ambient

Table 2.1 List of optimum deposition conditions.

2.4 Physical characterization of thin films

Several analytical techniques were used to determine the material properties of the pulsed laser deposited c-BZN and m-BZN thin films. The deposited films were characterized for its thickness, stoichiomectry, chemical bondings, structure and microstructure using the techniques such as surface profilomectry, Energy dispersive analysis of X-rays (EDAX), X-ray photo electron spectroscopy (XPS), X-ray diffraction (XRD) and atomic force microscopy (AFM). A brief introduction about each of these experimental techniques is given below.

2.4.1 Thickness measurement

Profilomectry is a fast and simple method to measure film thickness. It works by gently dragging a mechanical stylus across the sample surface. The stylus is placed in contact with, and then gently dragged along the surface of the substrate. The vertical reflection measures the change in step height and the trace is recorded. To measure the

thickness of thin films used in this work, a part of the substrate was covered with a piece of scotch tape during film deposition. After the thin film deposition, the tape was removed and the film thickness was then measured over the step. For the experiment done in this work an Ambios XP-1 stylus profiler was used and the instrument was calibrated using standard substrates.

2.4.2 Composition analysis

Semi-quantitative composition analysis of the films was carried out using the energy dispersive analysis of X-rays (EDAX) method in a scanning electron microscope. EDAX uses the technique in which emitted X-rays from the target sample are resolved in energy electronically by pulse height analysis instead of resolving them in wavelength by a diffraction crystal. In an SEM, the incident electron beam on the sample generates X-rays due to the interaction between the high-energy electron beam and the sample [16]. The generated X-rays consist of the characteristic wavelengths of the elements constituting the sample. Each emitted x-ray photon adds a count to the appropriate channel of a multi-channel analyzer (MCA), which reproduces the x-ray spectrum. Intensity of each peak is related to the concentration of that element in the sample. The intensity of the x-ray signal depends on the beam current, accelerating voltage, geometry of the system and concentration of the constituent elements. Analysis of an acquired spectrum comprises accounting for spurious peaks and identifying the elements present in the sample. The energy of the characteristic X-ray is given by Mosley's law

$$E \cong C_1(Z - C_2) \tag{2.8}$$

where, Z is the atomic number, C_1 and C_2 are constants. Thus, from the energy location of the peaks in the spectrum, software routines sort out the elements present by comparison with the tabulated characteristic energy values. For EDAX measurements the sample was prepared by coating a thin conducting layer of gold by sputtering to avoid charge buildup. The (Bi+Zn)/Nb and Bi/Nb ratios were used as standards and the film composition was normalized with respect to these ratios.

2.4.3 X-ray Photoelectron Spectroscopy (XPS)

In an XPS analysis, a sample is irradiated by an X-ray beam, which contains photons whose energy is $h\upsilon$ (h = $6.63 \cdot 10^{-34}$ J·s). As a consequence, a photoelectric effect is produced and, thus, the sample emits electrons with a kinetic energy:

$$E = h\nu - E_B \tag{2.9}$$

Here, E_B is the binding energy of the electron bond, which is a characteristic of each chemical element. Free electrons pass through an electrostatic energy analyser, and a spectrum with the yield as a function of E *or* E_B is obtained, which informs us about the surface chemical composition of the sample. The incident radiation energy is higher than 1 keV, so the ionisation in the deep energy levels and the valence band is produced. Mg or Al anticathode work as X-ray sources when they are bombarded by accelerated electrons coming from a filament. The interaction of the incident electrons with the anticathode produces a group of X-ray lines, from which only the one corresponding to Kα is filtered for the measurements.

An XPS spectrum consists of a line distribution superposed to a background radiation. The different proportions of the areas defined by every line indicate the stoichiomectry. In general the spectral lines will be broadened and there are three factors contribute to line broadening: the broadening of the radiation line, the uncertainty of the bond energy and the detection band of the instrument. The chemical shift affecting the lines is originated by the influence of the atomic environment of the probed elements. Thus, an XPS spectrum also provides information about the nature of the chemical bond. In-depth chemical profiles are measurable by varying the detection angle, and in the cases of thickness greater than nanometers this is possible by combining XPS analysis combined with sputter stages using Ar+ ions. The XPS measurements have been performed at a base pressure of $1x10^{-10}$ m bar using a commercial electron energy analyzer with five chanel electrons from GmbH, Germany, and an Al K_α X-ray source which provides 1486.6eV photons. These measurements were performed at the consortium for scientific research (CSR) Indore center.

2.4.4 Structural analysis

The crystallographic structures of the films were determined from the obtained X-Ray Diffraction (XRD) patterns. In the present work, two types of X-ray diffractometer were used to characterize the samples. One was with Co Kα (λ=1.7889Å) radiation in a wide angled powder X-ray diffractometer (INEL Model CPS120) equipped with a

position sensitive detector and the other one was with Cu K_α (λ=1.54056 Å) radiation, using a Philips PW 1830 diffractometer. Calibration using a Si standard was done to account for the instrumental line broadening and the value was approximately 0.15^o. The patterns were compared with standard patterns (JCPDS) and the phases and degree of crystallinity were determined. A slow scanning rate of 1°/min was used to extract data for the measurement of grain size from peak full width at half maxima (FWHM). These results gave important information regarding the film microstructure and changes in the grain size with thermal treatment. The grain size was determined from the Scherrer equation [17] given by

$$C_{size} = (k \times \lambda)/(\beta \times \cos\theta) \qquad (2.10)$$

where, k is a constant (normally 0.94 for Scherrer), λ is the wavelength, β is the FWHM of the peak and θ is the angular position of the peak. The determined grain sizes were compared for films grown under various processing conditions.

2.4.5 Atomic force microscope

The microstructures of the deposited films were obtained using an AFM. The AFM consists of a microscale cantilever with a sharp tip (probe) at its end that is used to scan the specimen surface. The cantilever is typically silicon or silicon nitride with a tip of radius of curvature of the order of nanometers. When the tip is brought into the proximity of a sample surface, forces between the tip and the sample lead to a deflection of the cantilever according to Hooke's law. Depending on the situation, forces that are measured in the AFM include mechanical contact force, Van der Waals forces, capillary forces, chemical bonding, electrostatic forces, magnetic forces, solvation forces, etc. Typically, the deflection is measured using a laser spot reflected from the top of the cantilever into an array of photodiodes. The AFM can be operated in a number of modes, depending on the application. The primary modes of operation are static (contact) mode and dynamic mode [18].

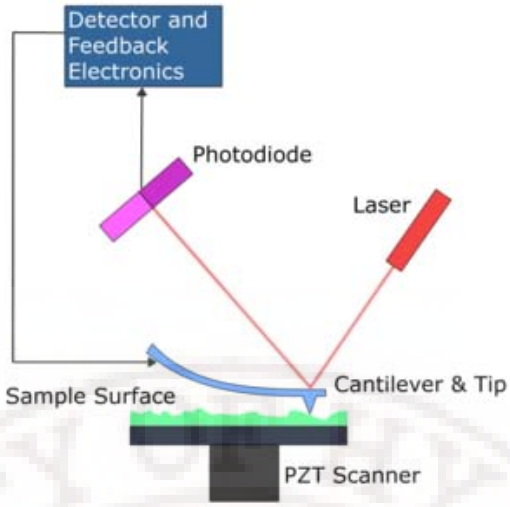

Figure 2.5 Schematic diagram of an atomic force microscope.

In the static mode operation, the static tip deflection is used as the feedback signal. Since the measurement of a static signal is prone to noise and drift, low stiffness cantilevers are used to boost the deflection signal. However, close to the surface of the sample, attractive forces can be quite strong, causing the tip to 'snap-in' to the surface. Thus static mode AFM is almost always done in contact where the overall force is repulsive. Consequently, this technique is typically called 'contact mode'. In the contact mode, the force between the tip and the surface is kept constant during scanning by maintaining a constant deflection through feedback circuitry. In the dynamic mode, the cantilever is externally oscillated at or close to its resonance frequency. The oscillation amplitude, phase and resonance frequency are modified by tip-sample interaction forces. These changes in oscillation with respect to the external reference oscillation provide information about the sample's characteristics. Schemes for dynamic mode operation include frequency modulation and the more common amplitude modulation. In frequency modulation, changes in the oscillation frequency provide information about tip-sample interactions. Frequency can be measured with very high sensitivity and thus the frequency modulation mode allows for the use of very stiff cantilevers. In this work, the microstructure of the oxide films was imaged in an atomic force microscope in the dynamic force mode [Model SPA400 of SII Inc, Japan).

2.5 Optical properties

The spectral transmission and Raman scattering studies of these thin films were carried out to have an understanding about the optical and local structural characteristics. The optical characteristics such as transmission, refractive index, and the lattice dynamics for the thin films were estimated. The details of these measurement techniques are given below.

2.5.1 Spectral transmittance studies

The optical constants of the thin films were calculated using the envelope technique [19]. The spectral transmission characteristics in the wavelength range 190-1500 nm were measured using a JASCO V570 UV-VIS-NIR spectrophotometer.

If light is incident on a film of refractive index n, coated onto a substrate of refractive index s, then at the air-film, film-substrate and substrate-air interfaces, part of the incident light is reflected and part of it is transmitted. Since the reflected and transmitted beams originate from a single source, the beams exhibit interference effects. The condition for constructive interference in such a case is given as

$$2nd = m\lambda \qquad (2.11)$$

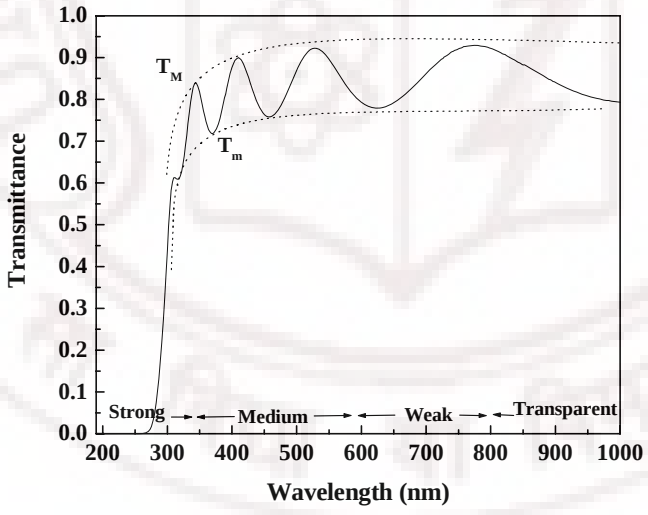

Figure 2.6 Typical transmittance spectrum of the film.

where, n is the refractive index of the film at a wavelength λ and m is the order of interference, d is the thickness of the film that can be calculated from the derived values of refractive indices.

In general, the transmission T, is given by the expression

$$T = \frac{Ax}{B - Cx\cos\phi + Dx^2} \tag{2.12}$$

where, $A=16n^2s$, $B=(n+1)^3 (n+s)^2$, $C=2(n^2-1) (n^2-s^2)$, $D= (n-1)^3 (n-s^2)$

$\phi=4\pi nd/\lambda$

For such a system, at the points of constructive and destructive interference, the transmittance T_M and T_m, respectively are given as

$$T_M = \frac{Ax}{B - Cx + Dx^2} \tag{2.13}$$

and $$T_m = \frac{Ax}{B + Cx + Dx^2} \tag{2.14}$$

For simplicity, it can be assumed that the transmission is a continuously varying function of the wavelength which can be approximated by drawing the envelope across the spectrum, connecting all the maximas and minimas as shown in figure 2.6.

$$n = \left[N + \left(N^2 - n_s^{\,2}\right)^{1/2}\right]^{1/2} \tag{2.15}$$

Here, N is a constant, S is the refractive index of the substrate used and n_s is the refractive index of the film at that particular wavelength.

$$N = 2S\frac{T_M - T_m}{T_M T_m} + \frac{S^2 + 1}{2} \tag{2.16}$$

Adding the reciprocals of equations 2.13 and 2.14 yields

$$\frac{2T_M T_m}{T_M + T_m} = \frac{Ax}{B + Dx^2} \tag{2.17}$$

and, solving x we get

$$x = \frac{F - F\left[F^2 - \left(n^2 - 1\right)\left(n^2 - s^4\right)\right]^{1/2}}{\left(n-1\right)^3\left(n - s^2\right)} \tag{2.18}$$

where, $$F = \frac{8n^2 s}{T_i} \tag{2.19}$$

and $$T_i = \frac{2T_M T_m}{T_M + T_m} \quad (2.20)$$

where, T_M is the maximum of the transmission on the envelope at a wavelength λ and T_m is the minimum of the transmission on the envelope at the same wavelength. The T_M and T_m at each wavelength can therefore be read off from the envelope and the refractive index can be derived at each wavelength.

From the equation of constructive interference, it can be seen that for two successive maxima occurring at λ_1 and λ_2, the equation becomes

$$2n_1 d = m_1 \lambda_1 \quad (2.21)$$

and $$2n_2 d = m_2 \lambda_2 \quad (2.22)$$

Also $|m_1 - m_2| = 1$.

Therefore, $$d = \frac{\lambda_1 \lambda_2}{2(n_1 \lambda_2 - n_2 \lambda_1)} \quad (2.23)$$

In the strong absorption region, from Beer-Lambert's law given by

$$I = I_o \quad (2.24)$$

where, I_o is the incident intensity =1, I is the intensity at a given wavelength λ, d is the thickness of the film and α is the absorption coefficient in cm^{-1}.

Since d is known from previous calculations and I is a measured quantity (i.e. transmission at a wavelength λ), the absorption coefficient α can be calculated. Knowing α from the expression for the so-called "Tauc gap", the fundamental absorption edge of the material can be determined. The expression for the Tauc gap is given as

$$\alpha h\nu = \text{constant} \times (h\nu - E_g)^2 \quad (2.25)$$

The X- Intercept of the extrapolation of the linear region in a plot of $(\alpha h\nu)^{1/2}$ vs. $h\nu$ will give the value of bandgap E_g. The error associated with the measurement of k, n and d is ± 0.005, ± 0.02 and ± 10nm respectively.

2.5.2 Raman spectroscopy

This is a versatile non-destructive technique to monitor short-range structural properties of materials. In this characterization method, a monochromatic light beam is directed at the sample, and the reflected light is measured. To this end, lasers of different wavelengths may be employed. This technique is based on the physical principle of molecular vibrations. Two kinds of light scattering are possible when a photon with $h\nu_0$ energy collides with a molecule. Rayleigh scattering occurs when the photon frequency remains constant after the collision. It corresponds to an elastic collision. On the other hand, Raman scattering is a process generated by inelastic collisions. The molecule is initially in the fundamental state of vibration and is then promoted to an excited state due to the absorption of the photon energy. The emitted radiation has an energy of $h(\nu_0 - \nu_\nu)$ which defines the radiation detected in a Raman spectrum.

Raman-scattering data were obtained using a T64000 spectrometer (Horiba Inc.) equipped with a triple-grating monochromator and a Coherent Innova 90C Ar^+-laser with the excitation wavelength at 514.5 nm. The measurements were performed using Raman microscopy with an LN_2–cooled charge coupled device (CCD). The spectral resolution was typically less than 1 cm^{-1}. This measurement was carried out at the speclab, university of Puerto Rico, USA.

2.6 Electrical characterization

For dc as well as the low and high frequency electrical characterization of the thin films, suitable test structures have to be fabricated onto the films. For the realization of these test structures a suitable micro fabrication process has to be optimized. In this work a single mask photolithographic process was used to pattern the metallization required for the test structures. The single step lift off process was chosen because it uses gentle organic chemicals, which do not react with the BZN thin films. The details of the photolithographic process, the electrode layer deposition and the electrical characterization techniques used are given in the subsequent sections.

2.6.1 Photolithography and lift off techniques

Photolithography is a reproducible process used in semiconductor device fabrication to transfer a pattern from a photo-mask to the surface of a substrate using light. A layer of photoresist is applied on top of the metal layer. The photo resist is

selectively hardened by illuminating it in specific places. For this purpose a transparent plate with patterns printed on it, called a mask, is used together with an illumination source to shine light on specific areas of the photoresist. Then, the photoresist that was not exposed to light is etched away with a chemical treatment. On top of this patterned surface, the required metal layer (pt, Au or Ag) is deposited. Finally, the hardened photoresist is etched using a different chemical treatment along with the metal layer on top of it, and all that remains is a layer of metal in the same shape as that of the mask. A brief description of clean room processing for image reversal lithography is described below.

Cleaning: To remove atmospheric dust and contamination, the film sample is cleaned for 5 minutes in an ultrasonic bath of acetone and then rinsed in de-ionized (DI) water. It is finally dried with dry nitrogen.

Dehydration Bake: The cleaned sample should be pre-baked at 110°C for 10 minutes for drying. Otherwise, the photoresist will be coated with water vapor.

Spin coating: OIR620-10M from Fuji films was spin coated. The spin speed depends on the desired thickness. 2500 RPM for 30 seconds gives an approximately 1.2 μm thick uniform layer.

Soft bake: Soft baking removes most of the remaining solvent from the photoresist film, thereby densifying it. Soft bake time and temperature also influence adhesion, speed, and dimensional control of the photoresist. Our samples were baked on a hot-plate at 100°C for 15 minutes.

Exposure: The exposure depends on resist thickness, lamp intensity and many other variables. The pattern was defined using a MJB4 mask aligner with a UV-light exposure of 10 seconds (35–45 mJ/cm^2).

Developing: The exposed resist was developed in a developer solution for 60 seconds.

After developing, the films were completely coated with the electrode metals followed by a lift off. The electrodes consist of a thick layer of silver of around 600nm thickness, covered by a thin layer of gold, of around 100nm thickness. Silver is chosen because of its high conductivity and the gold capping layer, for oxidation resistance. The deposition of the electrode metals is described in the following section. In the lift off process, the sample was put in an ultrasonic acetone bath for about 5 minutes, thereafter rinsed in DI water, and finally dried with nitrogen to remove the resist and unwanted metal.

Figure 2.7 Micro fabrication facility used for realization of test devices.

2.6.2 Top electrode deposition

From a device point of view, the optimization of the growth process for the BZN thin films, electrode material and a suitable process flow for fabrication, and integration of these films in the devices are three major steps. The fabrication technology for the metallization process is very important when preparing the microwave devices using these thin films. Material deposition techniques such as sputtering and thermal evaporation are compatible with the deposition of high quality metal films suitable for microwave devices. DC sputtering is a widely used deposition technique for a variety of metals. In the present work we have used RF magnetron sputtering for the metal deposition because it was found to be giving better adhesion and good film quality.

In its simple representation, the phenomenon of sputtering consists of material erosion from a target on an atomic scale, and the formation of a thin layer of extracted material on a suitable substrate. The process is initiated by a glow discharge produced in a vacuum chamber under pressure controlled flow. Target erosion occurs due to energetic particle bombardment by either reactive or non reactive ions produced in the discharge.

The RF magnetron sputtering technique consists of a target, which is a plate of metal to be deposited, and a substrate placed on a grounded sample holder. The glow discharge is initiated by applying power to the target in a controlled gas atmosphere and is constituted of a partially ionized gas of ions, electrons and neutral species. The ejected material diffuses until it reaches and nucleates on the substrate. The duration of this process controls the thin film thickness. The use of a radiofrequency (RF) generator is essential to maintain the discharge and to avoid the charge build up when sputtering the insulating materials. The presence of a matching network between the rf generator and the target is necessary in order to optimize the power dissipation in the discharge. Magnets are used to enhance the sputtering rate by increasing the ionization effect of the electrons magnetically trapped in the vicinity of the target (magnetron sputtering). Their use provides the advantage of trapping not only the electrons, but also the charged species at the target so that they do not hit the substrate to ensure an improved film quality. The details of the sputtering process are described elsewhere [20].

2.6.3 Low frequency dielectric measurements

The frequency and voltage dependent dielectric properties of these films grown on different substrates were characterized at low frequencies using a suitable capacitor structure. For these measurements different capacitors were designed and fabricated onto the films using the micro fabrication process described in section 2.9.1. The measurements were carried out using inerdigitated capacitors, parallel plate capacitors in the patch capacitor geomectry and a MOS capacitor. The details of these techniques are given in the subsequent sections.

2.6.3a Interdigitated capacitor

The low frequency dielectric properties of the c-BZN and m-BZN thin films grown on fused silica, sapphire, lanthanum aluminate and MgO substrates were measured using an interdigitated capacitor (IDC) structure. The IDC capacitors having a finger length of 90μm, with a total of 8 fingers and an overlap length of 80 μm were designed for these measurements. The finger width and finger gap was made equal and it was 10 μm. These capacitors were defined onto these films with gold as the electrode material, using the photolithographic technique described above.

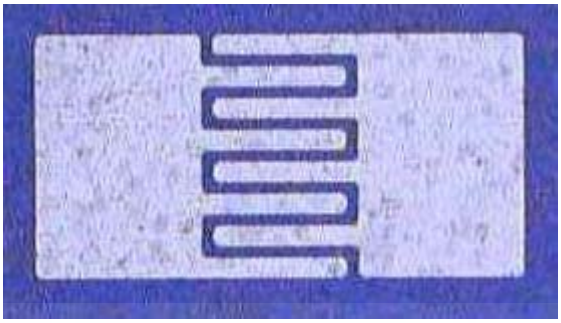

Figure 2.8 Microphotograph of the fabricated IDC capacitor.

To calculate the dielectric constant of thin film capacitors with the interdigitated electrode configuration shown in figure 2.8 an analytical model previously derived by Farnel et al [21] was employed. This method has been successfully used by many researchers to estimate the dielectric properties of thin films on the substrates precisely [22, 23]. Based on this model, the dielectric constant of a thin film can be calculated using the following expression.

$$\varepsilon_f = \varepsilon_s + \left(\frac{C - [K(1+\varepsilon_s)]}{K\left[1 - \exp\left(\frac{-4.6h}{L}\right)\right]} \right) \tag{2.26}$$

Here, ε_f and ε_s are the film and substrate dielectric constants, respectively, h is the film thickness, K is a constant which has units of pF, and C is the measured capacitance per unit finger length per electrode section of width L and is given by

$$C = \frac{C_m}{FL \times N} \tag{2.27}$$

where, C_m is the experimentally measured capacitance in (pF), FL is the IDC finger length in meters and N is the number of sections of width L in an IDC pattern that can be calculated from the following formula

$$N = 2P - 1 \tag{2.28}$$

where, P is the number of finger pairs in the IDE patterns. The constant K is given as

$$K = 6.5\left(\frac{D}{L}\right)^2 + 1.08\frac{D}{L} + 2.37 \tag{2.29}$$

For an IDC pattern with equal finger width and spacing L equal to 2D, the value of K will be 4.53pF. The IDC patterns used in this work all had equal finger width and spacing. This means that the value of K used throughout these calculations was 4.53pF. The capacitance and loss factor measurements were done on these films using an Agilent 4294A impedance analyzer.

2.6.3b Parallel plate capacitor

Parallel plate capacitors with the circular patch (CPC) electrodes were fabricated on platinised silicon substrates using Ag- Au as the top electrode. A lift off process was used to pattern the top electrode consisting of a central circular patch surrounded by a concentric ground plane. The schematic cross section and microphotograph of the CPC structure fabricated is shown in figure 2.9. The capacitance C of this capacitor is measured between the inner circular patch and the bottom platinum layer using a DC probe station connected to the Agilent 4294A impedance analyzer.

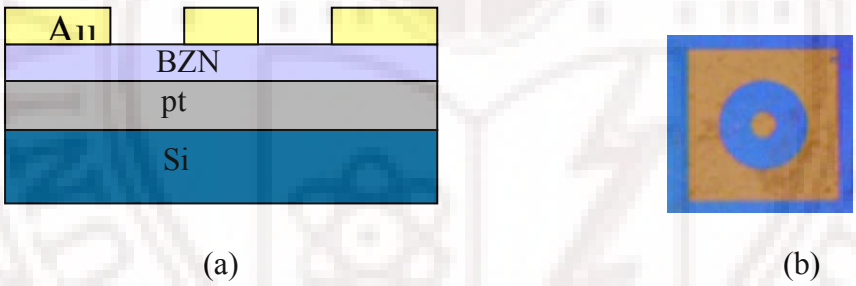

(a) (b)

Figure 2.9 Cross section and microphotograph of the tunable capacitor fabricated using BZN thin films.

The dielectric properties were calculated using the following equations.

$$\varepsilon_r = \frac{C \cdot d}{A \cdot \varepsilon_0} \tag{2.30}$$

$$\tan\delta = \frac{1}{Q} \tag{2.31}$$

$$\text{Relative } Tunability = \frac{\varepsilon_{\max} - \varepsilon_{\min}}{\varepsilon_{\max}} \tag{2.32}$$

Here, A and d are the capacitor area and film thickness respectively, and Q is the measured quality factor of the capacitor under test.

2.6.3c MOS capacitor

The MOS capacitor consists of a Metal-Oxide-Semiconductor structure as illustrated in the figure 2.10. It consists of the semiconductor substrate with a thin oxide layer and a top metal contact [26]. A second metal layer forms the contact to the back of the semiconductor and is called the bulk contact. The MOS capacitors having 300μm x 300μm square top electrodes were fabricated on films of m-BZN or c-BZN deposited p type silicon substrates using Au as the top electrode by the photolithographic process. The schematic cross section and microphotograph of the MOS structure fabricated is shown in figure 2.10. The MOS structure is treated as a series connection of two capacitors- the capacitance of the oxide and the capacitance of the depletion layer. In accumulation region there is no depletion layer. The remaining capacitor is the oxide capacitance, so that the total capacitance equals [27]:

$$C_{LF} = C_{HF} = C_{ox} \quad ; V_G \leq V_{FB} \tag{2.33}$$

Here V_G is the gate voltage and V_{FB} is the flat band voltage C_{ox} is the oxide capacitance The CV characteristics of the MOS capacitors are measured using the Agilent 4294A impedance analyzer connected to a DC probe station.

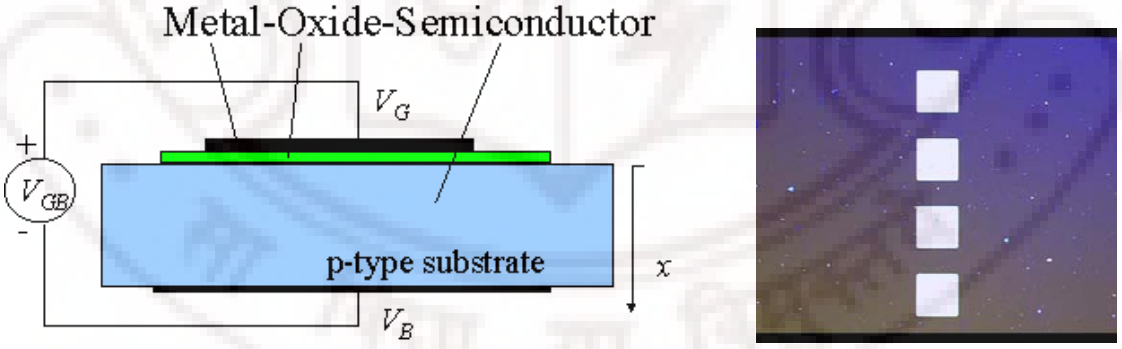

Figure 2.10 Schematic diagram and microphotograph of the fabricated MOS capacitors.

2.6.4 Leakage current characterization

All the DC measurements were done using a Radiant precession LC material analyzer, which could simultaneously act as a constant voltage source and measure the current flowing through the circuit to an accuracy of $1x10^{-14}$A. Leakage current measurements were done as a function of time and voltage. During the I-Vmeasurements to record the realistic leakage behavior, a waiting time of 50 seconds was introduced to

ensure the equilibrium leakage current at each voltage increment. For time dependent dielectric breakdown measurements, a high voltage was applied to the sample and the current was measured as a function of time. The breakdown was considered as complete when the sample current reached a value of 100mA.

References:

1. M.N.Rahaman "Ceramic processing and sintering" (Marcel Dekker, Inc, New York) 2003.
2. D.Seagal "Chemical synthesis of advanced ceramic materials" (Cambridge University Press, Cambridge) 1991.
3. R.E.Carter, *J.Chem.Phys*, 34, 2010 (1961).
4. C.Suryanarayana, *Progress in Mater. Sci*., 46, 1 (2001).
5. S-J. Kang " Sintering, densification, grain growth and microstructure" (Elsevier, Amesterdam) 2002.
6. D. Cullity, "X-ray Diffraction" (Addison-Wesley, Reading, MA) 1956.
7. K.D.Vernon-Parry, III-vs Review 13,40(2000)
8. Helene Hagerstrom,Katarina Edgman,Maria Stromme, *Journal of pharmasuitical science*, 92,1869(2003)
9. J.F.Johnson and R.H.Cole, J.Am.Chem.Soc.73,4536(1951)
10. Ginzton E. L.1957 Microwave Measurement, McGraw Hill Book Co.
11. M. V Jacob, J Mazierska, K Leong,., and J Krupka, *IEEE Transactions on Microwave Theory and Technique*, 49, 2401(2001)
12. Zoe H. Barber, *Journal of material chemistry*,16,334(2006)
13. Y.Yoneda, K.Sakaue and H.Terauchi, *Surf.Sci*, 529,283(2003)
14. Shingo Okaura, Muneyasu Suzuki,Shoji Okamoto, Hiroshi Uchida, Seiichirokoda and Hiroshi Funakubo, *Jpn.J.Appl.Phys,* 44, 6957(2005).
15. Y.P.Hong, S.Ha, H.Y.Lee, Y.C.Lee, K.H.Ko, D.W.Kim, K.S.Hong, *Thin Solid films,* 419,183(2002)
16. www.Edax.com
17. A.L.Patterson, *Physical Review*,56,978(1939)
18. www.nanoscience.com/education/AFM
19. R.Swanpoel, *J.Phys.E: Sci.Instrum*, 16, 1214 (1983).
20. M.Ohring, "The material Science of thin films" *Academic press Inc.Newyork*, USA(1992)

21. G.W.Farnell, I.A.Cermak, P.Silvester and S.K.Wong, *IEEE Trans on Sonics and ultra sonics* SU-17,188(1970)
22. H.N.AL.Shareef, D.Dimos, M.V.Raymond, R.W.Schwartz and C.H.Mueller. *J.Electroceramics* 1:2,145(1997)
23. G.Velu, J.C.Carru, E.Cattan, D.Remiens, X.Melique, D.Lippens, *Ferroelectrics*, 288, 59(2003)
24. K.Khamhane, A.Vorobiev, T.Claeson and S.Gevorgian, *Journal of applied physics*, 99, 034103(2006)
25. N.Delmonte, B.E.Watts, G.Chiorboli, P.Cova, R.Menozzi, *microelectronics reliability*, 47,682(2007)
26. H.Lu, J.S.Pan, X.F.Chen, W.G.Zhu and O.K.Tan, *Applied physics letters*, 88, 132907(2006)
27. C.W.Law, K.Y.Tong, K.L.Wong, J.H.Li, Kun Li, *IEEE Electron device meeting proceedings* , Hong Kong P54(1998)

Chapter 3

Microwave characterization techniques for high-k dielectric thin films

3.1 Introduction to microwave characterization of thin films

The characterization of the dielectric properties of bulk materials in the microwave frequency range is well developed while that of thin films is a challenge. New microwave characterization techniques are needed for thin films taking into account the fact that they are always deposited on a dielectric or conducting substrate and the thickness of the film is too less compared to the wavelength involved. This chapter describes various techniques that can be used for the microwave characterization of thin films and the techniques set up for this study. In recent years, the increasing requirements for the development of high speed and high frequency circuits and systems have made a good understanding of the properties of materials at microwave frequencies an essential requirement. High K thin films are being used in many microwave electronic circuits and devices [1, 2]. Often, the thin films for microwave applications are characterized at frequencies which are much lower than the frequency of operation of the devices in which they are going to get incorporated.

At the low frequency regions (up to a few MHz) the thin film dielectrics are characterized by making a metal-insulator-metal (MIM) capacitor structure. The dielectric constant and loss factor are calculated by directly measuring the capacitance and dissipation factor using an impedance analyzer or LCR meter [3]. This method cannot be directly used in the microwave frequencies because of the following limitations. At microwave frequencies, the dimensions of the capacitor become comparable with the wavelength of the electromagnetic wave used for the measurement and hence the capacitors can no more be considered as lumped elements but they will have to be considered as distributed elements. Also, at these frequencies the impedance of the capacitor will be very small compared to the resolution of the impedance analyzers. Hence, special techniques are to be used for the measurement of the dielectric parameters of thin films at microwave frequencies.

.

Many researchers are trying to study the microwave dielectric properties of thin films by employing various methods. Most of the measurement methods used for the determination of the complex permittivity and loss tangent of dielectric thin films involve two steps. Firstly, the electrical characteristics of the dielectric thin film containing device is monitored. Secondly, the dielectric permittivity and loss tangent of the material are derived from the obtained device data. The measurement techniques can be broadly classified into three different groups such as reflection measurements, transmission measurements and resonance measurements [4]. In reflection measurement, the reflection coefficient of the thin film capacitor is measured while in the transmission measurement techniques the transmission characteristics of the thin film based planar transmission lines are measured using a network analyzer. In the resonance method, the characteristics of a resonator containing the thin film material are investigated. The subsequent sections of this chapter describe the various techniques that have been employed in this study for the microwave characterization of thin films.

3.2 Resonance method

Microwave methods for the electromagnetic property characterization of materials generally fall into two categories, viz. non resonant methods and resonant methods. Non resonant methods generally include reflection methods or transmission / reflection method. Resonant methods include resonator methods and the resonant perturbation method. In resonator methods, the sample under measurement is excited as part of a resonator in the circuit and the materials electromagnetic properties are deduced from the resonator characteristics. In the resonant perturbation methods, the sample under measurement is introduced to a resonator (measurement fixture), thus altering the electromagnetic boundaries of the resonator, and the electromagnetic properties of the sample are deduced from the changes in the resonant properties of the resonator. In our experiments, we have employed two types of resonant perturbation techniques for characterizing the dielectric properties of thin films, at spot frequencies which are described below.

3.2.1 Modified cavity perturbation technique

The cavity perturbation technique is widely used in the measurement of dielectric parameters of materials [5]. This technique has also been used effectively to determine the complex permittivity of liquids [6]. In the conventional cavity perturbation technique, the changes in the resonant frequency and quality factor Q, when a material is introduced into the cavity give a measure of the complex permittivity of the material [7]. For materials having a complex permittivity ε'- jε", these changes may be expressed as:

$$\frac{f_1 - f_2}{f_2} = (\varepsilon' - 1)\frac{\int_{V_S} E_1^2\, dV}{\int_{Vc} E_1^2\, dV} \tag{3.1}$$

$$\left[\frac{1}{Q_2} - \frac{1}{Q_1}\right] = \varepsilon'' \frac{\int_{Vs} E_1^2\, dV}{\int_{Vc} E_1^2\, dV} \tag{3.2}$$

where,

$$E_1 = E_{10} \sin\left(\pi x / a\right) \sin\left(n \pi z / L\right) \tag{3.3}$$

and, f_1, f_2 are the resonance frequencies without and with the specimen respectively. Q_1 and Q_2 are the corresponding quality factors of the cavity. V_s and V_c are the sample and cavity volumes respectively. The conventional cavity perturbation technique can be extended to measure the complex permittivity of larger samples, provided the field perturbation by the sample lies within the prescribed limits [8]. In this case, the length of the sample is not small and the field E_1 in equations 3.1 and 3.2 is no longer a constant but it varies sinusoidally along the sample length. This method therefore involves solving the eigenvalue problem of a dielectric sample in a rectangular cavity. In our experiments we consider the substrate as a part of the cavity. The field inside the cavity with the substrate is taken as the initial field E_1. This approach has been used for quite a long time for the determination of the dielectric properties of liquids/solids in the powder form. A hole is drilled through the top surface of the cavity at the E_{max} position and a sample holder is inserted through that hole. The cavity with the sample holder is taken as the initial cavity, which has a resonance frequency f_1 with the sample holder [9]. Now the samples whose dielectric properties have to be determined are introduced to this sample holder and the properties are extracted from the shift in the resonance frequency and the shift in the quality factor of the cavity. In our approach, the uncoated substrate can be

considered as a part of the cavity, provided the substrate is of a low dielectric constant material. The cavity with the film coated substrate inside is taken as the perturbed cavity with a resonance frequency f_2. Q_1 and Q_2 are the corresponding quality factors of the cavity.

The main assumption of this method is that the dimension of the sample is small compared to the wavelength, which is always true in the case of thin films. If the sample surface lies across the cavity and everywhere else tangential to the electric field, then the dielectric constant is given as [10]:

$$\varepsilon' = K\frac{L}{\tau}\frac{\Delta f}{f_{0s}} + 1 \tag{3.4}$$

where, L is the cavity length, τ is the film thickness, Δf is the frequency shift, f_{0s} and f_0 are the resonance frequencies of the cavity with the substrate and the film coated substrate respectively. The coefficient K is a measure of the area of the sample with respect to the cross sectional area of the cavity. It is equal to unity when the whole cross section is occupied by the film and is less than unity when the cross section is partially filled with a film. Similarly, the dielectric loss is given as:

$$\varepsilon'' = K\frac{L}{2\tau}\left[\frac{1}{Q_{L_s}} - \frac{1}{Q_{L_0}}\right] \tag{3.5}$$

where, Q_{Ls} and Q_{L0} denote the unloaded Q factor of the cavity with and without the film coated substrate. This means that in this method the uncoated substrate is considered as a part of the cavity, giving a net resonant frequency f_0, provided the substrate is a low dielectric constant material. The cavity with the film coated substrate inside is taken as the perturbed cavity with a resonance frequency f_{0s}. Q_{L0} and Q_{Ls} are the corresponding quality factors of the cavity. It was assumed that the shift in the resonance frequency and the quality factor from (f_0, Q_{L0}) to (f_{Ls}, Q_{Ls}) is only due to the properties of the film since the substrate is considered as a part of the cavity. Hence equations 3.4 and 3.5 can be applied directly to find out the dielectric constant and loss of the thin films coated on low dielectric constant substrates.

3.2.2 Analysis of the accuracy of measurement.

The error in evaluating the dielectric permittivity can be calculated using the expression [10]:

$$d\varepsilon' = K\frac{\Delta f}{f_{0s}}\frac{1}{\tau}dL + K\frac{L}{\tau}\left[\frac{\Delta f}{f_{0s}}\left(\frac{d\tau}{\tau}+\frac{df_{0s}}{f_{0s}}\right)+\frac{d\Delta f}{f_{0s}}\right] \tag{3.6}$$

In most practical cases the last factor is at least 10 times larger than the sum of the other three factors. For very thin films the error related to the accuracy of measuring the thickness has a significant effect on the overall accuracy. In our case, this error is negligible because the thickness is measured by an optical method and cross checked with a surface profiler. In all the cases, the accuracy of measuring the cavity resonance frequency shift Δf is the main factor limiting the accuracy of determining ε'. We have taken extreme care to insert the sample at the E_{max} position of the cavity. Also, we ensured that the position remains the same in each measurement. The 8722ES Vector Network Analyzer (VNA) has a very good sensitivity and it got the resolution down to 1 Hz in the resonance frequency. It is therefore expected that our measurement accuracy in determining the dielectric constant is fairly high. The error in evaluating the dielectric loss can be given as:

$$d\varepsilon'' = \frac{KL}{2\tau}\left[\frac{1}{Q_{Ls}}-\frac{1}{Q_{L0}}\right]\left[\frac{dL}{L}+\frac{d\tau}{\tau}\right]+\frac{KL}{\tau}\frac{dQ_L}{Q_{Ls}} \tag{3.7}$$

This indicates that the main source of error in this measurement is the accuracy in measuring the Q factor. Also, if the Q factor of the empty cavity is too low there will be considerable error in the determination of the dielectric loss. Here we are using high Q cavities (≈ 5000) and the Q factor can be accurately measured from the VNA directly.

Figure 3.1 A picture of the WR-90 cavity connected to the VNA.

A TE_{10n} mode WR90 rectangular waveguide cavity was connected to Port 1 of the Agilent 8722ES VNA through the coaxial to waveguide adapter after the one port calibration at the adapter surface (figure3.1). The cavity can resonate at five different modes in the X band. We have selected the TE_{107} and TE_{109} modes for the measurements. A thin fused silica substrate of 5mm width and 1.2cm length is thoroughly cleaned and inserted into the cavity such that the sample surface is tangential to the electric field. The resonance frequency f_0 and the quality factor Q_{L0} of the cavity with the bare substrate are measured. The substrate is then coated with a ferroelectric thin film on one side of the substrate. This test sample is again inserted into the cavity and the corresponding resonance frequency f_s and the quality factor Q_{Ls} are determined. The experimental results of ε'and ε" are obtained from equations 3.4 and 3.5.

3.2.3 Split post dielectric resonator technique

This is a non-destructive and accurate technique for measuring the complex permittivity of dielectric substrates and thin films at a spot frequency [11]. For thin films deposited on a substrate, the frequency shift due to the film has to be separated from the overall frequency shift of the film substrate. For this purpose one has to measure the resonance frequency and quality factor ($f_{01,}Q_{01}$) of the empty resonator and do the same ($f_{s,}Q_s$) with the substrate. After the film deposition, the resonance frequency and quality factor of the ($f_{sf,}Q_{sf}$) substrate coated with the film have to be measured again.

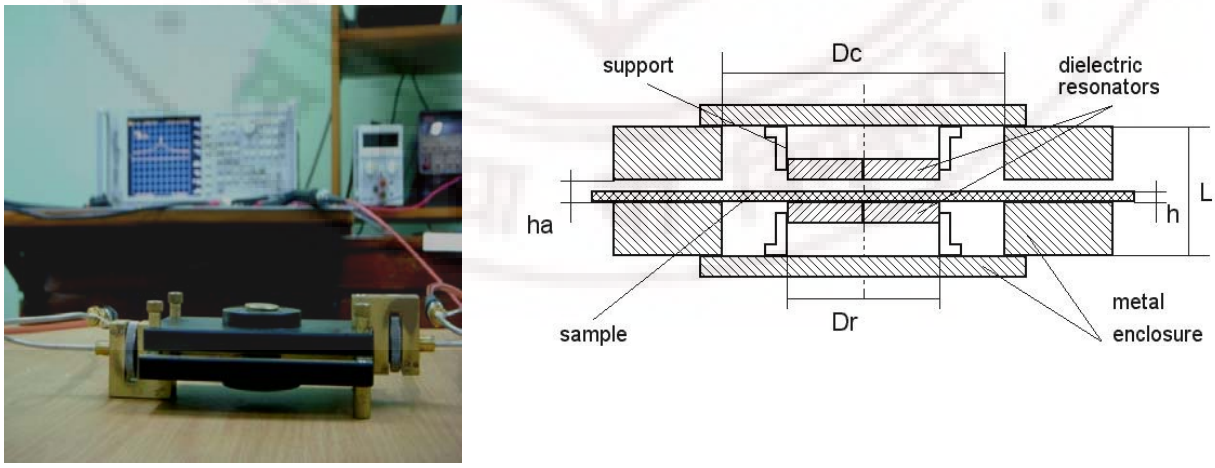

Figure 3.2 Picture of the SPDR measurement set up with the schematic diagram of an SPDR.

The SPDR typically operates in the $TE_{01\delta}$ mode that has only an azimuthal electric field component, so that the electric field remains continuous on the dielectric interfaces [12]. This makes the system insensitive to the presence of air gaps perpendicular to the z-axis of the fixture. The real part of permittivity ε_r of the sample is found on the basis of the measurements of the resonant frequencies and thickness of the sample as an iterative solution to equation 3.8.

$$\varepsilon' = \frac{1+(f_0 - f_s)}{h f_0 K_s(\varepsilon', h)} \tag{3.8}$$

Here, h is the sample thickness, f_0 is the resonance frequency of the SPDR with the substrate, and f_s is the resonance frequency of the SPDR with the film coated substrate. K_s is a function of the sample's dielectric constant ε_r and thickness h. Since K_s is a slowly varying function of ε_r and h, the iterations using the formula (3.8) converge rapidly.
The loss tangent is computed using the equation (3.9):

$$\tan\delta = \frac{Q^{-1} - Q_{DR}^{-1} - Q_c^{-1}}{p_{es}} \tag{3.9}$$

where, Q is the unloaded Q factor of the SPDR containing the dielectric sample and p_{es} is the electrical energy-filling factor of the sample. Qc is the Q factor depending on the metal losses of the SPDR containing the dielectric sample and Q_{DR} is the Q-factor depending on the dielectric losses in the dielectric resonators.

3.3 Transmission line method

The waveguide method is one of the first methods developed for characterization of dielectric materials at microwave frequencies. The transmission line method is a special case of the waveguide method. It consists of the measurement of the scattering matrix of a planar transmission line which is patterned on to the dielectric thin film. Generally two types of planar transmission lines are used for the characterization of thin films named as the coplanar waveguide (CPW) transmission line and microstriplines. A schematic diagram of the CPW lines and microstriplines are shown in figure 3.3. The scattering parameters of these transmission lines are determined with the help of a network analyzer. From the scattering parameters the propagation constant of these transmission lines are derived. From the derived propagation constant one can obtain the information about the dielectric constant and dielectric loss at the microwave frequencies. The most recent technique to determine the propagation constant is the calibration

comparison technique. For implementing these techniques, one should need to know some basics of microwave network analysis, planar transmission lines, on wafer measurements and calibration techniques. A brief description of these topics is given in the subsequent sections.

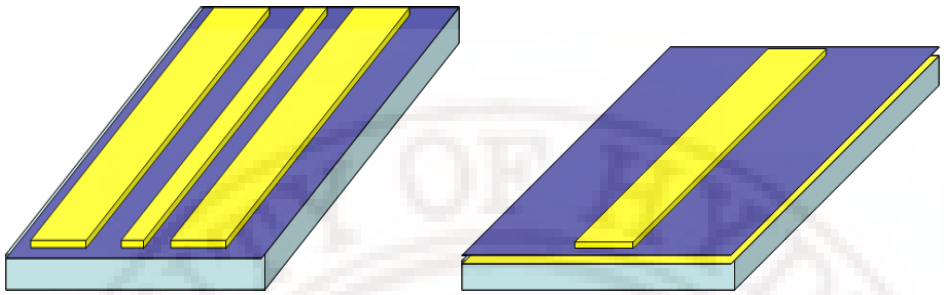

Figure 3.3 Schematic diagram of (a) CPW based and (b) micro strip based transmission lines.

3.3.1 Microwave network analysis

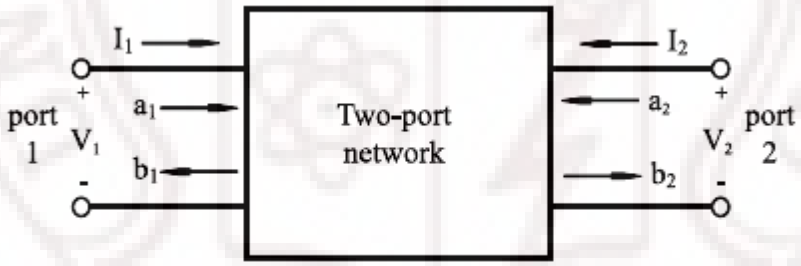

Figure 3.4 Schematic representation of a two port network with voltages, currents, input wave a and output wave b.

The basic concept of the microwave network is developed from the transmission line theory, and it is a powerful tool in microwave engineering. The microwave network method studies the responses of a microwave structure to external signals, and it is a complement to the microwave field theory that analyzes the field distribution inside a microwave structure [13]. In the network approach, we do not care about the distributions of electromagnetic fields within a microwave structure, and we are only interested in how the microwave structure responds to external microwave signals. Two sets of physical parameters are often used in network analysis. As shown in figure 3.4, one set of parameters are voltage V (or normalized voltage v) and current I (or normalized current i)

and the other set of parameters are the input wave *a* (the wave going into the network) and the output wave *b* (the wave coming out of the network). Different network parameters are used for different sets of physical parameters. For example, impedance and admittance matrices are used to describe the relationship between the voltage and current, while scattering parameters are used to describe the relationship between the input waves and output waves.

3.3.2 Impedance and admittance matrices

For a two port network shown in the figure 3.4, we have

$$[V]=[Z][I] \tag{3.10}$$

$$[I]=[Y][V] \tag{3.11}$$

where, [V] is the unnormalized voltage, [I] is the unnormalized current.

The impedance and admittance matrix are:

$$[Z]=\begin{bmatrix} Z_{11} & Z_{12} \\ Z_{21} & Z_{22} \end{bmatrix} \tag{3.12}$$

$$[Y]=\begin{bmatrix} Y_{11} & Y_{12} \\ Y_{21} & Y_{22} \end{bmatrix} \tag{3.13}$$

Z_{11} is the input impedance at port 1 when the other port is open. Z_{12} is the transition impedance from port 2 to port 1 when port 1 is open. Y_{11} is the input admittance at port 1 when the other port is shorted. Y_{12} is the transition admittance from port 2 to port 1 when port 1 is shorted [13].

From the above equations, we can get the following relationship between [Y] and [Z]

$$[Z][Y]=1 \tag{3.14}$$

3.3.3 Scattering parameters

The responses of a network to external circuits can also be described by the input and output microwave waves. The input waves at port 1 and port 2 are denoted as a_1 and a_2 respectively, and the output waves from port 1 and port 2 are denoted as b_1 and b_2 respectively. These parameters may be either voltage or current, and in most cases, we do not distinguish whether they are voltage or current. The relationships between the input wave [a] and the output wave [b] are often described by scattering parameters [S]

$$[b] = [S]a \tag{3.15}$$

$$[S] = \begin{bmatrix} S_{11} & S_{12} \\ S_{21} & S_{22} \end{bmatrix} \tag{3.16}$$

When port 1 is connected to a source and the other port is connected to a matching load, the reflection coefficient at port 1 is given as [14]

$$\Gamma_{11} = S_{11} = \frac{b_1}{a_1};\ and\ a_2 = 0 \tag{3.17}$$

Similarly, the transmission coefficient is given as:

$$S_{12} = \frac{b_1}{a_2};\ \ and\ \ \ a_1 = 0 \tag{3.18}$$

3.3.4 On-wafer test and analysis

For the measurement of the scattering parameter of any test device, the device has to be connected to a vector network analyzer. Before the advent of coplanar probes, finding the RF behavior of a device was a complicated process. The wafer had to be diced and an individual die had to be mounted onto a test fixture [15]. Only then could the device performance be known. Fixturing involved attaching the die to a PCB, wire bonding to the bond pads, connecting RF cables to the fixture, and measuring. Discriminating between the device and the fixture response had become the central problem for high volume screening. One of the obvious advantages of the on-wafer prober at microwave frequencies is that one can get spot measurements on wafers. Thus

on-wafer characterization became inevitable in microwave measurements of un packaged devices. A typical on-wafer microwave measurement setup will consist of a Vector Network Analyzer (VNA), a probe station, on-wafer probes, RF cables and a calibration substrate. The quality of RF measurements depends on the VNA, the reliability of the RF cable and fixture, connectors and the calibration quality. A brief description of the measurement setup is given below.

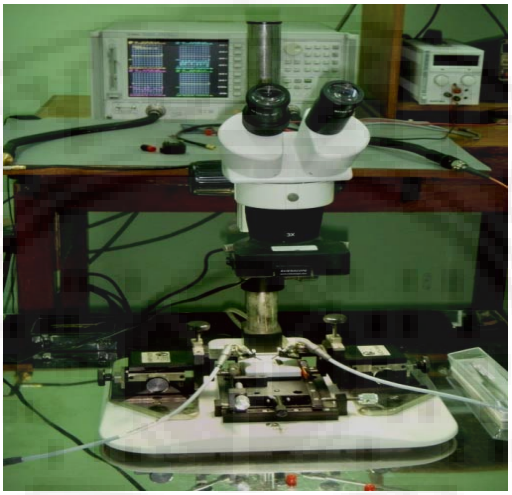

Figure 3.5 Picture of the on-wafer measurement setup.

Network Analyzer: Network analyzers are widely used to measure the four elements in a 2 port scattering matrix (S_{11}, S_{12}, S_{21}, and S_{22}). Basically, a network analyzer can separate and measure the four waves independently; two forward waves, a_1 and a_2, and two reverse traveling waves, $b_1$and b_2. The scattering parameters can then be obtained by a combination of these four waves. In our experiment, Agilent Technologies 8722ES VNA was used for the S parameter measurements. It can operate within a 50MHz to a 40GHz frequency range.

Probe station: In a probe station, the wafer is held on a vacuum chuck. The probes are fixed to micro positioners secured on the probe station. The micro positioners are the precision micrometers, enabling fine movement in the x, y and z dimensions. In this study the on-wafer measurements were performed on a J micro technology make LMS-2709 RF/DC probe station, which has got a rugged ball bearing stage with 1 inch of x and y travel, vacuum clamping and 0.05 inch of z lift. The probe station is equipped with KRN-09S probe positioners with 0.5 inch x, y and z movements with 40 tpi (turns per inch)

precession movement. The 250 μm pitch ground-signal-ground (GSG) probes from GGB industries were used for the measurement.

Calibration substrate: An accurate and easily usable calibration substrate with a well defined calibration coefficient and a detailed instruction set to allow accurate calibration of the measurement system (VNA+cabling+probes) is essential for the on-wafer test analysis. Typical elements for calibrating a microwave measurement system consists of an open, short, matched loads and a thru. These four elements have electrical characteristics that are very different from one another so that each element contributes an important part to the overall calibration process. In the present study the model Cs-5 calibration substrate (GGB industries) that contains high precision elements for calibrating out the unavoidable errors and losses in a microwave network analyzer, its associated cabling, and the probes for on-wafer testing was used. It covers SLOT (Shorts, Opens, Loads and Thrus), TRL (Through-Reflection-Load) and LRM (Load-Reflection-Match calibration) types with a G-S-G footprint with a pitch range of 75-250 microns.

3.3.5 Coplanar wave guide

The coplanar waveguide (CPW) is a type of planar transmission line used in microwave integrated circuits (MIC) as well as in monolithic microwave integrated circuits (MMIC). The unique feature of this transmission line is that it is uniplanar in construction, which implies that all the conductors are on the same side of the substrates [16]. This attribute simplifies the manufacturing and allows a fast and inexpensive characterization using on-wafer techniques. The basic structure of the CPW is illustrated in figure3.6.

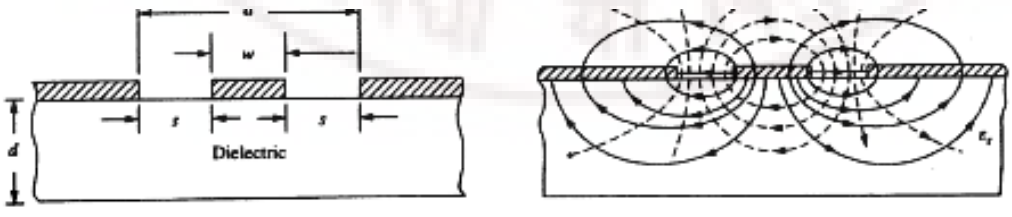

Figure 3.6 A typical coplanar waveguide (a) cross-sectional view of the structural dimensions, (b) electromagnetic field distribution. The solid lines represent electric fields and the dashed lines represent the magnetic field lines.

This arrangement is assumed to be symmetrical with the strip width w and the longitudinal gap s. The side conductors are ultimately grounded theoretically at infinity. The CPW has some advantages compared to the other transmission lines such as microstriplines. They are simple to fabricate and have reduced dispersion (for small dimensions) as well as radiation losses. They have a reduced cross talk between the lines with higher directivity and a low dependence on substrate thickness.

The current density on the CPW signal line is not uniform across its surface. The current crowds to the edges of the CPW signal line even more than that of a microstripline of the same dimensions. Hence this will lead to greater insertion losses. The CPW's advantage over the microstripline is that the CPW line width is independent of the line impedance. Therefore one can use a wider line which in turn helps to reduce the conductor's high frequency losses. Also it is possible to achive a wider range of impedance values in a CPW lines compared to that of other transmission lines like microstrip lines.

3.3.6 On-wafer calibration

A considerable challenge in the measurement of the S parameters using a vector network analyzer (VNA) is to define exactly where the measurement system ends and the device under test begins. This location is called the reference plane. This means that all error contributions inside the VNA and in the cables up to this reference plane will have to be calibrated out. The calibration of the VNA is performed by rather complex procedures such as Short-Open-Load-Through (SLOT) method, Through-Reflection-Load (TRL) method or Load-Reflection-Match (LRM) method. In this study,the SLOT and LRM calibration procedures are used and a brief description of these procedures are given in the subsequent sections. In an S parameter measurement using a VNA, 6 errors are identified in the forward direction and the same six errors are there in the reverse direction also. So in a full two port measurement there are a total of 12 errors. These errors can be corrected using the calibrations. The pairs of six errors associated with the VNA analysis are directivity, cross talk, source mismatch, load mismatch, reflection tracking and transmission tracking. The details about these systematic errors are given elsewhere [17].

3.3.6a SLOT calibration

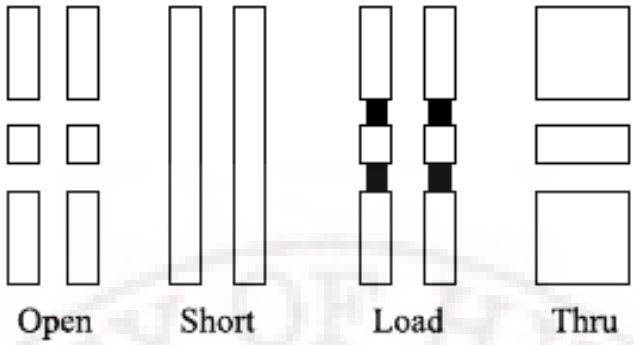

Figure 3.7 Circuit layout of SLOT standards for CPW structures in a Cs-5 calibration substrate.

SLOT (Shorts, Opens, Loads and Thrus) calibration relies on well known standards, all defined along the same reference plane. This is a basic reflection calibration for a ground-signal-ground (GSG) probe head [18]. For the open circuit standard, the probe should be lifted in the air or it can use the standard open in the calibration substrate. For the short circuit standard, the three contacts are made on a small bar of a conductor, usually a gold metallization. The 50 ohm load for a GSG probe uses a pair of trimmed 100 ohm resistors that are about 2 mils constituting a 50 Ohm load. The typical through calibration uses a very short 50 Ohm CPW through connection. Although popular, the SLOT method has disadvantages; the main concern is about the accuracy of the standards, since there is a direct connection between the knowledge of the standard's precise RF characteristics and the accuracy of the calibration. Well-known standards bring forth a better SLOT calibration. All standards used in SLOT are direct standards. Even small deviations from the ideal can lead to considerable errors. Furthermore, accurately characterizing the SLOT standards becomes laborious at frequencies above 20GHz.

3.3.6b LRM calibration

LRM (Line-Reflect-Match)[19] is very similar to TRL (Thru-Reflect-Line)[20]. The line and reflect are analogous to the thru and reflect standards in TRL, the difference being that LRM uses a precision match (or load) to define the system characteristic impedance Z_0. Again, either an open or short can serve as the reflect. As in SLOT, the load must be well defined, otherwise the calibration sensitivity is degraded. The line standard is kept as the electrical reference plane. The LRM technique takes advantage of the high quality coplanar transmission lines and loads that can be fabricated on many

microwave substrates. By using a pair of coplanar loads instead of offset transmission lines, the LRM method avoids the low frequency limitations of the TRL technique. Additionaly the LRM method can be used with fixed probes, and also accurate short and open references are not required.

3.3.7 Calibration comparison techniques

This is a broad band technique that can be used for the extraction of dielectric properties of thin films on a substrate. This technique can also be employed to extract the voltage dependent dielectric properties. The calibration comparison technique makes use of two identical coplanar waveguides (CPW) patterned on the surface of the film [21] and on the bare substrate. Two CPW test structures of a 100-micron gap and a 200 micron width were patterned simultaneously, one on the test film and the other on the bare substrate by a lift–off process. The scattering parameters of these CPW transmission lines were measured using a VNA and a probe station (LMS-2709) mounted with the GSG probes of 250-micron pitch.

(a) (b)

Figure 3.8 (a) picture of the CPW transmission lines fabricated for on-wafer measurement, mounted on the probe station.(b) The fabricated CPW line.

The test structure fabricated was designed and simulated using the full wave simulator momentum of the agilent ADS. The characteristic impedance of the CPW transmission lines were obtained from the electromagnetic simulation of the CPW line on the reference sample. A typical simulated result for the CPW line on a 0.5 mm thick $LaAlO_3$ substrate using ADS momentum is shown in figure 3.9

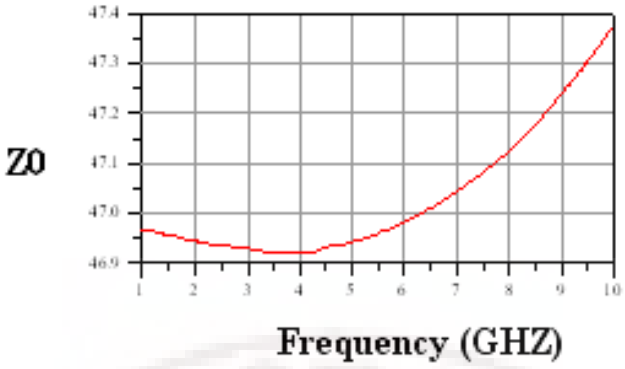

Figure 3.9 Simulated results for the characteristic impedance of the reference CPW line.

The method used in this study compares the propagation characteristics of the transmission lines fabricated on the bare substrate (reference sample) and the substrate with the thin film of BZN (test sample). This technique has been successfully used in the past for the characterization of low k as well as high k dielectric thin films [22]. The resistance and inductance of the reference and test CPW lines were assumed to be the same. Also the loss tangent of the low–loss microwave substrate is assumed to be negligible. The ratio of the propagation constants of the CPW lines in both the cases is given as:

$$\frac{\gamma_{test}}{\gamma_{ref}} = \frac{\sqrt{\left[\left(R_{test} + j\omega L_{test}\right)\cdot\left(G_{test} + j\omega C_{test}\right)\right]}}{\sqrt{\left[\left(R_{ref} + j\omega L_{ref}\right)\cdot\left(G_{ref} + j\omega C_{ref}\right)\right]}} \tag{3.19}$$

This can also be written as:

$$\frac{\left(\alpha_{test} + j\beta_{test}\right)}{\left(\alpha_{ref} + j\beta_{ref}\right)} = \frac{\sqrt{\left[G_{test} + j\omega C_{test}\right]}}{\sqrt{\left(j\omega C_{ref}\right)}} \tag{3.20}$$

where, α and β are the frequency dependent attenuation and the phase constant respectively. The R, L, C, and G are the resistance, inductance, capacitance and conductance per unit length of the CPW transmission line and they all are frequency dependent parameters. The conductance per unit length of the test sample can be expressed as:

$$G_{test} = \omega\left(C_{test}\tan\delta_{eff}\right) \tag{3.21}$$

where, $\tan\delta_{eff}$ is the effective loss tangent of the CPW structure. Substituting G_{test} from equation 3.21, and $C_{test} = C_{film} + C_{ref}$ in equation 3.20, and comparing the real and

imaginary parts of the left and right hand sides and solving them, we get the capacitance of the film (C_{film}). The dielectric constant of the film ε_{film} is determined from C_{film} using the conformal mapping technique [23]. In the limit of the dielectric film thickness t<<s, where s is the spacing between the centre conductor and the ground line,

$$\varepsilon_{film} = \left(s \cdot C_{film} / (2\varepsilon_0 t)\right) - \varepsilon_{substrate} \tag{3.22}$$

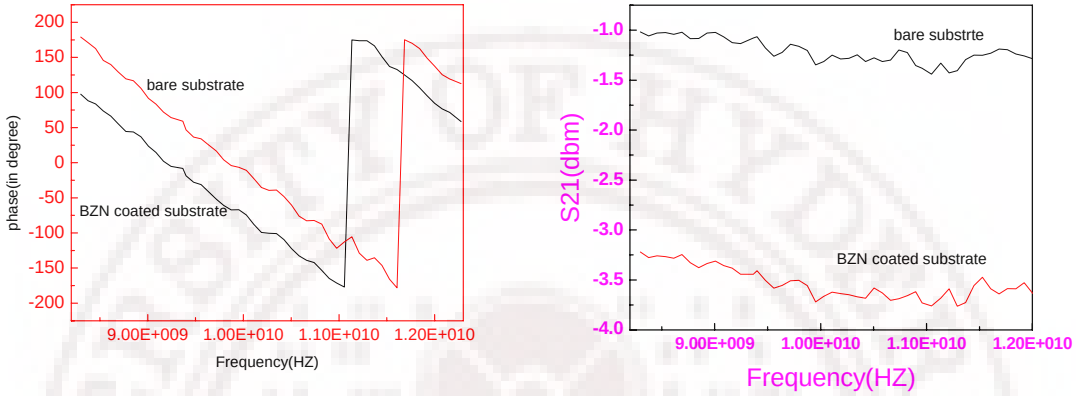

Figure 3.10 Measured S_{21} phase and magnitude for the test and reference line fabricated for the c-BZN thin films deposited on a fused silica substrate.

and the loss tangent of the film is given as

$$\tan\delta_{film} \approx \tan\delta_{eff} \cdot \left(1 + C_{ref} / C_{film}\right) \tag{3.23}$$

The frequency dependent attenuation and phase constants α and β for the test and reference lines are calculated from the measured magnitude and phase of the S_{21} for the reference and test sample. A typical measured S_{21} for the BZN thin films is given in figure 3.10.

3.3.8 Tunability measurement

The calibration comparison method can also be extended to measure the dielectric properties of the films under an applied electric field (tunability measurements) [24]. For the microwave tunability measurements, a DC bias voltage was applied to the CPW lines through the high voltage bias tees. DC blocking capacitors were used at both the ports of the VNA to give additional protection during these measurements. The magnitude and phase of the S_{21} of the CPW lines patterned on the c-BZN thin films are measured under a bias voltage of 100 V. This voltage was able to produce a field of around 10 KV/cm only

in the test structures employed. For higher field strength either the CPW of smaller gap or bias tees of higher voltage rating are to be employed.

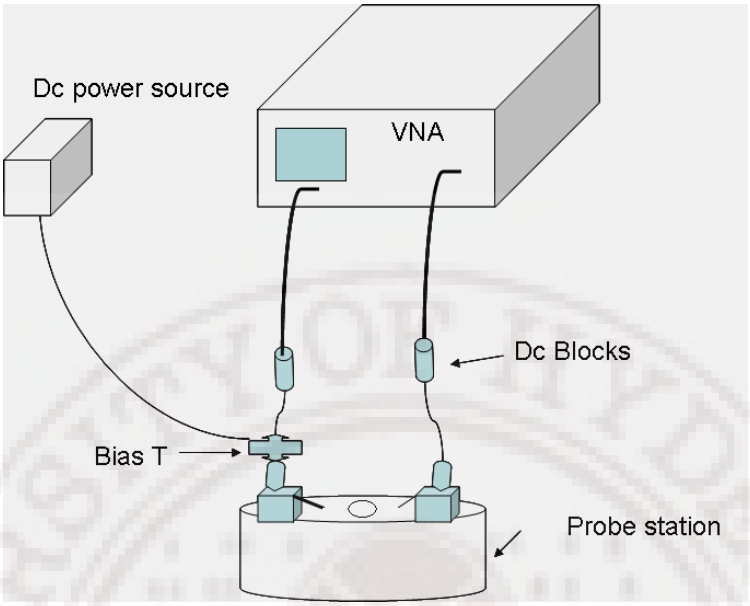

Figure 3.11 Block diagram of the tunability measurement set up.

3.4 Reflection measurements

This method is also known as a direct measurement method. In this technique the reflection measurement are carried out directly on a capacitor made out the films whose characteristics has to be evaluated. The capacitors can have either a planar, parallel plate or interdigitated configurations. The capacitances of these capacitors are calculated directly from the measured complex reflection coefficient (S_{11}). Appropriate modeling has to be done to extract the dielectric permittivity and loss tangent of the films from the calculated capacitance. In the present study we have used parallel plate capacitors in the circular patch capacitor geometry for characterizing the BZN thin films grown on platinised silicon substrates.

3.4.1 Circular patch capacitor technique

This is a reflection type measurement technique. The cross section of the electrode layout of the test structures used for the experiment is shown in Figure 3.12

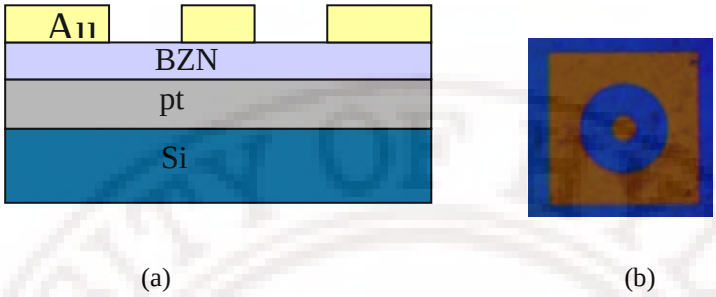

(a) (b)

Figure 3.12 Cross section and microphotograph of the tunable capacitor fabricated using BZN thin films.

In this structure the total capacitance measured between the center patch and the surrounding concentric electrode is:

$$C = (C_f C_{out}) / (C_f + C_{out}) \qquad (3.24)$$

where, C_f is the capacitance between the center patch and the bottom plate and C_{out} is the capacitance between the top outer electrode and the bottom plate. Typically $C_{out} >> C_f$ and the top outer electrode provides an effective microwave connection to the bottom plate resulting in[25]

$$C \approx C_f \qquad (3.25)$$

All microwave measurements are carried out at room temperature using the VNA and GSG probes. One port open short load calibration procedure is used to measure the S_{11} parameters of the test structures between the central patch and the circular electrode surrounding it. The measured reflection coefficient S_{11} is converted into impedance for the test structure Z_T using [26].

$$Z_T = Z_0 \frac{1 + S_{11}}{1 - S_{11}} = R + jX \qquad (3.26)$$

Here, Z_0 =50 Ohm. The capacitance and loss tangent of the capacitor can be derived from the complex impedance using the following relations:

$$C = -\frac{1}{\omega X} \qquad \tan\delta = -\frac{R}{X} \tag{3.27}$$

The relative permittivity of the materials can be calculated using the simple parallel plate model. The real and imaginary part of the permittivity can also be computed using the ADS momentum electromagnetic simulation tool by fitting the simulated S parameters to the measured one. The dielectric permittivity of these films was also determined using the analytical procedure developed by Georgian et al [27].

The main task in this measurement procedure is to extract the capacitance C_F and the loss tangent $\tan\delta_f$ of the dielectric films from the calculated capacitance C and the dissipation factor of the test device. These calculated parameters include the parasitic capacitance from the top and outer electrodes and the parasitic resistance between them. To avoid the parasitic effect, a number of CPC structures were designed on the same thin films of thickness *t* with the same outer electrode radius but with different inner electrode radii a_1. The dielectric constant of the film can be calculated using:

$$\varepsilon' = \frac{t\left(\frac{1}{a_2^2} - \frac{1}{a_1^2}\right)(X_1 - X_2)}{\omega\pi\varepsilon_0\left\{(X_1 - X_2)^2 + \left[R_1 - R_2 - \frac{R_s}{2\pi}\ln\left(\frac{a_2}{a_1}\right)\right]^2\right\}} \tag{3.28}$$

Here, X_1, X_2, R_1, and R_2 can be calculated from the measured S_{11} of the CPC structures having the inner radii a_1 and a_2, using the equation 8. Here, R_s is the surface resistance of the bottom electrode.

Similarly, the loss tangent of the film is given by:

$$\tan\delta_f = \frac{1}{\omega C_f R_f} = \frac{\frac{R_s}{2\pi}\ln\left(\frac{a_2}{a_1}\right) - R_1 + R_2}{X_1 - X_2} \tag{3.29}$$

The measurement structure consists of a BZN thin film (in the thickness range of 200-350nm) on top of a 200 nm thick Pt film. The top electrode consists of a 500 nm gold film. Circular patches with different inner diameters ranging from 80 μm to 120 μm and a concentric ground plane with a constant diameter of 300μm are photo lithographically defined without damaging the BZN thin films. The real and imaginary part of the complex reflection coefficient is measured using VNA and a J microtechnology make

LMS-2709 RF probestation mounted with a GSG probe of 250 micron pitch . A typical measured real and imaginary parts of the S_{11} parameters of the CPC varactors is shown in figure 3.13

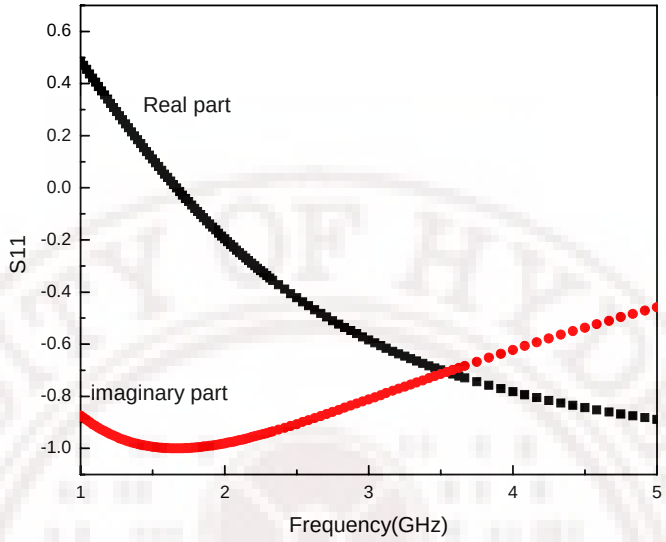

Figure3.13 Measured real and imaginary parts of the S_{11} parameter of the CPC capacitor fabricated using c-BZN thin films.

References

1. A.K.Tagantsev, V.O.Sherman. K.F.Astafiev, J.Venkatesh and N.Setter, *J.Electroceramics*, 11, 5 (2003)
2. G.Subramanyam, N.Moshina, A.Zaman, F.Miranda, F.Vankeuls, R.Romanofsky and J.Warner, *IEEE MTT-S* Vol 1, 471 (2001)
3. J.Hao, W.Si, X.Xi, R.Guo, A.S.Bhalla, L.E.Cross, *Appl.phys.Lett*, 76, 3100 (2000)
4. S.Tape, U.Bottger and R.Waiser, *Integr.Ferroelectrics*, 53, 455(2005)
5. Altschuler H M. in Handbook of Microwave Measurements, (Brooklyn Polytechnic Press, New York), 2: 530 (1963)
6. R. Thomas and D.C Dube, *Electronics Letters*, 33, 218(1997)
7. V. Subrahmanian , B.S Bellubai and J Sobhanadri, *Rev.Sci.Instrum*, 64 231(1993)
8. D.C Dube , M.T Lanagan , J.H Kim , and S. J Jang, *J.Appl.Phys*, 63, 2466 (1988)
9. Linfeng Chen, C.K Ong and B.T.G.Tan, *IEEE Transaction on instrumentation and measurement*, 48, 1031(1999)

10. M.A Rzepecka and M.A.K Hamid, *IEEE Trans.Microw.Theory Tech*, 20, 30(1972)
11. J. Krupka, R. N. Clarke O. C. Rochard, and A. P. Gregory, *XIII Int. Conference MIKON.2000*, Wroclaw, Poland, 305, (2000)
12. J Krupka., A.PGregory., O.C Rochard., R.N Clarke., B Riddle, J Baker-Jarvis., *Journal of the European Ceramic Society*, 10, 2673 (2001)
13. L.F.Chen, C.K.Ong, C.P.Neo, V.V.Varadan and V.K.Varadan, *Microwave electronics measurement and material characterization*, Jhon Wiley and sons (2004).
14. R.Mavaddat, Network Scattering parameters,World scientific(1996)
15. S.Wartenberg, Microwave journal, 46, 3 (2003)
16. C.P.Wen, IEEE Trans Microwave Theory and Tech, 17, 1087(1969).
17. H.J.Eul and B.Schiek IEEE Trans.Microwave Theory tech 39, 724(1991)
18. On-Wafer Vector Network analyzer calibration and measurements,Cascade microtech Application note(2007)
19. A.Davidson, K.Jones,E Strid " Achieving greater On wafer S. parameter accuracy with the LRM calibration technique" Cascade microtech application note-1995
20. A.Davidson, K.Jones, E Strid " Achieving greater on wafer S-parameter accuracy with the LRM calibration Technique" Cascade microtech application note-1995
21. Guru Subramanyam, Emily Heckman, James Grote, Frank Hopkins, Robert Neidhard and Edward Nykiel Microwave and optical Technology Letters 46, 278 (2005)
22. K.Venkata saravanan, K.Sudheendran, M.Ghanashyam Krishna and K.C.James Raju Ferroelectrics 35 ,1 (2007)
23. E. Carlsson and S. Gevorgian, IEEE Trans.Microwave Theory and Tech 47, 1544 (1999)
24. G.Subramanyam, C.Chen and S.Day, Integrated Ferroelectrics,77,189(2005)
25. K.Khamchane, A.Vorobiev,T.Claeson and S.Gevorgian, Journal of applied physics,99, 034103 (2006)
26. S.Sheng, P.Wang, X.Y. Zhang and C.K.Ong, J. phys.D:Appl.phys, 42, 015501(2009)
27. P.Rundqvist, A.Vorobiev, S.Gevorgian and K.Khamchane, Integrated ferroelectrics, 60, 1(2004)

Chapter 4

Structural and electrical properties of Bi_2O_3-ZnO-Nb_2O_5 based pyrochlore bulk ceramics

4.1 Introduction

This chapter presents details of the structural, microstructural and dielectric characteristics of BZN pyrochlore ceramics. c-BZN, m-BZN and titanium doped m-BZN ceramics systems were prepared as part of this study. These ceramics samples were prepared by solid-state reaction. Details of the preparation and characterization procedures have been described in chapter 2.

4.2 Structural and micro-structural properties of Bi_2O_3-ZnO-Nb_2O_5 based pyrochlore ceramics

Figures 4.1-4.3 show the XRD diffractograms of c-BZN, m-BZN and Titanium doped m-BZN ceramics recorded using CuK_α radiation. Figure 4.1 shows the X-ray diffraction patterns of c-BZN ceramics calcinated at two different temperatures. The reflection in the diffractogram shows the formation of the cubic pyrochlore structure with all the major peaks corresponding to the Fd3m space group [1]. The X-ray diffraction patterns of m-BZN ceramics calcined at two different temperatures are shown in figure 4.2. The diffractograms shows complete phase formation in m-BZN ceramics with a monoclinic zirconolite-like structure and all the major peaks are indexed to the ($C2/c - C_{2h}$) space group [1]. The X-ray diffraction patterns of all titanium substituted m-BZN ceramics are given in figure 4.3. All the reflections can be indexed with respect to the monoclinic zirconolite-like pyrochlore phase of $C2/c$-C_{2h} space group. Some small peaks appear in the patterns of the composition with x=0.4 which suggest the presence of some secondary phases. However, its minor amounts make it very difficult to identify these secondary phases. These diffractograms also show a shift in the (220) reflections of m-BZN ceramics with the increase in titanium substitution. This indicates that the size of the monoclinic pyrochlore cell changes with the Ti content. The variation of the crystallite size of m-BZN ceramics with respect to the level of Ti doping is shown in figure 4.4. It can be seen that as the Ti content increases the crystallite size starts decreasing.

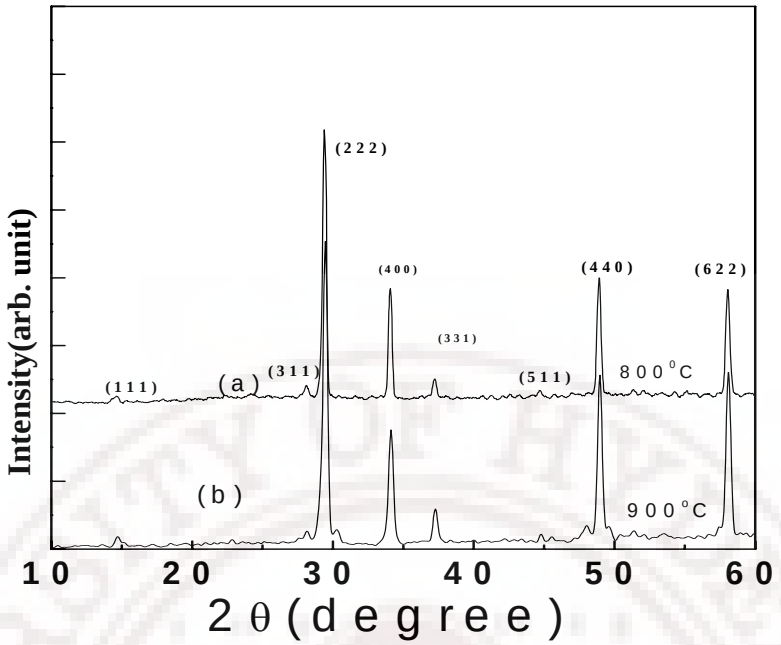

Figure 4.1 XRD diffraction patterns of c-BZN ceramics calcined at different temperatures.

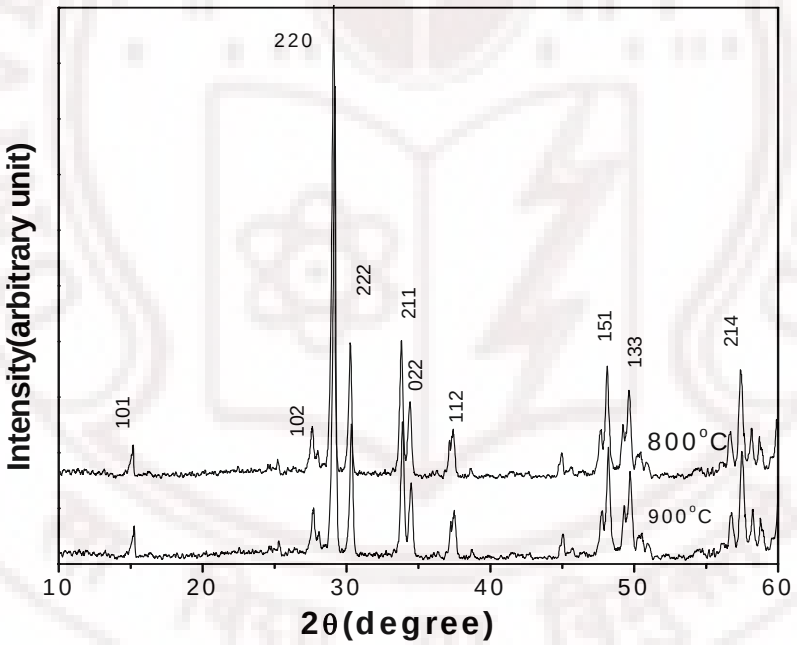

Figure 4.2 XRD diffraction patterns of m-BZN ceramics calcined at different temperatures.

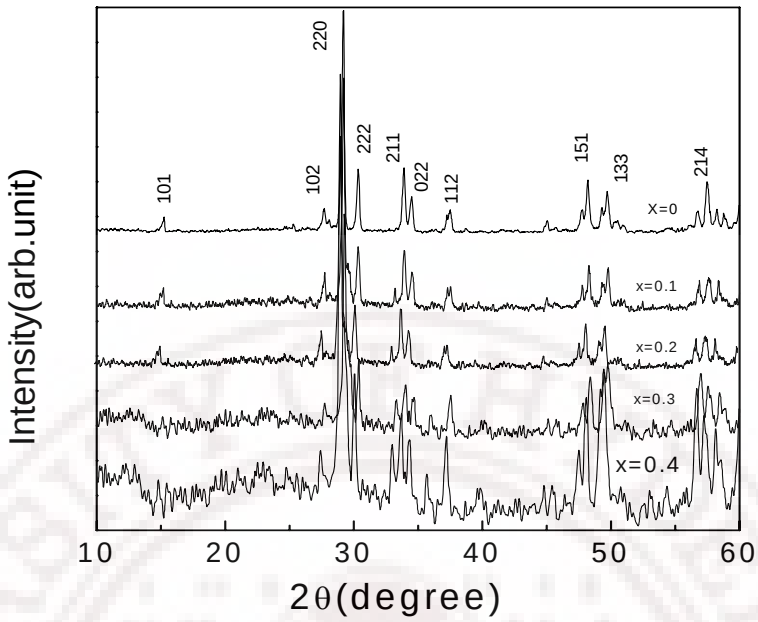

Figure 4.3 XRD diffraction patterns of Ti doped m-BZN ceramics.

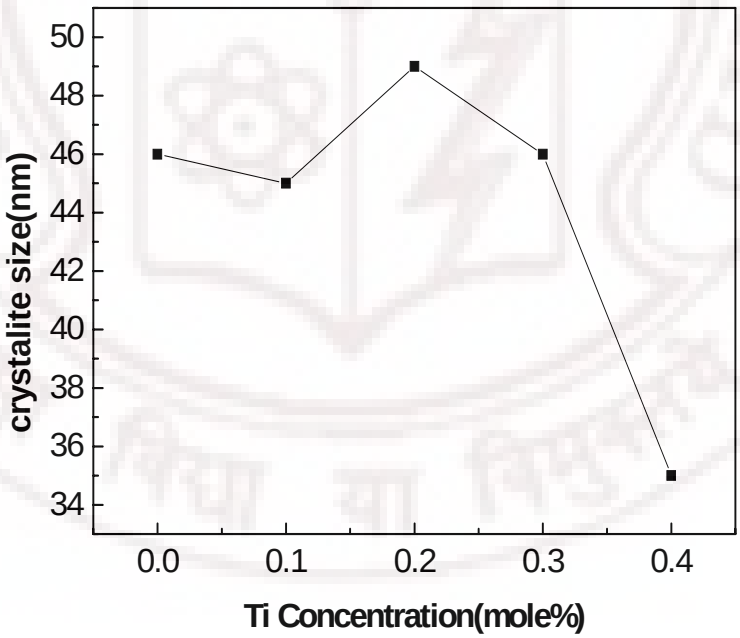

Figure 4.4 Variation of crystallite size with Ti concentration of m-BZN ceramics.

4.3 Microstructural characteristics:

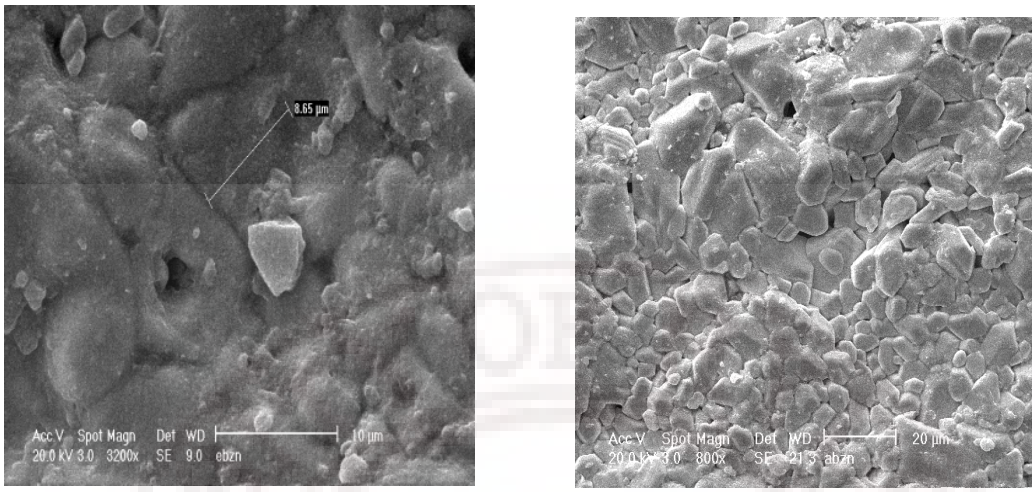

Figure 4.5 SEM micrograph of (a) c-BZN and (b) m-BZN.

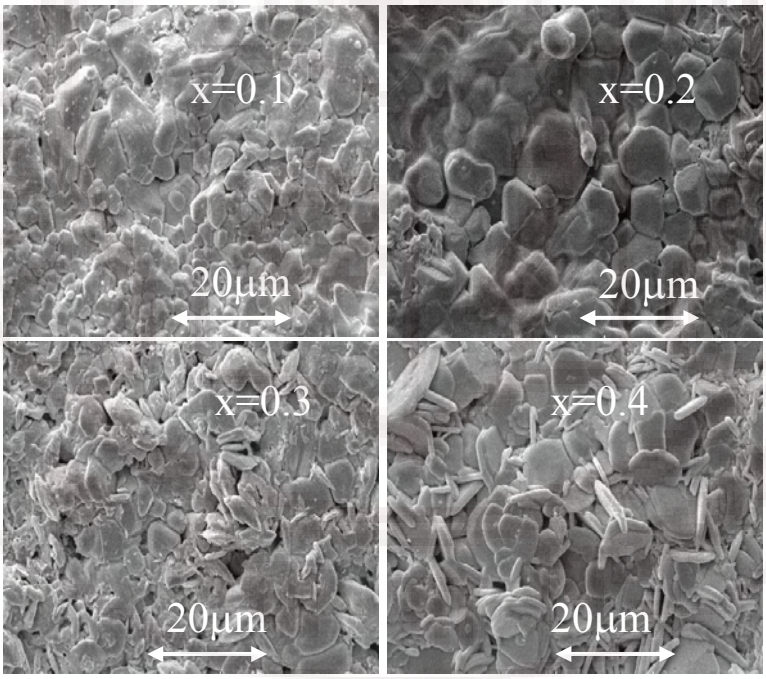

Figure 4.6 SEM micrograph of the Ti doped m-BZN ceramics.

The SEM micrographs of c-BZN and m-BZN ceramics samples, shown in figure 4.5, make it clear that both these ceramic samples prepared have larger grains with relatively dense microstructure. Figure 4.6 shows the SEM micrograph of Ti substituted m-BZN ceramics. The microstructure of these ceramics consists of well-defined and closely packed grains. Apparently, Ti substitution results in significant changes in the grain growth behavior of the samples sintered in air. As Ti doping increases, the grain morphology changes; the samples with a higher percentage of Ti doping showed needle-like grain morphology while at a smaller percentage, the grains were of a larger size with an average grain size of 5-10μm.

4.4 Low frequency dielectric properties

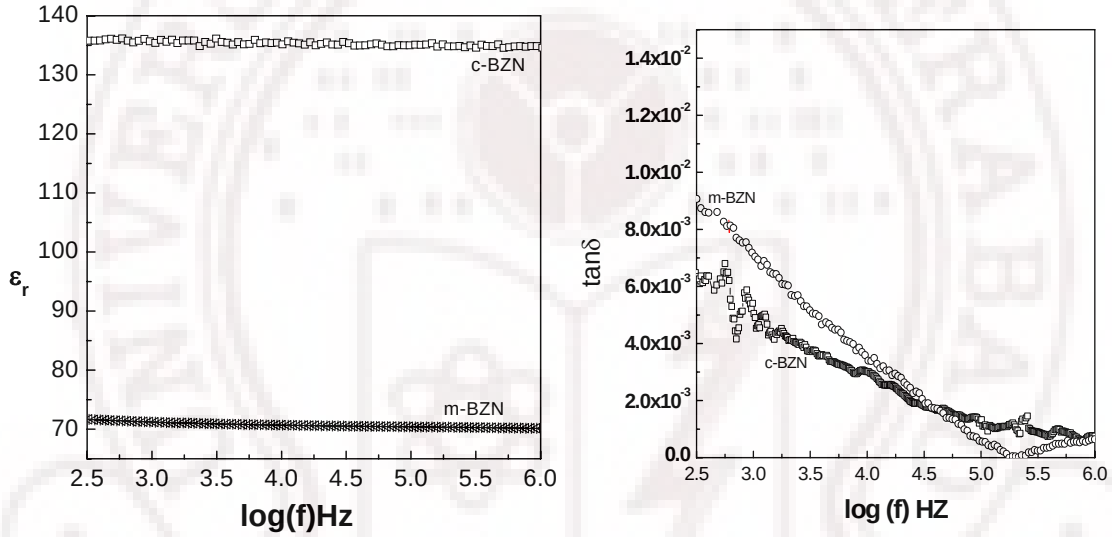

Figure 4.7 The frequency dependence of dielectric constant and loss tangent of c-BZN and m-BZN ceramics.

The low frequency dielectric properties of both c-BZN and m-BZN ceramics measured at room temperature up to 1MHz are shown in figure 4.7. The measured dielectric constant and loss tangent of c-BZN ceramics are 134 and 1.2 $x10^{-3}$ respectively where as m-BZN ceramics has a dielectric constant and loss tangent of 75 and $0.4x10^{-3}$ respectively. The measured dielectric properties of these ceramics do not show much frequency dispersion, which make them suitable for many applications. The variation of the dielectric constant and loss tangent of $Bi_2Zn_{2/3-x/3}Nb_{4/3-2x/3}Ti_xO_7$ ceramics with different Ti doping at B-site measured at 1MHz is shown in figure 4.8. The dielectric constant increases from 75 to 120 while the dielectric loss tangent increases from 0.0004 to 0.061 with an increase in x value from 0 to 0.4. The frequency dependent dielectric

properties of the samples are shown in figure 4.9. The frequency dispersion of dielectric properties was low in these samples. It is already reported that m-BZN pyrochlore, which has got completely ordered Bi atom, with no Zn substitution at A-site exhibits no dielectric relaxation [3]. In our study, we found that Ti substitution at the B-site of m-BZN ceramics results in an increase in dielectric constant and loss tangent. This indicates that titanium substitution disturbs the ordered structure of m-BZN ceramics.

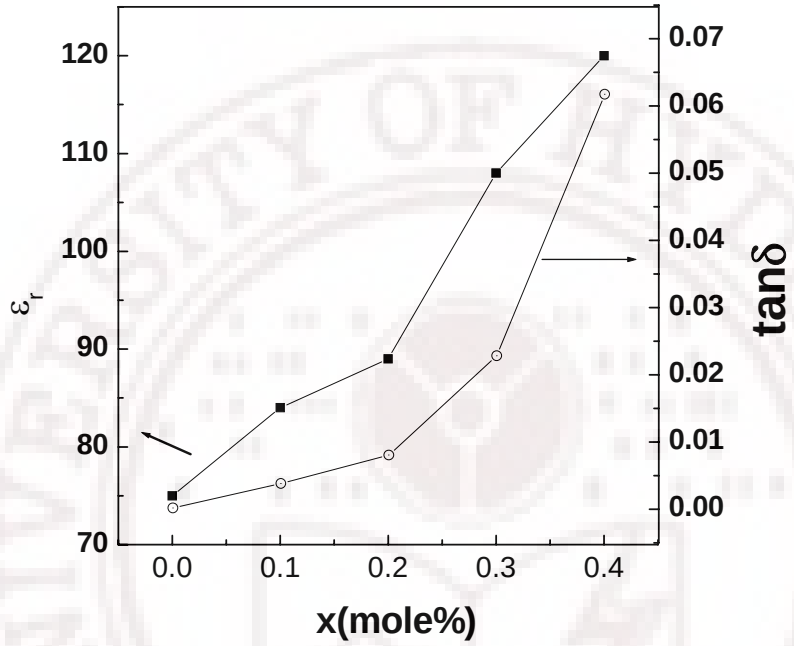

Figure 4.8 The variation of the dielectric constant and loss tangent of $Bi_2Zn_{2/3-x/3}Nb_{4/3-2x/3}Ti_xO_7$ ceramics with different x values

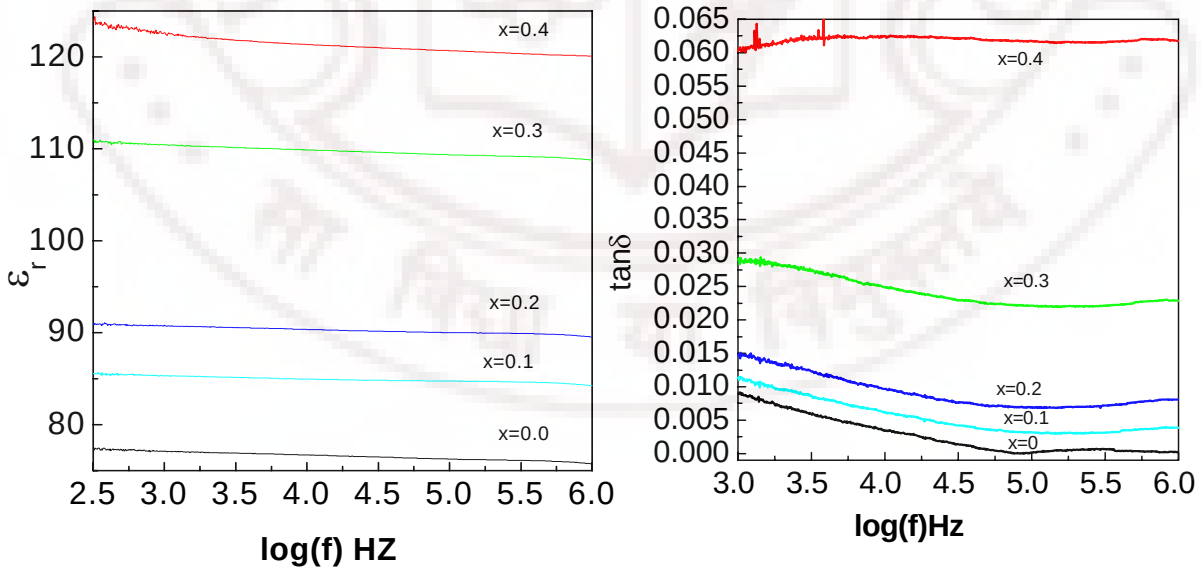

Figure 4.9 The frequency dependence of dielectric constant and loss tangent of $Bi_2Zn_{2/3-x/3}Nb_{4/3-2x/3}Ti_xO_7$ for various x values .

The Ti^{4+} ion can co-substitute Zn^{2+} and Nb^{5+} ions at B-site. The key ion located at the centre of the octahedra could be Ti^{4+}, Nb^{5+} or Zn^{2+}. TiO_6 and NbO_6 octahedra are highly polarizable and a strong correlation exists between them. The increase in dielectric constant with the increase of Ti substitution can be attributed to the presence of highly polarizable TiO_6 octahedra and its strong correlation with the NbO_6 octahedra.

4.5 Temperature dependent dielectric properties

The dielectric constant and loss tangent of m-BZN ceramics measured as a function of frequency at different temperatures are shown in figure 4.10. The dielectric constant and the loss tangent are seen to be increasing with the increase of temperature. At higher temperatures, the frequency dispersion in these samples is found to be high. Figure 4.11 shows the frequency dependent dielectric constant and loss tangent of the Ti-substituted m-BZN ceramics measured at a higher temperature (400°C). Both the real and imaginary parts of the dielectric constant are found to be large at lower frequencies. At higher temperatures, the high frequency side of the measured dielectric constant shows dispersion and a corresponding peak at the loss tangent. This dispersion type relaxation behaviour in Ti doped m-BZN ceramics can be explained by the hopping phenomenon

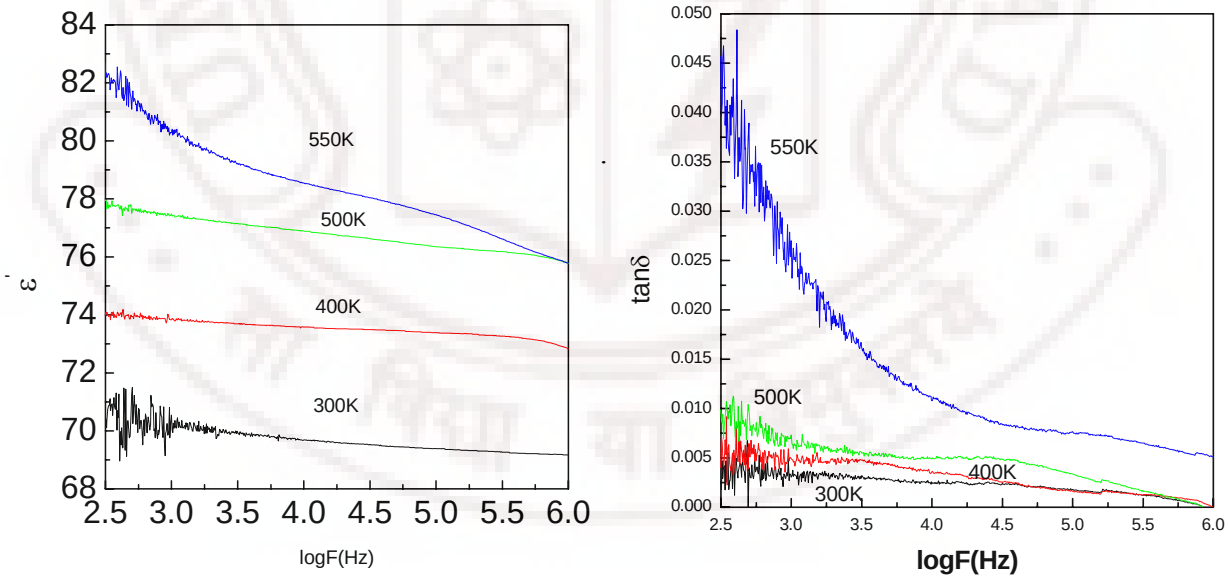

Figure 4.10 The frequency dependence of dielectric constant and loss tangent of m-BZN ceramics measured at different temperatures.

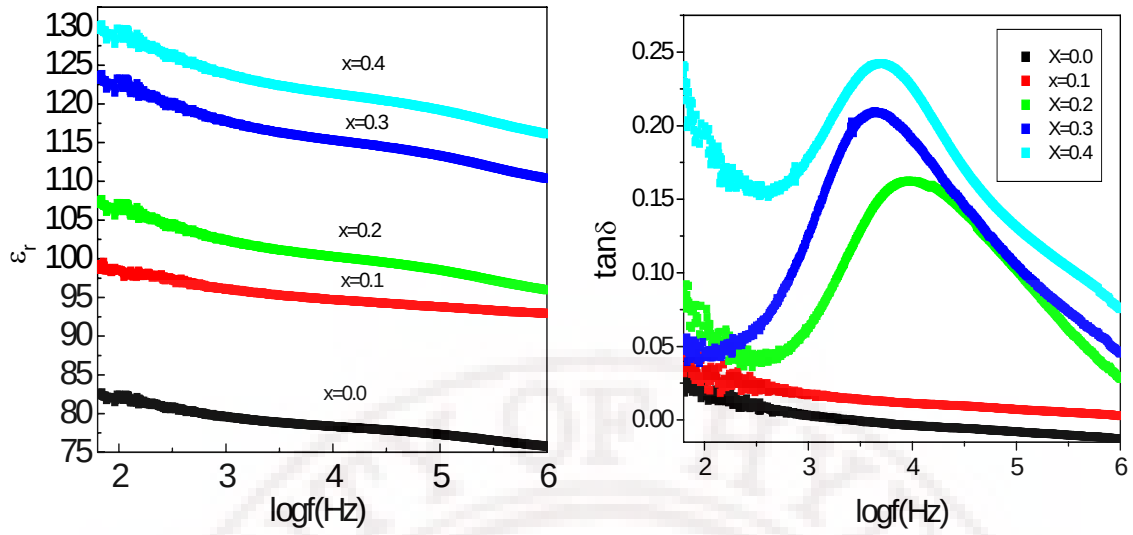

Figure 4.11 The frequency dependence of dielectric constant and loss tangent of $Bi_2Zn_{2/3-x/3}Nb_{4/3-2x/3}Ti_xO_7$ for various x values measured at 400°C.

To understand the physical nature of the dielectric anomalies in Bi based pyrochlores, the dielectric polarization mechanisms in these systems have to be understood properly. Studies of BZN ceramics using far infrared spectroscopy conducted by Kamba et al[5] indicate that the lowest frequency O′— A—O′ bending mode makes the strongest contribution to the dielectric constant. Withers et al [6] points out that the local short-range ordering of Bi and Zn ions at A-site and the associated structural relaxation in the A_2O' substructure result in a random field distribution in these systems. The disordered structure or the reorientation of the dipoles formed by the seventh oxygen with the A-site cation has been proposed as the origin of dielectric relaxation in cubic pyrochlore systems. Taking into account the complicated nature of the pyrochlore structure, the observed relaxation in Ti substituted samples can be related to a dynamical disorder in the alignment of the A- O′ dipoles. These types of relaxations are seen in dipolar glasses and can be explained by the hopping mechanism of charge carriers over the potential barrier between charged defect states. Each pair of sites is assumed to form a dipole that has a relaxation time depending on the activation energy [7]. Each pair of hopping ions may have different activation energies which result in the broadening of the relaxation peaks. This type of relaxation is common in many dynamically disordered dielectric systems implying that dielectric relaxation in these systems strongly depends on the local disorder and local chemical inhomogeneity.

It is known that substituting a third cation species in pyrochlore solid solutions at either A or B-site will drive the system into a state of disorder when the substitution increases the difference of the average radius of the species at A-site and B-site. In the system studied, the introduction of Ti increases the difference between the average radius of A-site and B-site cations. This results in the dynamical disorder in A_2O' which is responsible for the observed relaxation phenomenon in these systems [8].

4.6. Cryogenic microwave dielectric properties of Bi_2O_3-ZnO-Nb_2O_5 based pyrochlore ceramics

4.6.1 Cryogenic properties of c-BZN and m-BZN ceramics

The investigation of dielectric properties of ceramics at low temperatures is an area in which there is not much literature available. In most materials, the loss tangent and dielectric properties vary with temperature. The dielectric permittivity and loss tangent of a material at room temperature may not be the same as those at cryogenic temperatures. So, such studies will help to extend our understanding of the existing dielectric materials properties up to cryogenic temperatures. This will also help in the development of new composite materials that can be tailored for cryogenic applications [9]. Moreover, the microwave dielectric properties of these pyrochlore systems at cryogenic temperatures were measured because these dielectrics could be used with high temperature superconductors to produce high performance cryogenic microwave devices [10]. The dielectric properties of c-BZN and m-BZN ceramics measured at 3GHz in the temperature range of 15K to 290K are shown in figure 4.12. These figures show that the measured dielectric permittivity of both c-BZN and m-BZN is almost equal at very low temperatures. However, the measured dielectric properties of c-BZN ceramics increase drastically with a rise in temperature and reach a value of 114 at 294K. On the other hand, m-BZN ceramics show a very small increase in dielectric permittivity with a rise in temperature. In fact the dielectric permittivity of m-BZN increased only from 63 at 15K to 69 at a temperature of 294K. These variations could explain the nature of dielectric polarization of these samples. The dielectric loss tangent of c-BZN ceramics shows a broad peak in the temperature range of 150 to 200K. m-BZN ceramics show an almost temperature-independent dielectric loss tangent.

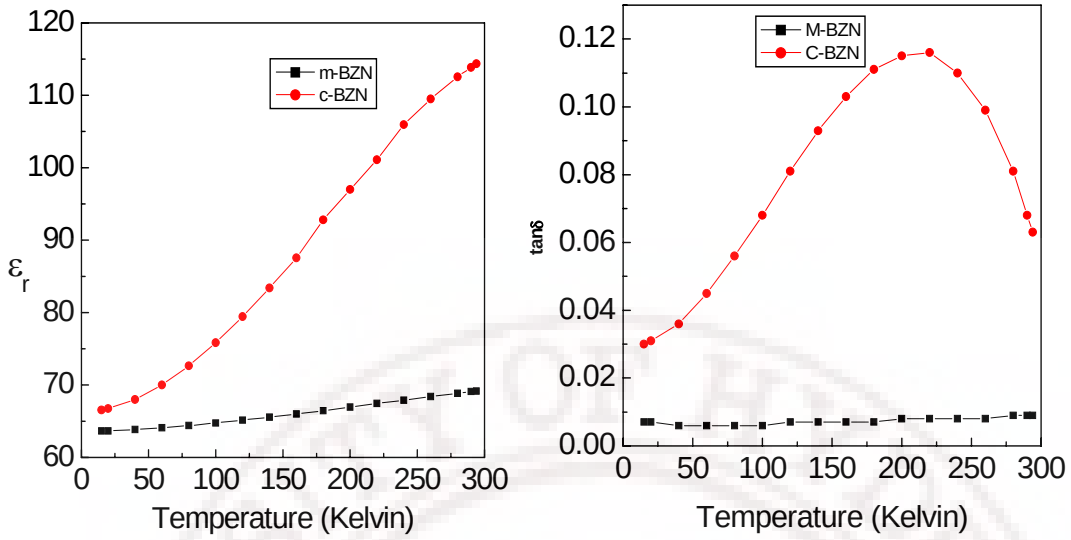

Figure 4.12 Cryogenic microwave dielectric properties of c-BZN and m-BZN measured at 3GHz.

The observed variation of the dielectric properties of c-BZN and m-BZN ceramics can be explained in terms of the displacive disorder from the ideal pyrochlore structures. Bismuth forms a peculiar and complicated structure particularly due to the presence of inert lone pair electrons. Chemical bonding in complexes with inert pair ions is largely determined by s-p hybridization. In Bi^{3+} ions, the 6s-6p hybridization results in a pair of electrons being pushed off to one side of Bi so that a strong ionic bond is formed at the opposite side [11]. This bond contributes heavily to the total dielectric polarization of the system. This lone pair of electrons affects stereochemistry and causes many peculiar properties in these Bismuth-containing pyrochlores. In the pyrochlore structure, the active A cations with these lone pair electrons frequently accommodate off centering in structure through incoherent local displacement. The studies of Levin et.al [2] has established that there is significant static displacement for A and O′ sites from the positions they would be expected to occupy in an ideal pyrochlore structure, where O′ is the oxygen atom attached only to the A-site cations. This disorder is an important factor in BZN systems since their dielectric properties are closely associated with A_2 O′ network.

The origin of the broad dielectric relaxation in c-BZN ceramics can be explained in terms of the recent structural refinement studies on these systems. c-BZN ceramics has a considerable amount of Zn substitution at A-site. Each A-site atom occupies one of the 6 closely spaced possible positions. The observed relaxation might arise from the hopping of thermally disordered A-site and O′ atoms among these closely spaced possible

positions. Moreover, the inhomogeneous distribution of Zn^{2+} ions at A-site and the vacancies at Bi^{3+} sites can give rise to additional randomness. This gives rise to multiwell potentials that have a wide distribution of height, and sets a transition rate of hopping for Bi^{3+} and Zn^{2+} cations. This inter atomic potential can cause a broad dielectric relaxation. It is interesting to note that the m-BZN pyrochlore, which has got a completely ordered Bi atom with no Zn substitution at A-site, exhibits no dielectric relaxation at these temperatures.

The measured dielectric permittivity and loss tangent of this system over the temperatures make it clear that both these ceramic systems have almost identical dielectric properties at cryogenic temperatures while their properties are totally different at higher temperatures. This implies that the atoms are in a more ordered state close to the ideal pyrochlore structure at lower temperatures. As temperature increases there is a random displacement of both Bi^{3+} and Zn^{2+} ions with respect to the O′ from their ideal pyrochlore structure. This displacement makes the Bi- O′ bond more polarizable thereby increasing its dielectric constant. The presence of Zn^{2+} ions at A-site does not affect the polarization of c-BZN ceramics at cryogenic temperatures. But as temperature increases the presence of Zn^{2+} at A-site of c-BZN ceramics systems results in thermal disorder which produces random electric fields. These fields introduce statistical distribution into the local potential barrier heights for charge hopping resulting in variable activation energy for the hopping ions, which broadens the loss peak compared to a single Debye type relaxation. In m-BZN ceramics, the relaxation is absent because of its most ordered state.

4.6.2 Cryogenic properties of Ti- doped m-BZN ceramics

The variation of the microwave dielectric constant and loss tangent of $Bi_2Zn_{2/3-x/3}Nb_{4/3-2x/3}Ti_xO_7$ ceramics with different Ti doping at B-site is shown in figure 4.13. The dielectric constant is found to increase from 70 to 114 while the dielectric loss tangent increases from 0.009 to 0.061 with an increase in x value from 0 to 0.4. The dielectric constant of the same ceramics varies drastically with temperature with the increase of Ti content. The variation of the microwave loss tangent with temperature measured at a frequency of 3 GHz is shown in figure 4.13(b)**.** m-BZN ceramics does not show any dispersion behavior at the measured temperatures, but the Ti substituted ceramics show dispersion in dielectric constant and a corresponding increase in dielectric

loss tangent, which shows a peak at about 200K. The peak in the dielectric loss tangent becomes more prominent with the increase of Ti content. The temperature at which the peak value of the dielectric loss tangent appears is found to decrease slightly with the increase of titanium doping. The dielectric relaxation characteristics of the cubic pyrochlore $Bi_{1.5}Zn_{1.0}Nb_{1.5}O_7$ have already been reported [12].

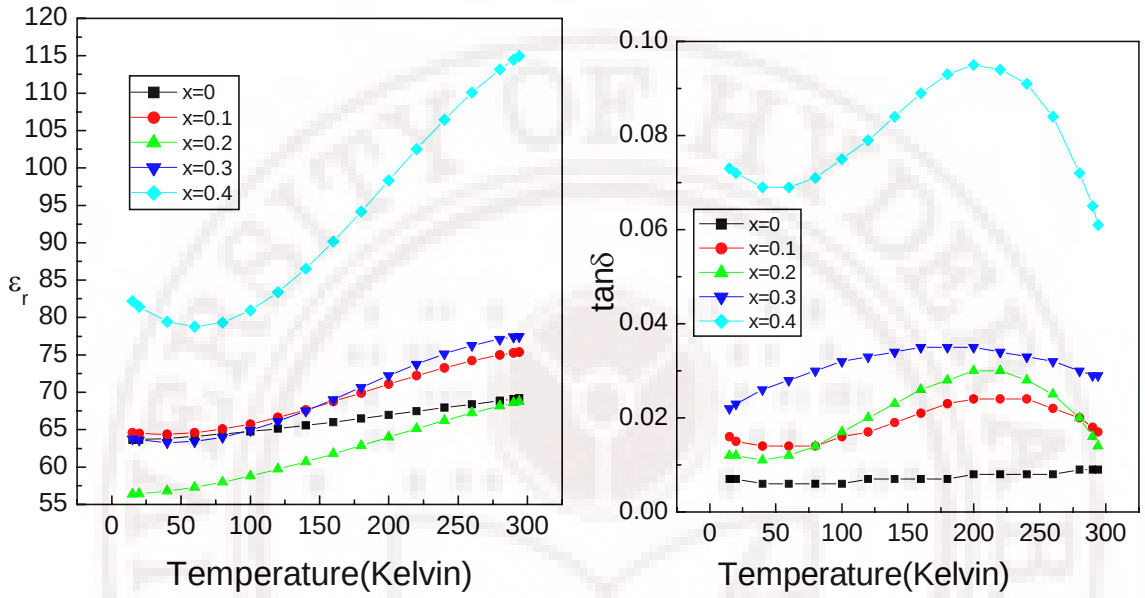

Figure 4.13 The temperature dependence of microwave dielectric constant and loss tangent of $Bi_2Zn_{2/3-x/3}Nb_{4/3-2x/3}Ti_xO_7$ for various x values measured at 3GHz.

The dipolar glass-like relaxation behavior observed in c-BZN is attributed to the random field present in the material due to disorder. The disorder occurs due to the static displacement of A and O^1 sites from an ideal pyrochlore structure. O^1 is the oxygen atom attached only to A-site cations. A similar type of relaxation behaviour is observed in bismuth zinc tantalate ceramics by Youn et al [13]. In the present study, the observed dielectric characteristics of titanium doped m-BZN ceramics can be attributed to the presence of relaxation in these materials originating from the disorder caused by Ti^{4+} substitution. A detailed study over a broad frequency range is necessary for a clear understanding of the relaxation mechanisms in these materials. It is already reported that m-BZN pyrochlore, which has got completely ordered Bi atoms (when there is no Zn substitution at A site), exhibits no dielectric relaxation [14]. However, c-BZN exhibits a broad relaxation at low temperatures even without any substitution. The dielectric properties of c-BZN ceramics with Ti^{4+} substitution at B site as well as at A site are studied by Hong Wang et al [15] and Xi Yao et al [12]. They have found that the disorder

among these atoms is only slightly influenced by Ti substitution at B site. Therefore there is no significant change in the relaxation characteristics of c-BZN with Ti substitution. However, in the present study, it is seen that Ti substitution at the B site of m-BZN ceramics results in a dispersion of dielectric permittivity with an increase in dielectric loss tangents peaking at low temperatures similar to that of c-BZN. Pure m-BZN ceramics does not show this behavior indicating that titanium substitution disturbs the ordered structure of m-BZN ceramics. The Ti^{4+} ion can co-substitute Zn^{2+} and Nb^{5+} ions at B-site. The mechanism of substitution can be presented by considering the condition of charge neutrality

$$3Ti^{4+} \rightarrow Zn^{2+} + 2Nb^{5+}$$

The key ion located at the centre of the octahedra can Ti^{4+}, Nb^{5+} or Zn^{2+}. TiO_6 and NbO_6 octahedra are highly polarizable and a strong correlation exists between them. The increase in dielectric constant with the increase of Ti substitution can be attributed to the presence of highly polarizable TiO_6 octahedra and its strong correlation with NbO_6 octahedra. Vugmeister et al [16] suggest that when the substituting ions are of smaller ionic radius or greater polarizability than the lattice ions, they will favor off-centering displacement in ferroelectrics and dipolar glasses due to loosening of the cations situated at the center of octahedra. It was recently found that substituting a third cation species in pyrochlore solid solution at either A or B sites can also drive the system to disorder when the substitutions decrease the difference in the average radius of the ions that occupy these sites [17]. The increase in dielectric constant of Ti doped m-BZN ceramics can be attributed to the presence of highly polarizable TiO_6 octahedra and the peak in the dielectric loss tangent can be attributed to the presence of a relaxation in these materials due to the off-centering of BO_6 octahedra because of the presence of Ti^{4+} ions at B site.

The temperature coefficient of frequency (τ_f) of the m-BZN dielectric resonator and the temperature coefficient of permittivity (τ_ε) are shown in Figs. 4.14 and 4.15 respectively. Both τ_f and τ_ε values confirm that a more stable operation of the device is possible with x=0 composition. However, a much higher dielectric constant can be obtained with x=0.4 composition. A change in composition will vary the dielectric constant significantly and a proper selection can assist in choosing the desired dielectric constant for a given application.

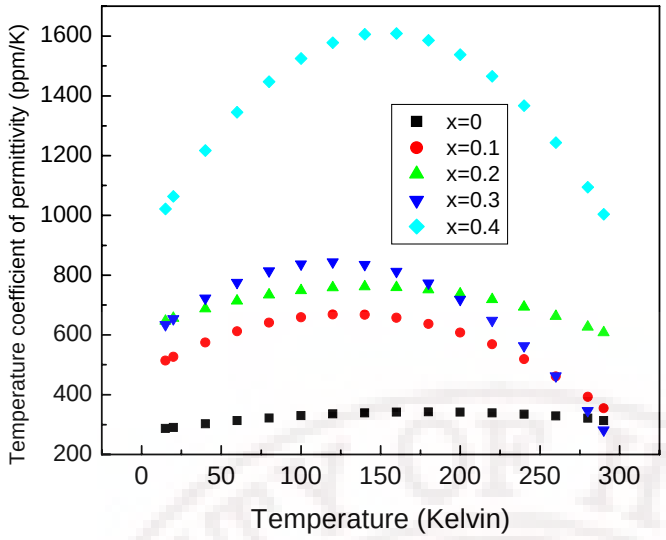

Figure 4.14 The variation of the temperature coefficient of permittivity (τ_ε) of $Bi_2Zn_{2/3-x/3}Nb_{4/3-2x/3}Ti_xO_7$ for various x values measured at 3GHz.

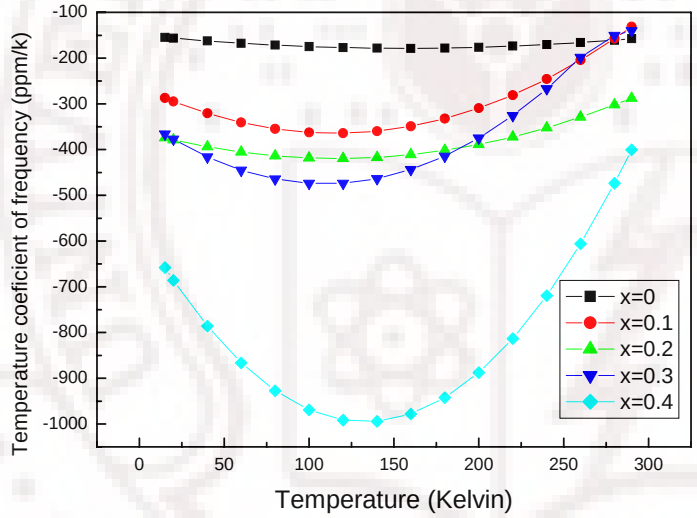

Figure 4.15 The variation of the temperature coefficient of resonance frequency of $Bi_2Zn_{2/3-x/3}Nb_{4/3-2x/3}Ti_xO_7$ for various x values measured at 3GHz.

4.7 Raman spectral analysis of Bi_2O_3-ZnO-Nb_2O_5 based pyrochlore ceramics

The Raman spectra of c-BZN and m-BZN ceramics are given in figure 4.16. We could not see a very large difference between the Raman spectra of these two compositions except for a band at 836cm^{-1} which is observed only for m-BZN ceramics. Some additional bands are also seen in m-BZN ceramics at the lower wavelength side which can be due to the lowering of symmetry in this system. The reported bands for BZN pyrochlores are located at 139, 195, 251, 271, 337, 369, 537, 623 and 764cm^{-1}[18-19]. According to Begg, in composite pyrochlores the Raman active vibrational modes originate from the localized short-range disorder of B-site atoms. Since c-BZN ceramics

are composite pyrochlore the A—O bonds include Bi—O and Zn—O bonds while the B—O bonds include Nb—O and Zn—O bonds. In the case of m-BZN ceramics, the A—O bonds include only Bi—O bonds since there are no Zn atoms at the A site of m-BZN pyrochlore ceramics. The bands at 251 cm^{-1} were assigned to Zn-O stretching mode while the bands at 195 and 764cm^{-1} correspond to Bi-O and Nb-O stretching modes respectively. The Raman characteristics of m-BZN ceramics with Ti substitution at B site were also studied, and are described below.

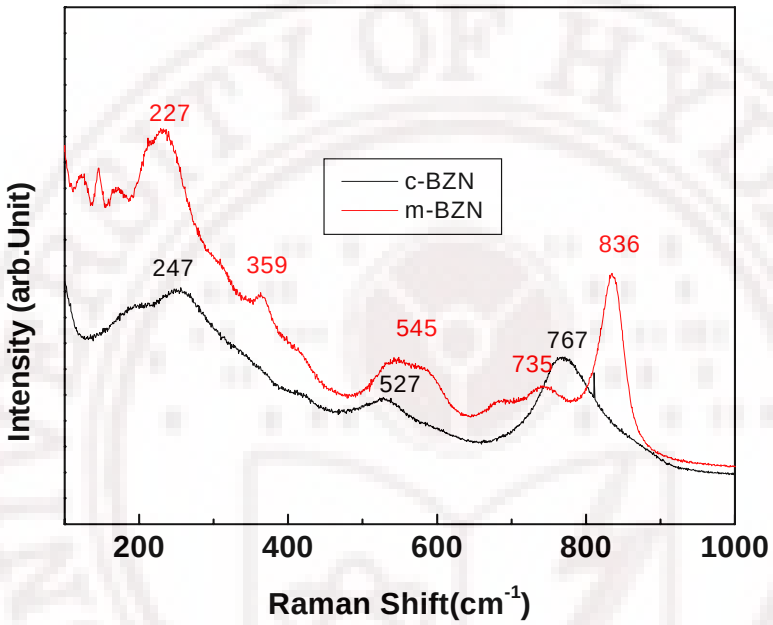

Figure 4.16 Raman spectra for c-BZN and m-BZN pyrochlore ceramics.

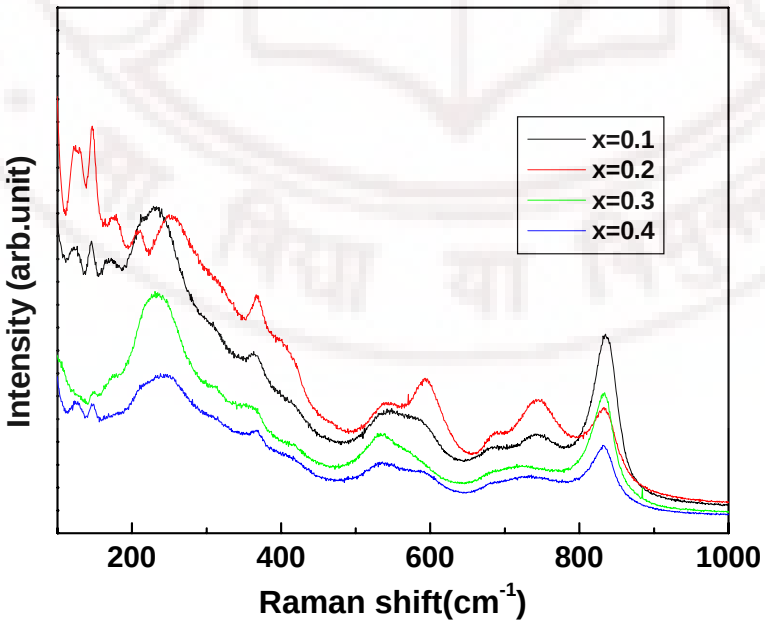

Figure 4.17 Raman spectra for $Bi_2Zn_{2/3-x/3}Nb_{4/3-2x/3}Ti_xO_7$ ceramics for various x values.

The room temperature Raman scattering data of Ti doped monoclinic BZN were obtained by employing normal backscattering geometry and the results are presented in Figure 4.17. The observed Raman spectra as presented are comparable to the earlier reported Raman spectra of m-BZN ceramics [20]. We did not observe any extra Raman mode in the Ti doped m-BZN in comparison to m-BZN which reveals that the Ti doped m –BZN are free of secondary phase. The Raman modes are broad due to irregular distribution of Zn^{2+}, Nb^{5+} and Ti^{4+} ions on the B site of the pyrochlore structure. This may also be a reason for observing much less number of Raman modes in monoclinic symmetry as excepted by group theory calculation. The observed Raman scattering in Ti doped m-BZN materials were slightly shifted towards the lower frequency and very similar for all compositions. This clearly indicates that Ti ions indeed occupy interstitial sites in the host m-BZN.

In Figure 4.17, we did not observe any remarkable changes in the lower range Raman modes at 124, 149, 171, which mainly originate with vibration of Bi against O_6 octahedra reveals that order of Bi atom is not influenced by Ti substitution. The Raman modes at 211 and 256 cm^{-1} show anomalous change with increasing the Ti concentration and it may be due to change in Zn – O bond energy due to substitution of Ti^{4+} ion. The O –Nb(Zn) – O bending vibration mode at 852 cm^{-1} shows decrease in frequency and increasing in intensity with Ti substitution. It is possible that the oxygen ions are freed from their defect bonding with Ti substitution, and thereby these are free to oscillate more like in single crystals resulting in a reduction of the oxygen bending mode vibration frequency. The observed Raman modes at 369, 412 538 and 682 cm^{-1} are showing a small deviation in frequency with increasing the Ti concentration in m-BZN and assigned as the polar mode. The intensity and line widths of these Raman modes were also found to be changing with Ti concentration, which suggest that the local lattice disorder. The local lattice disorder can be related to the decrease in binding energy of Nb – O, Zn – O bonds as a result of the substitution of Nb^{5+} by Ti^{4+}. It also suggests that the polarizability in NbO_6 octahedra change due to strong correlation between Ti^{4+} and Nb^{5+} ions present at the same site of Ti substituted m-BZN ceramics resulting in change of the dielectric constant and loss tangent.

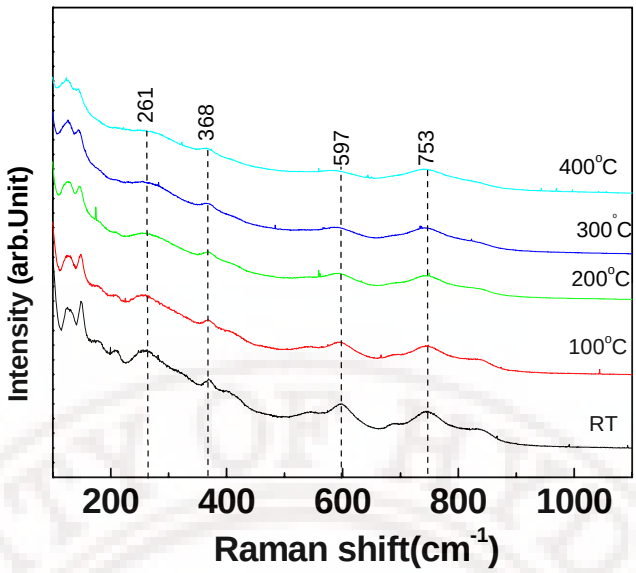

Figure 4.18 Temperature dependent Raman spectra of m-BZN ceramics with 0.2%Ti substitution.

The temperature evolution of the Raman spectra of m-BZN ceramics with 0.2 mole % of Ti substitution at B site is shown in figures 4.18 and 4.19. It is hard to describe in detail the temperature changes of Raman spectra on the lower wavelength side since it appears to consist of a higher number of overlapping weak lattice modes, for example, very low intensive tilt modes. The Raman modes are seen at 261, 368, 597 and 753 cm^{-1} for the 0.2% Ti doped ceramics at room temperature. It is seen that the intensity of the modes and the background increase with the increase of temperature.

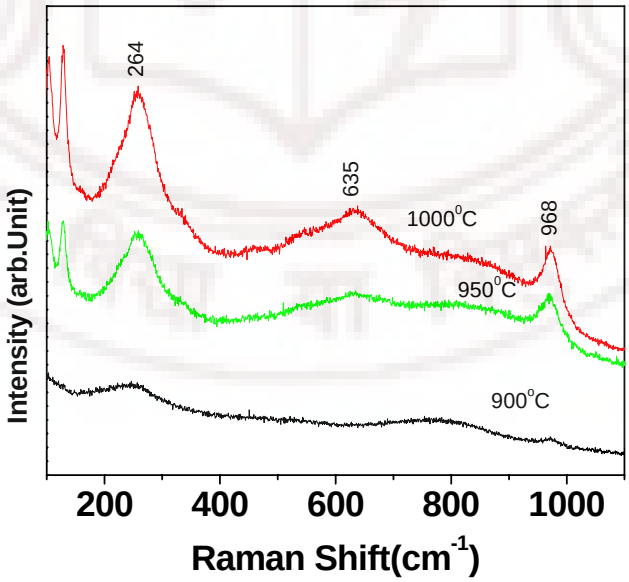

Figure 4.19 Raman spectra of m-BZN ceramics with 0.2%Ti substitution above 900 °c showing the evolution of phase transitions.

After 900°C, the emergence of some additional modes at 264, 635 and 968 cm^{-1} are observed. All other modes disappear and this indicates a structural phase transition in these materials at these temperatures. Further investigations are required in this direction which is, however, beyond the scope of the present study.

4.8 Summary

In summary, the structural, microstructural and dielectric characteristics as well as the Raman characteristics of c-BZN, m-BZN and titanium doped m-BZN ceramics were studied systematically. These ceramics were prepared using the conventional solid-state reaction method. The X-ray diffraction study confirms the formation of the cubic pyrochlore structure with all the major peaks corresponding to the Fd3m space group for c-BZN ceramics. It also confirms the monoclinic zirconolite-like structure with all the major peaks indexed to the C2/c space group for m-BZN ceramics. The measured dielectric constant and loss tangent of c-BZN ceramics are 134 and 1.2 $x10^{-3}$respectively and for m-BZN ceramics, 75 and $0.4x10^{-3}$ respectively. For titanium substituted samples, with an increase in Ti content from 0 to 0.4 mole% at B-site, the dielectric constant increased from 75 to 120 while the dielectric loss tangent increased from 0.0004 to 0.061. At higher temperatures, the measured dielectric constant of Ti substituted ceramics show dispersion and a corresponding peak appears for the loss tangent. This dispersion-type behavior in the Ti doped m-BZN ceramics can be explained by the hopping relaxation phenomenon. The dielectric loss tangent of c-BZN ceramics shows a broad peak at the temperature range of 150 to 200K while m-BZN ceramics shows almost temperature-independent dielectric loss tangent when measured at a frequency of 3GHz. The measured Raman spectra for c-BZN and m-BZN ceramics do not have a very large difference except for a band at $836cm^{-1}$ which is observed only for m-BZN ceramics. Some additional bands are also seen in m-BZN ceramics at the lower wavelength side which can be due to the lowering of symmetry in this system. The reported bands for BZN pyrochlores are located at 139, 195, 251, 271, 337, 369, 537, 623 and $764cm^{-1}$. The band at $251cm^{-1}$ was assigned to Zn-O stretching mode while the bands at 195 and $764cm^{-1}$ correspond to Bi-O and Nb-O stretching modes respectively. The additional modes at 264, 635 and 968 cm^{-1} which appear at higher temperatures in the titanium-substituted samples may be an indication of a phase transition in these materials at these temperatures. Additional studies are required to confirm this apparent phase transition.

References.

1. H Wang, S. Kamba, M. Zhang, X Yao, S. Denisov, F. Kadlec, and J. Petzelt, *J. Appl. Phys*, 100, 034109 (2006)
2. I.Levin, T.G.Amos, J.C.Nino, T.A.Vanderah, C.A.Randel and M.T.Lanagen, *J.Solid state chem*.,168,69 (2002).
3. J.C.Nino, M.T.Lanagan and C.A.Randal *Journal of applied physics*, 89, 4512 (2001)
4. A.R.West, D.C.Sinclair, N.Hirose, *J. Electroceramics* 1(1),65,(1997)
5. S.Kamba, V.Porokhonskyy.A.Pashkin et al. *Phys.Rev.B*, 66, 054106(2002)
6. R.L.Withers, T.R.Wellberry, A.K.Larsen et al, *J. Solid state chem*, 177,231(2004)
7. J.C.Guintini, J.V.Zanchetta, D.Julien, R.Eholie, P.Houenous, *J.Non-cryst.Solids*, 45, 57 (1981)
8. B.J.Wuench et al, *Solid state ionics*, 129, 111(2000)
9. Minghan Chen, D.B Tanner, Juan C Nino, *Phys. Rev. B*, 72, 054303(2005)
10. C.Y.Tan and C.K.Ong, *Supercond Sci.Technol*, 19, 212 (2006)
11. M.A.Subramanian, G.Aravamudan, G.V.Subba Rao, *Prog. Solid state Chem*,15, 55(1983)
12. H.L.Du, X.Yao, *Physica B*, 324, 121(2002)
13. H.J.Youn, T.Sogabe, C.A.Randall,T.R.Shrout and M.T.Lanagan, *J. Am. Ceram. Soc*, 84, 2557 (2001)
14. J. Petzelt and S. Kamba, *Mater. Chem. Phy.*, 79, 175(2003)
15. H.Wang, X. Wang, and X.Yao, *Ferroelectrics*,195, 19(1997)
16. B.E. Vugmerister and M.D. Glinchuk, *Rev. Mod. Phys*, 62, 993 (1990)
17. B.J. Wuensch, K.W.Eberman, C.Heremans, E.M.Ku, P.onnerud, S.M.Haile, J.K.Stalick, J.D.Jorgensen, *Solid state ionics*,129,111(2000)
18. H. Wang, Du HL, X. Yao, *Materials Science and Engineering ,* 99,20(2003)
19. S.M.Zanetti, S.A.da silva, *material research*,10,261(2007)
20. Q.A. Wang, H. Wang, X. Yao, *J. Appl. Phys*, 101,104116(2007)
21. N.T. Vandenborre, E. Husson, H. Brusset, *Spectrochim. Acta* 37A ,113(1981)

Chapter 5

Preparation of pyrochlore thin films in Bi_2O_3-ZnO-Nb_2O_5 system and their structural, microstructural and optical properties

5.1 Introduction

This chapter describes the structural, microstructural and optical properties of the pulsed laser deposited c-BZN and m-BZN thin films. The effect of process parameters such as oxygen pressure during deposition, annealing temperature etc on the structural and microstructural characteristics are carefully analysed. This chapter also presents a detailed study on the influence of process parameters on the local symmetry of thin films from the Raman scattering.

5.2 Preparation of BZN thin films

Pulsed laser deposition (PLD) is a physical vapor deposition technique based on the evaporation of material by means of a highly energetic pulsed laser beam focused on to the solid target by a lens. The PLD process for the thin film growth can be divided into four regimes, viz. (i) The interaction of the laser beam with the target resulting in evaporation of the surface layers (evaporation regime), (ii) Interaction of the laser beam with the evaporated materials causing the formation of isothermal expanding plasma (isothermal regime), (iii) The anisotropic three dimensional adiabatic expansion of the laser induced plasma with a rapid transfer of thermal energy of the species in plasma into their kinetic energy, and (iv) Thin film growth. Due to the interrelationship between these physical mechanisms involved in the PLD process, only an approximate description of the phenomena is possible. Therefore establishing a theoretical model to describe the whole PLD process is difficult. Instead, there exist several models; each of them analyzing in detail only one aspect of it, such as, the vaporization [1], plasma formation [2] and its expansion in vaccum or in presence of an ambient gas [3]. The plasma expansion process plays a crucial role in the PLD process. Eventhough as a thin film deposition process, PLD is a complex process it has offered many advantages necessary for a typical research work where in a fast window for thin film material study is available. Since PLD processing involved relatively few process parameters, it eventually led to easy generation of reproducible and quality thin films. If summarized briefly the main characteristic processing parameters include: the oxygen pressure within the chamber during deposition, the laser energy fluence, temperature of the substrate and post

deposition annealing process. An exhaustive study of the optimization process for a particular material involves check for composition, phase, and some of its important electrical or optical properties. In this study the films were deposited by varying the oxygen chamber pressure, reprate and laser fluence. The optimized growth conditions are given in chapter 2.

5.3 XPS analysis of BZN thin films

The composition and chemical state near the surface of the deposited films were obtained by X-ray photo electron spectroscopy (XPS). The XPS spectrum of c-BZN thin films in the binding energy range of 0-1200 eV is shown in figure 5.1. The peaks have been assigned as indicated in figure 5.1. It can be seen that Bi, Zn, Nb, and O exist near the surface. No other impurity elements are detected in the spectrum up to 1200eV except carbon, probably due to contamination. Apart from chemical analysis, XPS can also give information about the chemical bonding in the material. The narrow scan XPS spectra of Bi4f, Nb 3d, Zn 2p and O1s peaks for the c-BZN thin films are shown in figures 5.2 and 5.3. A doublet structure exists in the XPS spectrum of Bi4f peaks as shown in figure 5.2 The Bi 4f7/2 and Bi4f5/2 separates clearly at 157.17 and 162.46eV respectively. The spin orbit splitting between them is 5.29 eV. The peak positions of the Bi 4f are close to the earlier reported values of bismuth oxide [4, 5]. There is no spin orbit splitting in the case of Zn 2p atoms. This indicates that only one chemical state exist in the film for each Bi, Nb and Zn atoms. The Nb 3d peak position of these films is found to be at 207.23 eV. Previous report revealed that peak position is at 205.88eV for NbO_2 type network and 207.6eV for Nb_2O_5 type network [6]. The O1s peak position of the c-BZN thin film is at 530.52eV and the Zn 2p peak position is found at 1022.35eV. According to the binding energies, Bi, Zn and Nb ions are considered to be in the chemical state of Bi^{3+}, Zn^{2+}, Nb^{5+}. The XPS spectra of the m-BZN thin films deposited on fused silica substrates were also having the similar characteristic as that of c-BZN except that the binding energy peaks were shifted little to lower values.

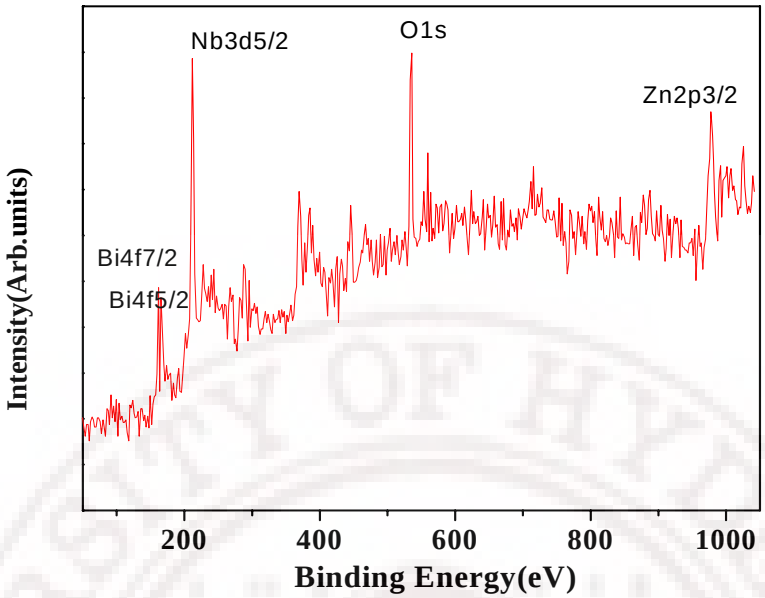

Figure 5.1 Wide scan XPS spectrum of c-BZN films on fused silica substrate.

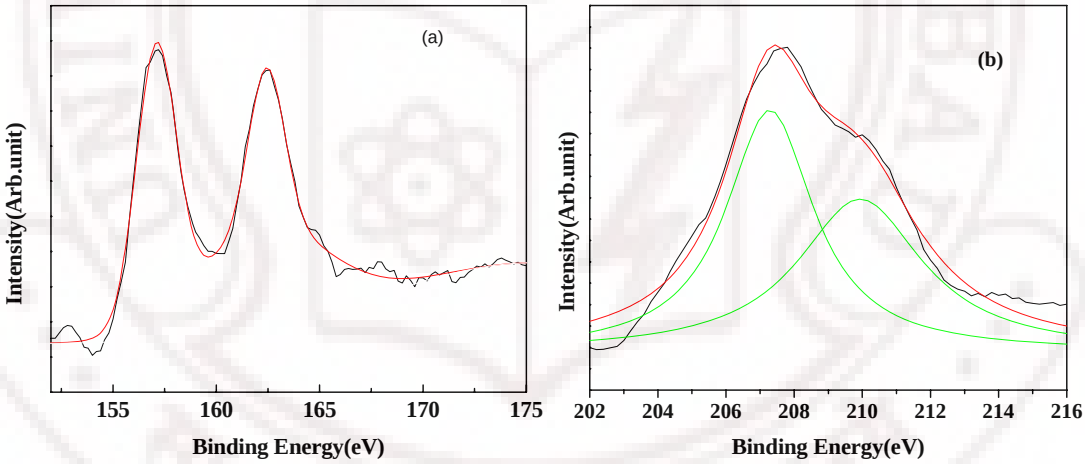

Figure 5.2 Narrow scan XPS spectrum of (a) Bi 4f and (b) Nb 3d peaks for c-BZN thin films on fused silica substrate.

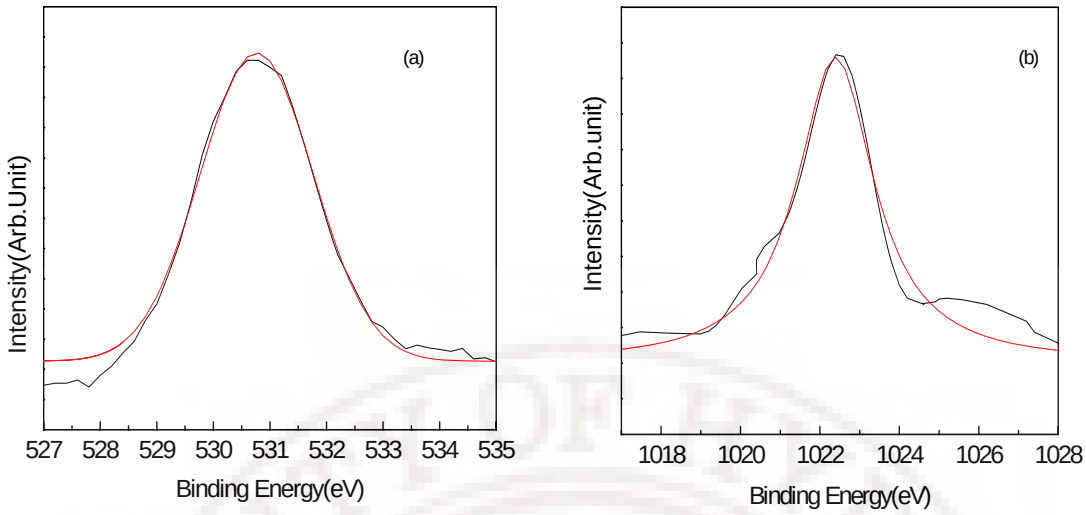

Figure 5.3 Narrow scan XPS spectrum of (a) O1s and (b) Zn 2p peaks for c-BZN thin films on fused silica substrate.

5.4 EDX analysis of BZN thin films

In order to investigate the compositional deviations if any in the PLD processed samples, Energy Dispersive X ray (EDX) analysis of the annealed films and the targets were carried out.

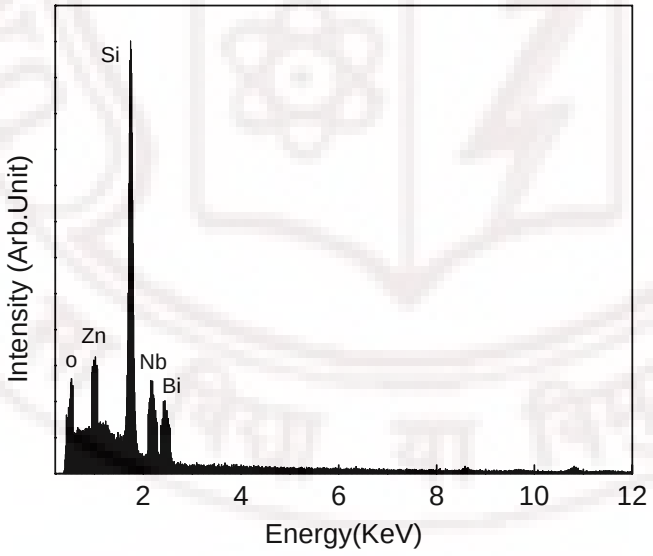

Figure 5.4 EDX spectra of the c-BZN thin film deposited on silicon.

The composition of the films was found to be close to that of the composition of the target. Figure5.4 present the EDX spectrum of the c-BZN thin films deposited on a silicon substrate. The Bi, Nb, Zn and O peaks appears in the EDX spectrum along with a large Si substrate peak.

5.5 Structural properties of Bi_2O_3-Nb_2O_5-ZnO based thin films

5.5.1 Effect of annealing to the structural properties of BZN thin films

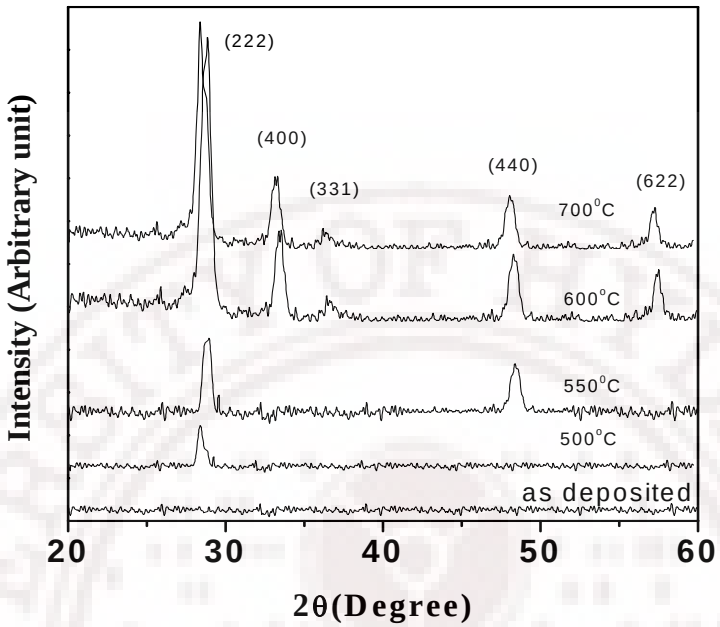

Figure 5.5 X-ray diffractograms of c-BZN films annealed at different temperatures on fused silica substrates.

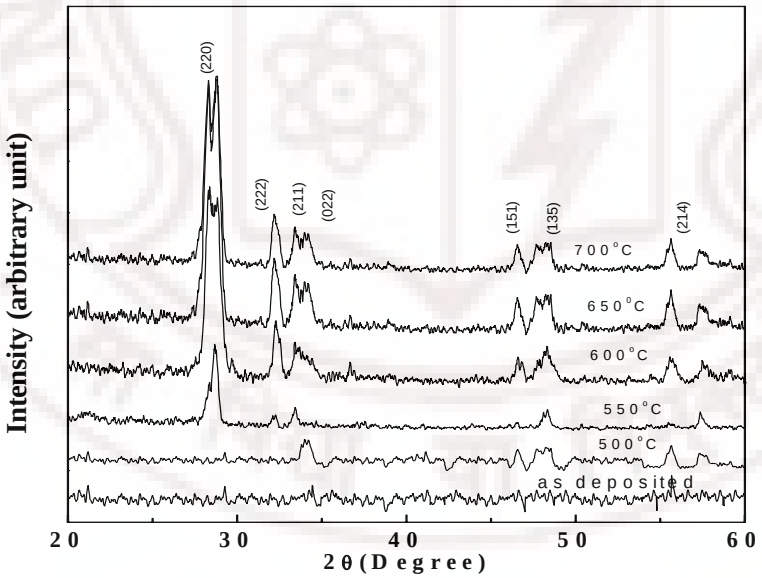

Figure 5.6 X-ray diffractograms of m-BZN films annealed at different temperatures on fused silica substrates.

The X-ray diffraction patterns of the as deposited and annealed c-BZN and m-BZN films are given in figures 5.5 and 5.6. The films were deposited using an excimer laser with 300mJ energy and at an oxygen pressure of 10 mTorr. No peaks were observed in the XRD of as deposited films indicating their amorphous nature. When the films are annealed at 500°C, one diffraction peak is seen for the c-BZN and three peaks were seen in the case of m-BZN thin films. On further increase of the annealing temperature, the crystallinity of the films was found to be improving. All the reflections in the diffractograms of c-BZN thin films show the formation of the cubic pyrochlore structure with all the major peaks corresponding to the Fd3m space group. Similarly, the reflections from the m-BZN thin films can be indexed with respect to the monoclinic zirconolite-like pyrochlore phase with C2/c space group [7, 8].

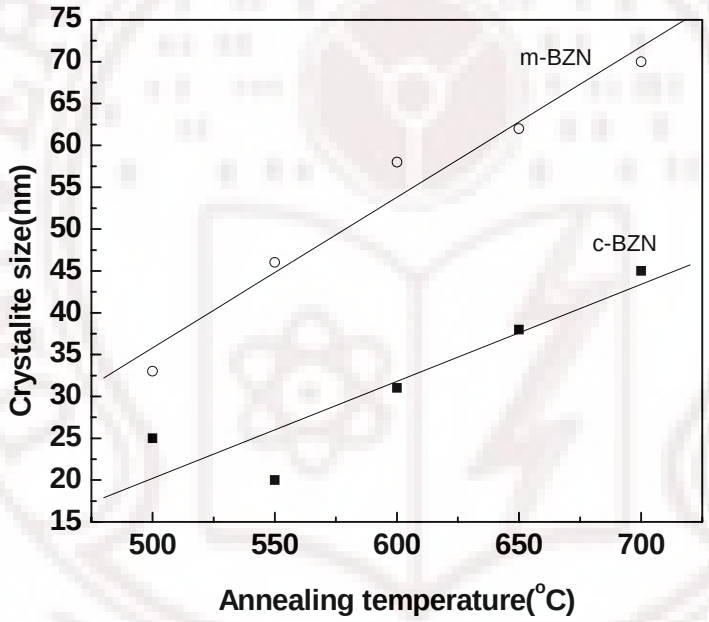

Figure 5.7 Variation of crystallite size with annealing temperature for c-BZN and m-BZN thin films.

The average crystallite size of the c-BZN and m-BZN thin films were calculated from the XRD peak broadening using the Scherrer formula and are given in figure 5.7. The crystallite size was observed to vary from 33 nm to 70 nm for m-BZN thin films and 25nm to 45 nm for the c-BZN thin films. It is also observed from figure 5.7 that for higher annealing temperatures, there is a rapid growth of crystallite size and m-BZN films were having large crystallite size compared to c-BZN thin films. This may be due to the rapid decrease of surface energy with crystalline growth of m-BZN thin films compared

to c-BZN thin films [9]. It is interesting to note here that the crystalisation temperature for m-BZN is lower than that of c-BZN and that could be also a reason for the observed higher values for the crystallite size in m-BZN.

5.5.2 Effect of Oxygen pressure on the c-BZN thin films

The X-ray diffraction patterns of the c- BZN thin films deposited at different oxygen pressures and annealed at 600°C are shown in figure 5.8. No peaks due to a crystalline phase could be detected in the as deposited films, which indicate that the films were amorphous. After annealing at 600°C, most of the peaks of the cubic pyrochlore BZN could be detected [7]. No peaks due to any crystalline impurity phase were observed in the XRD. The prominent peak in the XRD of c- BZN pyrochlore is the reflection from the (222) plane. This has a reported diffraction angle (2θ) of 34.175° and an inter atomic spacing (d) of 3.0456A° unit [7]. The second prominent peak is due to the reflection from the (400) plane at 2θ= 39.66° and an inter atomic spacing d=2.6376 A°.

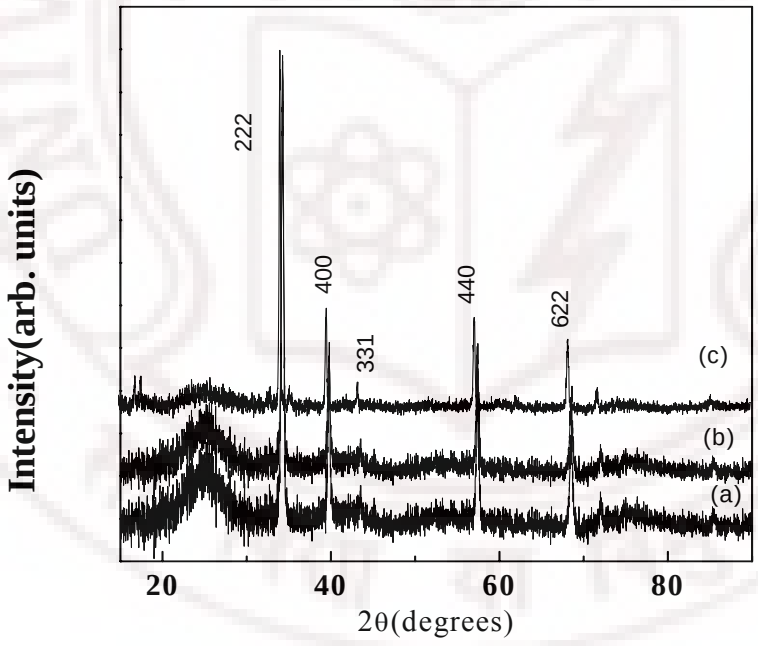

Figure 5.8 X-Ray diffraction patterns of c- BZN thin films deposited at oxygen pressures of (a) 2, (b) 6 and (c) 10mTorr and annealed at 600°C.

The Bragg reflection for the (222) planes occurs at 2θ values of 34.27, 34.17 and 34.28° respectively for films deposited at 2, 6 and 10mTorr oxygen pressure. The intensity of the (222) reflections also varies with the oxygen pressure. The relative intensity of the reflection from the (400) plane to the (222) plane was 0.39, 0.29 and 0.39

respectively for the films deposited at 2, 6 and 10 mTorr of oxygen pressures. From this analysis it is clear that the films deposited at 6 mTorr of oxygen pressure is more oriented in the (222) direction. The lattice parameters derived for these films from the (222) reflection plane are 3.039 A°, 3.046 A° and 3.038 A° respectively.

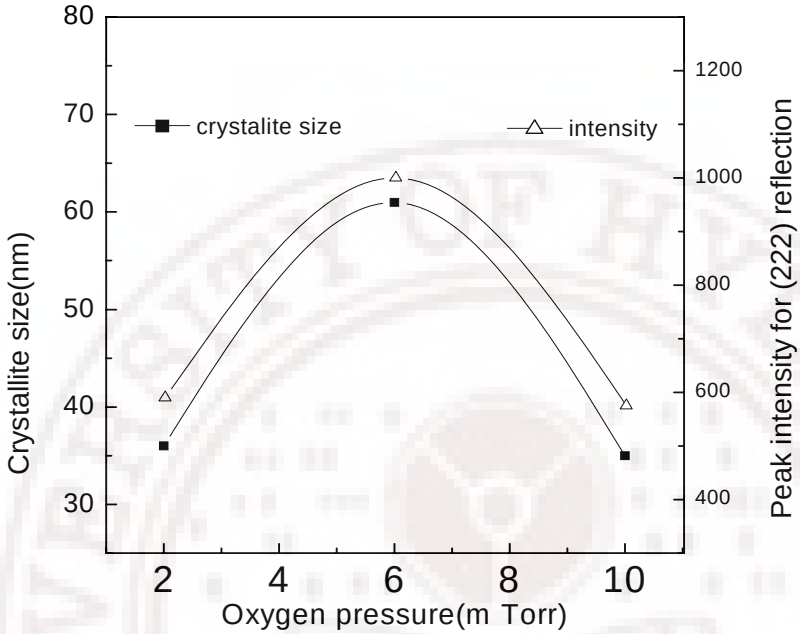

Figure 5.9 Variation of crystallite size and intensity of the (222) reflection with oxygen pressure of c-BZN thin films on fused silica substrate.

Figure 5.9 shows the variation of crystallite size with oxygen pressure. The crystallite size varies between 31 to 60nm with increase in oxygen pressure. It can be noted that as the crystallite size increases, the films are more oriented in the (222) direction.

5.5.3 Effect of oxygen pressure on m-BZN thin films

The XRD spectra of the m- BZN thin films deposited at different oxygen pressure and annealed at 600°C are shown in figure 5.10. No peaks due to a crystalline phase could be detected in the as deposited films, which indicated that the films were amorphous. The inter-atomic spacing for these films for the prominent (220) reflection plane are 3.574A°, 3.561 A°, and 3.547 A° respectively. On comparison with the standard d spacing, we can find that all these films are in compressive stress and the stress is decreasing with the increase in oxygen pressure.

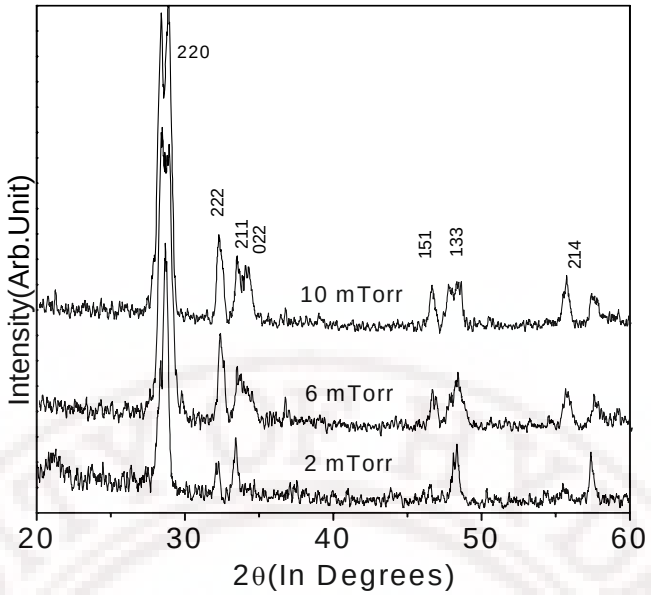

Figure 5. 10 XRD pattern of the m- BZN thin films annealed at 600°C.

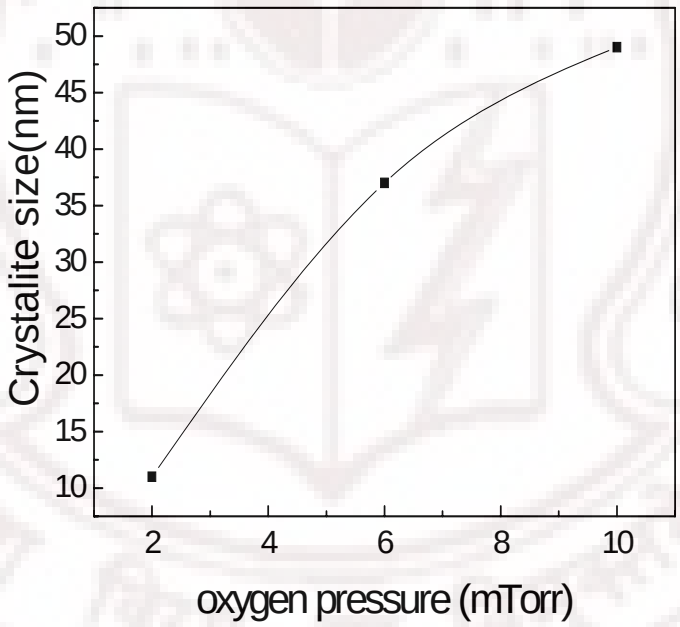

Figure 5.11 Variation of crystallite size of the m-BZN thin films with oxygen pressure during deposition.

Figure 5.11 shows a variation of crystallite size with the oxygen pressure, the crystallite size is found to be varying between 10nm to 50nm with respect to the oxygen pressure. It can be noted that as the oxygen pressure increases, the crystallite size also increases. At higher oxygen pressure, the ejected species from the target could undergo much more collision with oxygen molecule than those under lower oxygen pressure. These results in

the formation of larger clusters before their arrival at the substrate surface which undergoing nucleation and grain growth process results in larger crystallites.

5.5.4 Structural properties of c-BZN thin films grown on silicon substrates

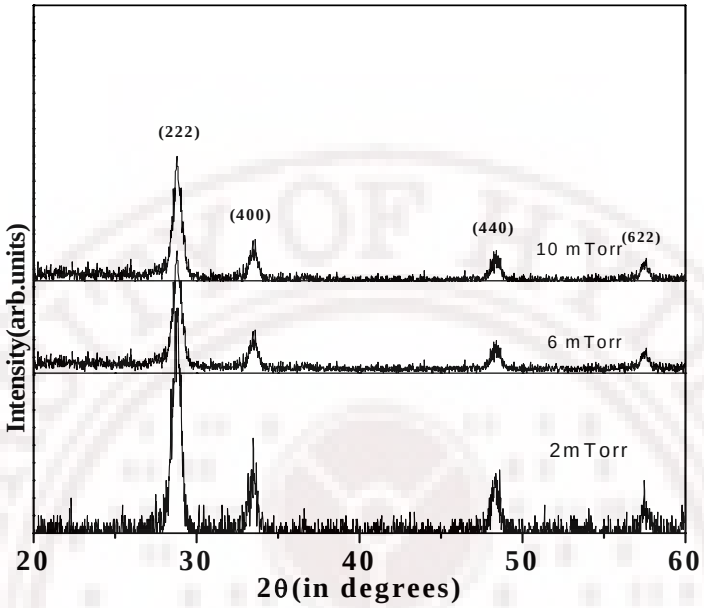

Figure 5.12 X-ray diffractograms of c-BZN films deposited on silicon at different oxygen pressures and annealed at 600°C.

Figures 5.12 and 5.13 shows the x-ray diffraction patterns for the c-BZN thin films grown on silicon and platinised silicon substrates respectively. The films were deposited at different oxygen pressures at ambient temperature and annealed at 600°C for 30 minutes. It is seen that the crystallinity of the films are varying with oxygen pressure. The crystallite size analysis using Scherrer equation reveals that there was a decrease in crystallite size with the increase in oxygen pressure. With the increase in pressure, the energies of the deposited species will get reduced, affecting the crystallinity which accounted for the decreased peak heights at higher oxygen pressures.

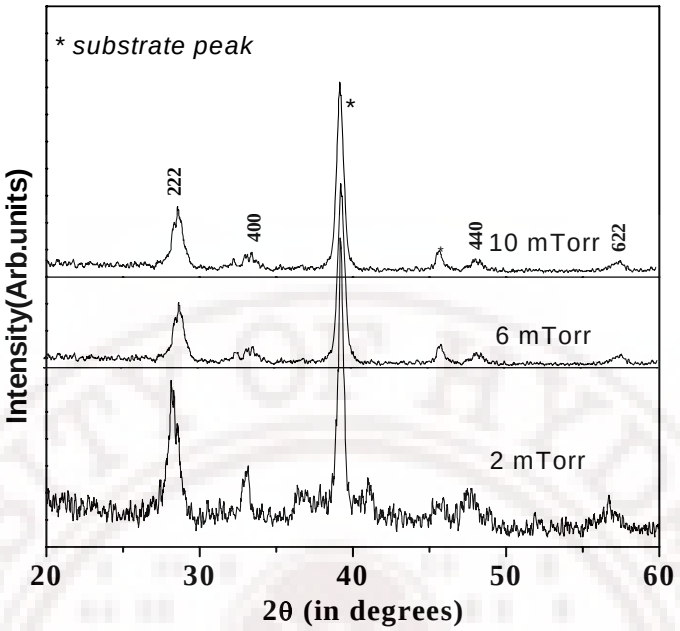

Figure 5.13 X-ray diffractograms of c-BZN films deposited at different oxygen pressures and annealed at 600°C on platinum coated silicon substrates.

5.5.5 Structural properties of m-BZN thin films grown on Silicon substrates

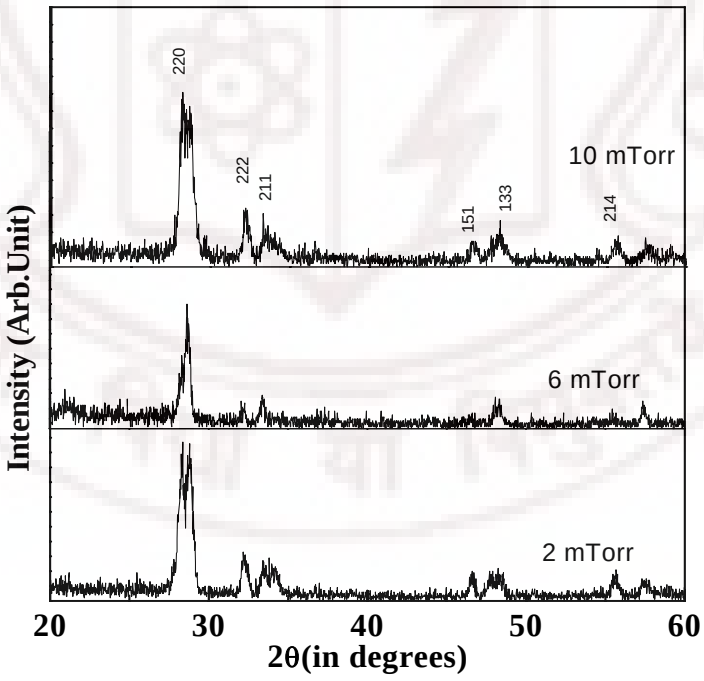

Figure 5.14 X-ray diffractograms of m-BZN films on silicon substrates deposited at different oxygen pressures and annealed at 600°C.

Figures 5.14 and 5.15 shows the X-ray diffraction patterns for the m-BZN thin films grown on silicon and platinised silicon substrates respectively. The films were deposited at different oxygen pressures at ambient temperature and annealed at 600°C for 30 minutes. It is seen that the crystallinity of the films are varying with oxygen pressure. From the x-ray diffraction pattern it can be seen that the crystallinity of the m-BZN thin films grown on pt coated silicon substrate are less compared to that grown on silicon substrates.

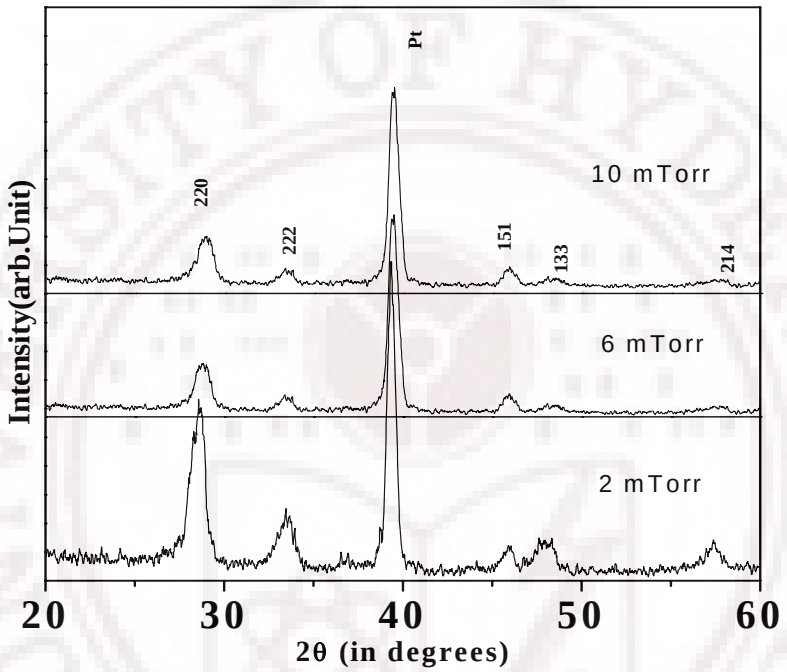

Figure 5.15 X-ray diffractograms of m-BZN films on platinum coated silicon substrates deposited at different oxygen pressures and annealed at 600°C.

5.6 Microstructural analysis

The microstructural characteristics of polycrystalline films are important because they control their properties, performance, and reliability in applications. In practical applications, the properties of polycrystalline films must be reproducible in order to control their performance and reliability. This, demands control over their microstructure, through effective process optimization that defines their structures. So a direct insight into the surface structural features of the BZN thin films is required in every step of processing. Detailed AFM imaging was performed for this purpose. AFM is a proven method to analyse the surface morphology of thin films which also allows the quantitative measurements of surface roughness.

5.6.1 Effect of oxygen pressure on the microstructure of BZN thin films

The surface topography evolution of the c-BZN thin films deposited at different oxygen pressures was determined using the atomic force microscopy and are shown in Figure 5.16. The annealed films show a nanostructured grain morphology with grain size in the range 69-90nm. The rms roughness of the as deposited films was found to be in between 0.5 to 1.5 nm whereas those of the annealed films were in between 1.6 and 3.4 nm. The ratio of the grain height to the grain diameters, for the un annealed thin films on fused silica substrates deposited at a total oxygen pressure of 2, 6 and 10 mTorr were found to be 0.0267, 0.037 and 0.051 respectively. On annealing these values changed to be 0.079, 0.085 and 0.096 respectively. The summary of the microstructural analysis of the c-BZN thin films grown on fused silica substrates is given in table 5.1.

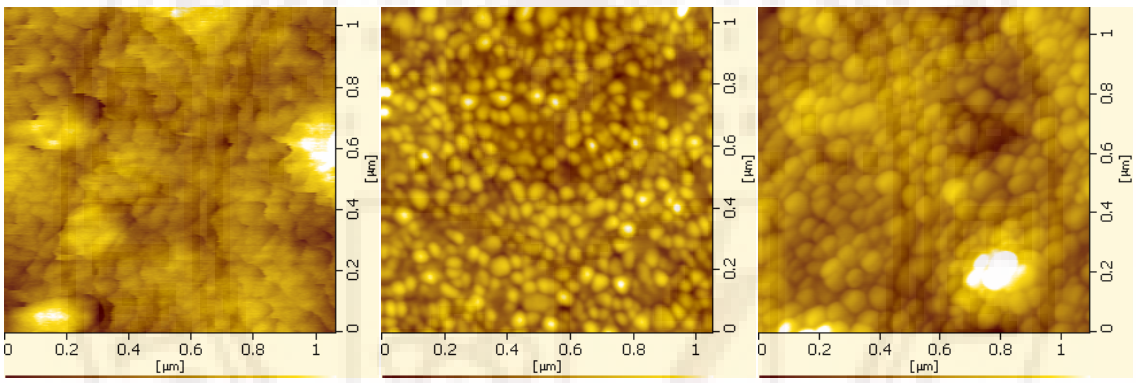

Figure5.16 AFM micrographs of the c-BZN thin films deposited at (a) 2, (b) 6, and (c) 10mTorr of oxygen pressures on fused silica substrates and annealed at 600°C.

Oxygen Pressure(mTorr)	Grain Size(nm)	RMS roughness(nm)
2	69	1.6
6	78	2.3
10	95	3.4

Table 5.1 Summary of grain size and RMS roughness of the c-BZN films deposited on amorphous fused silica substrates.

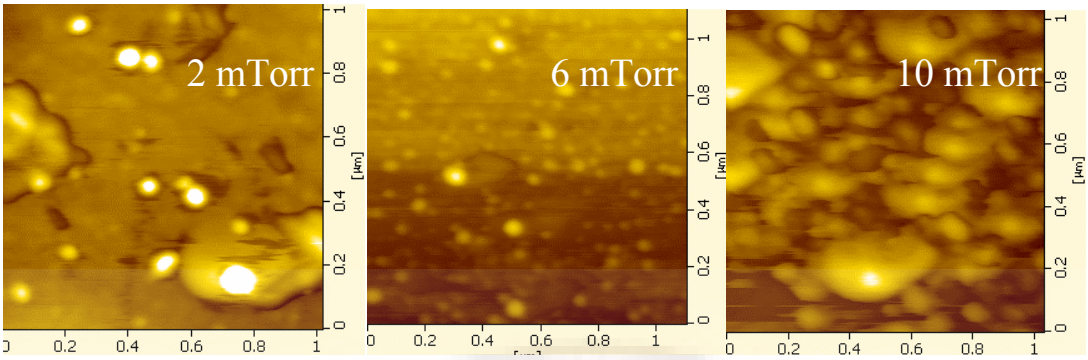

Figure 5.17 AFM micrographs of the annealed m-BZN thin films deposited at different oxygen pressures.

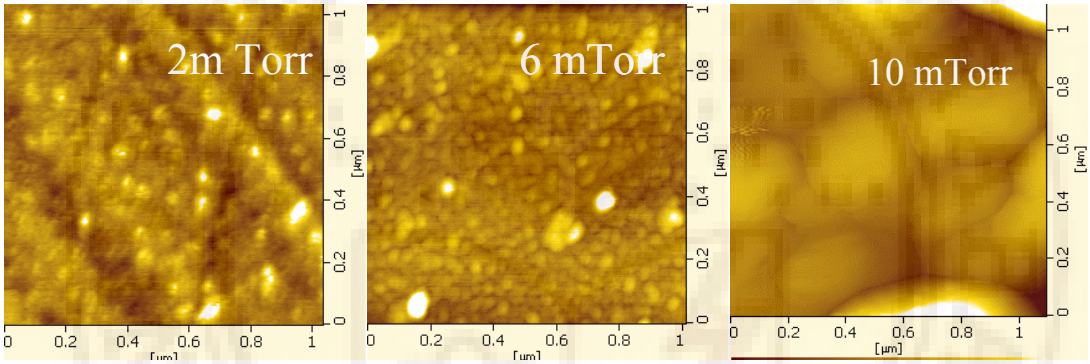

Figure 5.18: AFM micrographs of the annealed m-BZN thin films deposited at different oxygen pressures.

Oxygen pressure (mTorr)	Grain Size(nm)	RMS roughness(nm)
2	40	2.12
6	55	3.15
10	160	8.2

Table 5.2 Summary of grain size and RMS roughness of the m-BZN films deposited on amorphous fused silica substrates.

The effect of oxygen pressure on the microstructure of the PLD grown m-BZN thin films were investigated with AFM and found that oxygen pressure can significantly alter the surface morphology of these films. The scanning probe microscopic images of the as deposited and annealed m - BZN thin films deposited at different oxygen pressures

is shown in figure 5.17 and 5.18. The summary of the microstructural analysis of the m-BZN thin films grown on fused silica substrates is given in table 5.2. The rms roughness of the films is found to increase with the increase of oxygen pressure. For the films deposited at 6 mTorr of oxygen pressure, it can be noted that the crystallite size measured from the XRD and the grain size measured using atomic force microscopy are almost the same, which means that these films contain nano-sized grains whose size is approximately equal to that of a crystallite.

5.6.2 Effect of annealing temperature on the microstructure of the BZN thin films

The effect of annealing temperature on the microstructure of the c-BZN and m-BZN thin films has been observed using the atomic force microscopy as shown in figures 5.19 and 5.20. The surface roughness of the c-BZN thin films annealed at 500°C is 1.3nm and it is 3.5nm for the films annealed at 700°C. This shows that as the annealing temperature is increased, grain growth occurs, which results in increased grain size. This could be the result of an increase in the surface mobility available with increasing temperatures thus allowing the film to lower its total energy by decreasing the grain boundary area resulting in larger grains. Thus the films become more granular with the rise of temperature which results in increased surface roughness [10]. The m-BZN thin films are also exhibiting a similar behaviour.

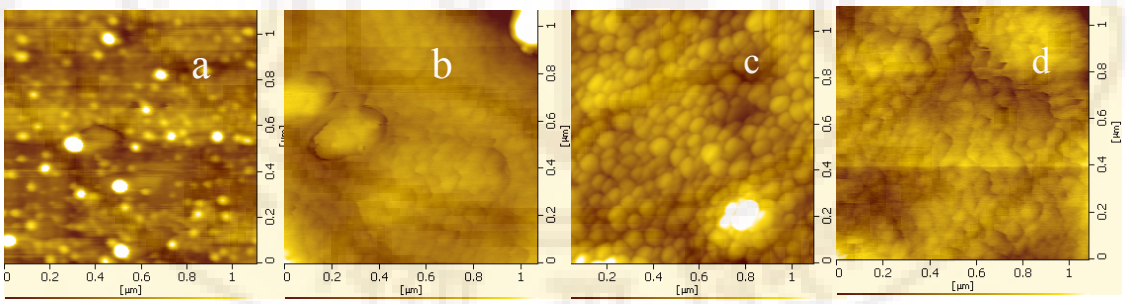

Figure 5.19 AFM micrographs of the c-BZN thin films annealed at (a) 400°C, (b) 500°C, (c) 600 °C and (d) 700°C deposited on fused silica substrates.

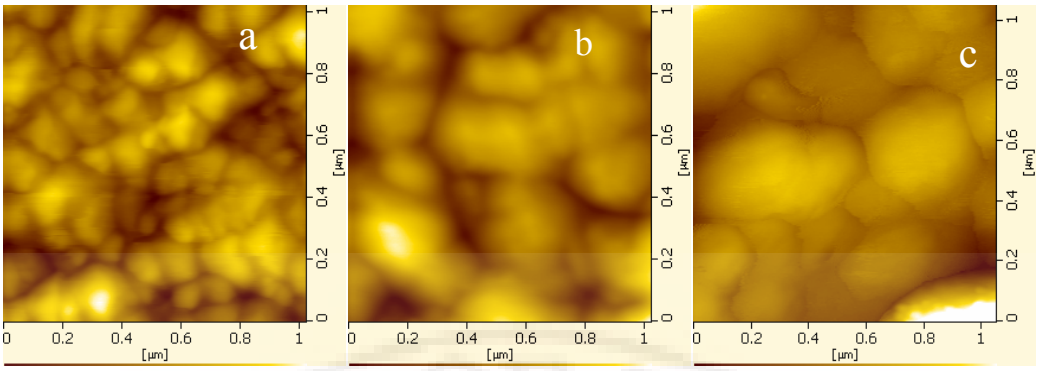

Figure 5.20 AFM micrographs of the m-BZN thin films annealed at (a) 600°C, (b) 700 °C and (c) 800°C deposited on fused silica substrates.

The microstructure of the m-BZN films annealed at 600°C shows closely packed tiny grains. With the increase in annealing temperatures, these closely packed individual grains are fused together to form larger grains. The films annealed at 700°C show a porous microstructure due to the presence of a mixture of clusters of grains and individual grains. The films annealed at 800°C shows a dense microstructure with bigger and closely packed grains due to a complete grain growth in these films.

5.6.3 Microstructure evolution of BZN thin films grown on different substrates

The AFM micrographs of the c-BZN and m-BZN thin films grown on different substrates are shown in figures 5.21 to 5.23. The c-BZN thin films grown on LAO, ALO and MgO substrates are showing a homogeneous and dense microstructure with larger grains. The microstructure of the c-BZN thin films grown on silicon substrates is not well evolved. Different microstructure induced by different substrates can be observed in the present study. Similarly the microstructure of m-BZN thin films grown on Silicon, LAO and ALO substrates shows a dense microstructure while the films grown on the MgO substrates shows a porous microstructure. The summary of microstructural analysis of c-BZN and m-BZN thin films grown on different substrates are given in tables 5.3 and 5.4

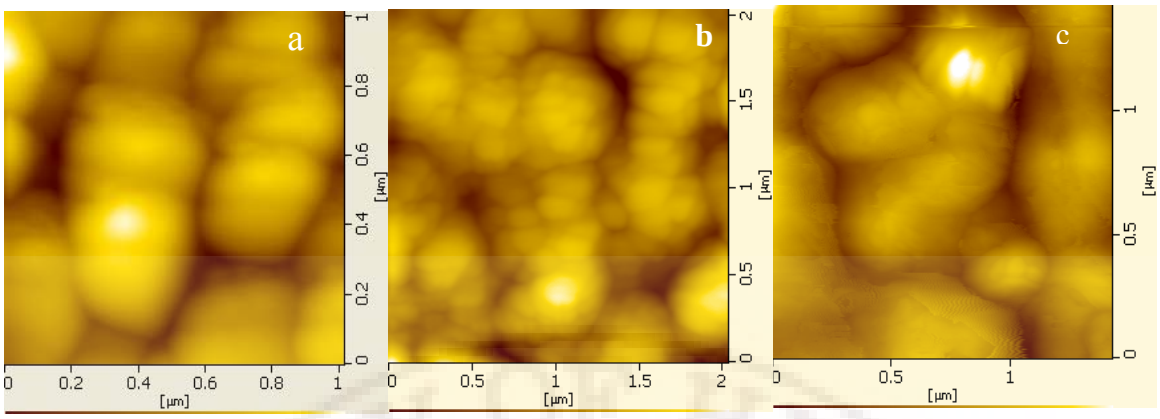

Figure 5.21 AFM micrographs of the c-BZN thin films deposited on (a) LAO (b) ALO and (c) MgO substrates and annealed at 600°C.

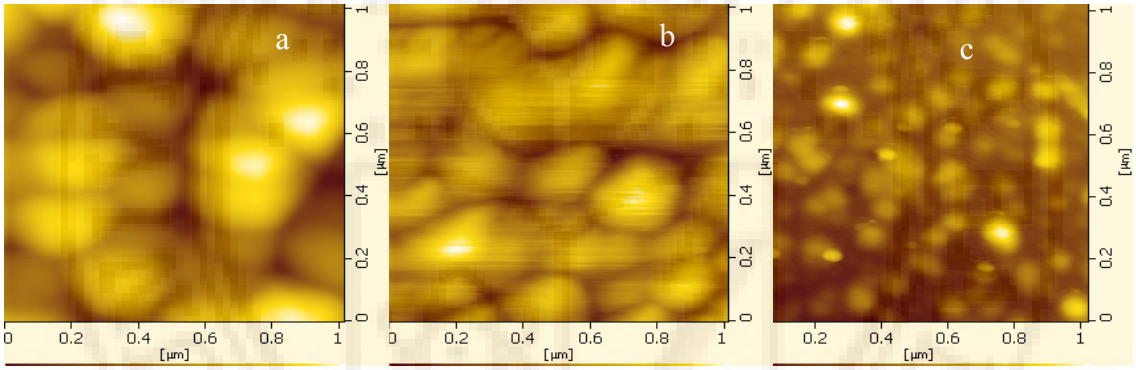

Figure 5.22 AFM micrographs of the m-BZN thin films deposited on (a) LAO (b)ALO and (c) MgO substrates and annealed at 600°C.

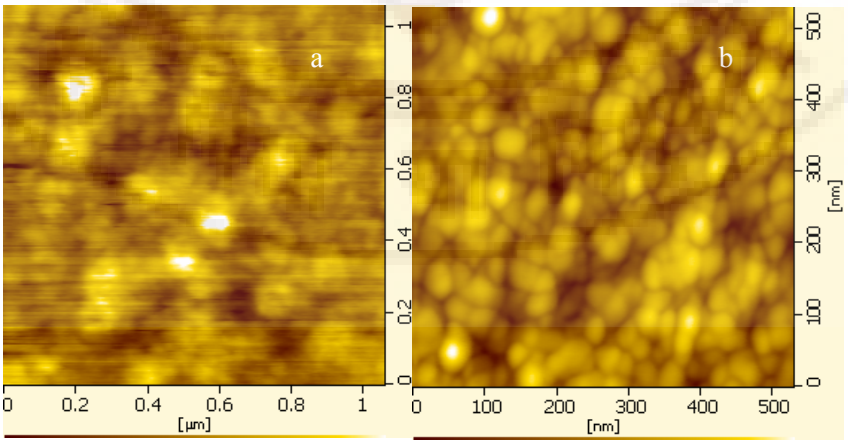

Figure 5.23 AFM micrographs of the (a) c-BZN thin films and (b) m-BZN thin films grown on silicon substrates.

Substrate	Grain Size(nm)	RMS roughness(nm)
ALO	125	6.2
LAO	197	8.2
MgO	220	12
Si	93	2.48

Table 5.3 Summary of grain size and RMS roughness of the c-BZN films deposited on various substrates.

.

Substrate	Grain Size(nm)	RMS roughness(nm)
AlO	290	7.5
LaO	240	6.3
MgO	103	2.9
Si	61	1.7

Table 5.4 Summary of grain size and RMS roughness of the c-BZN films deposited on various substrates.

Although the mechanisms of PLD are complicated, the interaction between the plume and the substrate is a major factor for the multicomponent material depositions. This interaction involves the energy exchange between the substrate thermal energy and the plume's kinetic energy. This interaction ultimately determines the thin film orientation and microstructure in each substrate. The microstructural development of the thin film grown on different substrates will depend on the adatom mobilities and sticking coefficient of the individual substrates. The lattice mismatch and the difference between the thermal expansion coefficients between the film and substrate materials are also responsible for the different microstructure in these substrates.

5.7 Raman spectral characteristics of Bi_2O_3-Nb_2O_5-ZnO based thin films

Raman spectroscopy is a powerful technique for studying vibrational modes in condensed matter which helps to identify the chemical bonds present in the system. Most of the fundamental vibrational modes in condensed matter lie in the energy range that corresponds to the middle infrared part of electromagnetic spectrum with wave numbers from 500 to 4000 cm^{-1}. Raman effect can be interpreted as inelastic scattering of light due

to superposition of skeletal vibrations and dipole oscillations induced by electric field of the incident wave. The vibrational modes are Raman active only if it affects the local polarizability. Since the dielectric properties of ionic solids are primarily dictated by their lattice dynamics, knowledge of the lattice dynamics is important for both bulk and thin film dielectrics. Therefore Raman spectroscopy is important for dielectrics as it is one of the simple techniques which give a good insight into the lattice dynamics of the material. Moreover, it is a nondestructive technique and it does not require any special treatment of the samples.

5.7.1 Effect of oxygen pressure on the Raman characteristics of c-BZN thin films

For the analysis of Raman scattering data, we consider that the c- BZN thin film is characterized by face centered cubic symmetry with the space group Fd3m. The six Raman active modes can then be classified as follows [11]: $\Gamma = A_g + E_g + 2F_{1g} + 4F_{2g}$. The room temperature Raman scattering data of c- BZN thin film and bulk were obtained by employing normal backscattering geometries, and their results are presented in figure 5.24. We observed Raman modes at 139, 195, 251, 271, 337, 369, 537, 624, and 764 cm^{-1} in c-BZN thin films, which are comparable to the recently reported Raman spectra of c-BZN thin film with the same Fd3m symmetry [12]. The optical phonon mode at 251 was assigned to Zn – O vibration mode whereas the modes at 194 and 764 cm^{-1} are due to pure Bi-O and Nb –O stretching vibrations [13]. The difference of the cation ionic radius in A site and B site will affect the force constants of the A-O, A-O' and B-O vibrational modes, thus the whole Raman bands will have to undergo some shift to the red or blue directions and even some new vibrational modes will emerge. As we compare the observed Raman data of thin film and bulk, we observe that the Raman modes in thin film are relatively more intense and additional Raman modes appear in thin films in the low frequency range. These results suggested that the local symmetry in thin films is different from that of the bulk due to strain in thin films. The change in local symmetry in thin films arose due to strain, which changes the correlation lengths between the dipoles.

In figure 5.24, we observed one strong Raman peak at 893 cm^{-1} marked with a single asterisk, which is only observed in thin film Raman spectrum. The Raman modes at 764 and 893 cm^{-1} seem to be related to oxygen octahedra (NbO_6) stretching mode. The FWHM and Raman shift of 764 cm^{-1} Raman modes showed blue or red shifts with oxygen pressure. The intensity of the Raman mode at 893 cm^{-1} showed an abrupt change

in thin films deposited at 6 mTorr compared to 2 and 10 mTorr and it reveals the rigidity of the octahedral NbO_6 cage in c- BZN thin films that changed with oxygen pressure.

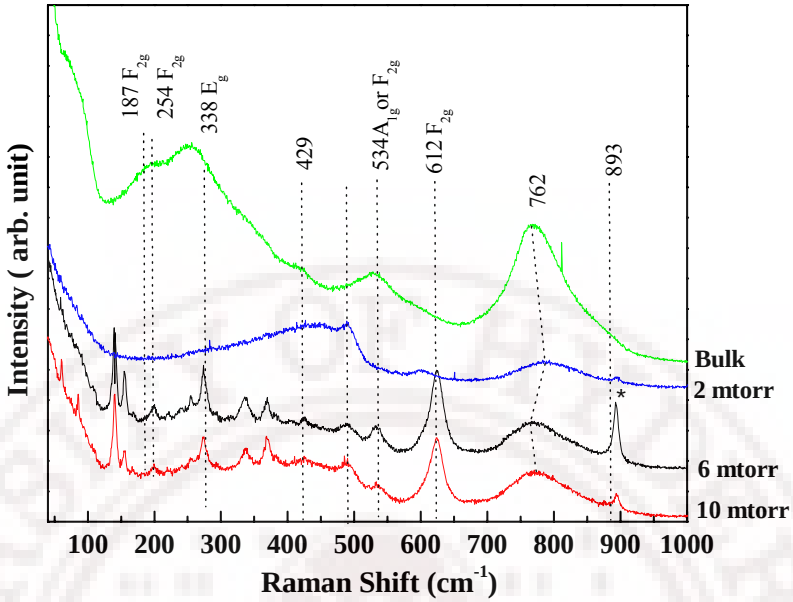

Figure5.24 Raman spectra for the c - BZN thin films deposited at 2, 6 and 10 mTorr oxygen pressures and bulk.

We observed additional Raman lines at 141, 158, 223 and 340 cm^{-1} in films which are deposited at 6 and 10 mTorr. The presence of new Raman modes in some thin films could be attributed to the change in local symmetry brought in by strain in the thin films prepared at some oxygen partial pressures. Presence of movable Zn^{2+} ions in the pyrochlore structure also could contribute to this effect [14]. These new modes are absent in BZN thin films deposited at low oxygen pressure at 2 mTorr and in bulk BZN. The intensity of Raman modes at 155, 271, 369, 623 and 893 cm^{-1} are found to decrease with increase in the oxygen pressure whereas the intensities of the other modes are either constant or they increased with oxygen pressure.

5.7.2 Effect of oxygen pressure on the Raman characteristics of m-BZN thin films

Raman scattering is highly sensitive to find the changes in local lattice distortions arising mainly from oxygen deficiency. The $Bi_2Zn_{2/3}Nb_{4/3}O_7$ m-BZN thin films are characterized by monoclinic zirconate – like pyrochlore structure with the space group (C2/c – C_{2h})[15] The 69 Raman active modes can then be classified as $\Gamma = 34A_g + 35B_{1g}$. The room temperature Raman scattering data of m – BZN thin films were obtained by employing normal backscattering geometries and their results are presented in Fig 5.27 along with the Raman scattering of c-BZN deposited in similar

oxygen pressures (Figure 5.25). We observed Raman modes at 165, 204, 246, 362, 429, 488, 556, 602, 778, 849, and 1053 cm^{-1} in m-BZN thin films, which are comparable to the earlier reported Raman spectra of m-BZN bulk materials with the same monoclinic symmetry [16]. The Raman modes are broad due to the disorder of Zn^{2+} and Nb^{5+} on the B site of the pyrochlore structure. This may be a probable reason for observing much less number of Raman modes in m-BZN thin films.

The difference of the cation ionic radius in A site and B site will affect the force constants of the A-O, A-O' and B-O vibrational modes, thus the whole Raman bands will have to undergo some shift to the red or blue directions and even some new vibrational modes will emerge. As we compare the observed Raman data of monoclinic and cubic BZN thin films, we observe that the number of observed Raman modes in m-BZN is greater than c- BZN as expected from the factor group analysis. The optical phonon mode at 764 cm^{-1} is due to Nb –O stretching vibrations in c-BZN [17]. This mode probably splitted in two mode in case of m-BZN and we observed Raman modes at 778 and 849, [18] which are originated from the symmetrical vibration in NbO_6 octahedra and assign as A_g mode [19]. These results suggested that the local symmetry in m-BZN is different from that of the c-BZN due to the disorder of Zn^{2+} at A and B sites, which changes the correlation lengths between the dipoles.

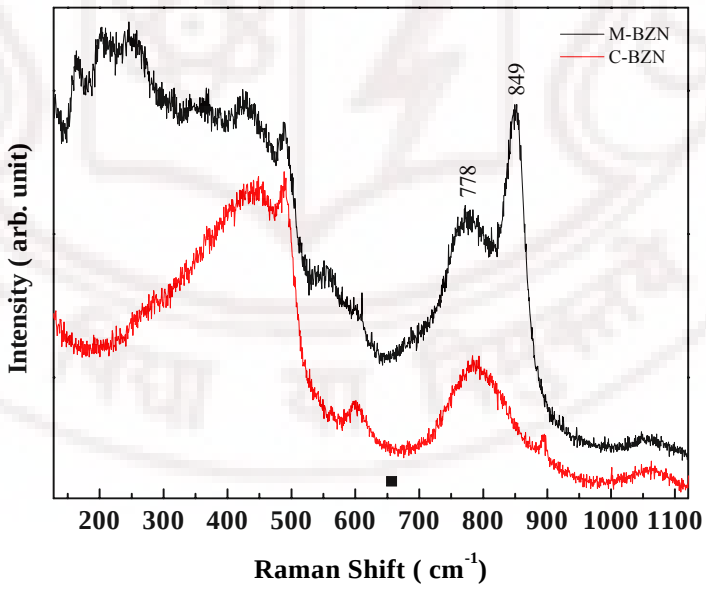

Figure 5.25 Raman spectra for the m - BZN and c – BZN thin films deposited at 10 mTorr oxygen pressures.

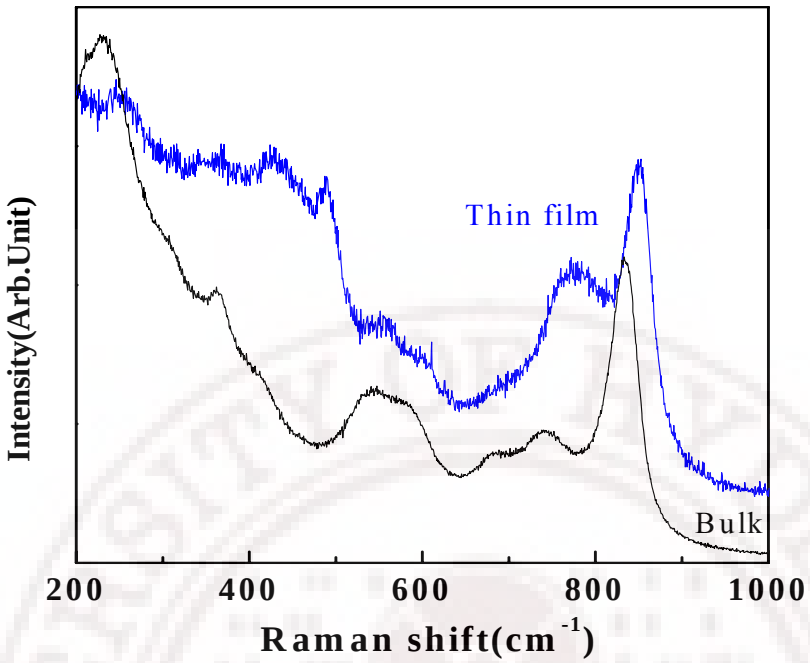

Figure 5.26 Raman spectra for the m - BZN bulk ceramic and thin film deposited on fused silica substrate.

The Raman scattering spectra of m-BZN thin films and m-BZN bulk ceramics are shown in figure 5.26. The Raman peaks of the films are found to be shifted towards the higher frequency side with respect to the bulk values. Assuming the compositions and crystal structure of the thin films are identical to that of their bulk counterpart, shifts in the peak positions of the Raman spectra can be interpreted as the result of changes in the local environment of the vibrating ions. The shifts in the Raman modes to the higher frequency side is an indication of the stiffening of the bonds i.e. it indicates the shorter anion-cation distance which will result in vibration at higher frequencies. The observed shift in Raman modes toward the higher frequency side for the m-BZN thin films indicate that the films are under compressive stress. This may be influencing the optical and electrical properties of the films which are discussed in the sixth chapter.

Figure 5.27 shows the Raman scattering spectra of m-BZN thin films deposited at 2, 6, and 10 mTorr oxygen pressures. We observed that low frequency Raman modes are not appearing in the thin films deposited at 2 mTorr and 6 mTorr oxygen pressures. The A_{1g} Raman modes at 764 and 893 cm^{-1} corresponds to Nb – O – Zn stretching mode. The frequency shift of the two A_g Raman modes showed blue or red shifts with oxygen pressure as presented in Fig. 5.28. These results

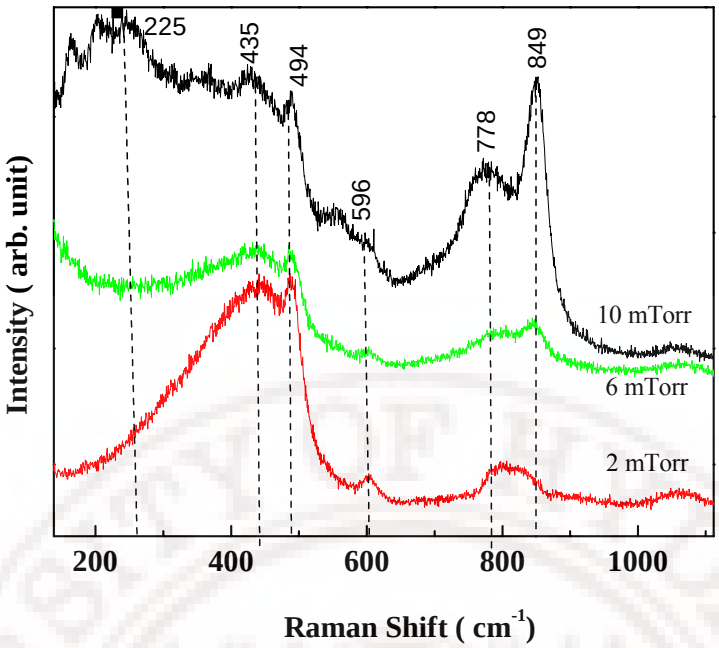

Figure 5.27 Raman spectra of the m - BZN thin films deposited at 2, 6 and 10 mTorr oxygen pressures.

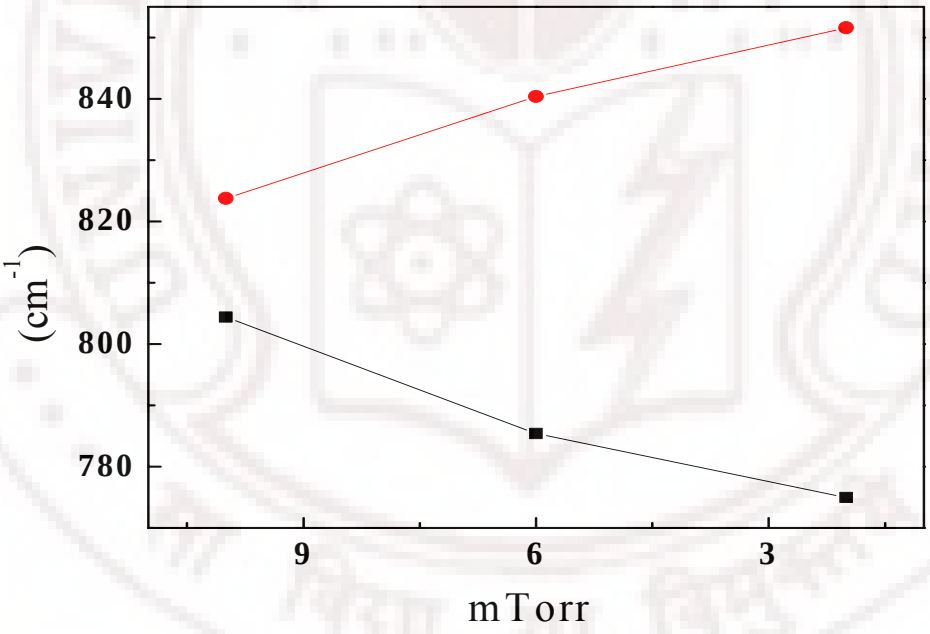

Figure 5.28 Frequency shift with oxygen pressure for Ag Raman modes, observed at 778 and 849 cm^{-1} for the samples deposited on fused silica substrates.

reveal that the polar distortion got suppressed with increasing oxygen pressure. The intensity and line width of these Raman modes also showed abrupt changes in thin films deposited at 10 mTorr compared to 2 and 6 mTorr and it reveals that the rigidity of the NbO_6 octahedral cage in BZN thin films have changed with oxygen pressure. As shown in the figure 5.28 the A_{1g} Raman modes appears at $778cm^{-1}$ shows a shift towards higher

frequency side with increase in oxygen pressure while the mode at 849 cm^{-1} shows decreasing frequency. It is possible that oxygen ions are freed from their defect bonding with increasing oxygen pressure, and thereby free to oscillate more like in single crystals resulting in a reduction of the oxygen bending mode vibration frequency. However the Nb – O – Zn stretching mode becomes more rigid. The dielectric properties of oxygen octahedra based systems increases when the octahedra are aligned, as this configuration increases the local Lorentz field factor at the metal ion inside the octahedra [20] making it highly polarizable.

5.7.3 Raman characteristics of c-BZN and m-BZN thin films on different substrates

In order to have a better understanding of the effect of the substrates on the films studied, the Raman spectrum of the films was collected as described in chapter 2. A compilation of the Raman spectra for c-BZN thin films on MgO, LAO. ALO and fused silica substrates at 10mTorr oxygen using pulsed laser deposition from 150-1200cm^{-1} is shown in figure 5.29. From the visual inspection of the spectra, several intensity peaks are evident. It has been shown before from the factor group analysis of c-BZN of the regular pyrochlore structure that, it has six Raman active modes [21]. However it has been shown that for the c-BZN films, the dynamic displacement of the ions from their regular pyrochlore atomic positions leads to the possibility of having more number of Raman active modes [22]. Similar observations were made by Nino and co-workers also [23]. Such a situation is possible, if the local symmetry is different from the regular pyrochlore symmetry. For the c-BZN thin films grown on MgO substrates the Raman active modes were seen at 260,518,605,783,891 and 1119cm^{-1} respectively. On comparison with the standard Raman modes, the modes at 260cm^{-1} can be assigned to F_{2g} mode corresponding to the A-O vibrations. Similarly the mode at 518cm^{-1} can be assigned to the F_{2g} modes due to BO_6 octahedral and the mode 605 is assigned to an F_{2g} mode due to the B-O and O-B-O bond vibration. The c-BZN grown on LAO substrates exhibited the Raman modes at 268,353,485,591,746 and 1014 cm^{-1}, while they are observed at 267,368.415,578 and 745cm^{-1} for the films grown on sapphire substrates and at 261,446,488,605,790 and 907cm^{-1} for the films grown on amorphous fused silica substrates. The Raman mode at 764 and 893 cm^{-1} can be associated with the oxygen octahedral (NbO_6) stretching mode. From the figure it is clear that the NbO_6 vibrating mode is located at 783 cm^{-1} for the films grown on MgO substrate and at 790cm^{-1} for the films grown on fused silica substrate. For the lanthanum aluminate and sapphire substrates these modes appear at 746

and 745 cm^{-1} respectively. Assuming identical composition and overall crystal structure for the films, shift in peak positions of the Raman spectra can be interpreted as the results of changes in the local environment of the vibrating ions. Specifically, they can point to

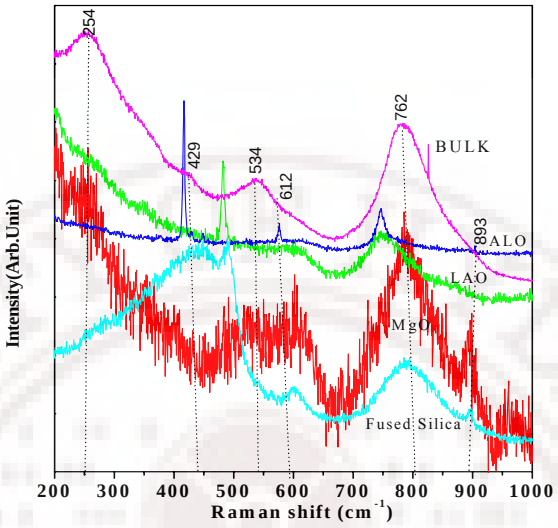

Figure 5.29 Raman spectra for the c - BZN thin films grown on different substrates and bulk.

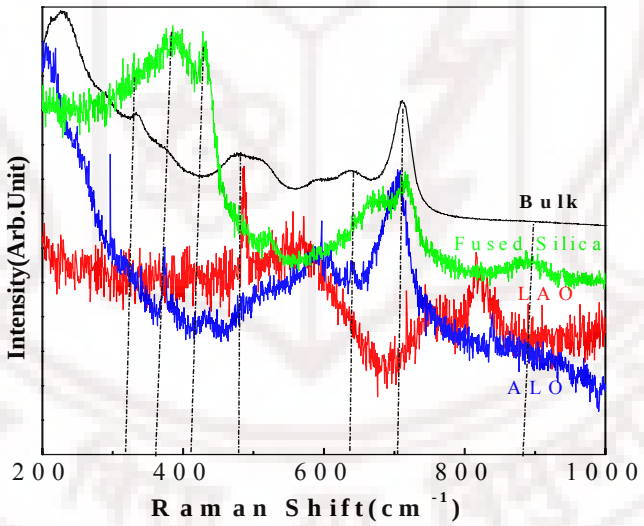

Figure 5.30 Raman spectra of the m - BZN thin films grown on different substrates.

stiffening of bonds (shorter anion-cation bond distance) resulting in vibration in higher frequency and vice versa (longer bonds means lower frequencies). The shift towards the higher frequency side in comparison with the mode at 764cm^{-1} of bulk c-BZN in the thin films grown on MgO and fused silica substrates can be attributed to the compressive state in the films. Similarly, the films grown on LAO and sapphire are in a state of tensile

stress. Such changes in local environment vibrating atoms could affect all the observed optical and electrical properties of the films.

Similarly, the Raman spectra for m-BZN thin films grown on lanthanum aluminate, sapphire and fused silica substrate at 10mTorr oxygen using pulsed laser deposition is shown in figure 5.30. For the bulk m-BZN ceramics, the Raman modes are observed at 849,746,695,594,366 and 260 cm^{-1}. The A_{1g} modes at 849 and 746 cm^{-1} are attributed to a combination of Nb-O-Zn stretching mode, oxygen bending vibration, B site ion vibration against O stretching vibration inside the octahedra and the BO_6 octahedra vibrations. On comparing the A_{1g} modes at 849 and 746cm^{-1} of the m-BZN bulk, the corresponding modes in the films are having shifts. These modes are appearing at 848 and 790 cm^{-1} respectively for the m-BZN thin films on fused silica substrate. Similarly for the films on lanthanum aluminate substrates the modes are appearing at 815 and 753 cm^{-1} respectively. In the case of films on sapphire substrates the first and second A_{1g} modes are seen at 749 and 833 cm^{-1} respectively. Assuming identical composition and overall similar crystal structure for the films, shift in peak positions of the Raman spectra can be interpreted as the result of changes in the local environment of the vibrating ions [24]. On comparing the second A_{1g} mode which appears to be prominent in the films, the films grown on sapphire and lanthanum aluminate seems to be tensile strain, while the film on fused silica are in compressive strain.

5.8 Optical properties of thin films in the Bi_2O_3-Nb_2O_5-ZnO system

As mentioned in the first chapter, the thin films in the Bi_2O_3-Nb_2O_5-ZnO systems are mainly being considered for dielectric applications in microelectronics. However, the optical properties of these thin films are also interesting for a number of reasons including identifying the electronic component of polarizability in these films and monitoring the film growth as well as degradation processes. Variations in optical parameters such as refractive index and band gap with changes in processing conditions are good indicators of the growth patterns of the dielectric films. Moreover high dielectric constant thin films with high optical transparency have considerable importance in the transparent optoelectronic devices. So a systematic investigation on the optical properties of these thin films is important for understanding the growth process as well as identifying the suitability of these films in transparent electronic application.

5.8.1 Effect of oxygen pressure on the optical properties of c-BZN thin films

The spectral transmission curves of the c-BZN thin films before and after annealing are shown in the figures 5.31 and 5.32. All the transmission spectra show interference fringes, which originate due to interference at the air – film and substrate-film interfaces. The sharp fall in transmission and disappearance of the fringes at the shorter wavelength is due to the fundamental absorption of the films. There is a clear shift in the interference-free regions suggesting a remarkable change in the optical band edge for films prepared at different oxygen pressures. The spectral transmission behaviour shows a strong dependence on thickness of the films as well as oxygen pressure during film growth. The XRD pattern given in figure 5.8 already reveals that the as deposited films were amorphous in nature, but they crystallised after annealing at 600°C. The BZN film with a thickness 420 nm deposited at 10 mTorr oxygen pressure shows a transmittance T of 90% at a wavelength of 546nm. The deposited films were quite transparent in visible region. Furthermore the absorption edge shifted to the shorter wavelength region with increasing oxygen pressure indicating that the optical band gap, E_g increased with increasing pressure.

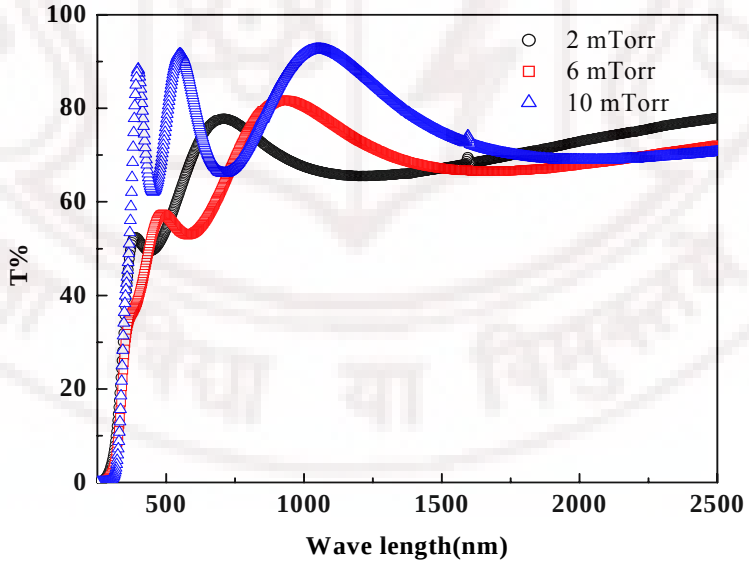

Figure 5.31 Measured spectral transmission curves of as deposited c-BZN thin films.

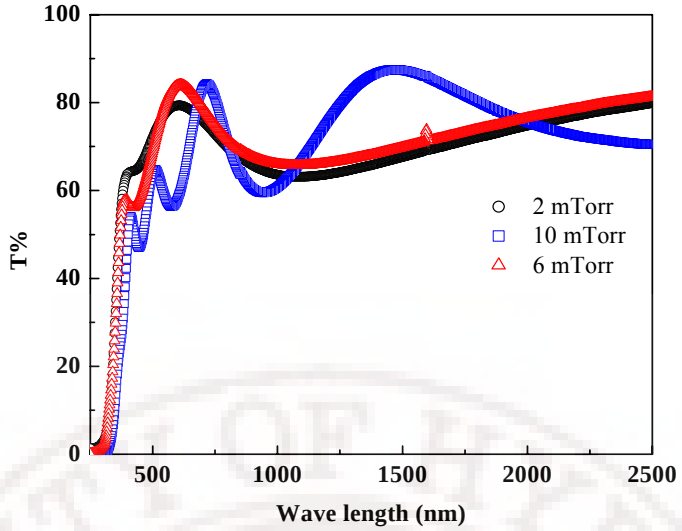

Figure 5.32 Measured spectral transmission curves of annealed c-BZN thin films.

The optical band gap E_g can be determined from the absorption coefficient α, calculated as a function of incident photon energy, E, for indirect allowed transitions. At shorter wavelengths close to the optical band gap, scattering losses are dominated by fundamental absorption and α at a given wavelength, λ, is often expressed as

$$\alpha = -\frac{1}{d}\ln\left(\frac{1}{T}\right) \qquad (5.1)$$

where d is the film thickness, and T is the transmittance at that wavelength.

The optical band gap E_g for all the films were calculated using the Tauc relation [23], which is given by

$$\alpha E = B\left(E - E_g\right)^m \qquad (5.2)$$

where B is the constant that is a measure of crystalline order in the deposited films. E is the incident photon energy and m=0.5, 1.5, 2 or 3 for allowed direct, forbidden direct, allowed indirect and forbidden indirect electronic transitions. Interband optical transitions that can be described by wave functions localized over a distance of the order of lattice constant are relatively unchanged by disorder. Therefore, optical band gap and the constant B estimated from $(\alpha E)^{1/2}$ vs E reflects the local atomic structure undetected by XRD. That is, these parameters can be correlated with the short-range order at the nanoscale and particularly amorphous phase alone or phases coexisting with crystalline materials in films grown at low temperatures. In the current study, the calculated E_g increases with increase in oxygen pressure. The optical band gap also shows an increase

on annealing, indicating onset of crystallinity. All the films show E_g values of the orders of 3.30 to 3.60eV.

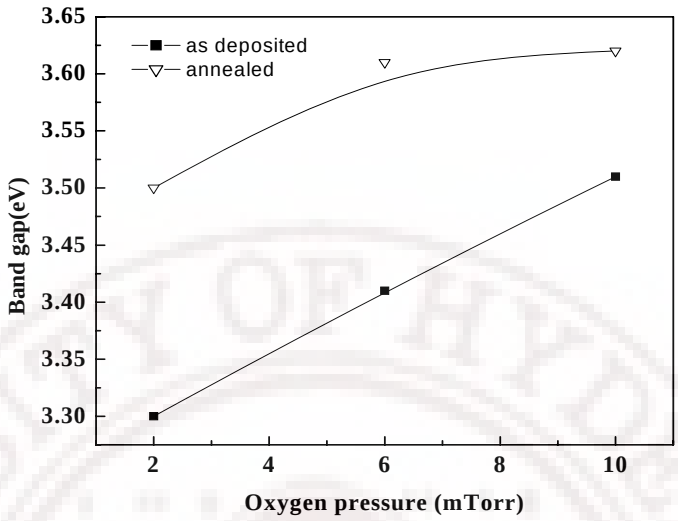

Figure 5.33 Variation of the optical band gap of the as deposited and annealed c-BZN thin films deposited at different oxygen pressures.

The low band gap in the as deposited thin films may be due to the disorder crystalline structure and the increase in optical band gap reflects the crystallinity in the BZN thin films. The change in the shape of the fundamental absorption edge is considered to reflect the variation in density of states and the short-range structural change undetected by XRD. The refractive index (n) of the films as a function of oxygen pressure is shown in figure 5.34. It is found that the refractive index decreases with the increasing oxygen pressure. The as deposited films show a decrease in refractive index with increase in oxygen pressure from 2.52 to 2.36. Post deposition annealing, however, results in a relatively pressure independent refractive index of 2.55±0.2. This can be correlated with the crystallization of the films, thus approaching single crystal values. Biegalski et al [25] reported a refractive index of around 2.5 at 700nm for the BZN thin films. The theoretically estimated value of bulk BZN ceramics reported by Chen et al at 700nm is 2.5. Cheng et al. [26] reported a refractive index value in the range of 2.2 to 2.35 for laser annealed BZN thin films. The experimental value of refractive index for $Bi_{1.5}Zn_{1.0}Nb_{1.5}O_7$ thin films measured at 700nm in this study is comparable with that of those reported in the literature.

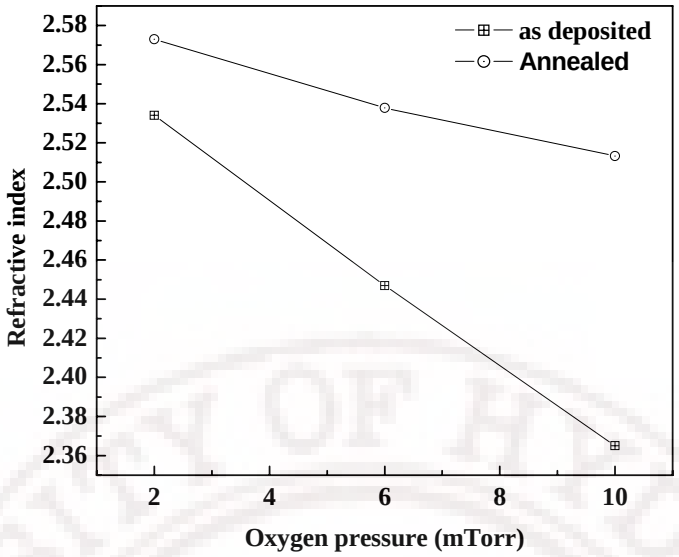

Figure 5.34 Variation of the refractive index at the wavelength of 600nm of the as deposited and annealed c-BZN thin films deposited at different oxygen pressures.

5.8.2 Effect of oxygen pressure on the optical properties of m-BZN thin films

The spectral transmission curves of the m-BZN thin films before and after annealing is shown in the figures 5.35 and 5.36. All the transmission spectra show interference fringes, which originate due to interference at the air-film and substrate-film interfaces. The sharp fall in transmission and disappearance of the fringes at the shorter wavelength is due to the fundamental absorption edge of the films. There is a clear shift in the interference free regions suggesting a remarkable change in the optical band edge. The spectral transmission behaviour shows a strong dependence on thickness of the films as well as oxygen pressure during film growth. The XRD spectrum, given in figure5.9, already reveals that the as deposited films are amorphous in nature but they crystallised after annealing at 600°C. The as deposited m- BZN films deposited at different oxygen pressures shows a transmittance T of 70-80% in the visible region. The optical transmittance increases for the annealed films. It was found that the absorption edge shifted to the longer wavelength region with increasing pressure indicating that the optical band gap, E_g decreased with increasing pressure. Recently, Chen et al. [27] reported a refractive index of 2.05 to 2.5 for the pulsed laser deposited m-BZN thin films on ITO coated glass substrates. The measured optical properties films of this study are also in good agreement with their results.

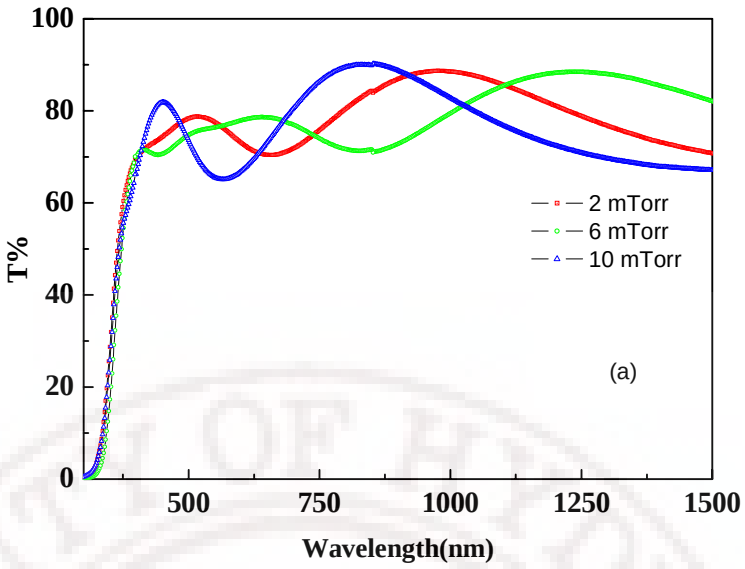

Figure 5.35 Measured spectral transmission curves of as deposited m-BZN thin films.

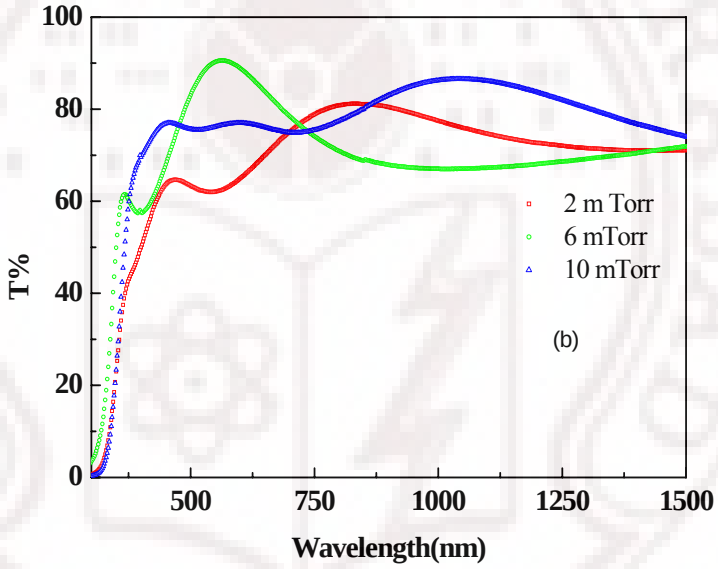

Figure 5.36 Measured spectral transmission curves of as deposited m-BZN thin films.

The calculated E_g shown in figure 5.37 shows an increase with increase in oxygen pressure. The optical band gap of the films deposited at 2, 6 and 10 mTorr of oxygen pressures shows a decrease on annealing. All the films show E_g values of the orders of 3.50 to 3.60eV. The possible reasons for higher value of band gap in the un-annealed m-BZN thin films is the existence of the density of states with in the gap as explained by Davis and Mott[29], causing the formation of a fundamental absorption edge due to band tailing rather than an optical band gap as stated earlier. In the crystalline states the states within the gap disappear and the optical band gap then approaches the single crystal value. The films deposited at 6 mTorr of oxygen is having higher band gap and it may be because it got a nano-structured grain morphology.

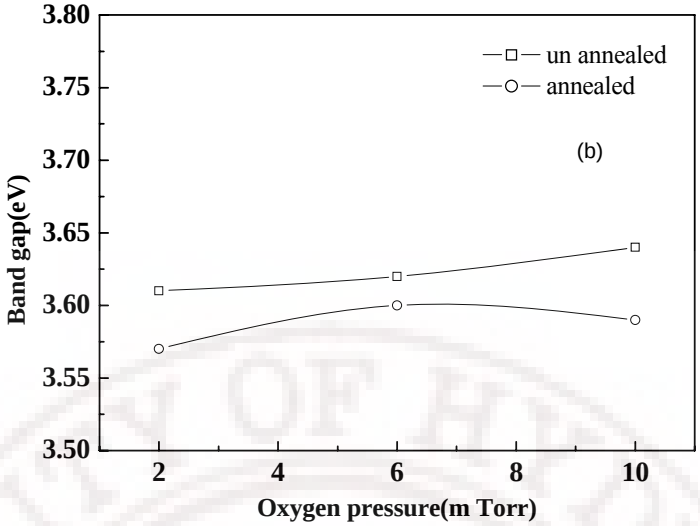

Figure 5.37 Variation of the optical band gap of the as deposited and annealed m-BZN thin films deposited at different oxygen pressures.

The refractive index (n) of the films as a function of oxygen pressure is shown in figure 5.38. It is found that the refractive index increases with the increase in oxygen pressure. The as deposited films show a increase in refractive index with increase in oxygen pressure from 2.06 to 2.15. Post-deposition annealing, however, results in a relatively pressure-independent refractive index of 2.25±0.2. This can be correlated with the crystallization of the films thus approaching their single crystal values.

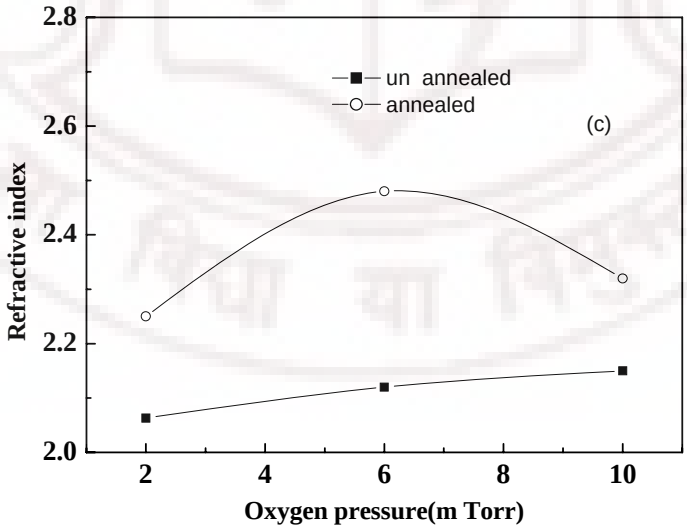

Figure 5.38 Variation of the refractive index of the as deposited and annealed m-BZN thin films deposited at different oxygen pressures and measured at 600nm.

5.8.3 Effect of annealing on the optical properties of c-BZN and m-BZN thin films

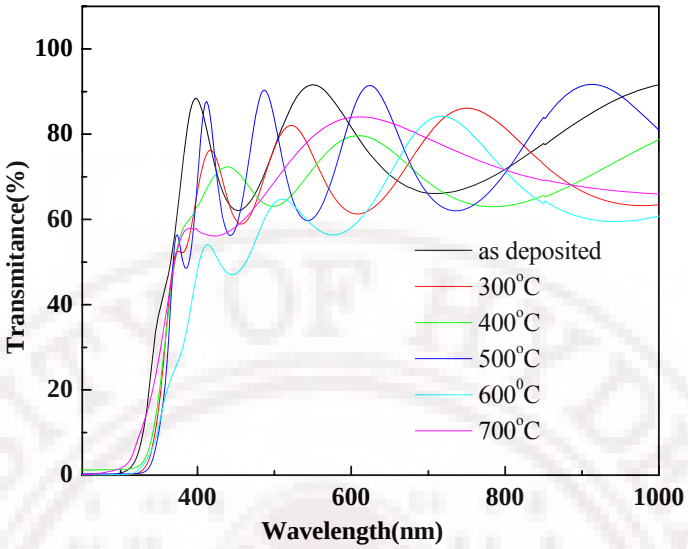

Figure 5.39 Transmittance spectra of c-BZN thin films annealed at different temperatures from 300 to 700°C.

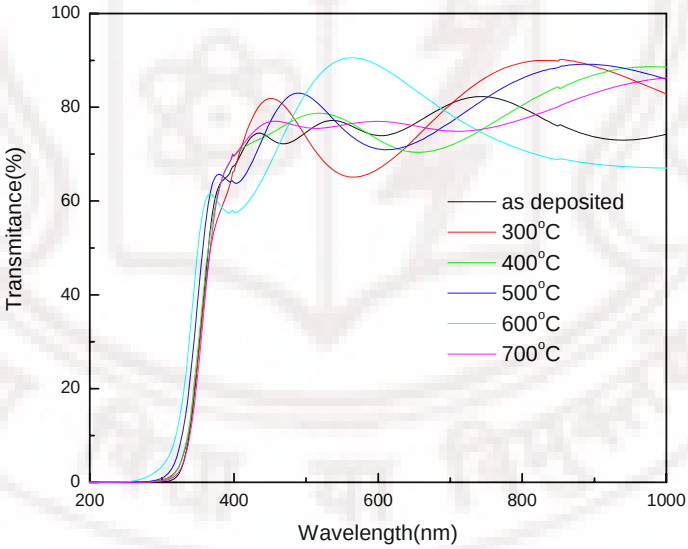

Figure 5.40 Transmittance spectra of m-BZN thin films annealed at different temperatures from 300 to 700°C.

Figures 5.39 and 5.40 shows the optical transmittance spectra of the c-BZN and m-BZN thin films deposited on fused silica substrates at 10 mTorr of oxygen pressure and annealed at different temperatures. The interference fringes seen in the transmission spectra are a result of the interference between the air-film and film-substrate interfaces.

The films are highly transparent with a transmittance between 75-85% in the visible regions. The transparency of the films drop sharply in the UV region and the absorption edge is located below 330nm for these films. Annealing shows a slight decrease in transmittance at higher temperatures. The films annealed at 700°C shows a considerable decrease in optical transmittance for both c-BZN and m-BZN thin films. This can be attributed to an increased scattering films with larger grains and because of the increase in packing density of the films. From the transmittance spectra the refractive index (n) and thickness (d) were calculated using the envelop method [30] The allowed direct band gap energy E_g of the film were obtained by plotting $(\alpha h\upsilon)^2$ vs hν curves with the extrapolation of the linear region to the low energies as shown in figure.

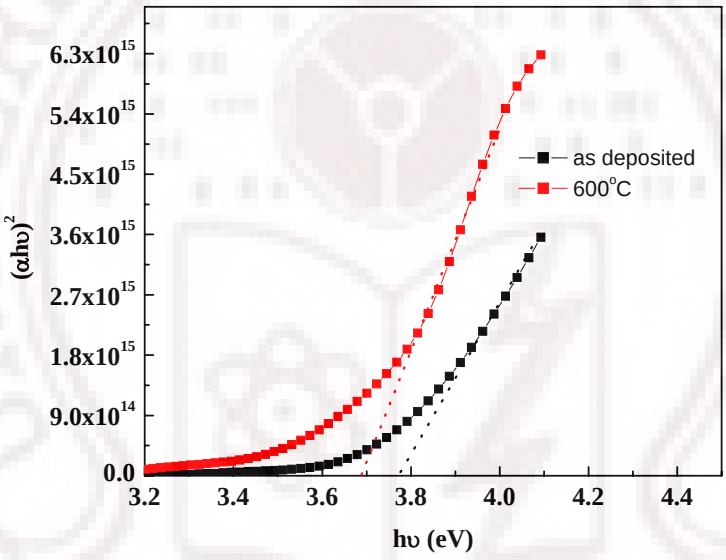

Figure 5.41 Plot of $(\alpha h\nu)^2$ vs $(h\upsilon)$ for the as deposited films and the films annealed at 600°C.

The band gap of the crystalline films is higher than that reported for BZN powders treated at 700°C [31]. This increase in band gap may be due to the nanocrystalline character of the films. Similar behaviour has been reported earlier also [32].

As shown in figure 5.42 the value of E_g of the as deposited thin films c-BZN is about 3.6 eV which is less than that of the earlier reported values of c-BZN thin films. There is a gradual increase of the optical band gap of c-BZN thin films with the annealing temperature. The optical band gap of the films annealed at 700°C is found to be 3.68eV. These values are in agreement with the earlier reported band gap values of c-BZN thin films. Hence the increase in band gap energy after annealing is due to the crystallization of c-BZN thin films. The difference of 0.48eV between these two phases can be attributed

to the fact that the structure of amorphous solids can be characterized as an irregular arrangement of atoms. This disorder is known to influence the optical band gap of amorphous semiconductors as well [33]. Similar behaviour has also been reported for HfO_2 thin films [34].

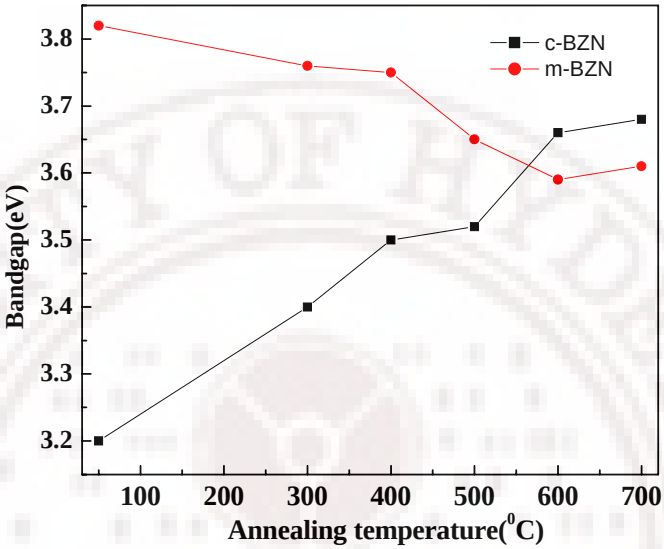

Figure 5.42 Variation of the optical band gap of the c-BZN and m-BZN thin films annealed at different temperatures.

Variation of the optical band gap of m-BZN thin films with annealing temperature is also shown in figure 5.42. The as deposited films were having an optical band gap of 3.82 eV which has got decreased to 3.6 on annealing at 700°C. The decrease in band gap on annealing is a common feature exhibited by many oxide materials. It is attributed to several reasons such as the grain size effect, stress in the films and the amorphous nature of the material itself. In the present case, no significant grain size difference is observed for the films annealed at these temperatures and hence the grain size effect may not be an important factor in the observed optical properties. The higher band gap in the amorphous thin films can be attributed to an increase in inter-atomic spacing due to excess volume and absence of long range order in the lattice. Similar trends were also reported for $BaTiO_3$ thin films. If the higher band gap in the amorphous thin films is due to the increase in inter-atomic spacing or lack of long range order, there should be a large deviation in the band gap on crystallization. In the present case, a change in band gap of 0.2eV only was observed. The most probable reason for this could be the presence of oxygen vacancies. On annealing, the oxygen vacancies are filled and hence, the band gap

decreases. It has already been reported that for the films deposited at lower temperatures there is a possibility of forming larger number of oxygen vacancies and free electrons [35].

The refractive index of c-BZN and m-BZN thin films annealed at different temperatures is calculated and is shown in figure 5.43. As shown in the figure, the refractive index increases with the increase in temperature. The low values of refractive index for the as deposited films can be attributed to the pulsed laser deposition process that produces films with porous microstructure and consequently with low packing density at ambient temperature. However, as the annealing temperature increases, the packing density of the films increases, resulting in an increase in the refractive index. The relationship between the packing density and the refractive index has been discussed in detail by many researchers and they have found that when the film achieves the bulk value of refractive index, its packing density will be the highest [36]. Thus, it is reasonable to assume that one of the causes for increase in refractive index with temperature for the films in the present study is the increase in their packing density.

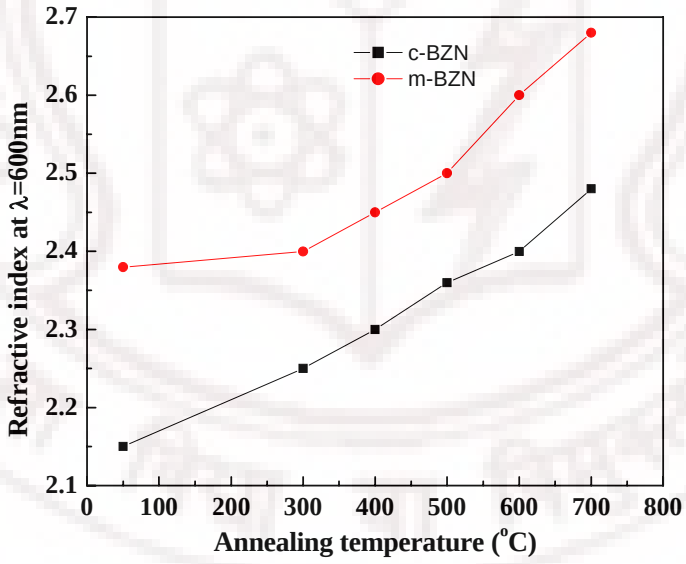

Figure5.43 Variation of the refractive index at the wavelength for 600nm of the c-BZN and m-BZN thin films annealed at different temperatures.

5.9 Summary

In summary, the thin films of c-BZN and m-BZN ceramics were grown on various substrates under different deposition conditions. Depositions conditions were optimized to produce c-BZN and m-BZN thin films with good structure and microstructural characteristics. The XPS analysis confirmed the presence of Bi, Zn, Nb,and O near the surface. From the observed binding energies, the Bi, Zn and Nb ions were found to be in their chemical states as Bi^{3+},Zn^{2+},and Nb^{5+}respectively. The EDX analysis confirmed the composition of the films deposited. The reflections from the X-ray diffractograms of c-BZN thin films show the formation of the cubic pyrochlore structure with all the major peaks corresponding to the Fd3m space group and the reflection from the m-BZN thin films shows the formation of a monoclinic zirconolite like pyrochlore phase. The crystallite size of the films are found to be varying with the oxygen pressure during the processing. From the study of the influences of oxygen partial pressure during deposition, annealing temperature and substrate type on the microstructure in the PLD growth of BZN thin films, it is confirmed that these factors can significantly alter the surface morphology of these thin films. The Raman analysis of c-BZN thin films and bulk reveals that the local symmetry in thin films is different from that of the bulk due to strain in thin films. The change in local symmetry in thin films could arise due to strain, which changes the correlation lengths between the dipoles. The anomalous changes in FWHM, intensity, and frequency shift of the two higher frequencies, of Ag modes appearing at 778 and 849 cm^{-1} on varying oxygen pressure suggest polar distortion suppression in the m-BZN films**.** The as deposited c-BZN thin films exhibit refractive index in the range of 2.36-2.53 with an optical absorption edge value between 3.30-3.52eV. The as deposited m-BZN films exhibit refractive index in the range of 2.06-2.15, with an optical absorption edge value between 3.59-3.67eV. The refractive index of the films increase on annealing, indicating the onset of crystallinity. The packing density of these films was found to be increasing with the increase of annealing temperature which in turn results in the increase of refractive index.

References.

1. T.Gibert, B.Dubrueil, M.F.Barthe, J.L.Debrun, *J.Appl.Phys*., 74, 3506(1993)
2. A.D. Boardman, B.Cresswell, J.Anderson, *Appl.Surf.Sci*., 96-98, 55(1996)
3. S.I.Anisimov, B.S.Luk'yanchuk, A.Luches, *Appl.Surf.Sci*., 96-98 (1996)
4. C.F.Miller,G.W.Simmons and R.P.Wei, *Scr.Mater*, 42, 227(2000)
5. H.T.Fan, S.S.Pan, X.M.Teng, C.Ye , G.H.Li and L.D.Zhang, *Thin Solid Films*, 513, 142(2006)
6. W.Xiaohong, Q.Wei and H.Weidong, *J.Mol.Catal.chem*, 261,167 (2006).
7. Internationl centre for diffraction data(ICDD),Joint committee on powder diffraction standards(JCPDS) card no 54-971
8. Internationl centre for diffraction data(ICDD),Joint committee on powder diffraction standards(JCPDS) card no 54-972
9. G Sinha,K.Adhikary and S.Chaudhuri, *Optical materials,* 29(6),718(2007).
10. S.Chopra, S.Sharma, T.C.Goel, R.G.Mendirata, *Applied surface science*, 230, 207(2004).
11. M Chen, D.B.Tanner and Jaon.C.Nino, *Phys.Rev B*, 72,054303,(2005)
12. S.M.Zanetti, S.A.D Silva, *Materials Research*, 10, 261, (2007)
13. B.E.Scheetz and N.B.White, *J.Am.Ceram.Soc*, 62, 468(1979)
14. Wang Hong, Du Huilling, Yao Xi, *Material science and Engg B***,** 99, 20,(2003)
15. H.Wang, S.Kamba, M.Zhang, X.yao, S.Denisov, J.Petzelt, *Journal of applied physics*, 100, 034109(2006).
16. M Chen, D.B.Tanner and Jaon.C.Nino, *Phys.Rev B*, 72,054303,(2005)
17. K. Sudheendran, K C James Raju, M. K. Singh, R. S. Kayiyar, *J. Appl. Phys*, 104, 104104 (2008).
18. H.Du,X.Yao, L.Zhang, *Ceramic international*, 28,231 (2002)
19. Wang Hong, Du Huilling, Yao Xi, *Material science and Engg B***,** 99,20,(2003)
20. P.Sheng, Z Chen, *Physical review Lett*, 60**,** 227(1987)
21. Z.Qu, C.Wan and W.Pan, *Chem.Mater*., 19(20), 4913,(2007)
22. S. Kamba, V. Porokhonskyy, A. Pashkin, V. Bovtun, J. Petzelt, J.C. Nino, S. Trolier-McKinstry, M.T. Lanagan and C.A. Randall, *Phys. Rev. B,* 66 , 054106, (2002)
23. J.C. Nino, M.T. Lanagan, C.A. Randall and S. Kamba, *Appl. Phys. Lett.,* 81**,**4404, (2002)
24. J.C.Nino, W.Qiu, J.L.Jones, *Thin solid films*, (in press)

25. M.Biegalski, R.Thayer,J.Nino,S.Trolier-Mckinstry, *Proc. 13th IEEE Int. Symp. Appl. Ferroelectrics.* **7,** 10 (2002)
26. J.G.Cheng, J.Wang, T.Dechakupt, S.Trolier-Mckinstry, *App.phys lett* 87, 232905(2005)
27. H.F.Cheng, Y.C.Chen, and I.N.Lin, *Journal of applied physics*, 81,479(2000).
28. J.CTauc. Optical properties of solids. Amsterdam: North-Holland 1972
29. E.A.Davis, N.F.Mott, *Philos Mag*, 22,903 (1970).
30. R. Swanepoel, *J. Phys. E: Sci. Instrum*. 16, 1214 (1983).
31. S.M. Zanetti, S.A. da Silva and G.P. Thim, *J. Solid State Chem.* 177,456 (2004).
32. S.M.Zanetti, S.A.daSilva, *Thin Solid film*,497,72(2006)
33. J.M.Khoshman and M.Kordesh, *J.Appl.Phys*.101,103532(2007)
34. J.M.Khoshman,A.Khan and M.E.Kordesh, *Surface and coating technology,* 202, 2500 (2008).
35. S.C.Roy, G.L.Sharma,M.C.Bhatnagar, *Solid state communications*,141,243(2007).
36. F.K.Shan and Y.S.Yu*, J.Eur ceramic Soc*.24,1869(2004).

Chapter 6

Electrical and dielectric properties of Bi_2O_3-ZnO-Nb_2O_5 based pyrochlore thin films.

6.1 Introduction

As discussed in chapter1 the studies of the BZN thin films for RF/microwave applications have employed single crystal substrates such as MgO and $LaAlO_3$ [1]. Another common approach followed is to deposit BZN films on to pt coated Si substrates [2]. There have been comparatively few reports on the electrical and dielectric properties of BZN films grown directly on amorphous fused silica substrates despite the excellent microwave properties of this material as a microwave substrate. This chapter presents a study of the electrical and microwave dielectric properties of c-BZN and m-BZN thin films grown mainly on amorphous fused silica substrates. This chapter also discusses the microwave dielectric properties of these films grown on different single crystal substrates. The deposition process and the structural, microstructual and optical properties of these films were already discussed in chapter 5. Electrical properties of the films, especially parameters like dielectric constant, loss tangent and leakage current judge the suitability of thin films for various electronic applications. A detailed investigation is required to have a clear understanding of the effect of process parameters on the electrical properties of these thin films. The leakage characteristics of the films grown on pt coated silicon substrates were measured using a metal insulator metal capacitor structure. The low frequency dielectric properties of these films grown on different substrates were determined using appropriate capacitor structures such as metal insulator semiconductor (MIS) capacitor, metal insulator metal (MIM) capacitors and inter digitated capacitor (IDC). The details of these measurement techniques were discussed in chapter 2. The microwave dielectric properties of these thin films grown on fused silica substrates were measured nondestructively at few spot frequencies in the X-band using the extended cavity perturbation technique as well as spilt post dielectric resonator techniques. The broad band microwave dielectric properties of these films were characterized using calibration comparison techniques. Circular patch capacitor based techniques were used to characterize the microwave dielectric properties of both c-BZN and m-BZN thin films grown on pt coated silicon substrates. The voltage dependent dielectric properties of these thin films grown on sapphire, MgO and fused silica substrates were measured using calibration comparison technique by applying a bias voltage of 100V through an external

bias Tee to the coplanar waveguide test structures fabricated. The details of these measurement techniques were given in chapter 3.

6.2 DC electrical properties

Conduction mechanisms in thin films are an important part of study from the application as well as academic point of view [3]. In general, for any electronic application, the leakage current flowing through the dielectric material should be as low as possible. High leakage current meant that the energy stored in the dielectric material will easily get dissipated resulting in higher power consumption. It is also interesting to understand the mechanism of conduction so that ways to limit the conduction current could be explored. The type of charge carriers, mobility and their relationships with the lattice defects, impurities, grain boundaries and electrode effects are topics of active research. As electronic devices become more and more miniaturized, the electric field across the devices will be higher [4]. So the understanding of high field conduction through the dielectric thin films becomes increasingly important. The theory of high field conduction through bulk solid dielectrics has been described in detail by O Dwyer [5]. Basically the high field conduction mechanism could be classified in to electrode and bulk limited conduction. Electrode limited conduction included Fowler-Nordheim emission [6], Schottky emission [7] and thermionic field emission. Bulk limited conduction includes the Poole-Frenkel effect[8], space charge limited conduction and ionic conduction [9].

Figure 6.1 and 6.2 shows the J-E characteristics of the films deposited at 10 m Torr of oxygen pressure and annealed at different temperatures. The leakage current density is found to be increasing with the annealing temperatures. However it is still low in the range of 2-3 $\mu A/cm^2$ at 50KV/cm. This is much lower when compared with that of ferroelectric thin films [10]. The leakage characteristics are known to be related to many factors which include impurities in the film, microstructures and film thickness. The leakage current density of BZN films is showing strong annealing treatment dependence

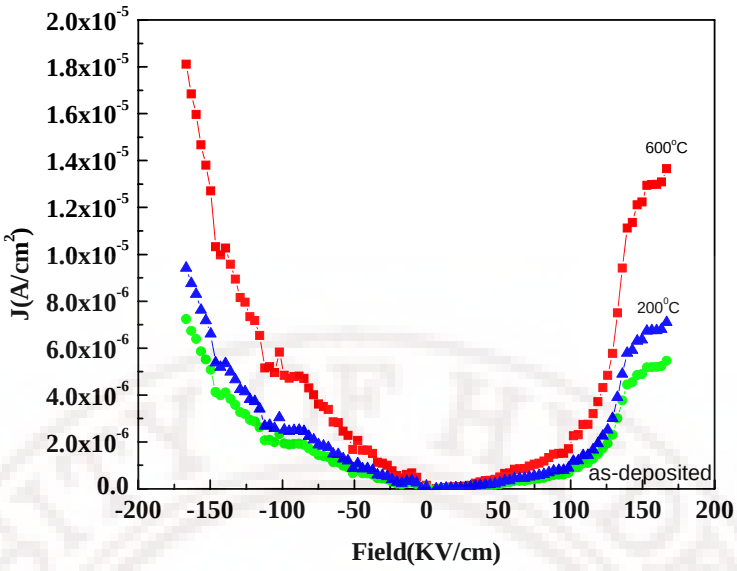

Figure 6.1 Leakage characteristics of c-BZN thin films on Pt coated Silicon.

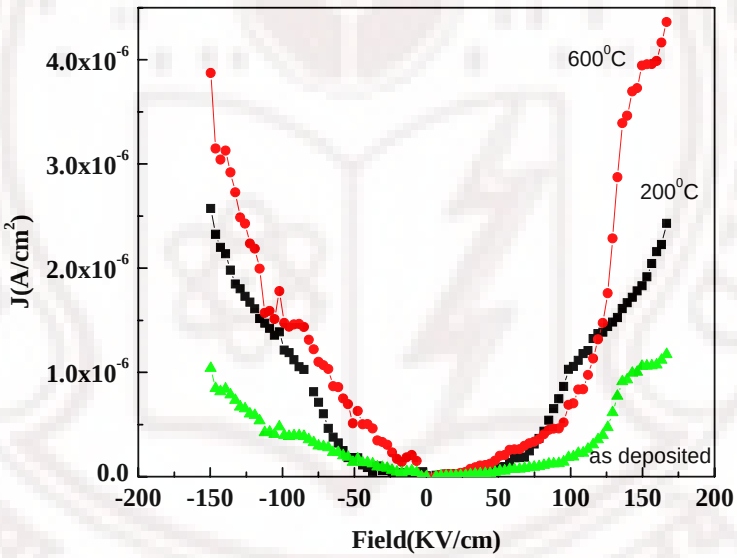

Figure 6.2 Leakage characteristic of m-BZN thin films on Pt coated Silicon.

The measured leakage current in most of the oxide dielectrics can have both electronic and ionic contribution. To identify the predominant conduction process in these films

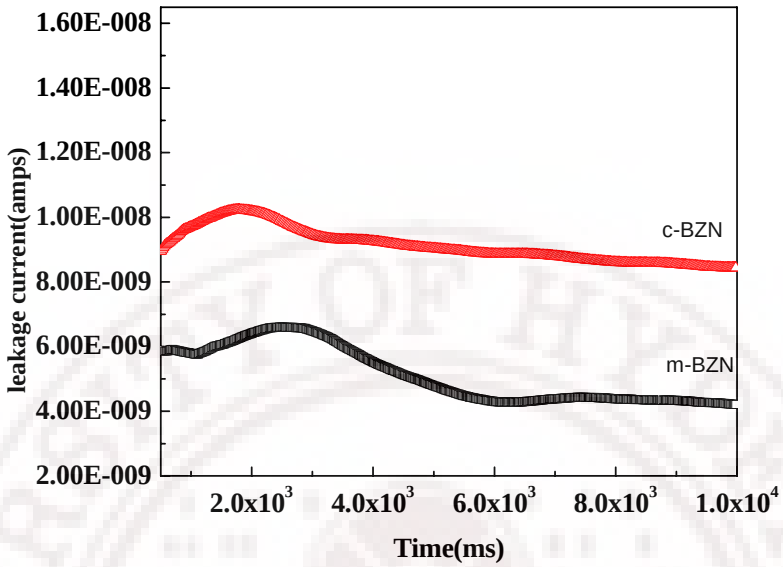

Figure 6.3 Time dependent leakage characteristic of c-BZN and m-BZN thin films on Pt coated Silicon.

a time dependent leakage current measurement was carried out. Figure 6.3 illustrates the time dependent dc leakage current of c-BZN and m-BZN thin films. In general when a dc bias voltage is applied to dielectric thin films the response current may follow a power law of time dependence known as Curie-von Schweridler law. This power law dependence is either due to the presence of a dielectric relaxation current [11] or an ionic conduction current. It can be clearly observed from the figure 6.3 that the leakage current density is independent of time and hence it cannot be attributed to dielectric relaxation or ionic conduction mechanisms. So the measured leakage current indicates that the conduction process is predominantly electronic. The leakage current density was less for the as deposited films and it was considerably high for the films annealed at higher temperature. For the films annealed at high temperature large number of oxygen vacancies was considered to exist and they produce free electrons according to the equations [12]

$$O_o = V_o^{\bullet\bullet} + 2\bar{e} + (1/2)O_2 \qquad (6.1)$$

where O_o is the oxygen ion in the normal site $V_o^{\bullet\bullet}$ is the oxygen vacancy e^- is the free electrons. Hence the increase of leakage current with annealing temperature can be explained in terms of the formation of oxygen vacancies.

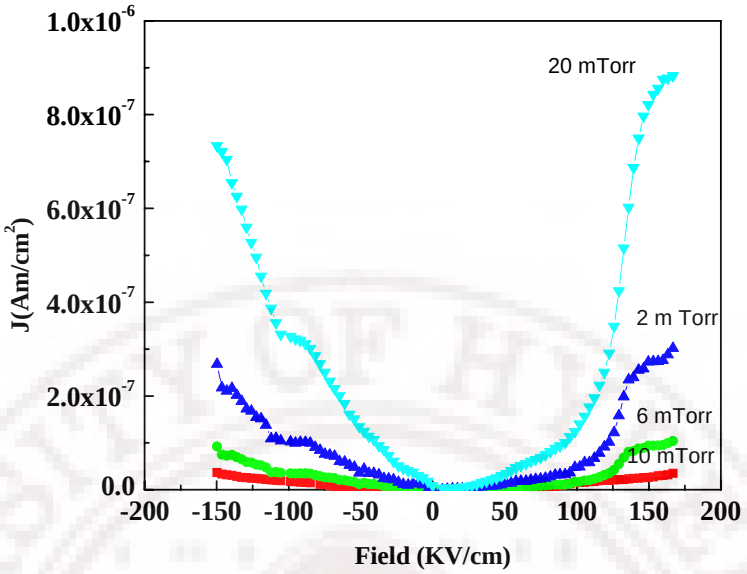

Figure 6.4 Leakage characteristic of m-BZN thin films on Pt coated silicon substrates and deposited at different oxygen pressures.

Similarly the leakage current is found to be higher for the films deposited at smaller oxygen pressures. This is because the films deposited at lower oxygen pressures may have large number of oxygen vacancies which will produce large number of free electrons as given in equation (6.1). It has observed that with slight increase of oxygen pressure the leakage current decreases and this can be attributed to the reduction of oxygen vacancies. However the leakage current is found to be increasing and the film electrical properties are found to be deteriorating for the films deposited at higher oxygen pressures. This may be due to the formation of oxygen interstitial ions at higher oxygen pressures. The oxygen interstitial ions will produce lot of holes which will also affect the leakage characteristics of the films. The formation of the holes due to the presence of oxygen interstitial ions is explained by the following equation [13].

$$1/2\,O_2 = O_i'' + 2h^{\bullet} \qquad (6.2)$$

where O_i'' is the interstitial oxygen ion and h· is the hole produced. So the degradation of the electrical properties of the BZN films deposited at higher oxygen pressures can be explained in terms of the formation of the interstitial oxygen ions.

In addition, these type of films may have additional conduction mechanisms such as interface controlled Schottky emission or bulk limited Poole-Frenkel emission. The field dependent dc leakage current of the c-BZN and m-BZN thin films were measured at

room temperature and it was observed that the film have leakage current densities of $1.05x10^{-6}Am/cm^2$ at an applied field strength of 100 KV/cm. Initially, the leakage current showed an ohmic behaviour for low fields. At slightly higher electric field, there was on set of non-linearity, the cause of which could be attributed to several conduction processes. Like any other polycrystalline sample the deposited films could be thought of a series of grains, grain boundaries and electrode interfaces. The field dependent conductivity of the films is combined response of these three regions. Variation in the influence of these different regions gives rise to the variation of the leakage characteristics. At room temperature, it could be assumed that enough charge carriers were present within the film, so as to contribute to the conduction process and hence a linear field dependence of conductivity could be observed. To analyze the conduction mechanism in the non–ohmic regions, we should obtain similar current voltage characteristics as a function of temperature which is beyond the scope of the present study.

6.3 Low frequency dielectric properties

The low frequency dielectric properties of ceramic thin films are of special importance when they are considered for capacitor applications. The dielectric constant, dielectric loss and bias stability are some of the important factors that decide materials suitability for a specific application [14]. The dispersion in dielectric properties with frequency and applied bias is to be carefully studied for predicting the device performance. In this section we are highlighting the low frequency dielectric properties of c-BZN and m-BZN thin films deposited on various substrates. Based on the nature of substrates we have used different test geometry and techniques for characterizing the dielectric properties. The low frequency dielectric properties of these films which are grown directly on the substrates such as MgO, Fused Silica, $LaAlO_3$ and sapphire (Al_2O_3) are measured using interdigital capacitor (IDC) geometry. Parallel plate metal insulator metal (MIM) capacitors were used for characterizing the dielectric properties of the c-BZN and m-BZN thin films grown on platinised silicon substrate. Metal insulator semiconductor (MIS) capacitor structures used for characterizing the thin films grown on silicon substrates. Details of these characterization techniques are described in chapter 2.

6.3.1 Dielectric properties of BZN thin films grown on different substrates

The substrate effect on the structure and dielectric properties of oxide thin films has attracted attention in recent years [15]. By selecting appropriate substrates, epitaxial strain can be introduced in to the thin films which can alter their dielectric properties. Introduction of ferroelectricity is reported in the case of thin films of $SrTiO_3$ by modulating the epitaxial strain by the usage of appropriate substrate [16]. However the substrate effect to the in plane dielectric properties of c-BZN and m-BZN thin films were not yet studied in detail. The dielectric properties of c-BZN and m-BZN thin films were measured using an interdigitated capacitor (IDC). The IDC capacitors were having a finger length of 90μm, with a total of 8 fingers and an overlap length of 80 μm were designed for this measurements. The finger width and finger gap was made equal and it was 10 μm. These capacitors were fabricated on BZN thin films deposited on LAO, MgO and ALO substrates using standard photolithography and a lift-off process. The frequency dependent dielectric properties of the BZN thin films were measured with an Agilent 4294A impedance analyzer. The details of the measurement techniques are given in chapter 2.

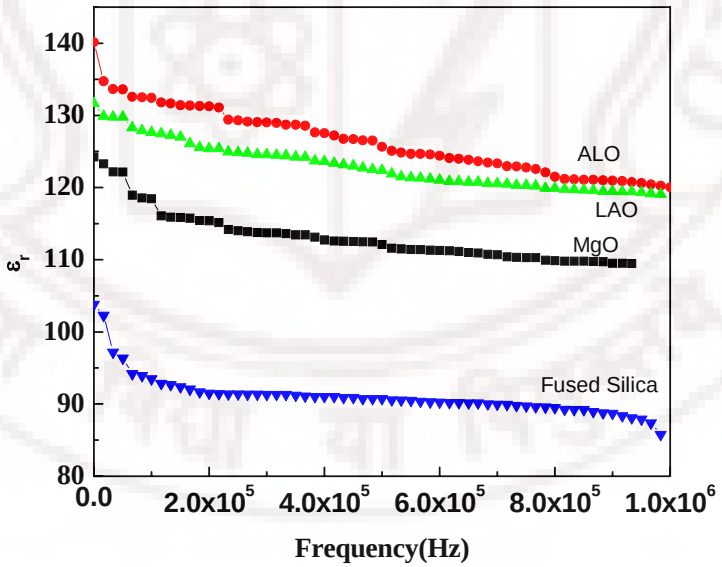

Figure 6.5 Frequency dependent dielectric permittivity of c-BZN thin films deposited on different substrates.

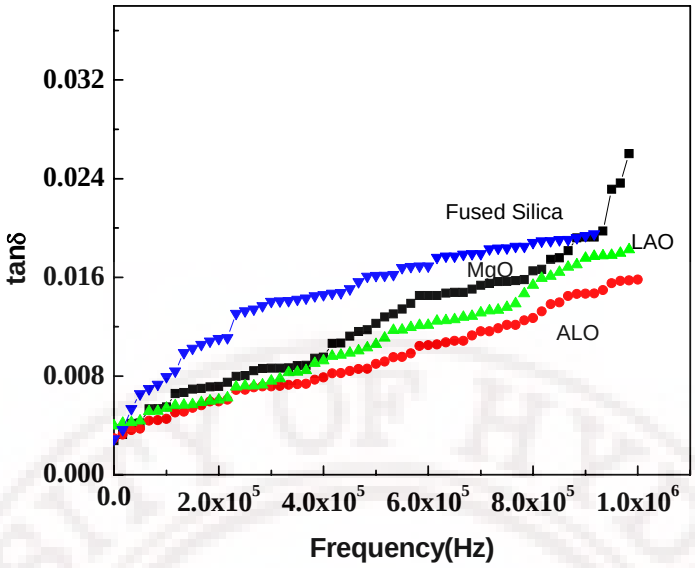

Figure 6.6 Frequency dependent dielectric loss tangent of c-BZN thin films deposited on different substrates.

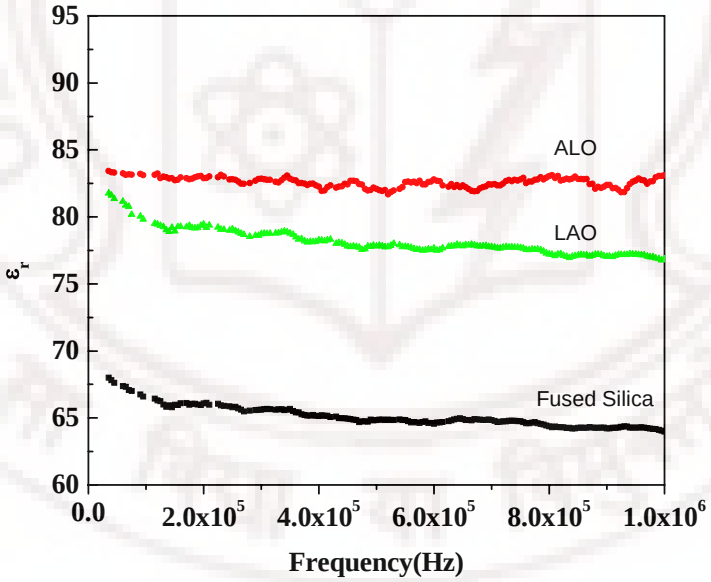

Figure 6.7 Frequency dependent dielectric permittivity of c-BZN thin films deposited on different substrates.

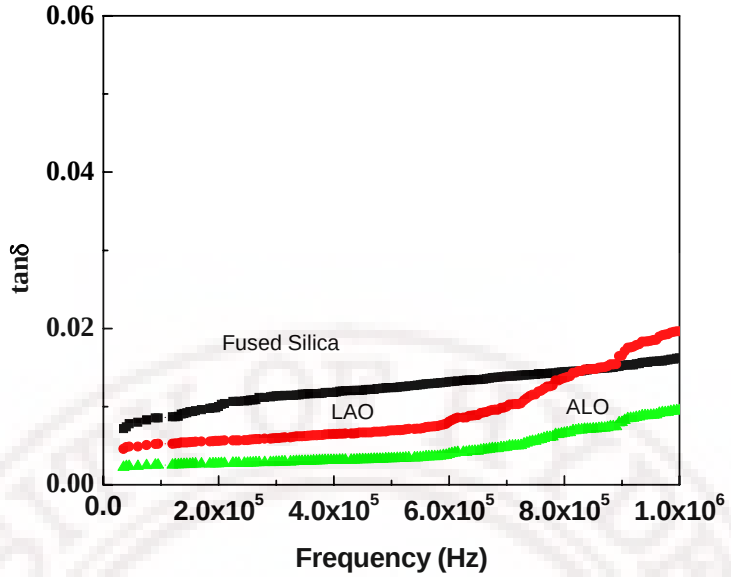

Figure 6.8 Frequency dependent dielectric loss tangent of m-BZN thin film deposited on different substrates.

The variation of dielectric constant and dielectric loss tangent as a function of frequency for c-BZN and m-BZN films deposited on different substrates is given in figures 6.5 to 6.8. The dielectric constant and dielectric loss tangent measured at 1 MHz are 120 and 0.015,119 and 0.018, 109 and 0.026, 85 and 0.031 respectively for the c-BZN thin films deposited on ALO, LAO, MgO and fused silica substrates respectively. Similarly the dielectric constant and dielectric loss tangent at 1 MHz are 83.09 and 0.009, 76.84 and 0.016, 64.9 and 0.06 respectively for the m-BZN thin films deposited on ALO, LAO and fused silica substrates. The dielectric constants of m-BZN thin films are found to be less than that of c-BZN thin films grown on all these substrates. The dielectric loss tangent of m-BZN thin films grown on ALO and LAO substrates are less than that of c-BZN thin films grown on the similar substrates.

The BZN thin films are exhibiting different dielectric behaviour when grown on different substrates. There can be many factors such as crystallinity, microstructure, strain etc which are responsible for this behaviour [17]. The microstructure and strain state of the films plays an important role in the dielectric behaviour. From the micro structural analysis of these films given in chapter 5 sections 5.5, it can be observed that for the films grown on fused silica substrates are having smaller grain size compared to that of the films grown on single crystal substrate. The physical mechanism responsible for the grain size effect on the dielectric constant can be explained as the change of crystal field caused

by the surface bond contraction. It has been proven that the films with nano structured grain morphology has an enhanced crystal field due to its surface bond contraction and rise in the surface area to volume ratio[18]. Decreasing the particle size increases the crystal field and subsequently decreases the dielectric constant.

Apart from this the substrates can modify the physical property of the thin films via inducing strain either by the lattice misfit or by the difference in thermal expansion between the film and the substrate [19]. As a result the properties of thin films can be remarkably different than the intrinsic property of the corresponding unstrained bulk material. This strain some time leads to degradation of films properties also. Even though a careful choice of substrates and growth parameters, strain offers an opportunity to enhance particular properties of a chosen material in thin film form and this is called strain engineering. Strain engineering is a very hot topic in the state of art of dielectric thin film studies since strain is an effective way to change thin films dielectric properties.

Material	**Latice constant(A°)**	**Thermal Expansion coefficient(10^{-6}/K)**
$LaAlO_3$	3.789	9.2
MgO	4.213	12.8
Al_2O_3	4.758	5.91
Fused Silica	---	0.55
c-BZN	10.562	7.92

Table 6.1 Lattice parameter and thermal expansion coefficient of different materials which are under investigation in the present study.

The growth of a polycrystalline thin film on single crystal substrates has to be analyzed in terms of energy minimization. The total energy for any films grown on these substrates can have three components termed as (a) surface energy of the film (b) film substrate interface energy and (c) strain energy [20]. The film should grow such a way that the total energy should be minimized. The interfacial energy minimization favores the growth of epitaxial films on single crystal substrates. In most of the cases the films prefer to grow in a plane parallel to the surface of the substrate which is having the lowest surface energy. The lattice parameter and thermal expansion coefficients of the materials used for the present investigation is tabulated in table 6.1. The films grown on these substrates will be experiencing a stress field caused by the lattice mismatch, thermal expansion mismatch and by the defects presented in the films due to processing. It can be

observed that the lattice parameters of all the single crystal substrates used are found to be less than that of BZN. So on all these substrates the lattice of the films may try to compress near the interfaces to match the smaller lattices of the substrates. Moreover the films grown on MgO and LAO substrates will experience a compressive stress at their substrates film interfaces due to the difference in thermal expansion coefficient. Similarly the films grown on fused silica and sapphire substrates will try to expand during cooling. This shows that there are two competing force factors on all these films affecting the stress state. It is known that the films under tensile stress can have a larger dielectric constant compared to the films with compressive stress [21]. It should be noted that the estimation of the film stress due to film substrate mismatch and thermal expansion coefficient is complicated because of the additional changes in the lattice parameters of the films due to processing

In order to have a better understanding of the nature of stress experienced by these films a detailed investigation of the local atomic structure of the BZN thin films grown on different substrates has to be performed. For this purpose an extensive study of the local symmetry and lattice modes of these thin films grown on different substrates were carried out using Raman spectroscopy and the results are shown in chapter 5. From the Raman analysis given in chapter 5 for c-BZN thin films it is clear that the NbO_6 vibrating mode are located at 783 cm^{-1} for the films grown on MgO substrate and at 790cm^{-1} for the films grown at fused silica substrate. For the lanthanum aluminates and sapphire substrates these modes are coming at 746 and 745 cm^{-1} respectively. Assuming identical composition and overall crystal structure for the films shift in peak positions of the Raman spectra can be interpreted as the results of changes in the local environment of the vibrating ions. Specifically they can point to stiffening of bonds (shorter anion-cation bond distance) resulting in vibration in higher frequency and vice versa (longer bonds means shorter frequencies). The shift towards the higher frequency side in comparison with the mode at 764cm^{-1} of bulk c-BZN in the thin films grown on MgO and fused silica substrate can be attributed to the compression state in the films. Similarly the films grown on LAO and sapphire are in a state of tensile stress. These local environment vibrating atoms can affect all the observed optical and electrical properties of the films. So the reduction of dielectric constant of c-BZN thin films grown on MgO and fused silica substrates can be attributed to the compressive strain in these films. Similarly the Raman analysis of m-BZN thin films grown on different substrates shows that the A_{1g} modes at 849 and 746cm^{-1} shows a red sift or blue shift on various substrates. These modes are

appearing at 848 and 790cm^{-1} respectively for the m-BZN thin films on fused silica. substrate. Similarly for the lanthanum aluminates substrate the modes are appearing at 815 and 753cm^{-1} respectively. For the sapphire substrate the first and second A_{1g} modes are seen at 749 and 833cm^{-1} respectively. Assuming identical composition and overall crystal structure for the films, shift in peak positions of the Raman spectra can be interpreted as the results of changes in the local environment of the vibrating ions [21]. On comparing the second A_{1g} mode which appears to be prominent in the films the films grown on sapphire and lanthanum aluminates seems to have tensile strain, while the film on fused silica are in compressive strain. The dielectric properties given in figure shows that the films grown on fused silica substrates are having smaller dielectric constant compared to that of the films grown on LAO and sapphire substrate. The measured Raman data could explain these variations in dielectric constant.

6.3.2 Dielectric properties of BZN films grown on Pt coated Silicon substrates

The dielectric properties of the c-BZN and m-BZN thin films grown at different oxygen pressures on to the platinised silicon substrates were measured using the parallel plate capacitor structures.

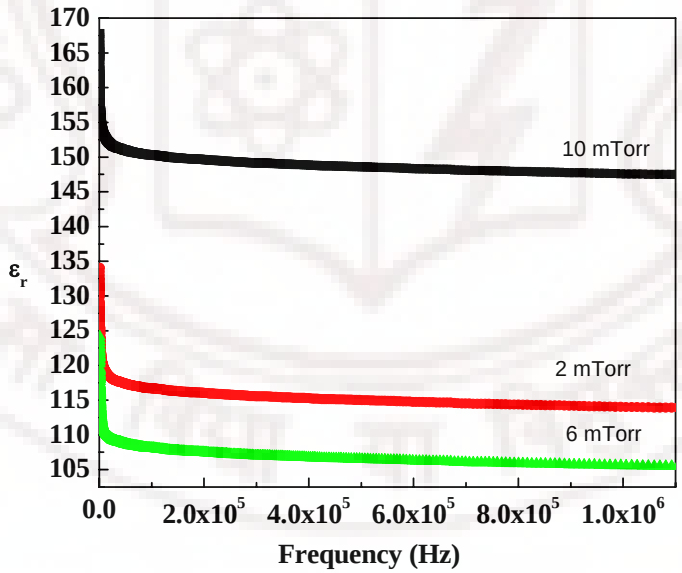

Figure 6.9 Frequency dependent dielectric permittivity of c-BZN thin films deposited at different oxygen pressures.

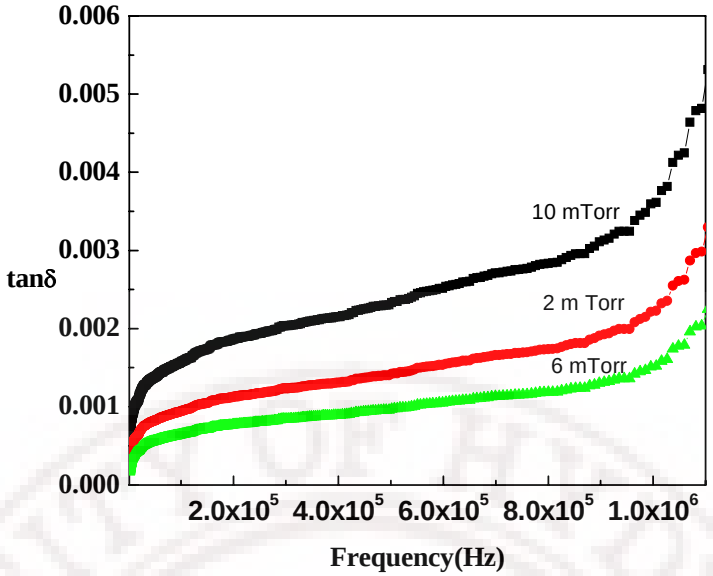

Figure 6.10 Frequency dependent dielectric loss tangent of c-BZN thin films deposited at different oxygen pressures.

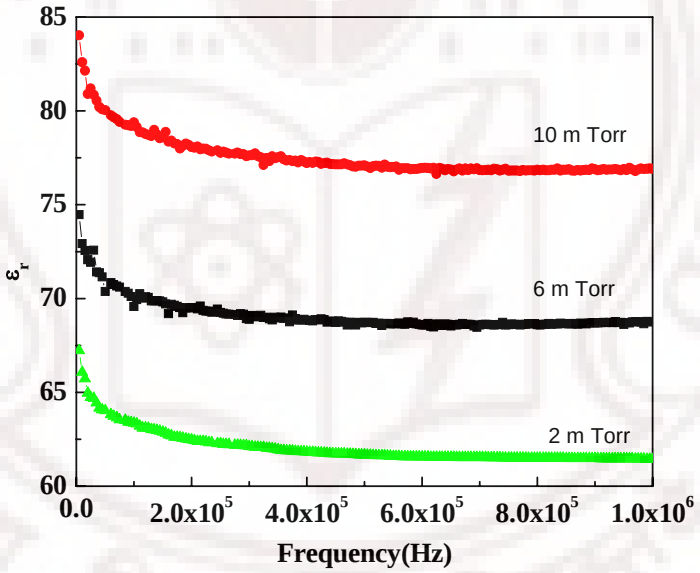

Figure 6.11 Frequency dependent dielectric permittivity of m-BZN thin films deposited at different oxygen pressures.

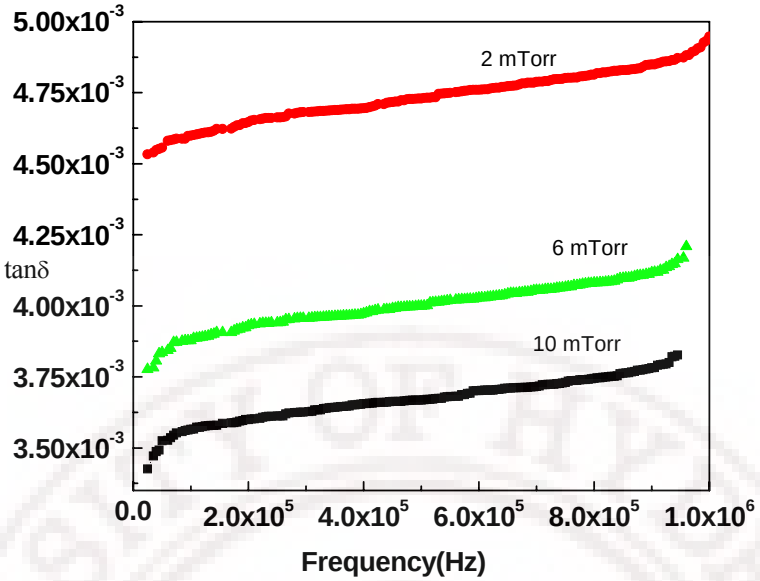

Figure 6.12 Frequency dependent dielectric loss tangent of m-BZN thin films deposited at different oxygen pressures.

The parallel plate capacitors of 80 and 100 μm of top electrode diameters are fabricated using the standard photolithography. Their capacitance and loss tangents were measured using the Agilent 4294A impedance analyzer connected with a DC probe station. The dielectric constant (ε_r) and loss tangent (tanδ) of the c-BZN and m-BZN thin films with respect to frequency are evaluated and are plotted in figures 6.9 to 6.12. From these figures it is clear that the dielectric constant of both c-BZN and m-BZN are decreasing gradually with the increase in frequency. Similarly the dielectric loss found to be increasing with frequency. The dielectric properties of these thin films are found to be quite sensitive to the oxygen pressure. The c-BZN thin films grown under low oxygen pressures of 2 mTorr are found to have a dielectric constant of 125; however it decreased to 105 for the films deposited at 6 mTorr of oxygen pressure. The dielectric constant is found to be increased to 145 for the films annealed at 10 mTorr of oxygen pressure. The dielectric loss is also following the same trend. The higher dielectric constant for the films deposited at low oxygen pressures can be attributed to the presence of oxygen vacancies, since the presence of oxygen vacancies produces quasi dipoles which will increase the total polarizability and hence the dielectric permittivity. The lower value of dielectric constant for the films deposited at 6 mTorr may be the result of reduced number of oxygen vacancies. The increase in dielectric constant for the films deposited at 10 mTorr may be due to large interstial polarization due to the presence of interstitial oxygen

ions. A similar effect was already reported for $Bi_4Ti_3O_{12}$ ceramics [22]. For the m-BZN thin films the dielectric constant is found to be increasing with the increase in oxygen pressure. This may be due to the increasing lattice constant at low oxygen pressures due to the presence of oxygen vacancies in m-BZN thin films because of its monoclinic structure. As the oxygen pressure increases the oxygen vacancies get reduced and hence the lattice constant decreases, this will increase the dielectric constant. In c-BZN thin films the lattice constant change may be negligible due to its cubic crystal structure which is relatively more stable than a monoclinic structure. Similar behaviour is reported for different thin films by H. Wang et al[23].

6.3.3 Dielectric properties of BZN thin films grown on silicon substrates

To study the applicability of c-BZN and m-BZN thin films as gate dielectrics in microelectronic devices and CMOS technology, one has to study the electrical properties of these films in MOS capacitor configuration. To analyse its characteristics one would require a profound understanding of the underlying physics of the MOS structure under various condition [24]. A MOS capacitor has a conducting gate electrode on top of a thin layer of an insulator grown usually on silicon substrate. The high frequency capacitance-voltage(C-V) measurement of a MOS capacitor will show three distinct behaviour under three different regions of operation. They are called accumulation, depletion and inversion phases.

Consider a MOS capacitor on p-type silicon substrates. A negative voltage $-V_g$ applied to the gate would attract the majority carriers (holes) in the substrate to accumulate at the oxide silicon interface, since there is no depletion, the device acts as a resistance in series with a capacitor and the capacitance measured would be simply the capacitance of the oxide layer C_{oX} [25]. If the applied voltage is slowly reduced till it turns positive, the carrier accumulation slowly reduced or the holes in the substrate are pushed away by a positive gate voltage, forming a depletion layer. The flat band capacitance C_{FB} which is a characteristic capacitance of the MOS capacitor can be calculated as

$$\frac{1}{C_{FB}} = \frac{1}{C_{ox}} + \frac{1}{C_D} = \frac{1}{C_{ox}} + \frac{L_D}{\varepsilon_0 \varepsilon_{si}} \tag{6.3}$$

Here C_D is the depletion layer capacitance which is acting in series with the oxide capacitance C_{ox}. ε_0 is the permittivity of free space and ε_{si} is the permittivity of silicon which is taken as 11.7 in our present study. L_D is the Debye length defined as

$$L_D = \sqrt{\frac{\varepsilon_0 \varepsilon_{si} kT}{q^2 N_D}} \tag{6.4}$$

Here N_D is the carrier concentration and q is the electronic charge.

Charge balancing by a –ve charge in the substrate is necessary to account for any positive charge on the gate for charge neutrality. That is,

$$|Q_G| = |Q_D| = N_D L_D \tag{6.5}$$

Where Q_G and Q_D are the number of chargers per unit cm^2 in gate and depletion layer respectively

If the +ve bias of the gate is further increased, the silicon will be inverted from a p- type to n-type. The positive voltage at the gate will attract the minority carriers (electrons) to the interface. The gate voltage at which this happens is called threshold voltage V_{TH}.In this region also the charge at the gate is opposed by an equal charge in the substrate. Hence

$$|Q_G| = N_D L_D + |Q_I| \tag{6.6}$$

Here Q_I is the charge density in the inverting layer. Q_D being lower during depletion the additional gate charge during inversion is balanced by Q_I. The width of depletion layer W_D reaches a maximum value yielding the least capacitance.

The capacitance at the inversion region can be calculated using

$$\frac{1}{C_{\min}} = \frac{1}{C_{ox}} + \frac{1}{C_{D\min}} = \frac{1}{C_{ox}} + \sqrt{\frac{4kT \ln\left(\frac{N_D}{n_i}\right)}{\varepsilon_0 \varepsilon_{si} q^2 N_D}} \tag{6.7}$$

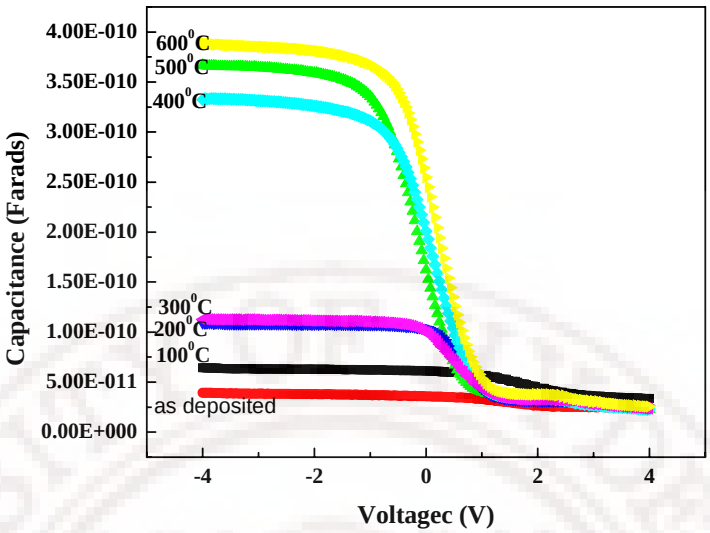

Figure 6.13 C-V characteristics of the MIS structures using c-BZN thin films annealed at different temperatures.

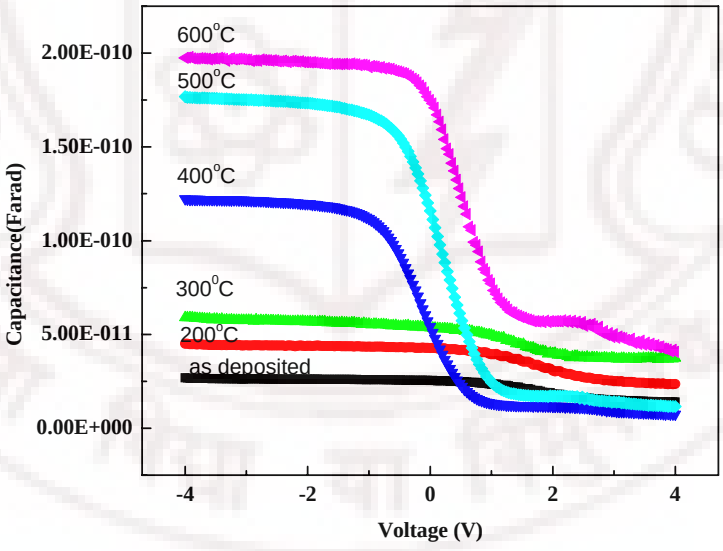

Figure 6.14 C-V characteristic of the MIS structures using m-BZN thin films annealed at different temperatures.

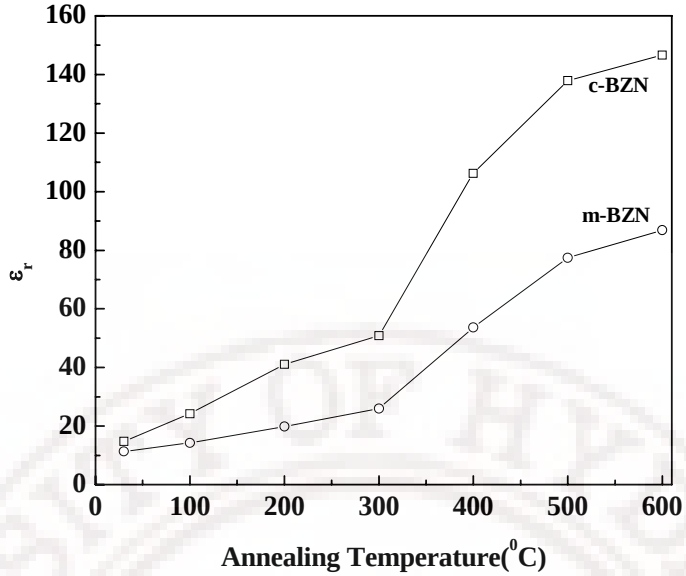

Figure 6.15 Variation of dielectric constant derived from the C-V curves for the c-BZN and m-BZN thin film with annealing temperature.

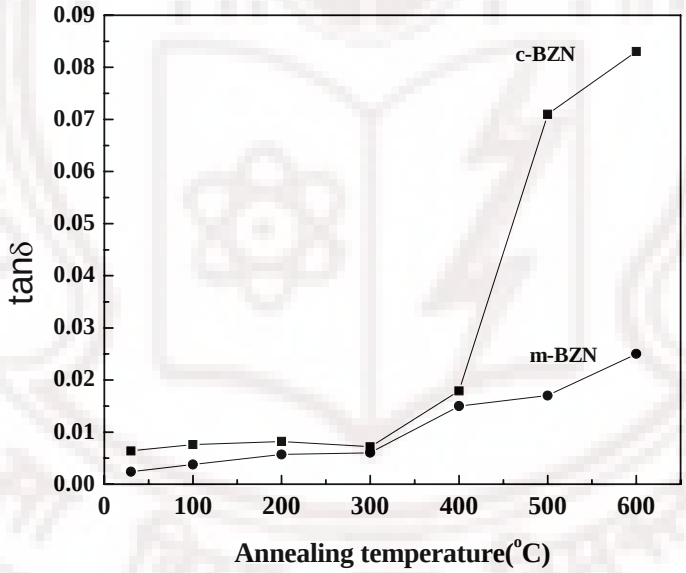

Figure 6.16 Variation of dielectric loss tangent of c-BZN and m-BZN thin film with annealing temperature deposited on p-type silicon substrates.

The high frequency (1MHz) capacitance Vs voltage (C-V) characteristics of the MIS structure using c-BZN and m-BZN thin films are shown in figures 6.15 and 6.16. The C-V behavior shows the typical n-type MOS action showing accumulation, depletion and inversion behaviors at the BZN silicon interfaces. A decrease in accumulation capacitance values was observed for the c-BZN thin films annealed above 400°C at higher voltages. This may be due to the nonlinear dielectric behaviour of the crystalline c-

BZN thin films. The threshold voltage V_{TH} which marks the onset of deep inversion is observed around 3.2 volts for these samples under study. The V_{TH} is found to be decreasing with the increase of annealing temperature for all these samples. The flat band voltage was in between 1.2 to 2 volt depending up on the annealing conditions. The dielectric constant and loss tangent calculated from the accumulation characteristic of the C-V curve is shown in figure 6.16. The dielectric constant and loss tangent of the c-BZN and m-BZN thin films found to be increasing gradually with the annealing temperature. There was a sudden increase of the dielectric properties for the films annealed at 400°C and above. The sudden increase in dielectric properties of these thin films can be attributed to the onset of crystallinity.

6.4 Microwave dielectric properties of BZN thin films

The potential applications of the dielectric thin films in microwave devices have accelerated the research in the development of new materials and the thin film processing methods and optimization. The reliable and reproducible measurements of the dielectric properties of these thin films at microwave frequencies have become an essential requirement of these research activities. The thin films for microwave applications are characterized mostly at a much lower frequencies than their actual frequency of application due to the lack of proper higher frequency characterization techniques. Microwave characterization techniques for bulk materials are well developed field but for thin films there are many challenges. There are not many studies on the microwave dielectric properties of thin films even though it is quite important both in terms of application and academic point of view. In this section a detailed study of the microwave dielectric properties of BZN thin films are presented. The BZN thin films deposited on low dielectric constant substrates were characterized at a few spot frequencies in the X-band using an extended cavity perturbation technique as well as split post dielectric resonator techniques. The broadband microwave dielectric properties of these thin films were measured using calibration comparison techniques. The microwave dielectric properties of these thin films deposited on conducting substrates were characterized using circular patch capacitor techniques. Details of these measurement techniques are described in chapter 3.

6.4.1 Effect of oxygen pressure on the microwave dielectric properties of c- BZN thin films on fused silica substrates

Substrates generally chosen for the growth of thin films meant for microwave applications are sapphire, magnesium oxide, and lanthanum aluminum oxide [26]. These substrates are very costly and generally not readily available in large sizes and hence the entire process becomes expensive. It is already mentioned that fused silica is a well known low cost microwave substrates which can be used for the growth of thin films for microwave applications. There are some reports about the growth and microwave dielectric properties of c-BZN thin films on single crystal substrates. However there are no reports however on the microwave dielectric properties of c-BZN thin films grown directly on to amorphous fused silica substrates. This section describes the microwave dielectric characteristics of c-BZN thin films deposited directly on to fused silica substrates. Microwave measurement of permittivity and loss tangent of the as deposited and annealed BZN thin films were carried out at an X band spot frequency of 12.15 GHz using the extended cavity perturbation technique [27,28]. The details about the measurement techniques are given in chapter 3.

The microwave dielectric constant and loss tangent of the as deposited and annealed BZN thin films measured at a spot frequency of 12.15 GHz are shown in figures 6.17 and 6.18. It is observed that the as deposited amorphous films show low values of dielectric permittivity and loss tangent when compared to that of the annealed crystalline films. The low value of the dielectric constant of these films implies that the formation of the electrical polarization is largely suppressed. Moreover in the amorphous thin films there is no loss associated due to the lattice vibrations. After annealing at 600°C, these films exhibit high dielectric constant. From the figure 6.18 it is observed that there is a strong dependence of the microwave dielectric constant and loss tangent (tanδ) on the deposition pressure. The dielectric constant varied from 95-126 where as the dielectric loss tangent varied from 0.005 to 0.0075. These values were lower than the well-sintered c- BZN ceramic and the thin films grown on single crystal substrates of the same composition [29, 30]. At 6 mTorr of oxygen pressure the dielectric permittivity and loss tangent of the c- BZN films are lower compared with the other two cases. These variations can be explained in terms of the process related changes in the structure, microstructure and the stress presented in the films.

Recently c- BZN thin films were grown on platinised Sapphire substrate by stemmer et.al [31] and they have reported dielectric constant of about 160 and a loss tangent less than 0.001 when measured at microwave frequencies. Thin films of $Bi_{1.5}Zn_{1.0}Nb_{1.5}O_7$, $Bi_{1.5}Zn_{1.0}Nb_{1.5}O_{6.5}$, and $Bi_2Zn_{2/3}Nb_{4/3}O_7$ were prepared via metal organic decomposition method by Thayer et al and their dielectric properties are reported [32]. The c-BZN thin films fired at 750°C are found to be having a dielectric constant (ε_r) of 150 when measured at a frequency of 10 KHz. The $Bi_{1.5}Zn_{1.0}Nb_{1.5}O_{6.5}$ phase is found to be having large dielectric constant compared to that of $Bi_{1.5}Zn_{1.0}Nb_{1.5}O_7$

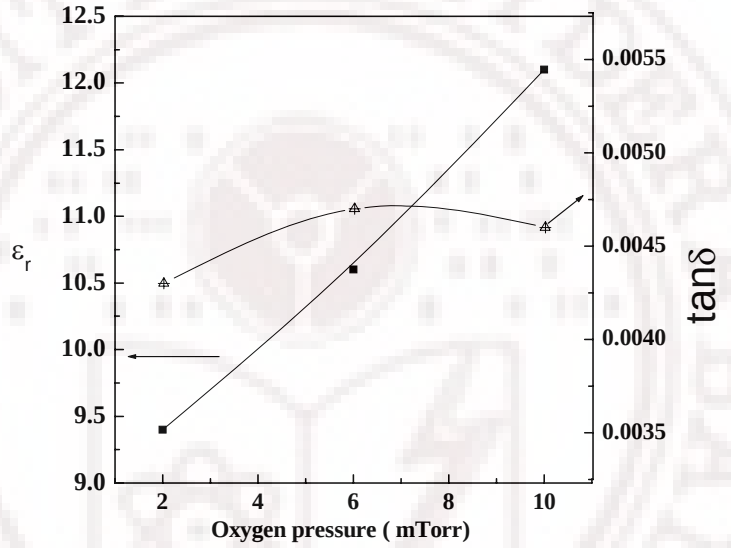

Figure 6.17 Variation of the microwave dielectric properties of as deposited c- BZN thin films with oxygen pressure measured at 12.15 GHz.

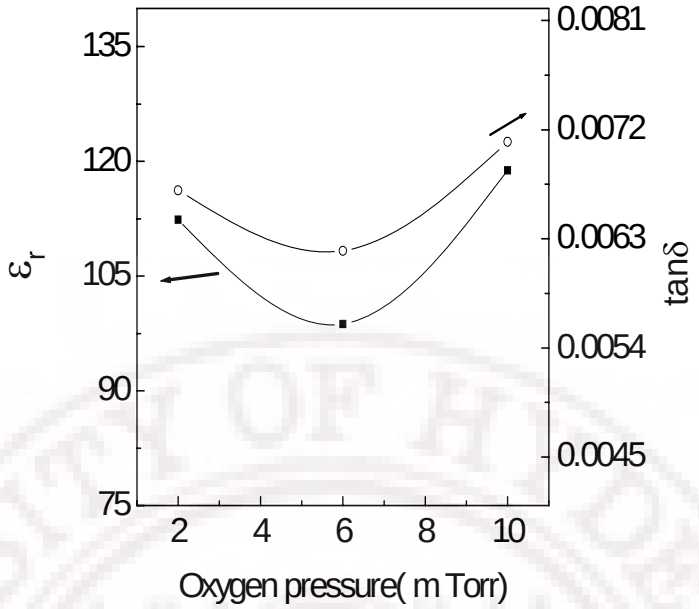

Figure 6.18 Variation of the microwave dielectric properties of annealed c- BZN thin films with oxygen pressure measured at 12.15GHz.

Microstructure, crystallographic texture and strain are factors that affect the dielectric properties of the thin films grown on a substrate. Porosity, which is a consequence of micro structural evolution, has a major role in controlling the dielectric properties of the thin film materials. It is known that relative permittivity decreases with increasing material porosity. Thus controlling the porosity can yield a spectrum of dielectric constants from a single material [33]. Degradation of dielectric constant due to the porous microstructure has been reported for the titanium silicate thin films by Brassard et al [34]. Improvement of the dielectric properties with dense microstructure is reported for $YMnO_3$ thin film by Hiroya et. al [35]. In the films of the current study, the low dielectric constant in comparison with the earlier reported values of BZN thin films can be attributed to the porous microstructure of the films as seen from the AFM images. Moreover recent studies of barium strontium titanate (BST) thin films deposited on various single crystal substrates such as $LaAlO_3$ and MgO indicate that there is a dependence of dielectric permittivity and dissipation factor of these thin films on the substrate type [36]. Dielectric properties of BST thin films on different polycrystalline substrates were studied by Koutsaroff et. al [37] and they also report that there is difference in dielectric properties of films grown on different substrates. They have attributed the difference in dielectric properties to the difference in thermal mismatch between the BST thin films and the substrate. In the earlier reports about the dielectric

properties of the BZN thin films, the films were grown on single crystal substrates. In the current study, the films were grown on amorphous fused silica substrates. The difference in dielectric constant from the earlier reports can also be attributed to the difference of substrates. Fused silica is known to have near zero thermal expansion coefficients. The reduction of dielectric permittivity for the films grown on substrates with smaller thermal expansion coefficient has already been reported [38]. The reduction of dielectric constant of the c-BZN thin films compared to that of bulk can be attributed to the residual stress presents in the films, which can be observed from the X-ray analysis.

The variation in interatomic spacing corresponding to the (222) reflection of the films deposited at different oxygen pressures are tabulated in table 6.2. For comparison, bulk data from Levin et al [39] is presented and used to calculate the relative strain. It can be observed from the table 6.2 that compared with bulk c-BZN, the films deposited on the fused silica substrates deposited at different oxygen pressures shows expanded lattice parameters.

c-BZN Deposition pressure	d-Spacing (A°)	a (A°)	ε_r
2 mTorr	3.052	10.57	112.4
6 mTorr	3.058	10.59	98.7
10mTorr	3.051	10.57	118.8
c-BZN bulk	3.049	10.562	160

Table 6.2 Lattice parameters of the c-BZN thin films deposited on fused silica substrates under different oxygen pressures.

It has already been reported that the compressive stress will result in slightly larger d-spacing than tensile stress. From the table it is clear that the $d_{hkl}^{c-BZN(film)} \langle d_{hkl}^{c-BZN(bulk)}$ for the (222) reflection planes. The film deposited at 2, 6 and 10 mTorr of oxygen pressures shows a change in inter atomic spacing of 0.098%, 0.029% and 0.073% respectively. This implies that the films experience a compressive stress. The films deposited at 6 mTorr of oxygen are experiencing the largest compressive stress while the films deposited at 10 mTorr of oxygen pressure are having the smallest.

The stress in the thin films will induce obvious changes in their dielectric behaviour. The effect of strain on the dielectric polarizability of BST thin films were studied by Tao et al [40]. A compressive stress in the film will decrease the ionic displacement in the field direction and hence decrease it's polarizability. In the current study, the low dielectric constant of the c-BZN thin films grown on fused silica substrates

can be attributed to the compressive stress present in the films. The compressive stress field present in the films will decrease the displacement between the Nb and O ions, which will decrease the polarization, resulting in a decrease of dielectric constant. In the case of crystalline films, those deposited at 6 mTorr of oxygen exhibited a lower dielectric constant compared to other crystalline films deposited at 2 mTorr and 10 mTorr of oxygen pressure. The lower value of the dielectric constant for the films deposited at 6 mTorr of oxygen pressure can be attributed to the large compressive stress present in the films, as evident from table 6.2.

. From the Raman spectral analysis of these thin films deposited on fused silica substrates presented in chapter 5, it is clear that the NbO_6 vibrating mode is located at 790 cm^{-1} for the films grown on fused silica substrate. Assuming identical composition and overall crystal structure for the films', shift in peak positions of the Raman spectra can be interpreted as the result of changes in their local environment of the vibrating ions. Specifically, they can point to stiffening of bonds resulting in vibration at higher frequency and vice versa. The shift towards the higher frequency side in comparison with the mode at 764cm^{-1} of bulk c-BZN in the thin films grown on fused silica substrates can be attributed to the compressive state in the films. So it can be concluded that the reduction of dielectric constant in these thin films compared to that of the films grown on various single crystal substrates is due to the compressive state in the film which in turn reduces the Nb-O bond distance and hence the polarization. Similar observations are reported by Nino et al for the c-BZN films grown on MgO substrates [21].

6.4.2 Effect of oxygen pressure on the microwave dielectric properties of m-BZN thin films

There are relatively few reports about the microwave dielectric properties of m-BZN thin films grown on different substrates even though it has lots of technological interest. In this section the microwave dielectric properties of m-BZN thin films grown on fused silica substrates are discussed in details. Microwave dielectric measurements of permittivity and loss tangent of the as deposited and annealed m-BZN thin films were carried out at an X band spot frequency of 10 GHz using the Split post dielectric resonator technique [41]. This is a non-destructive and accurate technique for measuring the complex permittivity of dielectric substrates and thin films at a spot frequency.

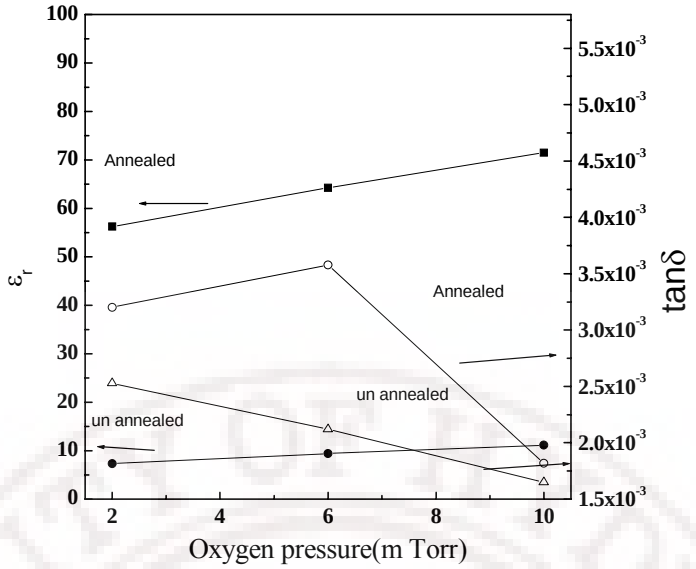

Figure 6.19 Variation of the microwave dielectric properties of as deposited and annealed m-BZN thin films with oxygen pressure measured at 10 GHz.

The microwave dielectric constant and loss tangent of the as deposited and annealed m-BZN thin films measured at a spot frequency of 10 GHz are shown in figure 6.19. From the figure it is observed that there is a strong dependence of the microwave dielectric constant and loss tangent (tanδ) on the deposition pressure. The dielectric constant of the annealed films varied from 56-71 where as the dielectric loss tangent is varied from 1.4 $x10^{-3}$ to 2.5 x 10^{-3} as the pressure varied from 2 to 10 mTorr. The variation in dielectric constant and loss tangent may be due to the process related changes in the structure and microstructure. From the XRD analysis it is clear that the films deposited at 10 mTorr of oxygen pressure is having larger crystallite size as well as smaller strain value compared to the other two films. The Raman analysis of these thin films presented in chapter 5 reveal that the polar distortion got suppressed with increasing oxygen pressure resulting in high dielectric constant and loss as we observed experimentally in Fig (6.19). The intensity and line widths of these Raman modes also showed abrupt changes in thin films deposited at 10 mTorr compared to 2 and 6 m Torr and it reveals that the rigidity of the NbO_6 octahedral cage in BZN thin films have changed with oxygen pressure. As shown in figure 5.28. The A_{1g} Raman mode corresponding to Nb – O – Zn stretching mode (778 cm^{-1}) shows higher frequency with increase in oxygen pressure while the oxygen bending vibration shows decreasing frequency (849 cm^{-1}). It is possible that the oxygen ions are freed from their defect bonding with increasing oxygen pressure, and thereby these are free to oscillate more like

in single crystals resulting in a reduction of the oxygen bending mode vibration frequency. However the Nb – O – Zn stretching mode becomes more rigid. The dielectric response of the oxygen octahedra based structures are increased when the octahedra are aligned, as this configuration increases the local Lorentz field factor of the metal ion inside the octahedra. A stiffening of this mode could mean an alignment of the octahedra resulting in higher values of dielectric constant as it could be seen in the present study. With more oxygen vacancies removed, the octahedra could be offering tight cages to the metal ions they contain, making the amplitude of the lattice vibrations containing B-ion smaller, keeping it within its harmonic limits and resulting in a lower value of dielectric loss as observed. So the improvement of dielectric properties at higher pressures could be attributed to the reduction of oxygen vacancies with the increasing oxygen pressure.

6.4.3 Effect of annealing temperature to the microwave dielectric properties of BZN thin films

The dielectric properties at microwave frequencies are found to be strongly affected by post deposition annealing temperature and duration. Hence a detailed study is required to understand the effect of annealing temperature on the microwave dielectric properties of c-BZN and m-BZN thin films. As explained earlier, the films were deposited on to fused silica substrates using pulsed laser deposition. In order to study the influence of annealing temperature the samples were annealed in air at different temperatures from 200°C to 800°C. The microwave dielectric measurements of permittivity and loss tangent of the as-deposited and annealed c-BZN and m-BZN thin films were carried out at a X-band spot frequency of 10GHz using a split post dielectric resonator techniques. The details about the measurement techniques are given in chapter 3. The measured dielectric constant (ε_r) and loss tangent ($\tan\delta$) of the m-BZN and c-BZN thin films as a function of annealing temperature are given in figures 6.20 and 6.21.

It can be observed from the figure 6.20 that the as-deposited films and the films annealed up to 300°C shows a low value of dielectric permittivity and loss tangent. There is a sudden increase of dielectric permittivity and loss tangent for the films annealed at 400°C and above. The dielectric permittivity was decreasing slightly for the films annealed above 700°C. According to the Clausius-Mosotti (C-M) relation [42] the theoretical dielectric constant of oxide components could be calculated as follows.

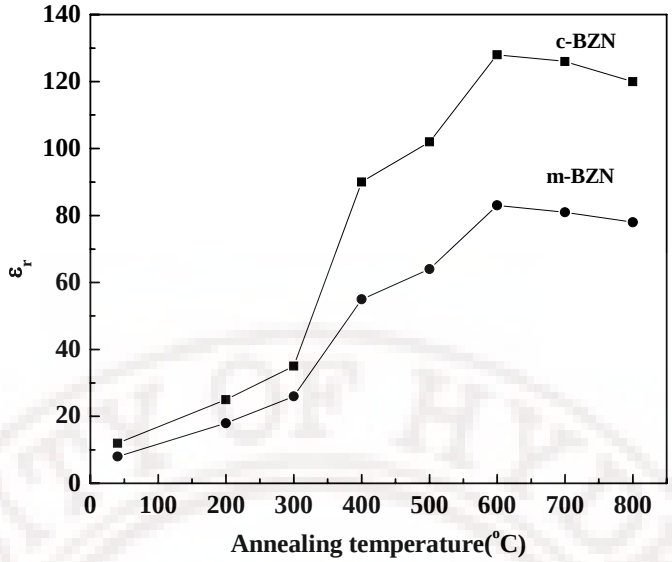

Figure 6.20 Variation of the microwave dielectric constant of c-BZN and m- BZN thin films as a function of annealing temperature, measured at 10 GHz.

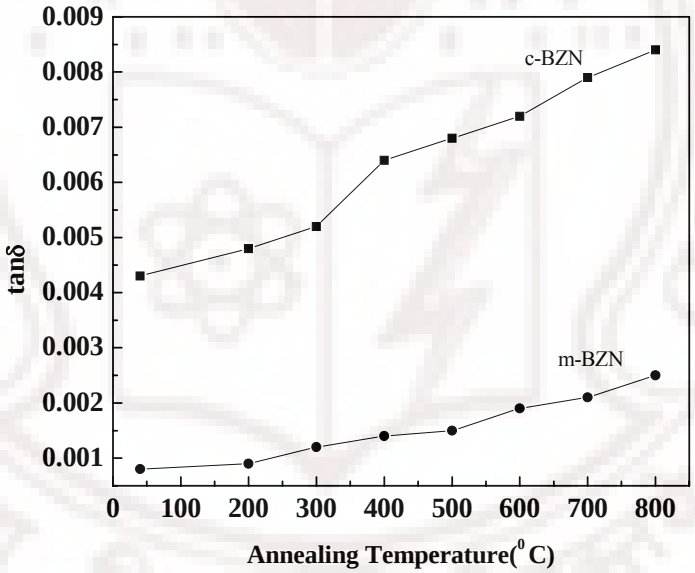

Figure 6.21 Variation of the microwave dielectric loss tangent of c-BZN and m- BZN thin films as a function of annealing temperature, measured at 10 GHz.

$$\varepsilon_r = \frac{3V_m + 8\pi\alpha_D}{3V_m - 4\pi\alpha_D} \tag{6.8}$$

Where V_m is the molar volume in $A^{\circ 3}$ and α_D is the sum of polarization of the constituent ions in the c-BZN and m-BZN. The total ionic polarizability of the c-BZN and m-BZN can be calculated in terms of the ionic polarizabilities of the constituent atoms according

to Shannon's theory [43,44]. The predicted dielectric constant for c-BZN ceramics was 144 and m-BZN ceramics was 88 [45].

From the X-ray diffraction studies presented in Chapter 5, it is clear that the as-deposited films and the films annealed below 400°C are all amorphous. In the amorphous phase, the observed dielectric constant of these thin films is found to be less than that of the predicted values using the C-M theory. The lower dielectric constant can be attributed either to the change in polarizabilities or to the change in the cell volume. The ionic polarizabilities of the constituent atoms of the BZN thin films will be the same in the amorphous and crystalline states. Hence the total molecular polarizability will remain the same. So the deviation from the predicted value is because of the possible increase in the molar volume V_m due to the amorphous nature of the films. On annealing the film, packing density, grain size and the crystallinity starts improving; this will result in an increase in dielectric constant. The slight decrease in dielectric constant for the films annealed above 700°C may be due to the formation of oxygen vacancies in the film, which in turn change the lattice parameters. Another possible reason for the decrease in dielectric constant at high temperature can be the thermal strain developed in the film due to the difference in thermal expansion coefficients of the substrate and the film. It is observed that the amorphous thin films have a lower dielectric loss when compared to that of the crystalline thin films. This is because the amorphous films will have low intrinsic losses due to the absence of lattice modes. As the film crystallizes, it generates a lattice potential which will allow the phonon- phonon interactions and there by opening up many loss mechanisms [46]. The probing microwave field will couple to these phonon modes and thereby increases the dielectric losses. The further increase in dielectric losses for the films crystallized at higher temperatures could be extrinsic in origin. This can be attributed to the formation of oxygen vacancies in the films annealed and are one of the most dominant defect centers in oxide films. These defects will absorb the microwave photons by the generation of acoustic phonons that will increase the dielectric losses.

6.4.4 Broadband microwave dielectric properties of BZN thin films on fused silica substrates

The dielectric properties of c-BZN and m-BZN thin films deposited on fused silica substrates were characterized for a range of frequencies. Coplanar waveguide test structures were used for the experimental evaluation of the BZN thin films grown on fused silica substrates. The test structures were fabricated on bare substrates as well as on

the films deposited. The test samples were characterized for determination of the attenuation and phase constant with and with out the BZN thin films.

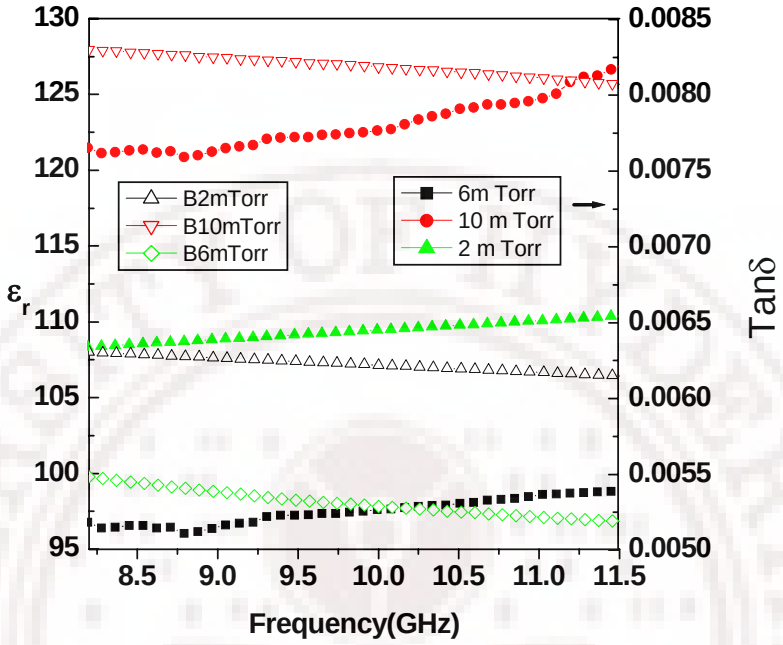

Figure 6.22 Broadband microwave dielectric properties of c-BZN thin films deposited on fused silica substrates.

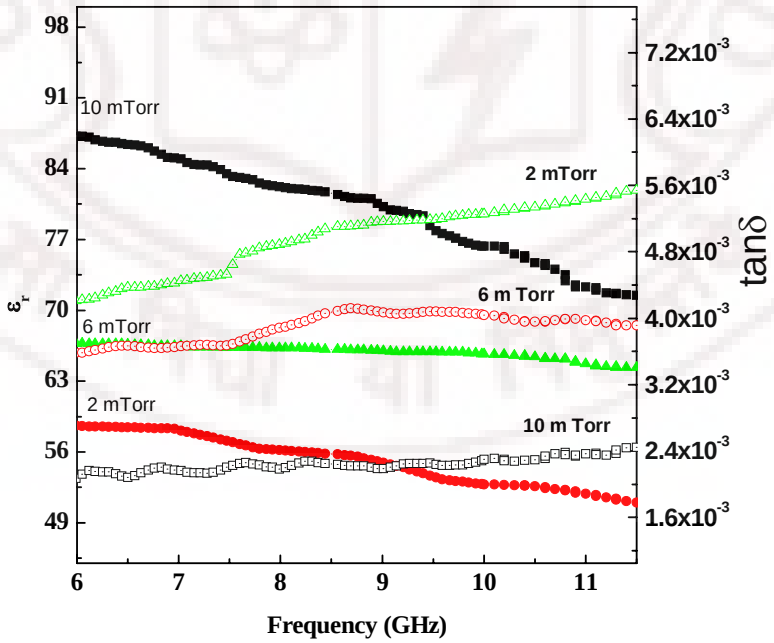

Figure 6.23 Broadband microwave dielectric properties of m-BZN thin films deposited on fused silica substrates.

The measured dielectric properties of the c-BZN and m-BZN thin films were shown in figures 6.22 and 6.23. The microwave dielectric permittivity of c-BZN was found to be varying between 126 and 124 for the films deposited at 10 m Torr of oxygen pressure and it is varying between 98-96 for the films deposited at 6m Torr of oxygen pressure over the X band range of frequencies (8.24-12 GHz). Corresponding dielectric loss tangents are found to be varying from 0.007 to 0.0085 and from 0.005 to 0.006 respectively. The permittivity exhibited a nearly frequency independent characteristic, while the loss tangent slightly increased with the increase in frequency. This kind of increase in loss tangent without a considerable change in the permittivity can be attributed to the conductor loss contribution arising from the printed transmission lines on these films deposited for the purpose of measurements [47].

The microwave dielectric permittivity of the m-BZN thin films deposited at 10 mTorr of oxygen pressure is found to be varying between 89 to 71 in the measured frequency range. Similarly, the loss tangent is found to be increasing with the increase of frequency. The films deposited at 6 mTorr of oxygen pressures were having a dielectric constant varying between 66 to 64 and a loss tangent varying between 0.0039 to 0.0054.

The observed dispersions in the dielectric properties of these thin films at microwave frequencies may not have their origin in an intrinsic mechanism. Rather, it is thought to be originating from extrinsic factors such as the test structures used for the measurements. Although the use of calibration comparison technique eliminates most of the parasitic components and reveals the real capacitance and conductance per unit length of the CPW lines over the films, there may still remains some small un compensated inductance and resistance due to the interfaces. The interface of the metal films sitting on top of the films and that sitting on top of the bare substrates will be slightly different and this could lead to some un compensated resistance or inductance. This may be the reasons for the observed variations of the dielectric constant and loss tangents of the c-BZN and m-BZN thin films grown on amorphous fused silica substrates. So it can be assumed that both c-BZN and m-BZN thin films exhibit nearly frequency independent dielectric properties over the measured microwave frequency range. The relatively low losses and frequency independent dielectric constant over this broad frequency range proves that these thin film materials can be used for realizing high Q and frequency stable microwave devices.

6.4.5 Microwave dielectric properties of BZN thin films on single crystal substrates

It has been stated earlier that the major focus of this thesis is to study the microwave dielectric properties of BZN thin films grown on fused silica substrates. However BZN thin films were also grown on single crystal substrates under the optimized conditions for a comparative study. This section presents the broadband microwave dielectric properties of c-BZN and m-BZN thin films grown on different single crystal substrates.

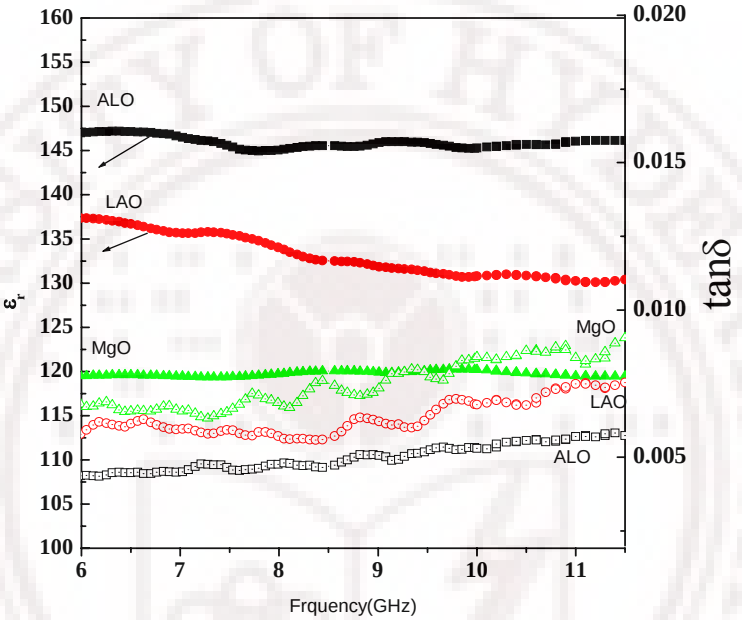

Figure 6.24 Broadband microwave dielectric properties of m-BZN thin films deposited on different substrates.

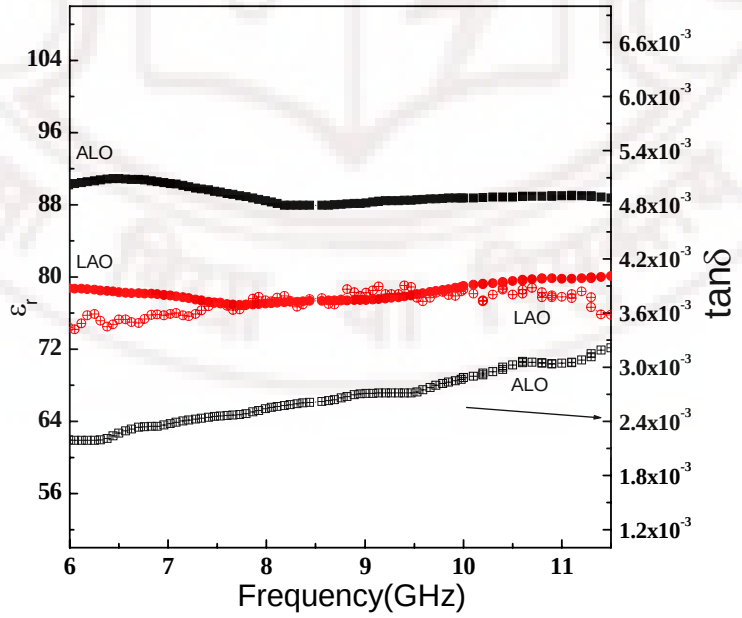

Figure 6.25 Broadband microwave dielectric properties of m-BZN thin films deposited on different substrates.

The broadband microwave dielectric properties of c-BZN and m-BZN thin films grown on single crystal substrates are given in figures 6.24 and 6.25. From these figures it is clear that the dielectric properties at microwave frequencies are strongly affected by the substrate type. The c-BZN thin films grown on sapphire substrate was having a larger dielectric constant while the films grown on MgO substrates were having lower dielectric constant values. The m-BZN thin films also showed the similar type of behaviour. It is already known that the substrates can modify the physical property of the thin films by inducing strain either by the lattice misfit or by the difference in thermal expansion between the film and the substrate. As a result, the properties of thin films can be remarkably different than the intrinsic property of the corresponding unstrained bulk material [48]. Here the observed difference in broadband microwave dielectric properties of these thin films grown on different substrates can be attributed to the differences in local symmetry in these thin films originated from the strain. The detailed Raman analysis on these thin films presented in chapter 5 already showed that the local symmetry is different in these films and the films are having different strain states. An analysis on the substrate effects on low frequency dielectric properties were already presented in section 6.3.1.

6.5 Electric field dependent dielectric properties of c-BZN thin films

It is already mentioned that many modern microwave applications demands dielectric materials whose dielectric permittivity can be varied as a function of the applied electric field. One of the most effectively used materials for this application is barium strontium titanate [49]. However the thickness dependent dielectric permittivity and the polarization and stoichiomectry dependent dielectric characteristics are considered to be the major drawbacks of this material [50]. The c-BZN thin films are now being explored by many researchers as an alternative candidate for BST thin films for frequency agile microwave devices. c-BZN thin films have got low losses, high dielectric constant which is less affected by the thickness and stoichiomectry. The dielectric characteristics of the c-BZN thin films were reported in the previous sections. In this section, the voltage dependent dielectric characteristics of the c-BZN thin films are systematically investigated as a function of frequency and electric field.

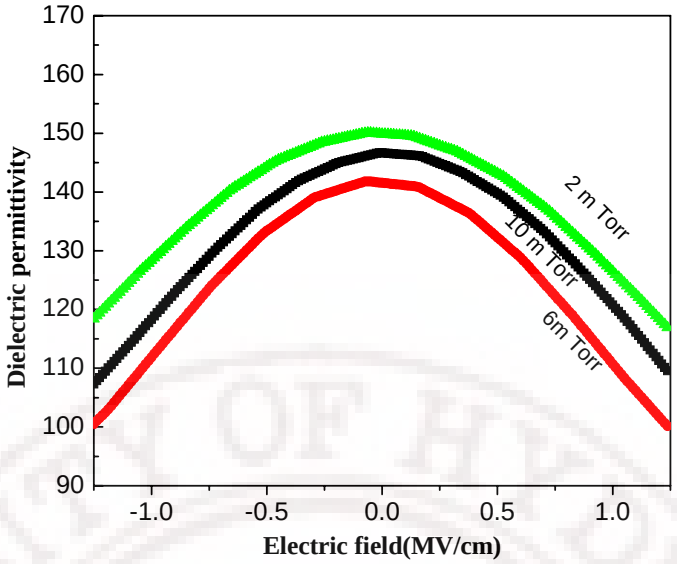

Figure 6.26 Electric field dependent dielectric permittivity of c-BZN thin films deposited on Pt-coated silicon substrates deposited at different oxygen pressures and measured at 1MHz.

Figure 6.26 shows the field dependent permittivity characteristic of the c-BZN thin films deposited on platinum coated silicon substrates. The c-BZN thin films were having a thickness of about 200 nm and the top electrode diameter was 100 micrometers. It has seen that the films deposited at low oxygen pressures were having larger dielectric constant and the dielectric constant reduces with the increase of oxygen deposition pressure. It is already known that the number of oxygen vacancies and the unit cell volume plays an important role in determining the dielectric properties. An increased number of oxygen vacancies will increase the number of dipoles associated with oxygen vacancies which in turn increases the total polarizability. The increased dielectric constant of the c-BZN thin films deposited at lower oxygen pressure can be attributed to the presence of oxygen vacancies in the films. The Q value of the c-BZN capacitors deposited at different oxygen pressures is given in figure 6.27. It has seen that the films deposited at 10 mTorr of oxygen pressure is having a Q value of 280, which is high compared to other tunable thin film materials. The Q value of the c-BZN thin films deposited at 6 mTorr and 10 mTorr oxygen pressures shows field independent characteristics, while the Q value of the film deposited at 2 mTorr of oxygen pressures shows a field dependent characteristics. The Q value is found to be decreasing as the bias field increases. This behaviour may be thought of originating from the field induced hopping of conduction through the films which in turn increases the dielectric loss and results in the reduction of the Q value. It has already seen in section 6.1 that the films

deposited at low oxygen pressures are having large leakage currents at high voltages, this leakage conduction will lead to the increase of dielectric loss. The measured field dependent characteristics of the c-BZN thin films shows that these materials can be used for voltage tunable devices.

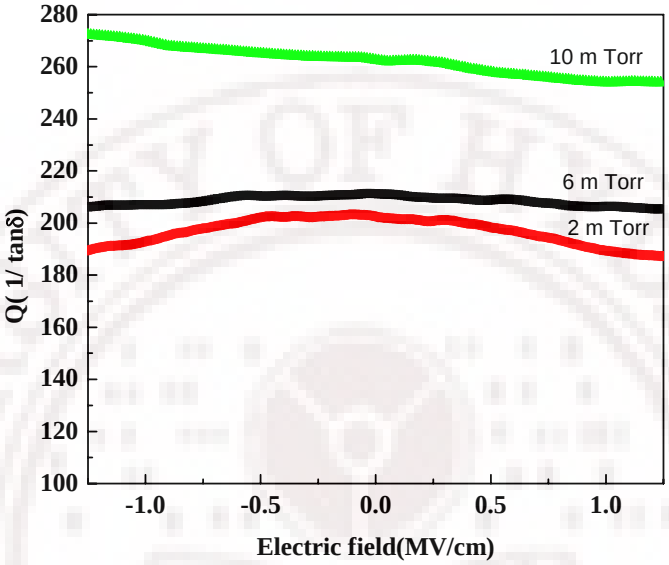

Figure 6.27 Electric field dependent dielectric quality factor of c-BZN thin films deposited on Pt-coated silicon substrates at different oxygen pressures and measured at 1MHz.

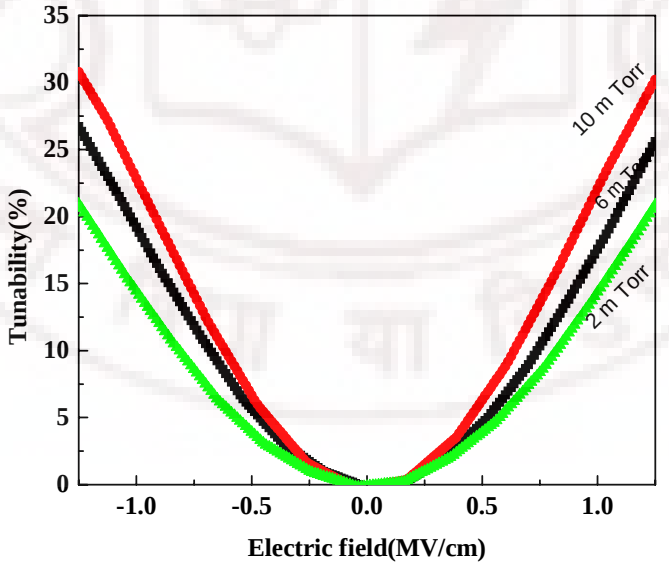

Figure 6.28 Electric field dependent dielectric tunability of c-BZN thin films deposited on Pt-coated silicon substrates measured at 1MHz

The bias field dependent tunability of the capacitors fabricated using the c-BZN thin films deposited under different oxygen pressures is shown in figure 6.28. The c-BZN thin films deposited at 2 mTorr of oxygen pressure was having a tunability of 20% and the films grown at 10 mTorr of oxygen pressure was having a tunability of 30% in an applied dc electric field of 1.25 MV/cm at a measurement frequency of 1 MHz. A tunability of 55% has been reported for the c-BZN thin films on pt coated Al_2O_3 substrates by Lu and stemmer [51]. The maximum electric field used by them was 2.4MV/cm. For our experiments we have used only an electric field of 1.25 MV/cm much lower than the field used by Lu et al. Here we are also expecting much higher tunability with an increasing DC electric field. From these results it can be clearly says that the c-BZN thin films grown around 10mTorr of oxygen pressure is having relatively high tunability with high quality factor a combination suitable for tunable microwave devices. The quality factor for the thin films deposited above 10mTorr of oxygen pressure is found to be decreasing. This may be due to the leakage conduction produced due to the interstitial oxygen atoms as explained in section 6.2

The frequency dependent microwave dielectric properties of c-BZN thin films deposited on to sapphire and fused silica substrates measured under different bias voltage are shown in figures 6.29 to 6.30.

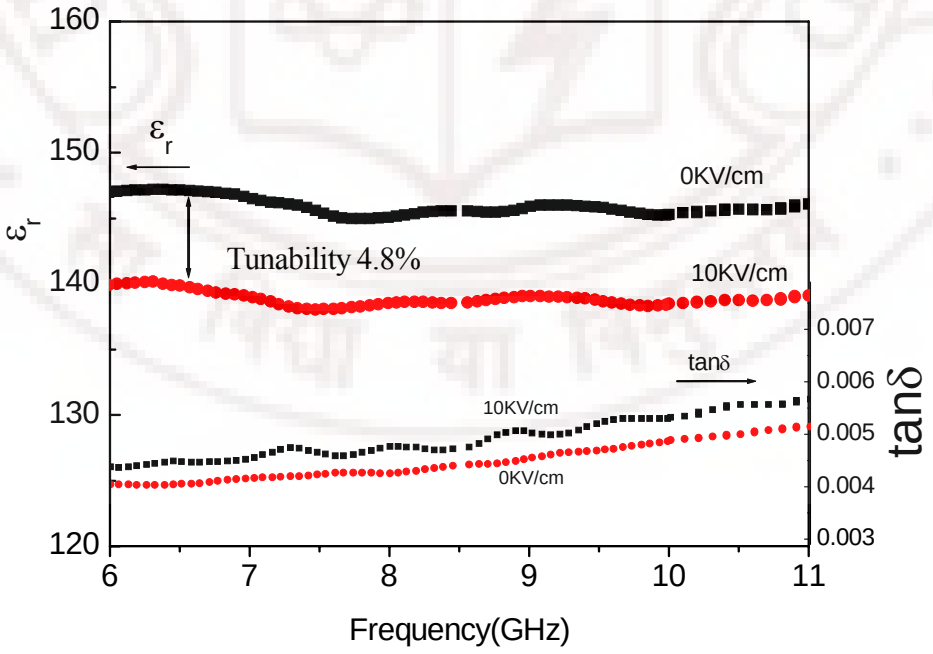

Figure 6.29 Voltage dependent broad band microwave dielectric permittivity of c-BZN thin films deposited on sapphire substrates.

.

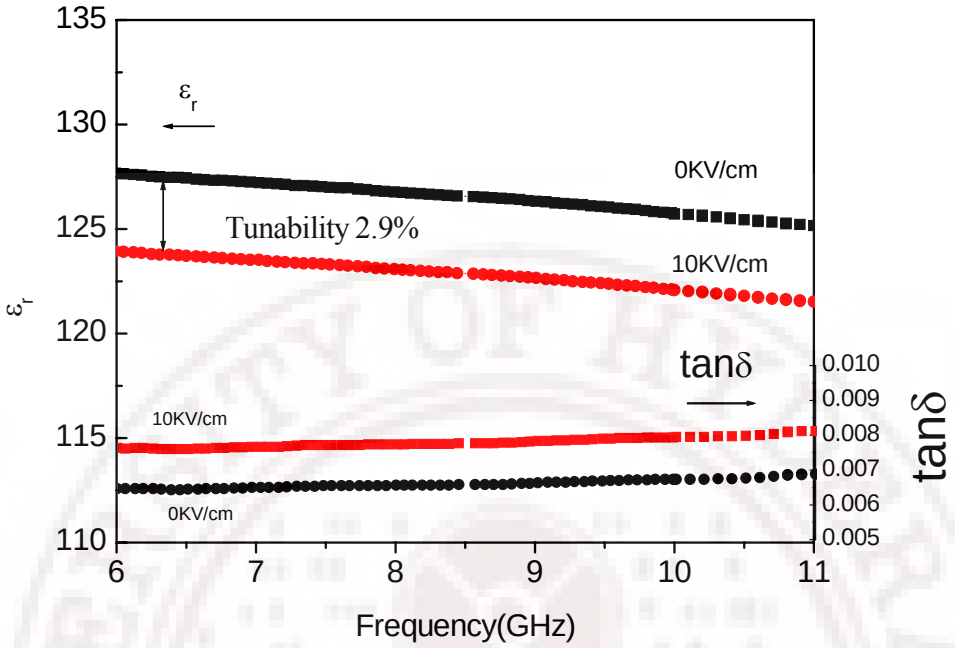

Figure 6.30 Voltage dependent broad band microwave dielectric properties of c-BZN thin films deposited on fused silica substrates.

The calculated dielectric permittivity (ε_r) at 10GHz for the c-BZN thin films grown on sapphire is 145.29(at zero bias) and 138.49 (at 10KV/cm bias). The calculated tunability is approximately around 4.8%. The loss tangent of the film at 10GHz was estimated to be approximately 0.0049 at 10KV/cm. Similarly the calculated dielectric permittivity for the c-BZN thin films grown on fused silica is 125.73 (at zero bias) and 122.07 (at 10KV /cm bias field). The estimated tunability for c-BZN films on fused silica substrate was 2.91% at a measurement frequency of 10 GHz. It could be seen that the magnitude of the measured tunability of these films are found to be apparently less compared to the reported values of tunability at lower frequencies. This is because of the applied bias voltage of 100V across the ground and central conductor of the CPW lines was only able to produce a field of around 10 KV/cm in our test structures. We could not go to higher fields because of the limitation of the bias tees used. The tunability around 50% is reported for these films at much higher fields (around 1.5MV/cm). Interestingly the films grown on fused silica substrates is also exhibiting tunability and very low losses which can be explored further for many low cost microwave devices. This is one of the important results of the present work.

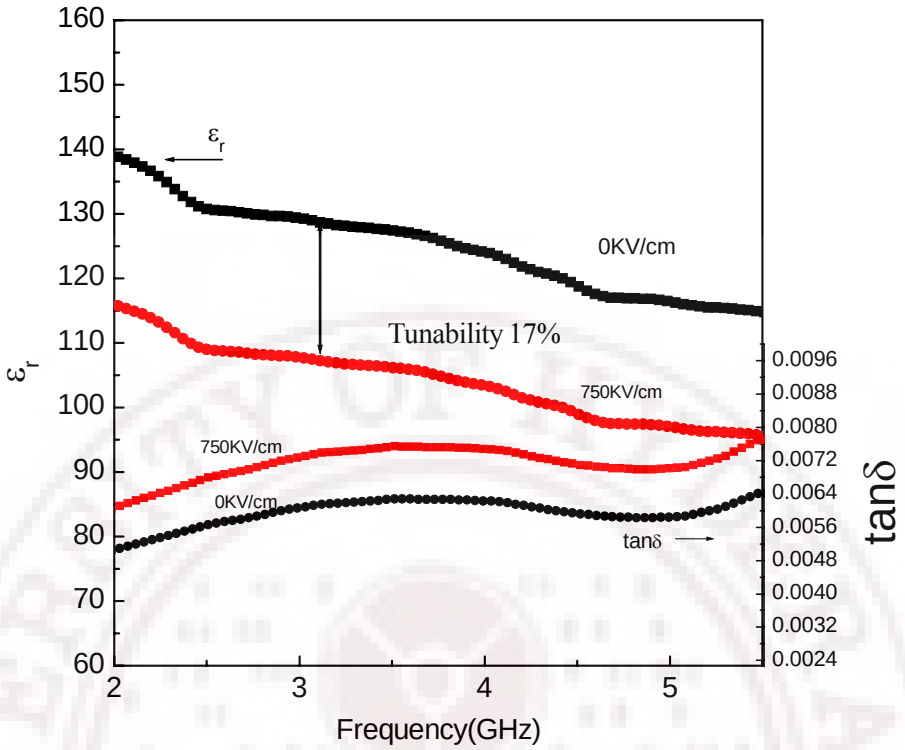

Figure 6.31 Voltage dependent broadband microwave dielectric permittivity of c-BZN thin films deposited on platinum coated silicon substrates.

The dielectric properties and tunability of the c-BZN thin films deposited on to the platinum coated silicon substrates are measured using the circular patch capacitor techniques. It consists of a disk shaped capacitor and an outer capacitor, surrounding it as shown in figures 3.10 in chapter 3. In order to remove the effect of the outer capacitor the measurements were carried out on two test structures which had the same outer diameter with different inner diameters. The complex dielectric permittivity of the c-BZN thin films calculated from the measured S_{11} of the CPC structures is shown in figures 6.31.

The measured dielectric permittivity results at 5 GHz shows that the films are having a dielectric constant of 116 with out any bias field. The dielectric constant has got changed to 96 with a bias voltage of 15V (field strength 0.75MV/cm). These results confirm that the films are having fairly high tunability at microwave frequencies also. The calculated tunability for the c-BZN thin films deposited at 10 mTorr of oxygen pressure was around 17% at 5GHz. The obtained tunability value is found to be numerically higher than that obtained for the c-BZN thin films grown on single crystals substrates and fused silica substrates because CPC being a parallel plate capacitor geometry, the field strength seen by the film is much higher in this configuration(0.75MV/cm vs. 10KV/cm).

6.6 Realization of tunable varactors

Varactors are the basic tunable circuit elements in the microwave circuits based on tunable dielectric thin films [52]. Two different approaches are available for the realization of tunable varactors based on the voltage dependent dielectric materials. The first approach is to place the tunable dielectric thin films between the top and bottom electrodes and the second approach is to fabricate a set of interdigitated electrodes on top of the tunable dielectric thin films [53]. In this section we describe the realization and characterization of parallel plate and interdigitated varactors using c-BZN thin films.

6.6.1 Inter digitated and parallel plate varactor realization

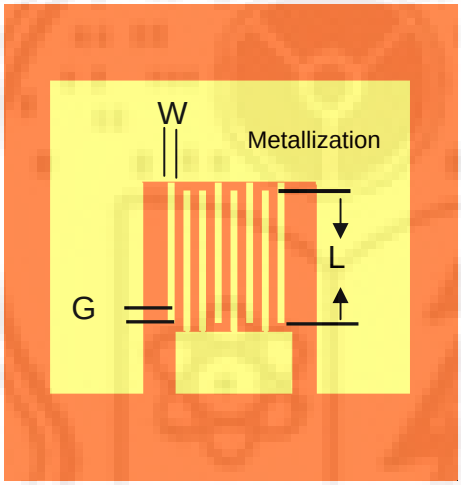

Figure 6.32 Schematic diagram of the interdigitated varactor in the GSG configuration.

A schematic diagram of a typical interdigitated varactor is shown in figure 6.32. For the interdigitated varactor fabrication, the c-BZN thin film is deposited directly on to the substrate and the electrode metallization is patterned on top of the c-BZN thin films. In the interdigitated varactors the minimum gap between the electrodes can be up to 2-3 micrometers using the standard photolithographic techniques available at our university. Each IDC varactors realized in the present study was having six pairs of interdigital electrodes having a width (W) of12 μm and a gap (G) of 8μm with an overlapping length (L) of 320μm. These varactors were designed in such a way that it can be probed using a ground signal ground (GSG) probes of 250 um pitch.

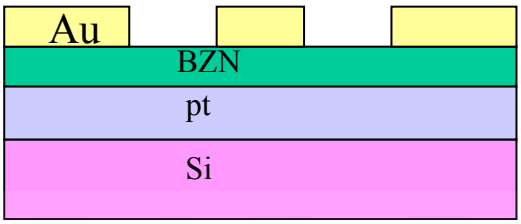

Figure 6.33 Schematic diagram of the parallel plate varactor in the CPC configuration.

The schematic diagram of the parallel plate c-BZN varactor in CPC configuration is shown in figure 6.33. In this configuration the bias field is applied across the thickness of the film resulting in a lower bias voltage requirement compared to that of interdigitated capacitor. An advantage of the parallel plate approach is that the integration of tunable components on industrially important Si substrate can be achieved easily. For the characterization purpose we have designed a parallel plate varactor having circular patch capacitor geometry (CPC). The inner circular patch was having diameters of 80,100 and 120 μm while the outer circular ring was having a diameter of 300μm. The outer circular patch will acts as a virtual RF ground for the device. These devises were characterised using the GSG probes of 250μm pitch.

Standard photolithography and metal lift off process was used to define the structure of the interdigital capacitors (IDCs) on the BZN coated fused silica substrates as well as the parallel plate varactors having the circular patch capacitor (CPC) structures on platinised silicon substrates. *I* line positive photo resist from Arch chemicals was used to make a thick layer of photo resist of about 1micron thick. After the standard UV exposure and development of photo resist, 0.5 μm thick gold electrodes were deposited by RF magnetron sputtering at room temperature followed by a lift off process to remove the metals in the unwanted places.

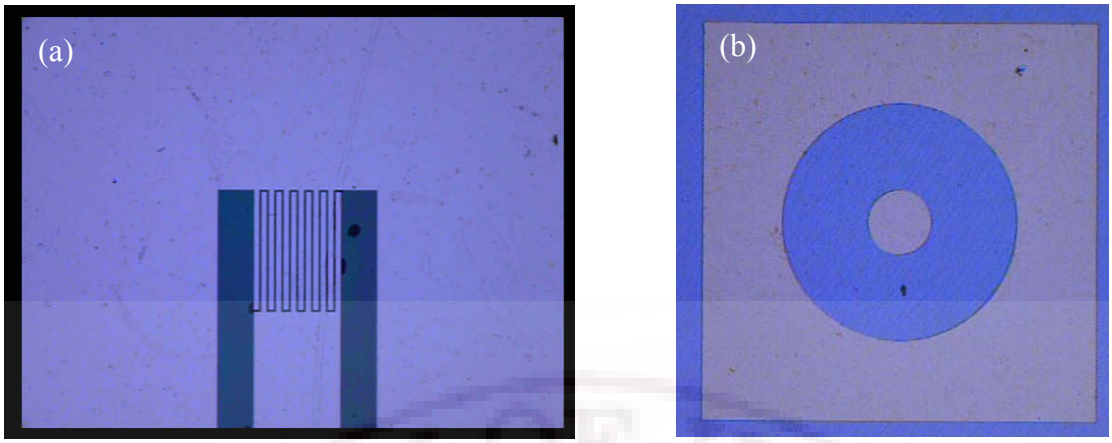

Figure 6.34 Microphotograph of the fabricated (a) IDC and (b) CPC varactors

The optical microscopic images of the realized IDC and CPC varactors using c-BZN thin films were shown in figure 6.34. Agilent 8722ES vector network analyzer (VNA) connected to a J micro technology make RF probe station mounted with GSG probes from GGB industries was used to characterize the microwave properties of the IDC varactors fabricated using the c-BZN thin films deposited on fused silica substrates. Prior to the testing, the 250μm pitch GSG probe was calibrated using the CS-5 calibration substrate from GGB industries.

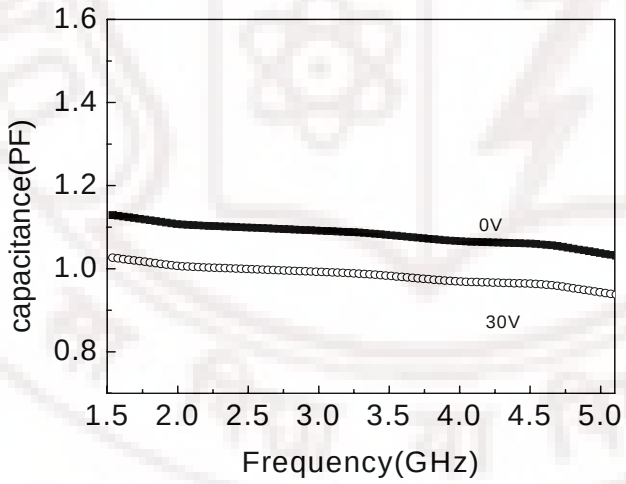

Figure 6.35 Frequency dependence of capacitance for the IDC varactors fabricated using the c-BZN films measured at different bias fields.

Figure 6.35 shows the calculated capacitance from the measured reflection coefficient S_{11} of the IDC varactor. The capacitance is calculated assuming a parallel resistor- capacitor model [54] for which the admittance is given by

$$Y = Y_0 \frac{1 - S_{11}}{1 + S_{11}} = j\omega C \qquad (6.9)$$

Here Y_0 is the reference admittance and S_{11} is the reflection coefficient. The calculated capacitance of the IDC varactor at 4 GHz with 0 V dc bias was 1.067 pF, which has got changed to 0.969 pF by the application of 1.2MV/cm exhibiting a tunability of 9%. The observed quality factor for the IDC varactors at 4GHz was about 38. The quality factor of the c-BZN varactors on amorphous fused silica is comparable to that of the reported quality factors of the BST based varactors [55] on single crystal sapphire substrates.

Agilent 4294A impedance analyzer was used to measure the voltage dependent capacitance and loss tangent values of the CPC varactors fabricated using c-BZN films at low frequencies. A voltage sweep was done from –15 to +15 V for CPC structures. Figure 6.36 shows the capacitance vs. voltage characteristics of the CPC structure fabricated and measured at 1MHz. The capacitance is changed from 60.8 pF at 0 V to 44.58 pF at 15 Volts. Percentage of tunability is defined as

$$n = \left[\frac{(C_{0V} - C_{15V})}{C_{0v}} \right] \times 100 \qquad (6.10)$$

where C_{0v} and C_{15V} are the capacitance at 0Volt and 15 Volts respectively. Hence the tunability is around 25% at 15 Volts bias.

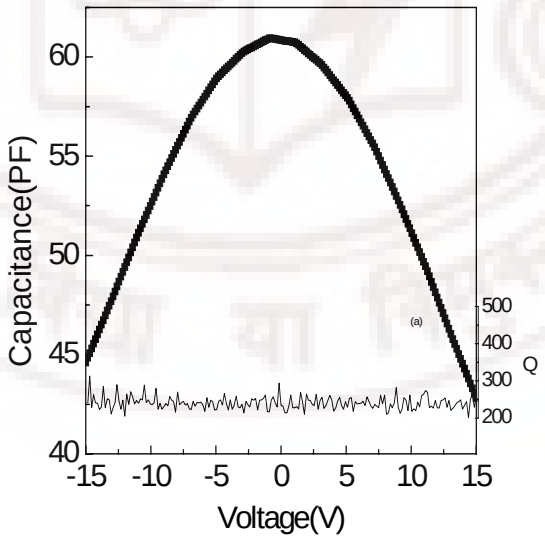

Figure 6.36 Variation of capacitance and loss tangent with voltage for the CPC varactors fabricated using the c-BZN films.

The microwave characteristics of the CPC varactors were determined using the Agilent 8722ES VNA connected to a 250 micron pitch GSG probe mounted on a J micro technology make RF probe station. The complex reflection coefficient of the CPC varactors was measured after the standard short – open - load calibration using the CS-5 calibration substrate. The measured reflection coefficient S_{11} is converted into impedance for the test structure Z_T using [56].

$$Z_T = Z_0 \frac{1+S_{11}}{1-S_{11}} = R + jX \tag{6.11}$$

Here, Z_0 =50 Ohm. The capacitance and loss tangent of the capacitor can be derived from the complex impedance using the following relations:

$$C = -\frac{1}{\omega X} \qquad \tan\delta = -\frac{R}{X} \tag{6.12}$$

The calculated capacitance of the CPC structure is shown in figure 6.37. It can be seen from the figure that the CPC varactor was having a capacitance of 38.78 pF at 5GHz which has changed to 32.32 pF with the application of a bias voltage of 15 V resulting a capacitive tunability of 16.6%.

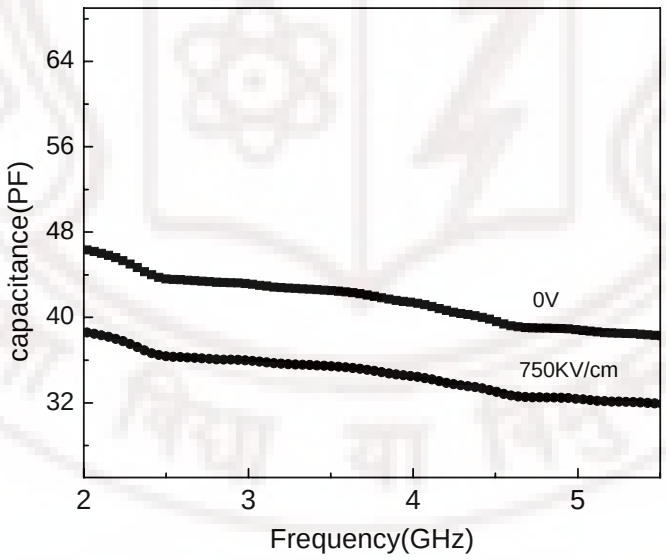

Figure 6.37 Frequency dependence of capacitance for the CPC varactors fabricated using the c-BZN films measured at different bias fields

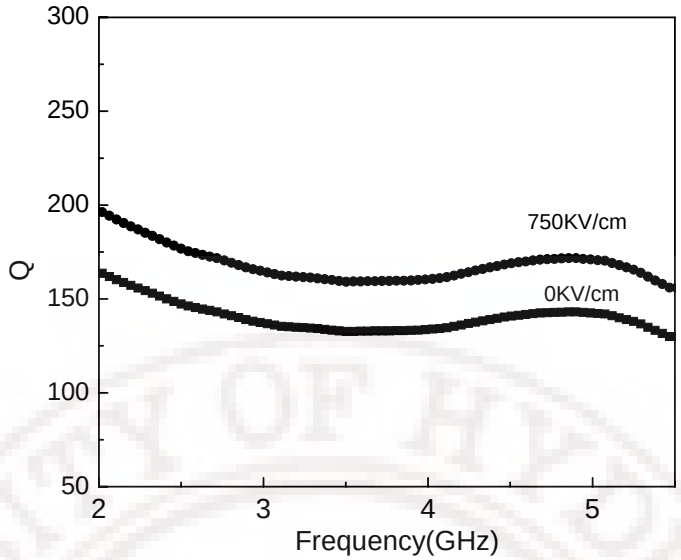

Figure 6.38 Frequency dependence of Q factor for the CPC varactors fabricated using the c-BZN films measured at different bias fields

Interdigitated and parallel plate varactors were fabricated and characterized on fused silica substrates and platinised silicon substrates respectively. The IDC varactors realized on fused silica substrates were having a tunability of 9% with a Q factor of 38. The observed Q factor on fused silica substrates is found to be comparable to the reported Q factor of BST thin films based varactors grown on single crystal sapphire substrates while the tunability was relatively low. The c-BZN thin film on fused silica substrate seems to be a very promising technology for the realization of low cost tunable varactors. It may be possible to improve the Q value further by depositing the films at elevated substrate temperatures since the lower Q value is thought to be due to the thermal strain present in the films. The parallel plate varactors are exhibiting a Q factor of 150 at microwave frequencies (figure 6.38) which is quite high in the microwave region. The observed microwave characteristics of the c-BZN varactors show that they can be potentially used for realisation of tunable microwave devices having high figure of merits.

6.7 Summary

In summary, this chapter presents a detailed study on the dielectric properties of c-BZN and m-BZN thin films grown on various substrates at low frequency as well as at microwave frequencies. The leakage characteristics of these materials in thin film form are also reported systematically in this chapter. The leakage current density of these thin films is found to be in the range of 2-3 $\mu A/cm^2$ at 50KV/cm. From the analysis of the leakage current characteristics, it is concluded that the conduction process in these thin films is predominantly electronic in nature. The leakage current in these thin films were found to be increasing with the increase of annealing temperature and it is attributed to the presence of free electrons in these films produced by the formation of oxygen vacancies due to high temperature annealing. The leakage current is found to be higher for the films deposited at smaller oxygen pressures which are attributed to the presence of large number of oxygen vacancies which will produce free electrons in the films.

The low frequency dielectric properties of these films which are grown directly on substrates such as MgO, fused Silica, $LaAlO_3$ and sapphire (Al_2O_3) are measured using interdigital capacitor geometry. The BZN thin films exhibit different dielectric behaviour when grown on different substrates. The films deposited on sapphire substrates are having larger dielectric constant while the films deposited on fused silica substrates are showing smaller dielectric constant values. From the microstructural analysis of these films it was found that for the films grown on fused silica substrates are having smaller grain size compared to that of the films grown on single crystal substrate. The microstructural dependence of dielectric properties is explained in terms of the change of crystal field caused by the surface bond contraction. From the Raman analysis it was evident that the films grown on these substrates are under different strain state and the reduction of dielectric constant of BZN thin films grown on MgO and fused silica substrates is also attributed to the compressive strain in these films.

The dielectric properties of c-BZN and m-BZN thin films deposited on p-type silicon substrates were studied using the MOS capacitor structures as a function of annealing temperatures. These studies found to be directly relevant to determine suitability of c-BZN and m-BZN thin films as gate dielectric in microelectronic devices and CMOS technology. The high frequency C-V behavior of these films shows the typical n-type MOS action showing accumulation, depletion and inversion behaviors at the BZN -silicon interfaces. The dielectric constant and loss tangent of the c-BZN and m-

BZN thin films are found to be increasing gradually with the annealing temperature. The relatively high dielectric constant of these films with the low dielectric loss tangents exhibited by them even at low annealing temperatures shows that these films can be potentially integrated in to CMOS technology.

The microwave dielectric constant and loss tangent of the as deposited and annealed c-BZN thin films were measured at a spot frequency of 12.15GHz. It is observed that the as deposited amorphous films show low values of dielectric permittivity and loss tangent than that of the annealed crystalline films. The low value of the dielectric constant of these films implies that the formation of the electrical polarization is largely suppressed in the amorphous films. After annealing at 600°C these films exhibit high dielectric constant. It is observed that there is a strong dependence of the microwave dielectric constant and loss tangent (tanδ) on the deposition oxygen pressure. The dielectric constant of c-BZN films varied from 95-126 where as the dielectric loss tangent varied from 0.005 to 0.0075 with a variation of deposition pressure from 1-10 mTorr. The microwave dielectric constant and loss tangent of the annealed m-BZN thin films measured at a spot frequency of 10GHz using the SPDR techniques. It is observed that there is a strong dependence of the microwave dielectric constant and loss tangent (tanδ) on the deposition pressure. The dielectric constant varied from 56-71 where as the dielectric loss tangent is varied from 1.4 $x10^{-3}$ to 2.5 x 10^{-3} as the pressure varied from 2 to 10 mTorr.

Broadband microwave dielectric properties of c-BZN and m-BZN thin films deposited on various substrates were determined using the calibration comparison techniques. Slight frequency dispersions were observed in the measured broadband dielectric properties of these thin films at microwave frequencies. This dispersion is attributed to the extrinsic factors such as the test structures used for the measurements. It has been concluded that the interface of the metal films sitting on top of the films and that sitting on top of the bare substrates are slightly different that is leading to some un compensated resistance or inductance which is responsible for the observed dispersion in the measured data.

The tunability studies on c-BZN thin films shows that the c-BZN thin films grown around 10 mTorr of oxygen pressure is having relatively higher tunability with higher figure of merits a combination suitable for tunable microwave devices. The figure of merits for the thin films deposited above 10 mTorr of oxygen pressure is found to be

decreasing. This may be due to the leakage conduction produced de to the interstitial oxygen atoms as explained in section 6.2. The calculated tunability for the c-BZN thin films deposited on sapphire substrates is approximately around 4.8% at a bias field of 10KV/cm. Similarly the calculated dielectric permittivity for the c-BZN thin films grown on fused silica is 125.73 (at zero bias) and 122.07 (at 10KV/cm bias). The estimated tunability for c-BZN films on fused silica substrate was 2.91% at a measurement frequency of 10 GHz.

Interdigitated and parallel plate varactors were fabricated and characterized on fused silica substrates and platinised silicon substrates respectively. The IDC varactors realized on fused silica substrates were having a tunability of 9% with a Q factor of 38. The observed Q factor on fused silica substrates is found to be comparable to the reported Q factor of BST thin films based varactors on costly single crystal substrates, while the tunability was relatively low. The c-BZN thin films on fused silica substrates seem to be a very promising technology for the realization of low cost tunable varactors.

References

1. T.Ning, Y.Zhou, H.Lu, D.Zhong, G.Yang, H.Wong, *Thin Solid films*, 517,4626 (2009)
2. J.Ryu, K.Yong kim, J.J choi, B.D Hohn, W.H.Yoon, D.S.Park, C.Park, *Journal of the American ceramic society*, 91, 3399(2008)
3. N.A.Hegab, *J. phys D.Appl. phys*, 33, 2356(2000)
4. J.I.Hong, S.M.Hwong and C.S. Hub, *J electromagnetic waves and applications*, 23, 5 (2009)
5. J.J. O'Dwyer, The theory of electrical conduction and break down in solid dielectrics (Clarendon press, 1973)
6. R.H.Fowler and L.W.Nordheim, *Proc.Roy.Soc.London*, A119,173(1928)
7. J.G.Simmons,. *J .Appl.Phys*, 35, 2472(1964)
8. J.Frenkal, *J.Phys.Rev*, 54, 647(1938)
9. A.J.Dekkar, Solid state physics, (prentice hall, UK,1957)
10. F.Yan, H.L.W chan, C.L.Choy, W.Wu, Y.Wong, *Thin solid films*, 406, 200(2002)
11. M.Schumacher, R.Waser, *Integratted ferroelectrics*, 22, 109,(1998).
12. L.Lehovec and G.Shirn, *J.Appl.Phys*, 33, 2036(1962)
13. K.H.Cho, C.H.Choi,J.Y.Choi, T.G.Seong, S.Nahm, C.Y.Kang, J.H Kim, *IEEE Electron device letters,* 29, 984 (2008)
14. K.M.A. Salam, H.Saito, H.Fukuda, *IEEE proceedings IWGI*, 489114, Tokyo (2003)
15. S.Sannian, Z.Jiwer and Xi Yao, *Solid state science*, 9, 1049 (2007)
16. N.A. Pertsev, A.K.Taganstev, N.Setter, *Physical review B*,65,825(2000)
17. S.N.Song, J.W.Zhai, X.Yao, *J.electro ceramics* 21,649 (2008)
18. H.Ye, C.Q.Sun and P.Hing, *J.phys.D.Appl.phys* 33,148(2000).
19. R.S.Katiyar,Y.I.Yuzyuk, *Vibrational spectroscopy*, 45,108(2007)
20. Hanchen.Huang.Texture evolution during thin film deposition, Hand book of materials modeling, Springer, Netherlands (2005)
21. J.C.Nino, W.Qiu and J.L.Jones, *Thin solid films,* 517,4325 (2009).
22. J.Y.Choi,C.H.Choi, K.H.Cho, T.G.Seng, S.Nahm, J.H.Kim, *Acta materialia*, 57, 2454 (2009)

23. T.Ning, Y.Zhou, H.Lu, D.Zhang, G.Yang and H.Wang, *Thin solid films*, 517,4626(2009)
24. E.A.Bobrova and N.M. Omeljanovskya, *Semiconductors*,42,1351(2009)
25. S.C.Rustagi, Z.O.Mohsen, S.Chandra and A.Chand, *Solid state electronics,* 39, 841(1996)
26. J.Park, J.W.Lu, D.S. Boesch ,S.Stemmer and R.A.York, *IEEE Microwave and wireless components Letters*, 16,264(2006)
27. K Venkata Saravanan, K Sudheendran, K.C. James Raju, M. Ghanashyam Krishna and Anil K Bhatnagar, *Vacuum*, 81,307 (2006)
28. M.A Rzepecka and M.A.K Hamid *IEEE Trans.Microw.Theory Tech*, 20, 30(1972)
29. K.Sudheendran and K.C.James Raju, *Ceramic international*, 34,897(2008)
30. J.Park, J.Lu ,S.Stemmer and R.A.York, *Journal of Applied Physics*, 97,084110(2005)
31. J.Park, J.Lu, S.Stemmer and R.A.York, *Integratted ferroelectrics*, 77, 21(2005)
32. R.L.Thayer, C.A. Randall, S.Trolier-Mckinstry, *Journal of Applied Physics*, 94, 1941 (2003)
33. X. Gong, W Han She, Eric E. Hoppenjans, Z. N. Wing, R. G. Geyer, J. W. Halloran, and W. J. Chappell, *IEEE Trans. Micro. Theo.Tech*, 53,3638 (2005)
34. D.Brassard and M.A.Elkhakni*, J.Appl.Phys*, 98, 054912(2005)
35. Hiroya Kitahata, Kiyoharu Tadanaga, Tsutomu Minami, Norifumi Fujimura, and Taichiro Ito, *J.Am.Ceram.Soc*, 81,1357 (1998)
36. J.Xu, W.Menesklou and E.L.Tiffee, *Journal of the European Ceramic Society*, 24, 1735(2004)
37. I.P. Koutsaroff, P.Woo, L. McNeil, M. Zelner, A. Kassam, M.Capanu , L.Chmiel, B. McClelland, and A. Cervin-Lawry, *Proceedings of the 13 th IEEE International Symposium on Applications of Ferroelectrics,* Nara, Japan, 247 (2002)
38. T. R. Taylor and P. J. Hanse B. Acikel, N. Pervez, and R. A. York S. K. Streiffer J. S. Speck , *Applied Physics Letters*, 80, 1978(2002).
39. I. Levin, T.G.Amos, J.C.Nino, T.A.Vanderah, C.A.Randal and M.T.Lanagan, *J.solid state chem*, 168, 69 (2002).
40. Y.M .Tao and Y.Z.Yu, *Journal of Applied Physics*, 101,024111 (2007)

41. J Krupka, A.PGregory, O.C Rochard., R.N Clarke., B Riddle, J Baker-Jarvis, *Journal of the European Ceramic Society*, 10, 2673 (2001).
42. M.A.Subramanian and R.D.Shannon, *Mater.Res.Bull*, 24, 1477(1989).
43. R.D.Shannon, G.R.Rossman, Am. Mineral, 77, 94 (1992)
44. R.D.Shannon *J.Appl.phys* 73,348 (1993)
45. Q.H.Xu, T.Q.Yang, H.W.Qiao,B.Shen, S.H.Diny, X.Yao, *Ferroelectrics*, 356,61 (2007)
46. D.A.Tenne, A.Soukiassian, X.X.Xi, H.Choosciwan and R.Guo and A.S.Bhalla, *Phys.Rev B*, 70,174302(2004)
47. F.Ayaguavives, Z.Jin,A .Tombak, J.Paul Mariya, A.Mortazawi, A.I.Kingon, G.T.Staut et al, *Integrated ferroelectrics*, 39, 393(2001)
48. J.Y.Kim, D.W.Kim, H.S.Jung, K.S.Hong, *J.Europian ceram.Soc*, 26,2161(2005)
49. Y.H.Chun, J.S.Hong, P.Bao,T.J.Jackson,M.J.Lancaster, *IEEE microwave and wireless components letters,*18,167(2008)
50. W.Y.Park and C.S.Hwang, *Applied physics letters*, 85,5313 (2004)
51. J.Park, J.W.Lu, D.S.Boesch, S.Stemmer and R.A.York, *IEEE microwave and wireless components letters*, 16, 264 (2006)
52. X.Y.Zhang, P.Wang, F.Xu and C.K.Ong, *Solid state electronics*, 53,993 (2009)
53. P.Bao, T.J.Jacksen, X.Wang and M.J.Lancaster, *J.Phys.D.Appl.phys*, 41,063001 (2008)
54. Y.L.Cheng, N.Chong, Y.Wang, J.Z.Liu,H.L.W.Chan, C.L.Choy, *Integrated ferroelectrics*, 55,939(2003)
55. .E.A. Faradin, A.S.Holland,K.Ghorbani,W.K.Siman,E.K.Akdogan,and A.afari, *IEEE proceedings of Asia Pacific Microwave conference*, 04429701,(2006)
56. S.Sheng, P.Wang, X.Y. Zhang and C.K.Ong, *J. phys.D:Appl.phys*, 42, 015501(2009)

Chapter 7

Conclusions and scope for future work

7.1 Conclusions

This thesis has investigated the physical, optical and microwave properties of the $Bi_{1.5}Zn_{1.0}Nb_{1.5}O_7$ and $Bi_2Zn_{2/3}Nb_{4/3}O_7$ ceramics and thin films in the Bi_2O_3-ZnO-Nb_2O_5 based pyrochlore system. The increasing demand for the microwave dielectric materials with improved properties suitable for modern integrated circuits was the major motivation for investigating these ceramics materials both in bulk and thin film forms. Bismuth zinc niobate based pyrochlore ceramics and thin films are being considered for many applications ranging from ceramic capacitors to frequency agile microwave devices. So this thesis presents the study of the BZN ceramics and thin films in an inter disciplinary perspective which include aspects of physics, material science and microwave engineering.

The structural, microstructural, dielectric characteristics as well as the Raman characteristics of c-BZN, m-BZN and titanium doped m-BZN ceramics prepared by the solid state route were investigated. The X-ray diffraction study confirms the formation of the cubic pyrochlore structure with all the major peaks corresponding to the Fd3m space group for c-BZN ceramics. It also confirms the monoclinic zirconolite-like structure with all the major peaks indexed to the C2/c space group for m-BZN ceramics. The measured dielectric constant and loss tangent at 1MHz for c-BZN ceramics are 134 and 1.2 $x10^{-3}$respectively and for m-BZN ceramics, 70 and $0.4x10^{-3}$ respectively. For titanium substituted samples, with an increase in Ti content from 0 to 0.4 mole% at B-site, the dielectric constant increased from 75 to 120 while the dielectric loss tangent increased from 0.0004 to 0.061. At higher temperatures, the measured dielectric constant of Ti substituted ceramics shows dispersion and a corresponding peak at the loss tangent. This dispersion-type behavior in the Ti doped m-BZN ceramics is explained by the hopping relaxation phenomenon. The dielectric loss tangent of c-BZN ceramics shows a broad peak at the temperature range of 150 to 200K while m-BZN ceramics shows almost temperature-independent dielectric loss tangent when measured at a frequency of 3GHz. The measured Raman spectra for c-BZN and m-BZN ceramics do not have a very large difference except for a band at 836cm^{-1} which is observed only for m-BZN ceramics.

Thin films in the pyrochlore bismuth zinc niobate system with the composition $Bi_{1.5}Zn_{1.0}Nb_{1.5}O_7$ (c-BZN) and $Bi_2Zn_{2/3}Nb_{4/3}O_7$ (m-BZN) were deposited by pulsed laser deposition on amorphous fused silica substrates as well as on various single crystal substrates. The PLD technique is proven to be a convenient way of growth of stoichiomectric c-BZN and m-BZN thin films with high reproducibility. The processing parameters such as oxygen pressure, annealing temperature, time and the substrate types were correlated to the dielectric and optical properties of these thin films. Through the variation of these processing parameters, optimal deposition conditions for the growth of the films with the required properties are identified.

The chemical compositions of the prepared films were analyzed using the x-ray photoelectron spectroscopy (XPS) and the stoichiomectry analysis were carried out using Energy Dispersive X ray Analysis. The XPS study confirmed the presence of Bi, Zn, Nb,and O near the surface of these thin films and these ions were found to be in their chemical states as Bi^{3+}, Zn^{2+}, and Nb^{5+}respectively. The X-ray diffractograms of c-BZN thin films show the formation of the cubic pyrochlore structure with all the major peaks corresponding to the Fd3m space group and that of m-BZN thin films shows the formation of a monoclinic zirconolite like pyrochlore phase. The crystallite size of the films is found be varying with the oxygen pressure during the processing. The Raman analysis of c-BZN thin films and bulk reveals that the local symmetry in thin films is different from that of the bulk. The change in local symmetry in thin films arises due to strain, which changes the correlation lengths between the dipoles. In m-BZN thin films the anomalous changes in FWHM, intensity, and frequency shift of the two higher frequencies, with Ag modes appearing at 778 and 849 cm^{-1} on varying oxygen pressure suggest polar distortion suppression in the films**.** The as deposited c-BZN thin films exhibit refractive index in the range of 2.36-2.53 with an optical absorption edge value between 3.30-3.52eV. The as deposited m-BZN films exhibit refractive index in the range of 2.06-2.15, with an optical absorption edge value between 3.59-3.67eV. The refractive index of the films increase on annealing, indicating onset of crystallinity. The packing density of these films was found to be increasing with the increase of annealing temperature which in turn results in the increase of refractive index.

The dielectric properties of c-BZN and m-BZN thin films grown on amorphous fused silica substrates were investigated in detail. The leakage characteristics of these materials in thin film form are also reported systematically. The leakage current densities

of these thin films are found to be in the range of 2-3 $\mu A/cm^2$ at 50KV/cm. From the analysis of the leakage current characteristics it is concluded that the conduction process in these thin films is predominantly electronic in nature. The leakage current in these thin films were found to be increasing with the increase of annealing temperature and it is attributed to the presence of free electrons in these films produced by the formation of oxygen vacancies due to high temperature annealing.

The low frequency dielectric properties of these films which are grown directly to the substrates such as MgO, fused silica, $LaAlO_3$ and sapphire (Al_2O_3) are measured using interdigitated capacitor geometry. The BZN thin films exhibit different dielectric behaviour when grown on different substrates. The films deposited on sapphire substrate were having larger dielectric constant while the films deposited on fused silica substrate were showing smaller dielectric constant. From the microstructural analysis of these films it was found that for the films grown on fused silica substrates are having smaller grain size compared to that of the films grown on single crystal substrate. The microstructural dependence of dielectric properties are explained in terms of the change of crystal field caused by the surface bond contraction. Decreasing the particle size will increases the crystal field and subsequently decreases the dielectric constant. From the Raman analysis it was evident that the films grown on these substrates are under different strain states and the reduction of dielectric constant of BZN thin films grown on MgO and fused silica substrates is also attributed to the compressive strain in these films.

The dielectric properties of c-BZN and m-BZN thin films deposited on p-type silicon substrates were studied using the MOS capacitor structures as a function of annealing temperatures. These studies are found to be directly relevant to determine the suitability of c-BZN and m-BZN thin films as gate dielectrics in microelectronic devices and CMOS technology. The high frequency C-V behavior of these films shows the typical n-type MOS action showing accumulation, depletion and inversion behaviors at the BZN silicon interfaces. The dielectric constant and loss tangent of the c-BZN and m-BZN thin films are found to be increasing gradually with the annealing temperature. The relatively high dielectric constant with the low dielectric loss tangents along with the typical MOS action for the films annealed at low temperatures shows that these films can be potentially integrated in CMOS technology.

The microwave dielectric constant and loss tangent of the as deposited and annealed c-BZN thin films were measured at a spot frequency of 12.15GHz using the

extended cavity perturbation technique. It is observed that the as deposited amorphous films show low values of dielectric permittivity and loss tangent when compared to that of the annealed crystalline films. The low value of the dielectric constant of these films implies that the formation of the electrical polarization is largely suppressed in the amorphous films. After annealing at 600°C these films exhibit high dielectric constant. It is observed that there is a strong dependence of the microwave dielectric constant and loss tangent (tanδ) on the deposition oxygen pressure. The dielectric constant of c-BZN films varied from 95-126 where as the dielectric loss tangent varied from 0.005 to 0.0075 with a variation of deposition pressure from 1-10 mTorr. The microwave dielectric constant and loss tangent of the annealed m-BZN thin films were measured at a spot frequency of 10GHz using the SPDR techniques. It is observed that in this case also there is a strong dependence of the microwave dielectric constant and loss tangent (tanδ) on the deposition oxygen pressure. The dielectric constant varied from 56-71 where as the dielectric loss tangent is varied from 1.4 $x10^{-3}$ to 2.5 x 10^{-3} as the pressure varied from 2 to 10 m Torr. Broadband microwave dielectric properties of c-BZN and m-BZN thin films deposited on various substrates were determined using the calibration comparison techniques. Slight frequency dispersions were observed in the measured broadband dielectric properties of these thin films at microwave frequencies. This dispersion is attributed to the extrinsic factors such as the test structures used for the measurements. It has been concluded that the interface of the metal films sitting on top of the films and that sitting on top of the bare substrates are slightly different that is leading to some un compensated resistance or inductance which is responsible for the observed dispersion in the measured data.

The tunability studies on c-BZN thin films shows that the c-BZN thin films grown around 10 mTorr of oxygen pressure is having relatively higher tunability with high quality factor a combination suitable for tunable microwave devices. The quality factor for the thin films deposited above 10 mTorr of oxygen pressure is found to be decreasing. This is attributed to the leakage conduction produced due to the interstitial oxygen atoms. The calculated tunability for the c-BZN thin films on sapphire substrate is approximately around 4.8% at a bias field of 10KV/cm. Similarly the calculated dielectric permittivity for the c-BZN thin films grown on fused silica is 125.73 (at zero bias) and 122.07 (at 10KV/cm bias). The estimated tunability for c-BZN films on fused silica substrate was 2.91% at a measurement frequency of 10 GHz.

Interdigitated and parallel plate varactors were fabricated and characterized on fused silica substrates and platinised silicon substrates respectively. The IDC varactors realized on fused silica substrates were having a tunability of 9% with a Q factor of 38. The observed Q factor on fused silica substrates is found to be comparable to the reported Q factor of BST thin films based varactors while the tunability was relatively low. The c-BZN thin film on fused silica substrate seems to be a very promising technology for the realization of low cost tunable varactors.

Hence in short this study on the growth of BZN thin films on amorphous SiO_2 (fused silica) substrates and the impact of thermal treatments on them will lead to the development of the process technologies for the BZN thin films compatible with Si technology. Industrially compatible fabrication processes are already available for Si and SiO_2. The SiO_2 can be directly deposited on Si substrates or it can be produced by the surface oxidization of the Si substrates. The BZN films can be grown directly on the SiO_2 layer and the required passive circuits can be fabricated on the SiO_2 layer which is a low loss microwave substrate. The active circuits can also be incorporated in the same wafer by exposing Si substrates through the selective etching of the SiO_2 layer. This will be helpful to explore further a cost effective way of integration of tunable microwave circuits in to the existing silicon technology.

7.2 Scope for future work

In future as the $Bi_2Zn_{2/3}Nb_{4/3}O_7$ (m-BZN) and the Ti –doped m-BZN ceramics are found to be able to get sintered below 1000°C, efforts can be initiated to reduce the sintering temperature of these materials by adding some sintering aids and study their microwave dielectric characteristics. So that these materials can be effectively used for LTCC applications. In the present study the BZN thin films grown on fused silica substrates are found to be crystallized at temperature above 500°C. Further efforts such as laser annealing and microwave annealing etc can be tried to reduce the crystallization temperatures further down so that these materials can be effectively incorporated in to polymeric substrates. A temperature dependent I-V and C-V characteristics of these thin films grown on pt could give more light in to the conduction mechanisms. Microwave dielectric properties and tunability characteristics of the *in situ* crystallized BZN thin films can be explored and compared with the present results. To improve the tunability and figure of merits, multilayered and composite films of BST and BZN thin films can be

grown on fused silica substrates and their characteristics can be studied. The non linear optical properties of these thin films can be explored in detail. The growth and dielectric properties of these thin films directly on SiO_2/Si wafers can be explored further. The nano mechanical properties of these thin films are interesting to study. These studies can be extended further to the other pyrochlores such as $Bi_{1.5}Zn_{1.0}Ta_{1.5}O_7$ and $Bi_2Zn_{2/3}Ta_{4/3}O_7$ ceramics and thin films.

List of papers published in journals as a part of this thesis work.

1. **K.Sudheendran**, M.Ghanashyam Krishna and K.C.James Raju. Effect of process parameters and post-deposition annealing on the microwave dielectric and optical properties of pulsed laser deposited Bi1.5Zn1.0Nb1.5O7 thin films Applied physics A Vol 95, 485 (2009).
2. **K.Sudheendran**, K.C James Raju Manoj K. Singh, Ram S. Katiyar. Microwave dielectric and Raman scattering studies on bismuth zinc niobate thin films J. Appl. Phys. **104**, 104104 (2008).
3. **K Sudheendran** and K.C.James Raju Temperature dependent dielectric, impedance and tunability studies on Bismuth Zinc Niobate ($Bi_{1.5}ZnNb_{1.5}O_7$) ceramics" Ceramic international VOL 34, 897-900(2008) .
4. **K.Sudheendran** and K.C.James Raju Realization of Tunable capacitors using ($Bi_{1.5}Zn_{0.5}$)($Nb_{1.5}Zn_{0.5}$)O_7 Thin films, International Journal of micro and nano systems **1,** 45-47**(2009)**
5. **K.Sudheendran** and K.C.James Raju Realization of Tunable varactors using Bismuth Zinc Niobate thin films, Key Engineering materials (in press).
6. **K.Sudheendran,** K.C.James Raju and Mohan.V.Jacob Microwave dielectric properties of Ti substituted Bi_2 ($Zn_{2/3}Nb_{4/3}$)O_7 pyrochlores at cryogenic temperatures, Journal of American ceramic society (in press).
7. **K.Sudheendran** and K.C.James Raju Microwave characterization techniques for tunable high K thin films, Key Engineering materials (in press).
8. K. Venkata Saravanan, **K.Sudheendran**, M Ghanashyam Krishna and K.C.James Raju "Broadband microwave dielectric properties of BST thin films on quartz substrates", Ferroelectrics **356** , 1-8 (2007)
9. K Venkata Saravanan, **K Sudheendran**, M Ghanashyam Krishna and K C James Raju Effect of the amorphous-to-crystalline transition in $Ba_{0.5}Sr_{0.5}TiO_3$ thin films on optical and microwave dielectric properties J. Phys. D: Appl. Phys. 42 045401 (2009).
10. **K.Sudheendran**, D Pamu, M Ghanashyam Krishna, K.C.James Raju, Determination of dielectric constant and loss of high-K thin films in the microwave frequencies (communicated)
11. **K.Sudheendran**, Manoj K Singh, K.C.James Raju Ram S Katiyar Effect of oxygen atmosphere to the polar distortion suppression and microwave dielectric properties $Bi_2Zn_{2/3}Nb_{4/3}O_7$ thin films(communicated)
12. **K.Sudheendran**, M Ghanashyam Krishna, Manoj K Singh, and K.C.James Raju, Microwave and optical properties of pulsed laser deposited monoclinic $Bi_2Zn_{2/3}Nb_{4/3}O_7$ thin films(communicated)
13. **K.Sudheendran**, Manoj K Singh, K.C.James Raj, and R S Katiyar Raman scattering and dielectric studies on Ti substituted Bi_2 ($Zn_{2/3}Nb_{4/3}$)O_7 pyrochlores (communicated)

List of papers published in journals which are not part of this thesis work

14. D.Pamu, **K.Sudheendran**, M.Ghanashyam Krishna and K.C.James Raju Optical and microwave characteristics of ambient temperature deposited Zirconium Tin Titanate high-k films, European Physics:Journal of Applied Physics(in press)

15. D.Pamu. **K.sudheendran**, M.Ghanashyam Krishna and K.C.James Raju Crystallographic texture, morphology, optical and microwave dielectric properties of DC magnetron sputtered nanostructured zirconia thin films, Journal of vacuum science and technology A 26, 185 (2008).

16. D. Pamu, **K. Sudheendran**, M. Ghanashyan Krishna, K. C.James Raju, AnilK.Bhatnagar Ambient temperature stabilization of crystalline Zirconia thin films deposited by direct current magnetron sputtering Thin solid fims,517,1587-1591(2009).

17. G.V.Ramesh, **K.sudheendran**,K.C.James Raju,B.sreedhar and T.P Radha Krishnan "Microwave absober based on Silver Nanoparticle Embedded polymer thin film Journal of Nano science and Nanotechnology Volume 9, Number 1, , pp. 261-266 (2009).

18. K Venkata Saravanan, **K Sudheendran**, K.C. James Raju, M. Ghanashyam Krishna and Anil K Bhatnagar, Structural, optical and microwave properties of solgel derived barium strontium titanate thin films, J material chemistry and physics **105** ,426-432 (2007) .

19. K Venkata Saravanan, **K Sudheendran**, K.C. James Raju, M. Ghanashyam Krishna and Anil K Bhatnagar Effect of process parameters and post deposition annealing on the optical, structural and microwave dielectric properties of RF magnetron sputtered $(Ba_{0.5},Sr_{0.5})TiO_3$ thin films. Vacuum 81, 307-316 (2006)

20. Pamu, **K.Sudheendran**, M.Ghnashyam Krishna, K.C.James Raju and Anil K Bhatnagar "Microwave dielectric behaviour of nanocrystalline Titanium dioxide thin films"., Vacuum ,81, 686-694 (2007).

21. V.Madhurima, **K.Sudheendran** and K.C.James Raju The possible formation of nano-clusters of succinic acid and maleic acid in tetrahydofuran due to in complete solvation Molecular simulation Vol 33 No 14 , 1119-1128 (2007).

22. V. Madhurima. **K.Sudheendran** & K.C.James Raju, "Dielectric studies of some nanoconfined liquid thin-films, J.Molecular liquids 133,28-32 (2007) **.**

23. V.Madhurima. **K.Sudheendran** & K.C.James Raju, Ab initio and dielectric studies of succinic acid and maleic acid in 1,4-dioxane. Molecular Simulation Vol.32 No.5, 331-337 (2006).

24. Charanjeet singh,Sukhleen Bindra-Narang,I S Hudiara,K.C.James Raju **K.Sudheendran** Complex permittivity and complex permeability of Sr ions substituted Ba ferrites at X-band. *Journal of magnetism and Magnetic materials VOL* 320,1657-1665,(2008) .

25. M S R N Kiran, **K Sudheendran**, M.Ghanashyam Krishna, K C James Raju, Anil K Bhatnagar "Chromium and nickel substituted iron oxide thin films by DC sputtering, Vacuum 81,133-137 (2006).

26. **K.Sudheendran** and K.C.James Raju. Temperature dependent impedance and dielectric properties of 0.7 $CaTiO_3$ –0.3$NdAlO_3$ ceramics Indian journal of Engineering and material Science **15** 133-136 (2008).

List of papers published in peer reviewed conference proceedings

1. **K.Sudheendran,** K.Venkatasaravanan, K.C.James Raju, M.Ghanashyam Krishna and Anil K Bhatnagar, **"**Microwave Behavior of Compositionally Modulated Barium Titanate based Thin Films for Rf-MEMS Applications**"** Proceedings of ISSS 2005 International Conference on Smart Materials, Structures and Systems, Vol.2, Pages SC-85 – SC-91 July 28-30 2005, Indian Institute of Science, Bangalore, India**.**
2. **K.Sudheendran**, K.C.James Raju, M.Ghanashyam Krishna and Anil K Bhatnagar "Microwave permittivity measurements of materials using a partially filed waveguides" Proceedings of XXVIIIth Genaral Assembly of International Union of Radio Sciences (URSIGA 2005) October 23-29 2005,New Delhi, India**.**
3. **K. Sudheendran**, D. Pamu, K.C.James Raju, M. Ghanashyam Krishna and Anil K.Bhatnagar "Determination of the microwave dielectric permittivity of thin films using the extended cavity perturbation technique." . Proceedings of Asia-Pacific Microwave Conference (APMC-2004), APMC/04/C/421
4. **K.Sudheendran**, and K.C.James Raju, *"Microwave dielectric properties of* $xCaTiO_3$-$_{(1-x)}NdAlO_3$ *ceramics"*. Proceedings of the DAE-Solid State Physics Symposium-2005. December 5-9 2005, Bhabha Atomic Research Center, Tata Institute of Fundamental Research, Mumbai, India.
5. K.C.James Raju and **K.Sudheendran** Tunable materials and their microwave characterization Proceedings of International Conference on Recent Advances in Microwave Theory and Applications, 978-1-4244-2690-4, IEEE P 378-381 (2008),
6. Karan, N. K. Pradhan, D.K. Saavedra-Arias, J. J. Murari, N. M. Thomas, R. Katiyar, R S. **Sudheendran**, **K**. Raju K.C.J. Effect of Sr substitution on tunability and dielectric properties in Pb(Zr0.50Ti0.50)O3 thin films fabricated by chemical solution deposition 17th IEEE International Symposium on the Applications of Ferroelectrics, Vol: 3 p 1-3 Feb (2008)

Papers presented in National and international conferences

1. **K.Sudheendran**, K, Venkata Saravanan, D Pamu, M Ghanashyam Krishna and K.C.James Raju, "Size dependence of the microwave dielectric properties of oxide thin films" presented in Nano2006 Aug 21-25 ISSC Bangalore.
2. **K Sudheendran** and K.C.James Raju "Temperature dependent dielectric, impedance and tunability studies on Bismuth Zinc Niobate ($Bi_{1.5}ZnNb_{1.5}O_7$) ceramics". Presented in AMEC 5 Thailand (december2006).
3. **K Sudheendran**, K.Venkata Saravanan ,M Ghanashyam Krishna and K.C.James Raju, "Broadband characterization techniques for dielectric and metallic thin films at microwave frequencies". presented at International symposium on Microwaves, Bangalore ,December 2006.
4. **K.Sudheendran** and K.C.James Raju, "Bulk and thin films of bismuth Zinc niobate for microwave device applications", International conference on Advanced materials and composites, Thiruvanathapuram, October 24-26,2007.
5. **K.Sudheendran**, M.Ghanashyam Krishna and K.C.James Raju "Tunable microwave dielectric properties in a non ferroelectric material: Bismuth Zinc Niobate", 10 th international conference on advanced materials IUMRS –ICAM 2007, Bangalore 8-13 october,2007
6. **K.Sudheendran** and K.C.James Raju "Realization of tunable varactors using $Bi_{1.5}Zn_{1.0}Nb_{1.5}O_7$ thin films". Presented in AMEC-6 ,Tsukuba, Japan, october 2008.
7. **K.Sudheendran** and K.C.James Raju "microwave charecterization technique for high K thin films" presented in AMEC-6 ,Tsukuba, Japan, october 2008
8. M. V. Jacob, **K. Sudheendran**, K.C. James Raju and Janina Mazierska, "Bi2 (Znx/3Nby/3)O7 Ceramics – A High Permittivity Microwave Dielectrics for Electronics Application" (APMC – Hong Kong, December 2008).
9. **K. Sudheendran**, K.C. James Raju and M. V. Jacob, "Bi2 (Zn2/3Nb4/3)O7 Ceramics and Thin Films as a Possible High -K Microwave Dielectrics for Electronics Application" (IUMRS-ICEM 2008, Sydney July 27- Aug. 1, 2008).
10. **K.Sudheendran**, G. Lakshmi Narayana Rao, K. C. James Raju, M.Ghanashyam Krishna, and A.K.Bhatnagar "A microwave characterization technique for thin film ferroelectrics", Presented at 13th National Seminar on Ferroelectrics and Dielectrics, University of Delhi, New Delhi, 23-25 November, 2004
11. **K.Sudheendran,** K.Venkata Saravanan,M Ghanashyam Krishna and K.C.James Raju, "Characterization techniques for thin film ferroelectrics in the microwave range", ,Presented in the national seminar on advances in electroceramics, Pune, may 5-6 ,2006.
12. **K.Sudheendran,** K,Venkata Saravanan,M Ghanashyam Krishna and K.C.James Raju, " Measurement of microwave dielectric properties of BST thin films on low K substrates for tunable microwave devices" Proceedings of the National conference on ferroics (NCF-2006) CVR college, Hyderabad India.
13. **K.Sudheendran**, K, Venkata Saravanan, M Ghanashyam Krishna and K.C.James Raju "Microwave characterization of ferroelectric thin films using CPW based transmission lines and the extraction of the conductor losses". presented in microwaves 2006, University of Rajasthan, Jaipur

14. **K.Sudheendran**, D Pamu, K Venkata Saravanan, M Ghanashyam Krishna and K.C James Raju Broadband Microwave characterization of Nano CrystallineTiO_2 and BST thin films presented in NSFD 2006 at IIT Kharagpoor in December 2006.
15. **K .Sudheendran** and K.C.James Raju Temperature dependent impedance and dielectric properties of 0.7 $CaTiO_3$ –0.3$NdAlO_3$ ceramics presented in NSFD 2006 at IIT Kharagur in December 2006
16. **K.Sudheendran** and K.C.James Raju "Dielectric properties and leakagecharacteristics of pulsed laser deposited $Bi_2(Zn_{1/3}Nb_{2/3})_2O_7$ thin films" (NSFD 15,patiyala November 2008)

Credentials/awards

- **AMEC-6 young scientist award:** Presented during the 6th Asian meeting on electro ceramics held at Tsukuba, Japan during October 2008, in recognition to an oral presentation entitled " Microwave charecterization technique for High K thin films.